Alma Mater Studiorum – Università di Bologna

DOTTORATO DI RICERCA IN

AUTOMOTIVE PER UNA MOBILITÀ INTELLIGENTE

Ciclo 34

Settore Concorsuale: 09/C1 – MACCHINE E SISTEMI PER L'ENERGIA E L'AMBIENTE

Settore Scientifico Disciplinare: ING-IND/08 – MACCHINE A FLUIDO

OPTIMIZATION AND DEVELOPMENT OF LOW ENVIRONMENTAL IMPACT PROPULSION SYSTEMS

Presentata da: Francesco Scrignoli

Coordinatore Dottorato

Prof. Nicolò Cavina

Supervisore

Prof. Enrico Mattarelli

Co-supervisore

Prof. Carlo Alberto Rinaldini

Esame finale anno 2022

Contents

List of Figures

List of Tables

Acknowledgements

The Institut für Verbrennungskraftmaschinen und Thermodynamik (IVT) at Technischen Universität Graz (TUGraz) is acknowledged for the stage proposed to the Ph.D. candidate for his research period abroad.

ANSYS is acknowledged for the ANSYS Academic license granted to the University of Modena and Reggio Emilia.

MathWorks is acknowledged for the MATLAB Academic license granted to the University of Modena and Reggio Emilia.

GAMMA TECHNOLOGIES is acknowledged for the GT-SUITE license granted to the University of Modena and Reggio Emilia.

Abstract

Achieving the carbon neutrality by the middle of the century is essential for our Planet, in order to keep the global warming below the threshold of 1.5 °C. For accomplishing this mission, all the economic sectors should invest in renewable energies, high efficiency energy conversion systems and green technologies in general.

As far as the transport sector is concerned, the research community, both in industry and academia, is focused on the reduction of carbon dioxide (CO_2) and pollutant emissions. A portfolio of innovative technologies, tailored on the specific characteristics of each field of application, appears as the best way to get the climate neutrality of the transport sector in the short and medium term. Despite the rise of electrical mobility for passenger cars, the internal combustion engine (ICE) can still play a fundamental role to reduce the greenhouse gas emissions. It should be considered that the path of electrification for commercial vehicles, boats, ships, off-road vehicles, aircraft is still very long and problematic. Moreover, in many places of the world, internal combustion engines are the only way to get the electric energy. Therefore, it is absolutely necessary to develop innovative solutions able to reduce (and possibly avoid) the use of fossil fuels, and to enhance the fuel conversion efficiency.

From this point of view, the Compression Ignition (CI) engine is particularly interesting, since it can provide high values of Brake Thermal Efficiency (BTE). Moreover, in comparison to Spark Ignition (SI) engines, this type of combustion can be more easily adapted to run on a variety of low carbon fuels, biofuels, et cetera. Unfortunately, the conventional CI (Diesel) engines are also characterised by higher nitrogen oxides (NO_x) and soot emissions than SI engines.

Low Temperature Combustions, and in particular Dual Fuel (DF) pilot-ignited and Reactivity Controlled Compression Ignition (RCCI) combustions are the most promising techniques to abate NO_x and soot emissions from CI engines. In both combustion concepts, a lean premixed charge, composed by air and a low reactivity fuel, is ignited by a small amount of high reactivity fuel, directly injected in the combustion chamber. A further improvement in terms of CO_2 and pollutant emissions can be obtained employing low carbon or renewable fuels, such as Natural Gas (NG) and biogas, respectively. However, some issues still need to be addressed before DF pilot ignited and RCCI combustions can be effectively applied to production engines. Hence, further investigations are required.

Based on the considerations discussed above, the main goal of this research activity, carried out during the Ph.D. course, was to investigate DF combustion, in order to understand the peculiarities of the concept, exploit its advantages and finally propose solutions able to mitigate its defects.

First of all, a comprehensive experimental campaign was performed on an automotive Diesel engine, modified in order to operate in DF NG-diesel combustion mode. Four operating points were selected, covering the range between low and medium-high loads (BMEP = 2, 4, 8 and 12 bar, corresponding to 44, 88, 177 and 265 Nm), at 3000 rpm. The experimental results show that DF NG-diesel combustion is effective at medium-high loads. Here, higher BTE and lower CO_2, NO_x and soot emissions, compared to Normal Diesel (ND) operation, were observed. Conversely, at low loads, a strong worsening of BTE was found, due to the overly lean NG-air premixed charge.

To gain a better understanding on DF combustion, a numerical study was performed, by means of a customized version of the KIVA-3V code. The study was focused on the diesel injection strategy, with a substitution rate of diesel with NG equal to 60% (in terms of energy, with respect to the ND operation). The operating condition is 3000 rpm – BMEP=12 bar. It was found that the number of diesel injections per cycle has negligible effects on performance and emissions, except on CO and soot, that can be minimised with a triple diesel injection strategy (the same adopted in the experimental activity). As far as the Start Of Injection (SOI) is concerned, a performance improvement can be obtained by advancing the diesel SOI, but at the expense of higher NO_x emissions.

Then, the attention was shifted to low load operations (3000 rpm – BMEP = 2 bar), on the DF case with the highest substitution rate of diesel with NG: here, the highest drop of BTE was observed during the experimental activity. The addition of hydrogen (H_2) to the NG-air mixture was numerically investigated by means of the commercial code ANSYS Forte. The results show that H_2 is an effective combustion enhancer for NG, able to extend the lower flammability limit of the lean NG-air premixed charge. As a consequence, carbon monoxide (CO) and Unburnt Hydrocarbons (UHC) emissions and BTE, can be strongly improved, compared to the reference DF NG-diesel case. Unfortunately, the above-mentioned enhancement was not enough to reach the efficiency and levels of CO and UHC emissions in ND operation. Therefore, a further numerical study was carried out with the aim to optimise the diesel injection strategy in terms of number of injections per cycle, SOI of each injection and diesel mass distribution among the

injections. Moreover, a sensitivity analysis to the swirl ratio was performed. A further strong improvement of BTE and CO and UHC emissions were observed with a double diesel injection strategy characterised by SOI1 = -35 °CA AFTDC, SOI2 = -20 °CA AFTDC, injection 1 diesel mass fraction equal to 0.6 and swirl ratio equal to 1.4.

A further step was to investigate the interchangeability between NG and biogas. The two gases have a different Wobbe index. Moreover, the biogas composition is extremely dependent on the biomass used for its production. The numerical study was carried out using KIVA-3V on the DF case with the highest substitution rate of diesel with NG, at 3000 rpm – BMEP = 8 bar. The results demonstrate that DF combustion is weakly affected by the change of the low reactivity fuel. Moreover, a slight modification of the diesel SOI is sufficient to restore the performance of the reference DF NG-diesel case.

One of the main limits of DF engines is the lower power density with respect to conventional Diesel engines. In fact, as the amount of low reactivity fuel increases, peak in-cylinder pressure and peak pressure rise rate tend to become too high. As a matter of fact, it is very hard to get a regular DF combustion at high/full loads, limiting the maximum engine power. Moreover, the lower the octane number of the low reactivity fuel, the lower the maximum power achievable. This shortcoming can be avoided, or at least mitigated, by switching from the 4-Stroke to the 2-Stroke cycle. Obviously, a specific design of the 2-Stroke engine is required.

This is the reason for studying the application of DF combustion to a novel 2-Stroke high-speed direct-injection loop scavenged Diesel engine. In particular, a preliminary investigation, performed by means of ANSYS Forte, was performed for the evaluation of the best technique to inject gasoline, minimising the fuel wall film on the intake ducts walls and the fuel short-circuiting during the scavenging process. It was found that the best solution is the Low-Pressure Direct-Injection, with the injectors oriented towards the cylinder head.

Finally, a part of the research activity was devoted to the study and optimization of the coupling between the thermal engine and the electric motor, in a hybrid powertrain. The study case was the Formula Student car of the University of Modena and Reggio Emilia, developed in two alternative configurations: the Combustion vehicle equipped with a conventional 4-cylinder SI engine, and the Hybrid car, with a power-unit made up of a single cylinder engine connected to an electric motor. The numerical comparison between the two race cars in terms of lap performance and CO_2 emissions, is based on the simulation of the Endurance event of the Formula Student UK competition. The telemetry data of the Combustion vehicle were used to

build and calibrate a 0D MATLAB-Simulink model. The comparison show that the hybrid vehicle not only yields lower CO_2 emissions, but it is able also to improve the average lap time during the Endurance event.

Nomenclature

Abbreviations and Acronyms

AFTDC	After Firing Top Dead Center
BDC	Bottom Dead Center
BEV	Battery Electric Vehicle
CDC	Conventional Diesel Combustion
CFD	Computational Fluid Dynamics
CI	Compression Ignition
COP	Conference of the Parties
CV	Combustion Vehicle
DF	Dual Fuel
DME	Dimethyl Ether
DOC	Diesel Oxidation Catalyst
DOS	Diesel Oil Surrogate
ECU	Electronic Control Unit
EGR	Exhaust Gas Recirculation
EPC	Exhaust Port Closing
EPO	Exhaust Port Opening
EU	European Union
EVO	Exhaust Valve Opening
FCEV	Fuel Cell Electric Vehicle
GDI	Gasoline Direct Injection
GHG	Greenhouse Gas

HACA	H-Abstraction-C_2H_2-Addition
HCCI	Homogeneous Charge Compression Ignition
HD	Heavy Duty
HEV	Hybrid Electric Vehicle
HRF	High Reactivity Fuel
HSDI	High-speed Direct-Injection
HTO	High Temperature Oxidation
ICE	Internal Combustion Engine
IPC	Intake Port Closing
IPO	Intake Port Opening
IVC	Intake Valve Closing
KH-RT	Kelvin-Helmholtz-Rayleigh-Taylor
LFL	Lower Flammability Limit
LPDI	Low Pressure Direct Injection
LRF	Low Reactivity Fuel
LTC	Low Temperature Combustion
LTO	Low Temperature Oxidation
ND	Normal Diesel
NDCs	Nationally Determined Contributions
NDIR	Nondispersive Infrared detector
NG	Natural Gas
PAH	Polycyclic Aromatic Hydrocarbons
PaSR	Partially Stirred Reactor
PCCI	Premixed Charge Compression Ignition

PFI	Port Fuel Injection
PM	Particulate Matter
PN	Particle Number
RANS	Reynolds-Averaged Navier Stokes
RCCI	Reactivity Controlled Compression Ignition
RNG	Renormalization Group
SI	Spark Ignition
TDC	Top Dead Center
TFC	Turbulent Flame Closure
UHC	Unburnt Hydrocarbons
VGT	Variable Geometry Turbine

Chemical formulae

CH_4	methane
C_2H_2	acetylene
C_2H_5	ethyl radical
C_2H_6	ethane
C_3H_8	propane
C_4H_{10}	butane
C_5H_{12}	n-pentane
C_6H_5	phenyl radical
C_6H_6	benzene
C_6H_{14}	n-hexane
C_7H_8	toluene
C_7H_{16}	n-heptane

C_8H_{18}	iso-octane
$C_{10}H_{22}$	n-decane
$C_{11}H_{10}$	1-methyl naphthalene
$C_{12}H_8$	acenaphthylene
CO	carbon monoxide
CO_2	carbon dioxide
H_2	hydrogen
HO_2	hydridodioxygen(+1)
H_2S	hydrosulfuric acid
N_2	nitrogen
NO	nitric oxide - nitrogen monoxide
NO_2	nitrogen dioxide
NO_x	nitrogen oxides
N_2O	nitrous oxide - dinitrogen oxide
O_2	oxygen
OH	hydroxyl radical
Pd	Palladium
Pt	Platinum

Symbols and Units

AFR	Air-to-Fuel Ratio (-)
AHR	Apparent Heat Release (J)
AHRR	Apparent Heat Release Rate (J/°)
BMEP	Brake Mean Effective Pressure (bar)
BSFC	Brake Specific Fuel Consumption (g/kWh)

BTE	Brake Thermal Efficiency (%)
CA5	Crank Angle corresponding to MFB5 (°)
CA10	Crank Angle corresponding to MFB10 (°)
CA10-90	Angular interval between CA10 and CA90
CA50	Crank Angle corresponding to MFB50 (°)
CA90	Crank Angle corresponding to MFB90 (°)
°CA	degree Crank Angle (°)
CAD	Crank Angle Degree (°)
CN	Cetane Number (-)
CO	concentration of carbon monoxide (ppm)
COV	Coefficient Of Variation (%)
E_{in}	Energy provided to the engine by means of the fuel(s) (J)
FMEP	Friction Mean Effective Pressure
GITE*	Gross Indicated Thermal Efficiency evaluated between IVC and EVO (%)
IMEP*	gross Indicated Mean Effective Pressure evaluated between IVC and EVO (bar)
ITE	Indicated Thermal Efficiency (%)
k	turbulent kinetic energy (m^2/s^2)
LHV	Lower Heating Value (MJ/kg)
LHV_{CO}	carbon monoxide Lower Heating Value (MJ/kg)
LHV_D	Diesel fuel Lower Heating Value (MJ/kg)
LHV_{H_2}	hydrogen Lower Heating Value (MJ/kg)
LHV_{NG}	Natural Gas Lower Heating Value (MJ/kg)

LHV_{H_2+NG}	hydrogen-Natural Gas mixture Lower Heating Value (MJ/kg)
m_{CO_EVO}	mass of carbon monoxide at Exhaust Valve Opening (mg)
m'_D	mass of Diesel fuel provided to the engine per cycle in dual fuel operation (mg)
m_D	mass of Diesel fuel provided to the engine per cycle in normal Diesel operation (mg)
$m_{H_2\_EVO}$	mass of hydrogen at Exhaust Valve Opening (mg)
m_{NG}	mass of Natural Gas provided to the engine per cycle in dual fuel operation (mg)
m_{H_2+NG}	mass of hydrogen- Natural Gas mixture provided to the engine per cycle in Dual Fuel operation (mg)
m_{UHC_EVO}	mass of Unburnt Hydrocarbons at Exhaust Valve Opening (mg)
$\dot{m_{air}}$	air mass flow rate delivered to the engine (kg/s)
$\dot{m_D}$	Diesel fuel mass flow rate (g/s)
$\dot{m_{NG}}$	Natural Gas mass flow rate (g/s)
ON	Octane Number (-)
P_{in}	Power provided to the engine by means of the fuel(s) (kW)
PPRR	Peak Pressure Rise Rate (bar/°)
RLHV	Relative Lower Heating Value (MJ/kg)
RoHR	Rate of Heat Release
RON	Research Octane Number
$\bar{S}_{FP}$	mean flame propagation speed (m/s)
SoC	State of Charge (%)
SOI	Start Of Injection (°CA)

SOI1	Start Of Injection of the first injection (°CA)
SOI2	Start Of Injection of the second injection (°CA)
SR	Swirl Ratio (-)
$X_D[\%]$	fraction of energy provided by Diesel fuel in dual fuel mode (%)
$X_{NG}[\%]$	fraction of energy provided by Natural Gas in dual fuel mode (%)
UHC	concentration of methane equivalent Unburnt Hydrocarbons (ppm)
V_d	engine unit displacement (m3)
Wl	lower Wobbe index (MJ/m^3)

Greek symbols

α_s	stoichiometric air-to-fuel ratio (-)
ε	dissipation rate of turbulent kinetic energy (m^2/s^3)
η_c	combustion efficiency (%)
λ_{NG-air}	lambda of the premixed NG-air mixture (-)
ϕ	equivalence ratio

Subscripts and Superscripts

c	combustion
D	Diesel fuel
H_2	hydrogen
H_2-NG	hydrogen-Natural Gas mixture
NG	Natural Gas
NG-air	Natural Gas-air mixture
s	stoichiometric

Dimensionless Numbers

Oh	Ohnesorge number → viscous / (inertia · surface tension)$^{(1/2)}$ force ratio

Re	Reynolds number → inertia / viscous force ratio
T	Taylor number → $Oh\sqrt{We}$
We	Weber number → inertia / surface tension force ratio

1 Introduction

In 2015, in response to the increasing concerns related to global warming and environmental degradation, the member Countries of the UNFCCC (United Nations Framework Convention on Climate Change) signed the so-called Paris Agreement, during the 21st Conference of the Parties (COP21). In detail, the member Countries agreed to work together to limit the average global temperature increase to 1.5 °C. In order to reach this goal, every Country agreed to draw up the "Nationally Determined Contributions" (NDCs), namely, the plans that define the strategies to reduce Greenhouse Gas (GHG) emissions.[1]

However, what has been done so far is not sufficient to comply with the Paris Agreement. Indeed, scientists warn that the average increase of the global temperature compared to the pre-industrial era could rise even up to 4 °C by 2100 if a carbon-neutral economy will not be reached by the middle of the century.[2]

Therefore, during the 26th Conference of the Parties (COP26) in 2021, Countries were asked to strengthen their actions to limit global warming to 1.5 °C. In particular, they must halve GHG emissions of all the economic sectors over the next decade and reach net zero carbon emissions by 2050. To accomplish this mission, Countries must dismiss coal and invest, and encourage investments, in renewable energies. Furthermore, it is essential to stop deforestation, since forests are able to capture huge amounts of carbon dioxide (CO_2), playing a crucial role against climate changes.[3]

As far as the European Union (EU) is concerned, in July 2021 it delivered the "European Green Deal",[4] namely, the path to make Europe the first climate-neutral continent in a fair, cost effective and competitive way. Such commitment is reaffirmed in the "NextGenerationEU" recovery plan,[5] which aims at promoting the use of renewable energies, increasing energy efficiency and investing on research to develop environmentally friendly technologies and greener vehicles.

Focusing on the transport sector, and in particular on the automobile sector, Fuel Cell Electric Vehicles (FCEV) and Battery Electric Vehicles (BEV) could represent the best technologies to achieve the above-mentioned objectives, since they guarantee zero CO_2 and pollutant emissions, provided that hydrogen (H_2) and the electrical energy used to charge the batteries are produced using renewable sources (hydropower, solar and wind are the most important),

without CO_2 emissions. In particular, H_2 should be produced recovering the excess of energy generated from solar and wind, optimizing the use of intermittent renewables.[6]

However, the share of renewable sources in global electricity production reached only 29% in 2020,[7] as shown in Figure 1,[8] while just 4÷5 % of global H_2 is produced by means of renewable electricity (the so-called green hydrogen).[9]

Moreover, many issues concerning the availability of the raw materials required for battery manufacturing, the battery disposal and the management of an extremely higher electrical energy demand, connected to a full electric mobility, still need to be addressed.

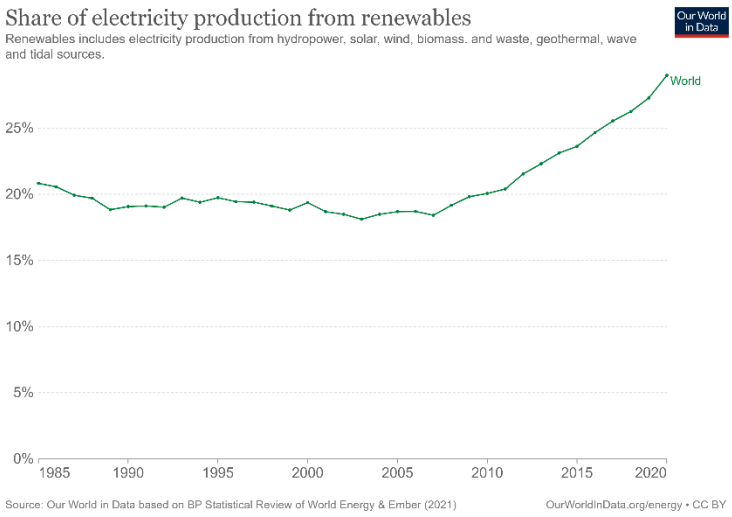

Figure 1. Share of electricity production from renewables[8]

A portfolio of innovative technologies, tailored on the specific characteristics of each field of application, appears as the best way to get the climate neutrality of the transport sector in the short and medium term. The internal combustion engine (ICE) can still play a fundamental role to reduce the GHG emissions, provided that its CO_2 and pollutant emissions are fully cancelled or at least strongly reduced. It should be considered that the path of electrification for commercial vehicles, boats, ships, off-road vehicles, aircraft is still very long and problematic. Moreover, in many places of the world, internal combustion engines are the only way to get the electric energy. In this scenario, the Compression Ignition (CI) engine is particularly interesting, since it can provide high values of Brake Thermal Efficiency (BTE). Moreover, in comparison to Spark Ignition (SI) engines, this type of combustion can be more easily adapted to run on a variety of low carbon fuels, biofuels, et cetera. Unfortunately, the conventional CI engines

(referred to as Diesels), are also characterised by higher nitrogen oxides (NO_x) and soot emissions than SI engines. Therefore, it is fundamental to find solutions able to mitigate the environmental impact of the CI engine, keeping or even improving its efficiency.

In order to make the ICE able to face the current and future challenges, the research community is focused on the following technologies:

- low temperature combustions;[10–12]
- pre-chamber combustion;[13]
- Miller/Atkinson cycle;[14]
- variable compression ratio;[15]
- engine waste heat recovery (Rankine cycle[16] and electric turbo-compound[17]);
- integration with electric motors (hybridization).

Hybridization is already widely applied to automobiles. It permits to skip the low efficiency ICE operations (i.e., very low or very high loads) thanks to an Electric Motor (EM) that assists the thermal unit, strongly reducing fuel consumption, hence CO_2 and local pollutant emissions, especially in urban driving. Moreover, thanks to the regenerative braking, a hybrid powertrain can recover part of the kinetic energy dissipated during braking, converting it into electric energy, stored in the battery pack. The use of this "free" energy further increases the overall efficiency of the powertrain.

Another promising technology is represented by the so-called Low Temperature Combustions (LTC), with particular reference to Dual Fuel (DF) pilot-ignited and Reactivity Controlled Compression Ignition (RCCI) combustions, which are described in Section 2. Such combustion strategies are able to strongly reduce NO_x and soot emissions of CI engines, while improving their BTE, as demonstrated by many researchers.[10]

Moreover, CO_2 and pollutant emissions can be further mitigated if DF pilot-ignited and RCCI combustions employ renewable fuels, such as biogas,[18] ethanol,[19] methanol,[20] biodiesel[21] and Dimethyl Ether (DME)[22].

Even if Natural Gas (NG) is a fossil fuel, it can provide a valuable contribution to the reduction of CO_2 emissions. In fact, NG is mainly composed by methane (CH_4), which is characterised by the highest hydrogen-to-carbon ratio among hydrocarbons. Furthermore, NG can be easily substituted with bio-methane, that is a renewable fuel. Finally, NG does not contain aromatics and Polycyclic Aromatic Hydrocarbons (PAH). This is why the EU is planning to consider NG as a green energy.[23–25]

As demonstrated by the "EU Hydrogen Strategy",[26] a fundamental enabler of the carbon neutrality in the transport sector can be the green H_2, applied to FCEV and to combustion vehicles. In the last ones, green H_2 can be burnt alone or in combination with other fuels.[27] Since H_2 does not contain carbon, its combustion does not produce CO_2, carbon monoxide (CO), Unburnt Hydrocarbons (UHC) and soot. The only critical pollutants are the NO_x, that can be effectively abated by means of Exhaust Gas recirculation (EGR) and/or a proper after-treatment device.

However, many issues still need to be addressed before the use of H_2 as a fuel in production engines, in particular for DF pilot-ignited and RCCI combustions.

In this scenario, the research activity carried out during the Ph.D. course, and presented in this thesis, aims at investigating the potential of DF pilot-ignited and RCCI combustions, considering different types and combinations of sustainable fuels. The attention is focused on the low reactivity fuels, and on their specific combustion patterns. Moreover, a small part of the research activity was devoted to explore the application of hybridisation to a Formula SAE race car.

In detail, Section 3 reports a comprehensive experimental campaign performed on a light-duty Diesel engine operated in DF NG-diesel combustion mode at different loads (Brake Mean Effective Pressure (BMEP) = 2, 4, 8 and 12 bar, corresponding to 44, 88, 177 and 265 Nm) and same engine rotational speed equal to 3000 rpm.

Based on the data collected during the experimental study, various 3D-CFD models of the investigated engine were built.

A first numerical investigation was carried out by means of a customized version of the KIVA-3V code, whose main models are described in Section 4. Such analysis was focused on the optimization of the diesel injection strategy on a selected DF case at the highest load experimentally investigated, i.e., 3000 rpm – BMEP = 12 bar (see Section 5).

Sections 6 presents a numerical study on the effects of different H_2-NG blends, with the H_2 mole fraction ranging from 0% to 30%, on a selected DF low load case at 3000 rpm (BMEP = 2 bar), since this operating condition is the most critical in DF mode.

Then, Section 7 describes a sensitivity analysis on DF H_2/NG-diesel combustion, considering as parameters of investigation the number of diesel injections per cycle, the start of injection of each injection, the diesel mass distribution among the injections and the Swirl Ratio (SR). Both

numerical investigations reported in Section 6 and Section 7 were performed by means of the commercial code ANSYS Forte.

As already mentioned, NG can be easily substituted by bio-methane. Conversely, the interchangeability between NG and biogas needs to be further investigated, due to the different Wobbe index of the two gases. Moreover, the biogas composition is extremely dependent on the biomass used for its production. Therefore, a numerical investigation on the interchangeability between NG and biogas in DF operation was carried out using KIVA-3V. The selected operating point was 3000 rpm – BMEP = 8 bar (see Section 8).

Section 9 is dedicated to a preliminary study, exploring the application of DF combustion to a new loop scavenged 2-Stroke high-speed direct-injection Diesel engine. In particular, the analysis, performed by means of ANSYS Forte, is focused on the evaluation of the best technique to inject gasoline, minimising the wall impingement and the fuel short-circuiting.

The last section (Section 10) reviews a study on the Formula Student car of the University of Modena and Reggio Emilia, developed in two alternative configurations: the Combustion vehicle, equipped with a conventional 4-cylinder SI engine, and the Hybrid car, with a power-unit made up of a single cylinder engine and a serially connected electric motor. The numerical comparison between the two race cars in terms of lap performance and CO_2 emissions, is based on the simulation of the Endurance event of the Formula Student UK competition. The telemetry data of the Combustion vehicle were used to build and calibrate a 0D MATLAB-Simulink model.

Finally, at the end of the Ph.D. course, a preliminary investigation on e-fuels was carried out in cooperation with the Institut für Verbrennungskraftmaschinen und Thermodynamik (IVT) at Technischen Universität Graz (TUGraz). The results are not published in this thesis because further work is still required to complete the study.

2 Low Temperature Combustions

2.1 Introduction

As discussed in the Introduction of this thesis (Section 1), the main drawback of CI engines is represented by NO_x and soot emissions. The increasing complexity, cost and encumbrance of exhaust gas aftertreatment systems of Diesel engines (due to more and more stringent emissions regulations), besides a negative impact on fuel consumption of such devices, have induced the research community to develop technologies capable of mitigating NO_x and soot genesis during the combustion process.

One of the most promising techniques able to abate NO_x and soot raw emissions of CI engines, assuring at the same time high BTE, is represented by the so-called Low Temperature Combustions (LTCs). Basically, LTCs combine characteristics of both SI and CI engines. In particular, a lean premixed charge, with a variable level of heterogeneity of the fuel(s) distribution inside the combustion chamber, auto-ignites close to the TDC. The use of a lean premixed charge avoids the presence of rich regions or fuel droplets at the combustion onset, inhibiting the soot formation. Moreover, the combustion of such a mixture is characterised by lower maximum temperatures. As a result, the NO formation rate is reduced, due to its strong temperature dependence. In fact, in combustion of lean and near-stoichiometric mixtures, the main reactions that govern the NO formation from N_2 are the following:[28]

$$N_2 + O \rightleftarrows NO + N \quad (1)$$

$$N + O_2 \rightleftarrows NO + O \quad (2)$$

$$N + OH \rightleftarrows NO + H \quad (3)$$

Reactions (1) and (2) were originally proposed by Zeldovich, composing the so-called "thermal" or "Zeldovich mechanism". Subsequently, Lavoie, Heywood and Keck[29] added the third reaction (reaction (3)) to the thermal mechanism, which was then called "extended Zeldovich mechanism". The forward reaction (1), as well as the reverse reactions (2) and (3), are characterized by large activation energies, resulting in a strong temperature dependence of the NO formation mechanism.[30]

Therefore, LTCs have the capability to overcome the traditional trade-off between NO_x and soot emissions that affects Conventional Diesel Combustion (CDC).

Furthermore, as mentioned above, LTCs also guarantee high thermal efficiency. This is due to the reduction of heat losses through the combustion chamber walls (thanks to lower maximum combustion temperatures) and a faster combustion process, which results in a more efficient engine cycle.[10]

However, LTCs are still affected by some issues, which have to be solved so that LTC engines can become a commercially viable technology.[12]

The main problem that needs to be addressed is the control of combustion phasing and Rate of Heat Release (RoHR) over the entire engine operating range in terms of revolution speed and load. In fact, LTCs are mainly governed by chemical kinetics, instead of physical processes such as fuel injection rate and turbulent mixing. Hence, ignition timing and RoHR are strongly dependent on initial charge composition and temperature, and Compression Ratio (CR). Various strategies have been investigated in order to effectively control LTCs by modifying initial charge composition and/or temperature, as well as charge temperature at the end of the compression stroke, such as:

- EGR;[31]
- variable intake air temperature;[32]
- Variable Valve Timing (VVT);[33]
- variable CR.[34]

However, these strategies do not completely solve the above-mentioned problem. As a consequence, it is not possible to operate LTC engines up to high/full loads (due to overly advance ignition timing and excessively high RoHR, which are responsible for unacceptable noise and vibrations), limiting the power density of such engines.[12]

Finally, LTCs are characterized by higher CO and UHC emissions compared to CDC. This is due to the lower combustion temperatures of LTCs compared to CDC.[35] Moreover, a fraction of the premixed charge enters the crevices during the compression stroke and leaves them during the expansion stroke, when the in-cylinder temperature is too low to permit the charge to achieve a complete oxidation. In addition, these phenomena are accentuated at low loads, because of lower combustion temperatures.[12]

2.2 Evolution path of Low Temperature Combustions

In an effort to overcome the aforementioned limits of LTC engines, paving the way for commercialization, various compression ignition combustion strategies have been developed by the research community, both in industry and academia, in the last decades.

The simplest and most ideal LTC concept is the so-called *Homogeneous Charge Compression Ignition* (HCCI) combustion. As suggested by its name, HCCI combustion concept consists in the compression ignition of a lean homogeneous charge. This leads to a volumetric heat release that involves the entire charge, resulting in an almost constant volume combustion. As a result, high RoHR and Peak Pressure Rise Rate (PPRR) are induced, limiting the maximum load achievable.[10] Conversely, at low loads, the charge temperature is too low to trigger the fuel-air mixture auto-ignition.[36]

In order to gain a better control over combustion phasing and RoHR, a combustion concept intermediate between HCCI and CDC, named *Premixed Charge Compression Ignition* (PCCI) combustion, was developed. In this combustion strategy, the fuel is injected early during the compression stroke in order to generate a premixed, but non perfectly homogeneous, charge.

Both HCCI and PCCI offer ultra-low NO_x and soot emissions, at the expense of higher CO and UHC emissions with respect to CDC. However, it was proven that CO and UHC emissions can be effectively reduced by means of higher intake pressures (boosted HCCI and PCCI)[37,38] and reduced crevice volumes.

Most of the research activities carried out on HCCI and PCCI concepts have involved either strictly gasoline or diesel fuel. However, neat gasoline shows poor ignitability at low loads due to its high Octane Number (ON).[39] Conversely, extremely high RoHR and PPRR are obtained at high loads. As far as diesel fuel is concerned, the maximum load achievable is even lower than gasoline, due to the superior auto-ignition quality of the former fuel. Therefore, with the aim to extend HCCI/PCCI operating range, it is necessary to dilute the fuel-air charge with relevant fractions of EGR.[40] However, high levels of EGR limit the maximum power obtainable due to the reduced air flow. Moreover, several engine cycles are required by the EGR system to adapt to a variation of the operating condition. As a result, combustion instabilities are induced during transient operations.[41]

Bessonette et al.[42] were able to extend the HCCI operating range up to BMEP = 16 bar using a gasoline with an ON of 80.7 (Cetane number (CN) of about 27). However, below BMEP = 2 bar, a conventional diesel fuel was necessary.

Such results suggest that to operate HCCI/PCCI combustions on a wide range of operating conditions, the adoption of a fuel blend, whose composition can be modified as a function of speed and load (High Reactivity Fuel (HRF) blend at low loads and Low Reactivity Fuel (LRF) blend at high loads), is required.

Based on the above considerations, EGR is not the best control parameter for HCCI/PCCI combustions. Moreover, single-fuel HCCI/PCCI combustions are not viable combustion concepts.

Therefore, various studies have been performed on dual fuelling strategies, namely, blending fuels with different ignitability. *Dual Fuel HCCI* and *Dual Fuel PCCI* combustions revealed to be effective in controlling combustion phasing and RoHR.[43–47]

In particular, Inagaki et al.[41] investigated a *DF stratified PCCI* combustion using iso-octane as the LRF and diesel as the high reactivity one. The former fuel was port-injected, forming a homogeneous mixture with air, while the latter was directly injected in the combustion chamber at early timing, in order to create a mild stratification in terms of equivalence ratio (ϕ) and Research Octane Number (RON). It was demonstrated that changing the ratio of the two fuels permits to control the ignition timing, while the stratification of ignitability induces a combustion process that develops gradually.

Inagaki et al.[41] developed this combustion concept based on the results of preliminary investigations aimed at identifying the key parameters affecting HCCI combustions. In particular, they tested three paraffins with different ignitability (see Table 1).

Table 1. Tested paraffins[41]

Fuel	Abbreviation	RON(CN)
n-pentane	n-C5	62(29)
n-hexane	n-C6	25(48)
n-heptane	n-C7	0(56)

As it can be seen from Figure 2, the tested paraffins are characterised by a two-stage ignition. It clearly appears that the Low Temperature Oxidation (LTO) advances and increases as the RON decreases (CN increases). Also the High Temperature Oxidation (HTO) advances as the CN increases.

If the RoHR is plotted as a function of in-cylinder temperature for the three paraffinic hydrocarbon fuels, an interesting result can be observed (see Figure 3). Namely, the higher the CN, the lower the starting temperature of LTO, while the starting temperature of HTO is not affected by the RON.

The same evidence is depicted in Figure 4, which also shows that the starting temperatures of LTO and HTO do not depend on the equivalence ratio of the homogeneous charge.

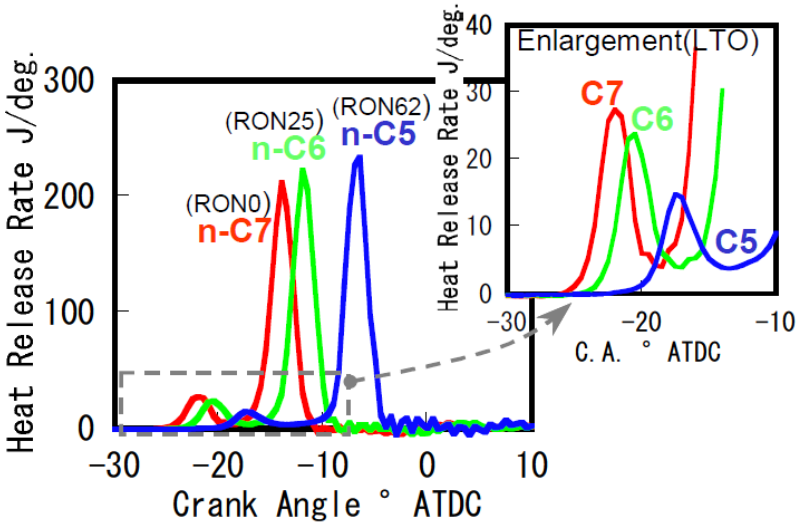

Figure 2. RoHR of n-pentane, h-hexane and h-heptane (ϕ =0.35, 1400 rpm, no EGR)[41]

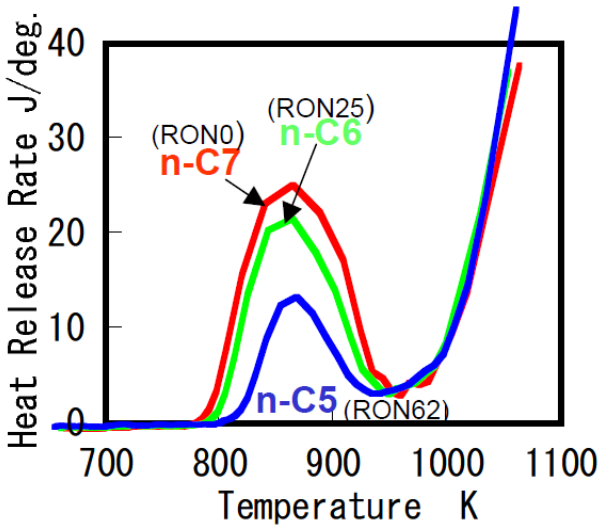

Figure 3. Ignition characteristics of n-pentane, h-hexane and h-heptane related to in-cylinder temperature (ϕ =0.35, 1400 rpm, no EGR)[41]

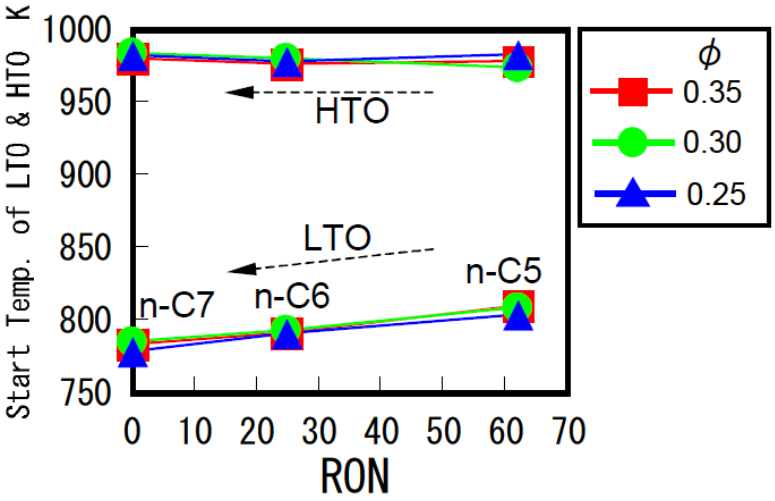

Figure 4. Temperature of starting Low Temperature Oxidation (LTO) and High Temperature Oxidation (HTO) of n-pentane, h-hexane and h-heptane related to Research Octane Number (RON) and equivalence ratio (ϕ)[41]

Moreover, Figure 5 shows that the starting temperatures of LTO and HTO are not affected by the equivalence ratio and EGR dilution of the homogeneous charge, and by the intake air temperature. The latter engine parameters simply modify the crank angles at which those temperatures are reached.

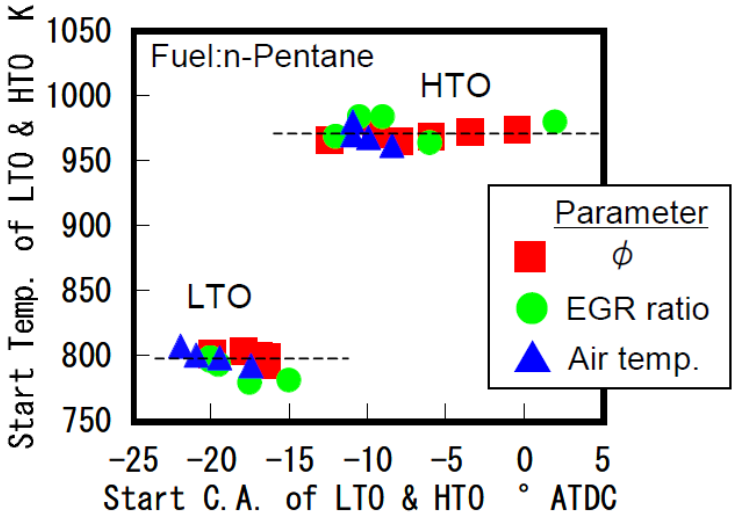

Figure 5. Low Temperature Oxidation (LTO) and High Temperature Oxidation (HTO) start temperatures for n-pentane at various intake air temperatures, EGR fractions and equivalence ratios (ϕ)[41]

Therefore, if an in-cylinder stratification of ignitability (CN) is created, a non-uniform distribution of temperature is determined during LTO. As a result, HTO does not involve the entire in-cylinder charge, inducing a gradual combustion process, and hence, moderate RoHR and PPRR.

Starting from the DF stratified PCCI combustion, two further combustion concepts were derived, i.e., *Dual Fuel pilot-ignited* and *Reactivity Controlled Compression Ignition* (RCCI) combustions.

Both in DF pilot-ignited combustion and in RCCI combustion, the LRF is port injected, while the HRF is directly injected into the combustion chamber. These two combustion concepts differ in the ignition mode. In particular, in DF pilot-ignited combustion mode, a pilot injection of the HRF close to the TDC is used as the ignition trigger of the lean premixed charge. Conversely, in RCCI combustion mode, the HRF is injected through a split injection strategy, early during the compression stroke in order to generate a stratification of equivalence ratio and ignitability. As a consequence, the ignition (and the combustion progress) depends on the dual fuel stratified chemical kinetics.

Figure 6 reports a classification of LTCs based on the corresponding fuel(s) injection strategies (CNG is assumed as the LRF for DF-PCCI combustion strategies).

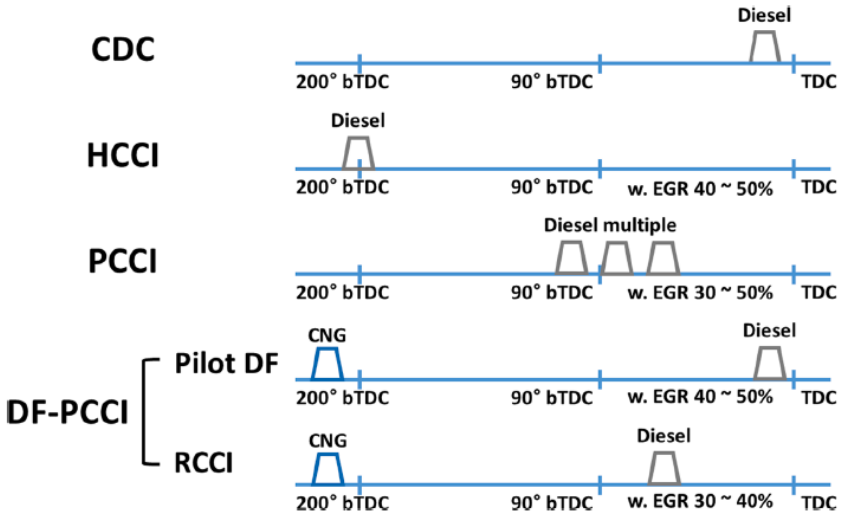

Figure 6. LTCs classification based on the corresponding fuel(s) injection strategies[48]

Figure 7 shows CDC and LTC regimes on an equivalence ratio-temperature (ϕ-T) plot. The regions characterised by the formation of NO and soot are depicted. As it can be seen, CDC

evidently crosses both NO and soot formation regions, while HCCI, PCCI and other LTCs develop mainly in NO and soot-free portions of the diagram.

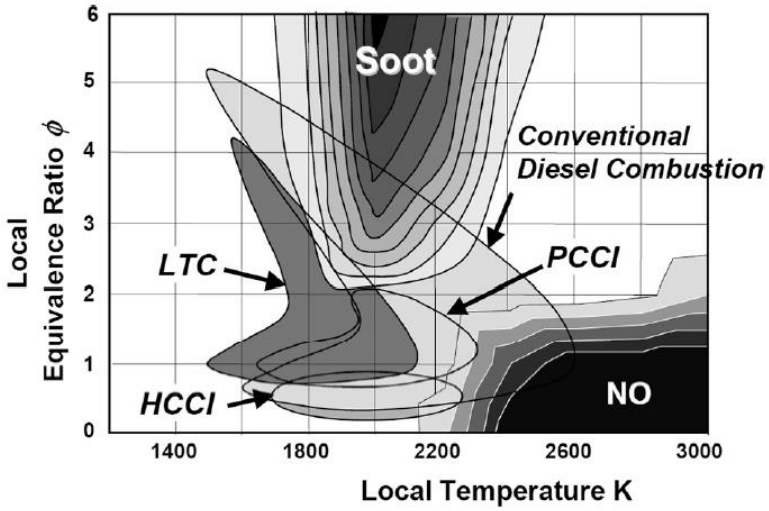

Figure 7. Different LTCs and CDC regimes shown in a ϕ-T plot[49]

2.3 Dual fuel pilot-ignited / Reactivity Controlled Compression Ignition combustion concepts

DF pilot-ignited and RCCI combustions using gasoline as the LRF and diesel as the HRF have been extensively investigated by many researchers.[50–60] However, such combustion strategies are particularly attractive when biofuels (renewable, low carbon fuels) are employed.

In detail, bio-methane, biogas and bio-alcohols (bio-ethanol and bio-methanol) can be used as LRFs, while diesel fuel can be successfully substituted by biodiesel and Dimethyl Ether (DME). For instance, researchers at the Centre for Advanced Powertrain and Fuels Research (CAPF), Brunel University London,[19] carried out a comparison between CDC and DF ethanol-diesel combustion on a single cylinder Heavy Duty (HD) Diesel engine (CR of 16.8) from Indicated Mean Effective Pressure (IMEP) = 3 bar to IMEP = 24 bar, at 1200 rpm. DF combustion achieved superior Indicated Thermal Efficiency (ITE) than CDC from IMEP = 6 bar to IMEP = 24 bar, and with a maximum value of 47.2% at IMEP=12 bar. Furthermore, NO_x emissions could be reduced by up to 90% with respect to CDC at IMEP = 3 bar, for an ethanol energy fraction of 0.56. At full load (IMEP = 24 bar), with an ethanol energy fraction of 0.19, the reduction of NO_x emissions was equal to 26%. Guan et al.[61] investigated a conventional DF methanol-diesel operation on a single-cylinder HD diesel engine at 1200 rpm and IMEP = 18 bar. Researchers found that, at the above-mentioned operating point, the methanol energy

fraction was limited to 28%, due to high levels of PPRR. However, the application of Miller cycle, EGR and intake air cooling permitted to increase the energy fraction of methanol to 40%, while ITE improved by 3.7% when compared to CDC. At the same time, NO_x emissions decreased by 37% with respect to CDC. Ning et al.[62] explored DF combustion at 2500 rpm – IMEP = 7.5 bar, employing, alternatively, methanol, ethanol, and n-butanol as LRFs. Various alcohol-diesel blends were tested in the range between 0 % (pure diesel) and 40 % diesel energy reduction, by steps of 10 %. This study showed that the use of alcohols as LRFs in DF combustion can increase UHC and NO_x emissions, while CO and soot emissions are reduced. Moreover, the comparative analysis between alcohol fuels highlighted that methanol permits to achieve the highest BTE, the lowest CO, NO_x, and soot emissions, but the highest UHC emissions among the three alcohols. Researchers at State Key Laboratory of Engines, Tianjin University,[21] compared pure biodiesel operation with DF (RCCI) combustion mode. In RCCI combustion mode, biodiesel was directly injected into the combustion chamber, while n-butanol, 2,5-dimethylfuran and ethanol were alternatively port injected. When 80% of the total energy was introduced by means of biofuels, lower soot emissions and higher CO and UHC emissions than neat biodiesel were obtained. Biodiesel/ethanol blend showed greater potential on reducing NO_x and soot emissions simultaneously, while biodiesel/n-butanol blend determined the highest ITE (47.5%). Finally, Chen et al.[22] explored, both experimentally and numerically, DF methanol-DME combustion. In particular, methanol was directly injected into the combustion chamber, while DME was port injected. Based on the results of the investigation, the authors concluded that late methanol injection permits to achieve smooth combustion and low NO_x emissions at high methanol concentrations. Conversely, moderate injection timing is suggested to achieve higher ITE at low methanol concentrations.

Also NG represents a valuable LRF in view of the following reasons:

- its main component is CH_4 (87.0÷96.0 vol%; see Table 2), which is characterised by the highest hydrogen-to-carbon ratio among hydrocarbons;
- it can be substituted by biogas and bio-methane (the latter gaseous fuel is the most suitable, since its Wobbe index is similar to that one of NG), that are a renewable, low carbon fuels;
- it does not contain aromatics and PAHs;
- it is characterised by a higher ON than gasoline and alcohols, making possible the adoption of Diesel-like CRs in order to obtain high thermodynamic efficiency;

- unlike alcohols, NG is not corrosive;
- it guarantees a better mixing capability with air than liquid fuels.

Table 2. Typical components of NG and corresponding volumetric fraction ranges[11]

Component	Range [vol%]
Methane	87.0÷96.0
Ethane	1.8÷5.1
Propane	0.1÷1.5
Isobutane	0.01÷0.3
n-Butane	0.01÷0.3
Isopentane	Trace to 0.14
n-Pentane	Trace to 0.14
Hexane	Trace to 0.06
Nitrogen	1.3÷5.6
Carbon Dioxide	0.1÷1.0
Oxygen	0.01÷0.1
Hydrogen	Trace to 0.02

Several researchers have demonstrated that DF NG-diesel combustion is able to effectively reduce NO_x and soot emissions and improve BTE.[63–66]

Detailed investigations have also been performed to deeply understand the phenomena involved in DF NG-diesel combustion. For instance, Niki et al.[67] examined the ignition process of pilot fuel sprays, surrounded by a premixed NG-air charge, by means of chemical-kinetics simulations and chemiluminescence imaging diagnostics. The chemical-kinetics simulations showed that both LTO and HTO of the HRF are delayed due to the consumption of hydroxyl radicals (OH) induced by the oxidation of the CH_4 entrained into the jets. Moreover, the higher the concentration of NG in the premixed charge, the larger the delay of both LTO and HTO. The chemiluminescence imaging diagnostics revealed that the increase of NG concentration has a more pronounced effect on HTO delay than on LTO delay. Then, as the LTO and HTO delays increase, also the corresponding Coefficient Of Variation (COV) increases. However, the ignition stability can be improved by increasing the injection duration, since it reduces the CH_4 entrainment into the jets, and hence, the OH consumption due to CH_4 oxidation. Rochussen et al.[68] characterized the mean flame propagation speed ($\bar{S}_{FP}$) in DF pilot-ignited CH_4-diesel

combustion using high-speed imaging of OH*-chemiluminescence. The authors observed that increasing the equivalence ratio of CH_4 from 0.4 to 0.69, $\bar{S}_{FP}$ increases from 4 to 8 m/s, while increasing the diesel pilot injection pressure from 300 to 1300 bar, $\bar{S}_{FP}$ passes from 8 to 14 m/s. Moreover, chemiluminescence imaging diagnostics revealed that the pilot diesel sprays do not ignite simultaneously, inducing an overlap between pilot diesel sprays ignition and flame propagation into the premixed charge.

Further studies have been carried out with the aim to understand the influence of the main engine parameters on DF combustion characteristics, such as: NG composition,[69,70] EGR,[71] diesel injection strategy (number of injections per cycle,[72] injection timing,[73] injection duration,[74] post injection strategy[75]), injector spray included angle,[76] diesel injector nozzle hole size,[77] SR,[78] combustion chamber shape.[79]

Researchers at the National Research Council Canada[71] performed an experimental investigation on a HD DF NG-diesel single-cylinder research engine at two loads, corresponding to 50 % and 75 % of full load, at a constant engine speed of 1000 rpm and NG-diesel fuel energy ratio of 3:1. Researchers found that the use of EGR in DF NG-diesel combustion enhances the NO_x-soot trad-off with respect to Normal Diesel (ND) operation. Wu et al.[72] carried out a numerical optimization (by means of a micro-genetic algorithm optimization code coupled with an commercial 3D-CFD code) on a HD single-cylinder Diesel engine operated in DF NG-diesel combustion at 1300 rpm, medium load. Two optimized diesel injection strategies (single and double injection), along with two piston bowl shapes (see Figure 8), were compared. The numerical results showed that both injection strategies guarantee low emissions and ITE close to 50 %. However, the single injection strategy showed higher heat transfer losses, with respect to the double injection strategy, due to the reduced presence of diesel fuel in the combustion chamber core. Moreover, the bathtub piston bowl offered lower heat transfer losses compared to the stock piston bowl, enhancing fuel efficiency.

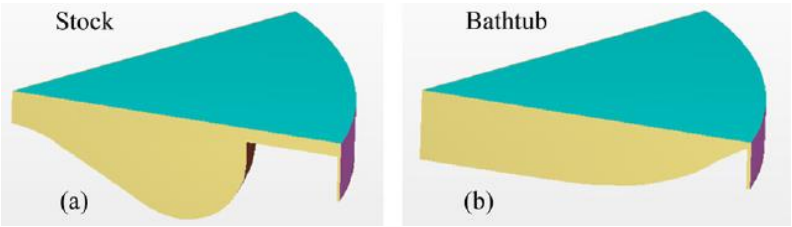

Figure 8. Sector meshes at TDC: (a) stock piston, (b) bathtub piston[72]

Yousefi et al.[73] analysed, both experimentally and numerically, the influence of diesel fuel injection timing on a HD DF NG-diesel single-cylinder engine under four different operating conditions (910 rpm – BMEP = 4.05 bar; 1750 rpm – BMEP = 11.24 bar; 910 rpm – BMEP = 12.15 bar; 1150 rpm – BMEP = 17.6 bar). The authors observed that the peak in-cylinder pressure, ITE and NO_x emissions increase for all the investigated operating points, when diesel injection timing is advanced. As far as unburnt CH_4 and CO_2-equivalent emissions are concerned, they significantly decrease under low load-low speed and medium load-high speed conditions, while unburnt CH_4 emissions increase and CO_2-equivalent emissions remain almost constant under medium to high load-low speed conditions, when diesel injection timing is advanced. Under low load-low speed and medium load-high speed conditions, the unburnt CH_4 are mainly located in the combustion chamber core. However, advancing diesel injection timing strongly enhances the oxidation of the NG-air premixed charge in this region. Simulation results also revealed that advancing diesel injection timing slightly increases the premixed charge trapped in the crevice volume. However, the latter effect is negligible with respect to the improved combustion of the premixed charge in the central zone on the combustion chamber. Conversely, at medium to high load-low speed conditions, most of the premixed charge in the combustion chamber core burns. Therefore, advancing diesel injection timing does not contribute to the oxidation of the NG-air mixture in this zone. However, advancing diesel injection timing slightly increases the premixed charge trapped in the crevice volume. As a results, unburned CH_4 emissions increase under medium to high load-low speed conditions when the diesel injection timing is advanced. Yousefi and co-workers[78] also numerically investigated the influence of SR on the combustion characteristics of the same engine, and under the same operating conditions, mentioned above. At the low load-low speed condition, with a diesel fuel injection timing of -14 °CA AFTDC, the early stage of the premixed-controlled diesel combustion can be improved by increasing SR from 0.5 to 1.5. The lowest unburnt CH_4 and CO emissions, besides the highest fuel efficiency, were achieved with SR of 1.5. Conversely, with a diesel fuel injection timing of -30 °CA AFTDC, a worsening of fuel efficiency was obtained by increasing SR. In fact, increasing SR, the higher heat transfer losses overwhelmed the improvement of the mixing-controlled diesel diffusion combustion. At medium load-high speed condition, the authors were able to enhance the diesel diffusion combustion and turbulent flame propagation of NG by increasing SR from 0.5 to 1.5. Furthermore, the fuel efficiency improved by 2.4 %, while unburnt CH_4 and CO emissions

decreased by 13.5 % and 11.8 %, respectively. However, NO_x emissions increased by 50 %. Also at high load-low speed condition, diesel diffusion combustion and flame propagation of NG could be enhanced by increasing SR from 0.5 to 1.5. As a consequence, unburnt CH_4 and CO emissions decreased by 22 % and 59 %, respectively, and fuel efficiency improved by 2.5 %. However, both peak in-cylinder pressure and NO_x emissions increased.

However, some issues still need to be solved, such as the low combustion efficiency that characterizes DF NG-diesel combustion at low loads. Here, the overly lean premixed NG-air mixture causes an excessive flame quenching, yielding high CO and UHC emissions and low BTE. This evidence is confirmed by Hutter et al.[80] and Kozarac et al.[81], which suggest that beyond total excess air ratio of 1.65, it is convenient to switch to ND operation in order to obtain higher ITE.

Li et al.[82] performed a numerical investigation on a HD Diesel engine operated in DF NG-diesel mode at 910 rpm – BMEP = 4.05 bar, with the aim to quantify the amount of unburnt CH_4 at a low load condition. The simulation results revealed that 27÷35 % of CH_4 is emitted by the engine without taking part to the combustion process.

Since NG is primarily composed by CH_4, the UHC emissions of a DF NG-diesel engine are mainly made up of unburned CH_4, whose oxidation in a conventional Diesel Oxidation Catalyst (DOC) is challenging, due to the high stability that characterises its molecule.[83] Furthermore, it is worth noting that CH_4 is a GHG with a global warming effect 28-time higher than CO_2 over a 100-year lifetime.[84] This is why the "European Green Deal" promotes actions to reduce CH_4 emissions from all human activities.[85] Therefore, it is essential to avoid (or at least strongly reduce) the slip of CH_4 at low loads in DF NG-diesel operation.

In order to mitigate the slip of unburned CH_4 at the above-mentioned operating conditions, the following strategies can be adopted:

- optimization of the diesel injection parameters (SOI,[86] injection pressure and number of injections per cycle[87]);
- use of EGR;[88]
- optimization of the piston geometry and of the radial clearance between piston and liner.[89]

For instance, Yousefi et al[87] carried out an experimental and numerical investigation on a HD DF NG-diesel single-cylinder engine at a low load-low speed condition (910 rpm – BMEP = 4.05 bar), with the aim to analyse the influence on performance and emissions of diesel injection

pressure and diesel split injection strategy. The results of the investigation revealed that, with single injection strategy, ITE can be improved by increasing the diesel injection pressure and/or advancing the diesel SOI. However, ITE follows the opposite trend for very advanced diesel SOI. As far as the combustion efficiency is concerned, it always increases by advancing the diesel SOI and/or increasing the diesel injection pressure. When diesel split injection strategy is employed, ITE decreases as the diesel injection pressure is increased, due to the overly advanced combustion phasing. However, optimizing the combustion phasing, ITE can be strongly improved. In detail, an ITE of 37.2 %, which is higher than the best one with diesel single injection strategy, is reached for the following set of engine control parameters: diesel SOI1 = −54 °CA AFTDC, diesel SOI2 = −16 °CA AFTDC, split ratio of 55%, rail pressure of 800 bar. However, a slightly lower combustion efficiency is obtained after the combustion phasing optimization. Furthermore, increasing the diesel injection pressure significantly reduces unburned CH_4 and soot emissions, both with single and split injection strategies. Conversely, NO_x emissions increase as the diesel injection pressure increases, both with single and split injection strategies. However, at the optimum operating condition (diesel SOI1 = −54 °CA AFTDC, diesel SOI2 = −16 °CA AFTDC, split ratio = 55 % and rail pressure of 800 bar), NO_x emissions are comparable to the best of Diesel engine. Shen et al.[89] numerically studied the influence of four piston clearances (0.5 mm, 0.76 mm, 1.0 mm and 1.54 mm) and four piston bowl shapes on combustion and CH_4 emissions. As it can be seen in Figure 9, three diesel-spray-orientated (DSO) piston bowls were designed by the authors in order to provide more NG-air mixture to the diesel sprays. Moreover, a protrusion-ring was designed at the bowl rim of DSO pistons to improve NG flame propagation. The results revealed that DSO pistons have greater influence on NG combustion than diesel combustion. Unburnt CH_4 emissions of DSO pistons with the radial clearance of 0.76 mm were decreased by 28.4 %, 43.1 % and 69.9 %, respectively, with respect to the original piston design (OPD), while soot emissions of DSO1, DSO2 and DSO3 with the radial clearance of 0.76 mm were decreased by 33.1 %, 34.7 % and 50.7 %, respectively, with respect to OPD.

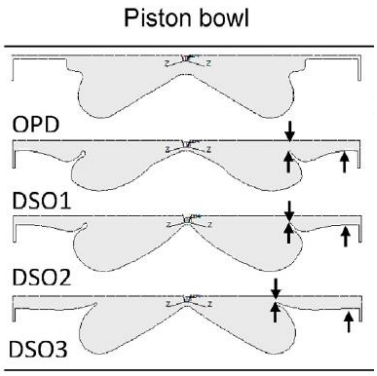

Figure 9. Piston bowl shapes (OPD: original piston design; DSO: diesel-spray-orientated)[89]

If such measures are not sufficient to improve DF NG-diesel combustion at low loads, an alternative solution could be the addition of a small amount of H_2 to the NG-air mixture. In fact, the presence of H_2 extends the Lower Flammability Limit (LFL)[90] of the lean premixed charge due to the increase of the OH radical pool during the combustion event, enhancing the oxidation of CO and UHC.[91]

Rahnama et al.[92] studied the effects of H_2 enriched intake air on a HD DF NG-diesel engine, varying the H_2 mole fraction from 0% to 5%. At the investigated operating condition (800 rpm – IMEP = 4 bar, 0% EGR) a strong decrease of CO (from 48 to 2.25 g/kWh) and UHC emissions (from 205 to 4.50 g/kWh) was obtained. Also combustion efficiency and Gross Indicated Thermal Efficiency (GITE) were strongly enhanced, with the latter that passed from 18.5 % to 50 %. Furthermore, the addition of H_2 reduced the combustion duration from 23 °CA to 7 °CA. However, PPRR increased (from 1.8 bar/°CA to 13.8 bar/°CA) along with NO_x emissions (from almost 0 to 0.43 g/kWh).

The capability of H_2 addition to the lean premixed charge to improve the combustion efficiency of DF NG-diesel combustion at low loads is confirmed by several authors. Ouchick et al.[93] demonstrated that H_2 enriched NG permits to reduce the difference in terms of BTE and COV of IMEP between DF NG-diesel combustion and CDC. Talibi et al.[94] investigated the combustion of different H_2-CH_4 blends, in the range between 20 vol% and 80 vol% H_2 fraction, on a naturally aspirated, direct-injection, CI single-cylinder engine. The experimental results showed that DF H_2/CH_4-diesel combustion is characterised by lower CO_2 emissions and higher CO and UHC emissions between IMEP = 1 and 7 bar with respect to CDC. However, a reduction of CO emissions by between 40% and 70% and of UHC emissions by between 50% and 75% was obtained increasing the H_2 fraction in the H_2-CH_4 blend from 20 vol% to 80 vol%.

Besides the positive effects on CO_2, CO and UHC emissions, researchers at Istituto Motori, National Research Council,[95] also proved that H_2 enriched NG guarantees, at least at low load (2000 rpm – 50 Nm), lower NO_x emissions than those ones in CDC. As far as soot emissions are concerned, Zhou et al.[96] reported a decrease in soot emissions as the H_2 content in the H_2-NG mixture is increased. This is due to the fact that the presence of H_2 slows down the transformation of benzene (C_6H_6) into PAHs.[97] Moreover, Wang et al.[98] reported that, thanks to the presence of H_2, the CH_4 oxidation reaction path tends to move towards the lower carbon one, inhibiting the soot formation. Such conclusion was drawn by the authors based on calculations on stoichiometric H_2-CH_4-air laminar premixed flames at normal temperature and pressure, using PREMIX code of CHEMKIN-II with GRI-Mech 3.0 mechanism.

Finally, Liu et al[99] investigated the effects of H_2 enriched NG on combustion characteristics in an optically accessible single-cylinder engine, considering an energy substitution ratio of H_2-NG mixture equal to 70 %. In particular, the authors, based on flame images, could divide the DF H_2/NG-diesel combustion process into five phases:

1. ignition delay phase;
2. diesel premixed combustion phase;
3. diesel mixing controlled combustion phase;
4. H_2-NG-air charge premixed combustion phase;
5. remaining diesel mixing controlled combustion phase.

Liu et al. also observed that H_2, thanks to its higher combustion temperature, favours the ignition of NG and of the remaining diesel fuel.

3 Experimental investigation on a light-duty Diesel engine operated in dual fuel natural gas/diesel combustion mode

3.1 Introduction and aim

The aim of the first activity was to experimentally investigate a light-duty Diesel engine operated in DF NG-diesel combustion mode. The effects on combustion characteristics and emissions of DF NG-diesel operation were analysed and compared with the CDC mode. Moreover, an optimization process was carried out in order to obtain the maximum benefit from the investigated LTC.

The modified engine could be used in non-road applications, such as agricultural and construction vehicles, or power generation sets, that must comply with more and more stringent emissions standards. As an example, the EU has adopted the Stage V emission regulations since 2018 for approval of new engines, and since 2019 for all sales.[100]

Typically, power generation sets are HD Diesel engines revving at 1500 or 1800 rpm, depending on whether the required electrical frequency is 50 or 60 Hz, respectively. Table 3 reports the main features of some commercial generator sets in the power range between 75 and 95 kW. [101–105] As it can be noted, the engines listed in Table 3 have excellent Brake Specific Fuel Consumption (BSFC). However, their specific prime power is quite low (< 20 kW/L). As a consequence, they are cumbersome and heavy.

Conversely, the investigated engine could be used as a compact generator set with a maximum prime power of about 80 kW at a rated speed of 3000 rpm. Moreover, as demonstrated by the present study, it would be able to complies with the Stage V emission standard, without the need of complex and expensive after-treatment systems thanks to the implementation of the DF NG-diesel combustion mode. Finally, the conduction costs could be strongly reduced thanks to the relevant substitution of diesel with NG.

The results of the experimental activity presented and discussed in this section have been reported in a paper entitled “Optimization of a High-Speed Dual-Fuel (Natural Gas-Diesel) Compression Ignition Engine for Gen-sets” and published in the SAE International Journal of Engines (SAE International).[106]

Table 3. Main features of some power generation sets

Manufacturer	DEUTZ	VOLVO PENTA	Cummins	HIMOINSA/ FPT_IVECO	MOTEURS Baudouin
Engine Type	CI	CI	CI	CI	CI
Cylinders arrangement	In-line	In-line	In-line	In-line	In-line
Number of cylinders	6	4	4	4	4
Turbocharger	✓	✓	✓	✓	✓
Injection type	DI	DI	DI	DI	DI
Bore x Stroke [mm]	102 x 132	108 x 130	107 x 124	104 x 132	105 x 130
Displacement [L]	6.47	4.76	4.46	4.49	4.50
Compression Ratio	n.a.	18.0:1	n.a.	17.5:1	18.0:1
Rated rpm@50 Hz	1500	1500	1500	1500	1500
Max. Prime Power at rated rpm [kW]	93.1	76.0	82.0	88.6	74.0
BMEP at max. Prime Power, rated rpm [bar]	11.51	12.76	14.71	15.80	13.15
Fuel consumption at max. Prime Power, rated rpm [L/h]	23.4	21.1	22.0	22.0	18.6
BSFC at max. Prime Power, rated rpm [g/kWh]	209	231	223	206	209
Specific Prime Power at rated rpm [kW/L]	14.39	15.95	18.39	19.75	16.43

3.2 Materials and methods

The baseline engine used in this activity is an automotive, 4-cylinder, turbocharged, common rail Diesel engine, manufactured by FCA - VM Motori, whose main characteristics are listed in Table 4.

Table 4. Main characteristics of the baseline engine

Engine Type	HSDI 4-S Diesel, EURO IV
N. of cylinders and arrangement	4 in-line
Total displacement [L]	2.78
Bore x Stroke [mm]	94 x 100
Compression ratio	17.5:1
N. of valves per cylinder	4
Air Metering	VGT + Intercooler
Injection system	Common Rail
Max. Injection press. [MPa]	160
Injector hole diameter [mm]	0.153
Number of injector holes	6
EGR system	High Pressure with EGR cooler
Max. brake power [kW@rpm]	130@3800
Max. brake torque [Nm@rpm]	440@1750
Max. Peak cylinder pressure [bar]	150
Max. engine speed [rpm]	4600

As it can be noticed, the investigated engine has a smaller displacement than the generator sets reported in Table 3. Furthermore, thanks to the relatively short stroke, it can easily run at 3000 rpm, permitting the direct coupling to a smaller electric generator. Indeed, if an electric generator revs at 3000 rpm, only 2 poles are required to guarantee an output electric frequency of 50 Hz. Consequently, such an electric generator is smaller and lighter than a 4-poles one that provides the same output electric frequency at a revolution speed equal to 1500 rpm.

At 3000 rpm – BMEP = 12 bar, the reference engine delivera 83 kW, a power close to those ones of the power generation sets listed in Table 3, with the following advantages compared to the latter:

- lower BMEP (except for the DEUTZ generator set);
- more compact dimensions and lower weight (the saved volume can be used to allocate the NG tanks).

The most important operating conditions considered for designing a power generation set are:

- rated speed (in this case corresponding to 3000 rpm), maximum power deliverable for an unlimited number of hours (in this case corresponding to 83 kW/BMEP = 12 bar);
- rated speed (in this case 3000 rpm), 70 ÷ 80 % of maximum power deliverable for an unlimited number of hours (in this case corresponding to 55 kW/BMEP = 8 bar).

During the experimental campaign, also some low load conditions, corresponding to 3000 rpm-BMEP = 2 and 4 bar, were investigated. However, as shown in Figure 10, low loads are generally less critical than high loads in a Diesel engine. This is due to the fact that the lower the load, the higher the Air-to-Fuel Ratio (AFR) and the lower the peak combustion temperatures. Therefore, NO_x and Particulate Matter (PM) emissions are lower. As far as UHC and CO emissions are concerned, even if the corresponding raw emissions are higher at low loads, these pollutants can be effectively reduced thanks to the DOC.

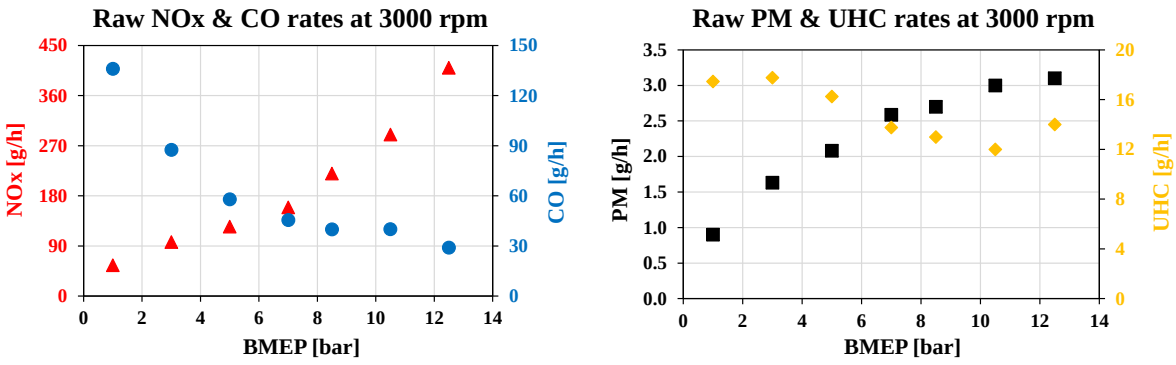

Figure 10. Mass flow rates of CO, UHC, NOx and PM as a function of BMEP for the baseline Diesel engine at 3000 rpm, without EGR

The experimental campaign was carried out at the test facility of the Department of Engineering "Enzo Ferrari" (University of Modena and Reggio Emilia), featuring an Apicom FR 400 BRP eddy-current dynamometer, whose operating range in terms of rotational speed, torque and power is shown in Figure 11.

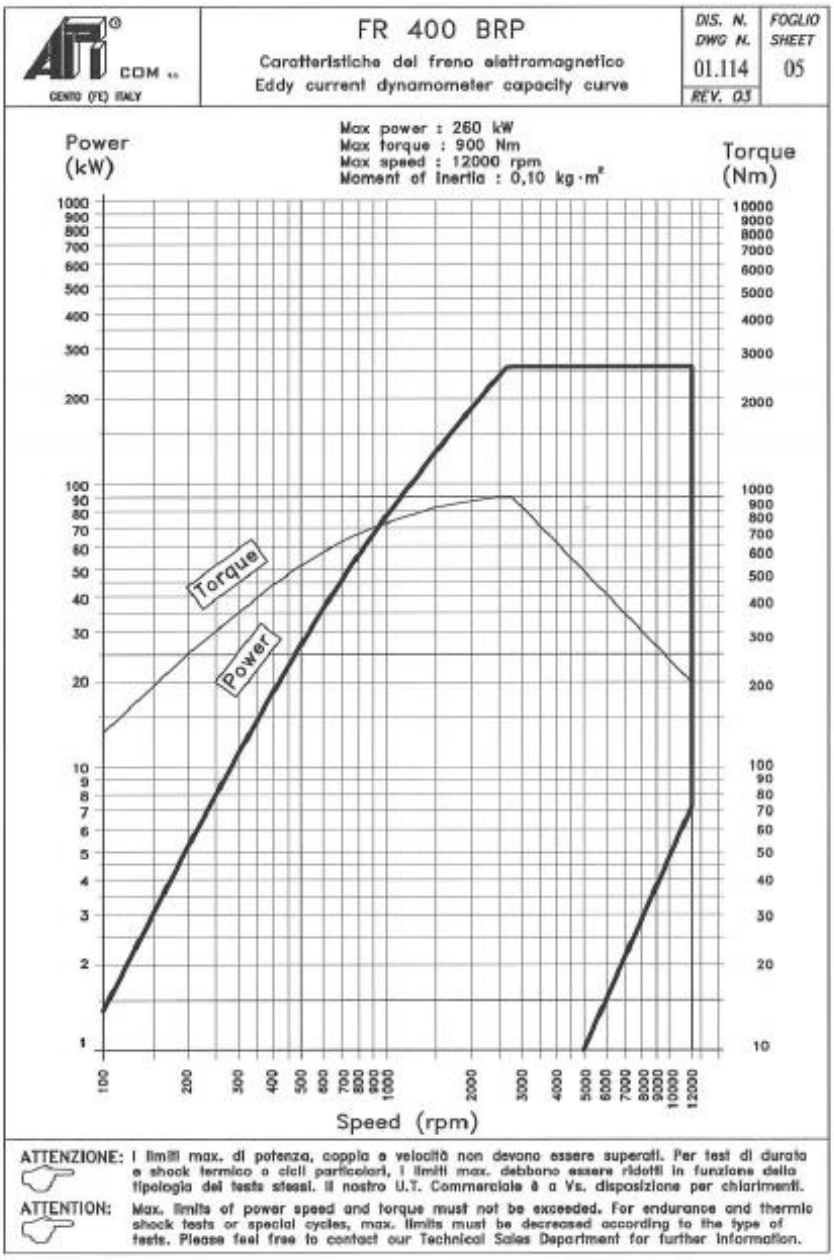

Figure 11. Apicom FR 400 BRP capacity curve

The Apicom Horus software permits to control important operating parameters of the engine, such as maximum intake air temperature (60 °C), maximum coolant temperature (90 °C), maximum lubricating oil temperature (120 °C), engine speed and load. In particular, the rotational speed of the dynamometer and the ICE torque output are controlled by means of two closed-loop controls. The Horus software also permits to acquire data from various pressure and temperature sensors, from a Coriolis flow meter that measures the diesel mass flow rate,

from a hot wire anemometer employed to measure the airflow rate and from the lambda meter module.

The test facility also features an indicating system for in-cylinder pressure measurements. The indicating system is composed by a Kistler 6058A piezo-electric transducer, (installed on one cylinder in place of the glow plug), a charge amplifier and an optical encoder made up of a metal disk with 120 holes and a Sensor Instruments FIA-F fork light barrier with integrated amplifier.

The signals produced by the piezo-electric transducer and the optical encoder are collected by the National Instruments Compact RIO hardware and processed by the Alma Automotive OBI software in order to obtain the in-cylinder pressure trace and to extract the related parameters, calculated in real time with an angular resolution of 0.1 °CA. It should be noticed that the in-cylinder pressure trace and the related parameters correspond to the ensemble average of 100 consecutive engine cycles.

During the experimental campaign, the Electronic Control Unit (ECU) of the baseline engine was replaced by an ETK engine ECU provided by ETAS. Such an ECU is equipped with an additional module, called ETK, that permits to control and modify, in conjunction with the ETAS INCA software, all the relevant engine control parameters (diesel injection pressure, number of injections per cycle, timing and duration of each injection, boost pressure, EGR rates, etc.). In order to reduce the engine control parameters, the EGR valve was kept always shut. Hence, the influence of charge dilution with exhaust gas was not explored in this study.

An oscilloscope was used to visualize the diesel injector command signal, together with the square-wave signal generated by the optical encoder.

The MRU VARIOplus Industrial was used to measure the gaseous emissions of the engine. In detail, the instrument measures the concentration of CO, CO_2 and CH_4 using Nondispersive Infrared (NDIR) detectors, while the concentrations of O_2, NO and NO_2 are measured by means of electrochemical sensors.

The AVL DiSmoke 4000 opacimeter was employed to measure PM emissions. It is important to highlight that both gaseous and PM emissions measured during the experimental activity are raw emissions, since the aftertreatment system is not installed.

Four NG PFI injectors (nominal mass flow rate of 1.5 g/s at 3 bar) were installed on the engine inlet pipe, at a distance of 0.5 m from the intake manifold in order to favour the formation of a homogeneous mixture between NG and air before the flow is split among the four cylinders.

The NG injectors were controlled thanks to a dedicated ECU, requiring the following input signals: engine rotational speed and load, intake air temperature, boost pressure, NG mass flow rate (measured by means of the Alicat MCE gas mass flow controller), temperature and pressure, and exhaust gas temperature.

The main properties of NG (96.0 vol% CH_4; 2.5 vol% C_2H_6; 0.5 vol% C_3H_8; 1.0 vol% N_2) and Diesel fuel employed during the experimental campaign are reported in Table 5.

Table 5. Main physical and chemical properties of NG and Diesel fuel employed in the experimental activity

Fuel properties	**NG**	**Diesel fuel**
Lower Heating Value (LHV) [MJ/kg]	49	43.5
Stoichiometric AFR (α_s) [-]	16.84	14.50
Relative Lower Heating Value (RLHV) [MJ/kg]	2.91	3.00
Heating value of stoichiometric mixture [MJ/kg]	2.75	2.81
Octane Number (ON) [-]	≈120	-
Cetane Number (CN) [-]	-	52
Autoignition temperature [°C]	650	200

As previously said, the experimental study covered four operating conditions:

- 3000 rpm – 44 Nm/BMEP = 2 bar;
- 3000 rpm – 88 Nm/BMEP = 4 bar;
- 3000 rpm – 177 Nm/BMEP = 8 bar;
- 3000 rpm – 265 Nm/BMEP = 12 bar.

For each operating point, the starting (reference) condition was the ND operation. Then, the mass of NG (m_{NG}) was progressively increased, while the mass of Diesel fuel (m_D) injected per cycle was diminished by the closed-loop control applied to the engine pedal, in order to keep the engine brake torque constant.

The energy provided in DF operation by NG, in comparison to the energy provided by diesel in ND mode, is defined by $X_{NG}[\%]$:

$$X_{NG}[\%] = \frac{m_{NG}.LHV_{NG}}{m_D.LHV_D}\ 100 \tag{4}$$

where:

LHV_{NG} is the Lower Heating Value of NG, while LHV_D is the Lower Heating Value of Diesel fuel.

Similarly, the energy provided by diesel in DF operation, in comparison to the energy provided in ND mode, is defined by $X_D[\%]$:

$$X_D[\%] = \frac{m'_D}{m_D} 100 \quad (5)$$

where:

m'_D represents the mass of diesel injected per cycle in DF operation.

Table 6 summarizes the investigated cases at the four operating points. As it can be seen, each case is defined by the percentage of subtracted Diesel fuel energy ($X_D[\%] - 100$) and by the percentage of energy provided by NG ($X_{NG}[\%]$), in comparison to the energy provided in ND mode. Table 6 also reports, for each case, the share of energy between Diesel fuel and NG.

Comparing $X_{NG}[\%]$ to ($X_D[\%] - 100$), the variation of BTE can be qualitatively estimated:

- if $X_{NG}[\%] > |X_D[\%] - 100|$, the energy provided by NG is higher than the subtracted diesel energy → BTE is decreased;
- if $X_{NG}[\%] < |X_D[\%] - 100|$, the energy provided by NG is smaller than the subtracted diesel energy → BTE is increased.

Looking at Table 6, it can be clearly noticed that BTE tended to drop passing from ND mode to DF operation. Therefore, in order to recover the lost efficiency, an optimization of the diesel injection strategy in terms of injection pressure and timings was performed on selected DF cases. In one case, also the boost pressure was optimized. In detail, the optimization process was carried out keeping the diesel mass constant, while minimizing the mass of NG. Moreover, particular care was devoted to maintaining acceptable values of peak in-cylinder pressure and PPRR, in order to limit mechanical and thermal loads, as well as NO_x emissions.

Table 7 shows the influence of the optimization process on engine thermal efficiency. For all the selected DF cases, a strong reduction of NG energy was observed thanks to the optimization. Furthermore, for all the selected DF cases characterized by a BMEP higher than or equal to 8 bar, the optimization guarantees a BTE even higher than that one of the corresponding reference (ND) cases. In fact, the condition $X_{NG}[\%] < |X_D[\%] - 100|$ is true for such DF cases.

Table 6. Summary of the investigated cases and corresponding share of energy between diesel and NG

Operating points	**DF cases**	**Percent diesel by energy [%]**	**Percent CNG by energy [%]**
3000 rpm – BMEP = 2bar 44 Nm	ND	100.00	0.00
	-20% Diesel fuel +46% NG	63.75	36.25
	-41% Diesel fuel +63% NG	48.81	51.19
	-60% Diesel fuel +132% NG	24.27	75.73
	-80% Diesel fuel +175% NG	9.60	90.40
3000 rpm – BMEP = 4bar 88 Nm	ND	100.00	0.00
	-20% Diesel fuel +36% NG	68.95	31.05
	-34% Diesel fuel +43% NG	60.90	39.10
	-64% Diesel fuel +86% NG	29.82	70.18
	-80% Diesel fuel +148% NG	12.15	87.85
3000 rpm – BMEP = 8bar 177 Nm	ND	100.00	0.00
	-27% Diesel fuel +32% NG	70.00	30.00
	-46% Diesel fuel +55% NG	49.52	50.48
	-60% Diesel fuel +66% NG	38.03	61.97
	-80% Diesel fuel +93% NG	17.47	82.53
3000 rpm – BMEP = 12bar 265 Nm	ND	100.00	0.00
	-28% Diesel fuel +30% NG	70.95	29.05
	-36% Diesel fuel +42% NG	60.43	39.57
	-60% Diesel fuel +63% NG	39.38	60.62
	-80% Diesel fuel +75% NG	21.55	78.45

Table 7. Selected DF cases before and after optimization

Operating points	DF cases before optimization	DF cases after optimization
3000 rpm – BMEP = 2 bar	-80% Diesel fuel +175% NG	-80% Diesel fuel +135%NG
3000 rpm – BMEP = 8 bar	-60% Diesel fuel +66% NG	-60% Diesel fuel +57% NG
	-80% Diesel fuel +93% NG	-80% Diesel fuel +74% NG
3000 rpm – BMEP = 12 bar	-60% Diesel fuel +63% NG	-60% Diesel fuel +52% NG

For the sake of completeness, the share of energy between diesel and NG is reported also for the optimized DF cases (see Table 8).

Table 8. Energy share between diesel and NG

Operating points	DF cases	Percent diesel by energy [%]	Percent CNG by energy [%]
3000 rpm – BMEP = 2bar 44 Nm	-80% Diesel fuel +135%NG	13.22	86.78
3000 rpm – BMEP = 8bar 177 Nm	-60% Diesel fuel +57% NG	41.70	58.30
	-80% Diesel fuel +74% NG	19.78	80.22
3000 rpm – BMEP = 12bar 265 Nm	-60% Diesel fuel +52% NG	43.56	56.44

3.3 Results and discussions

Figure 12 depicts the variation of BTE induced by the transition from ND to DF operation, before the optimization process. The variation of BTE is plotted as a function of the percentage of diesel energy reduction ($|X_D[\%] - 100|$). Figure 12 highlights that almost all the DF cases show lower BTE compared to the corresponding ND cases, except for the DF case corresponding to the highest load and the highest substitution of diesel with NG ("-80% Diesel fuel +75% NG" DF case).

Figure 13 shows the variation of BTE induced by the optimization process, considering the DF cases at higher percentage of diesel energy reduction ($|X_D[\%] - 100| > 60\%$). As in Figure 12, the variation of BTE, with reference to the ND operation, is plotted as a function of the percentage of diesel energy reduction. It should be noticed that only for the DF case corresponding to the lowest load (44 Nm, BMEP = 2 bar) it was not possible to enhance or match the value of BTE that characterizes the corresponding reference case. The higher the load, the higher the improvement of BTE achievable thanks to the optimization (up to 3.8%). Furthermore, at medium-high loads, a higher substitution of diesel with NG provides higher BTE enhancement. As an example, at 177 Nm – 8 bar, reducing the percentage of diesel energy from 60% to 80%, BTE enhancement passes from +1.4% to +2.5%.

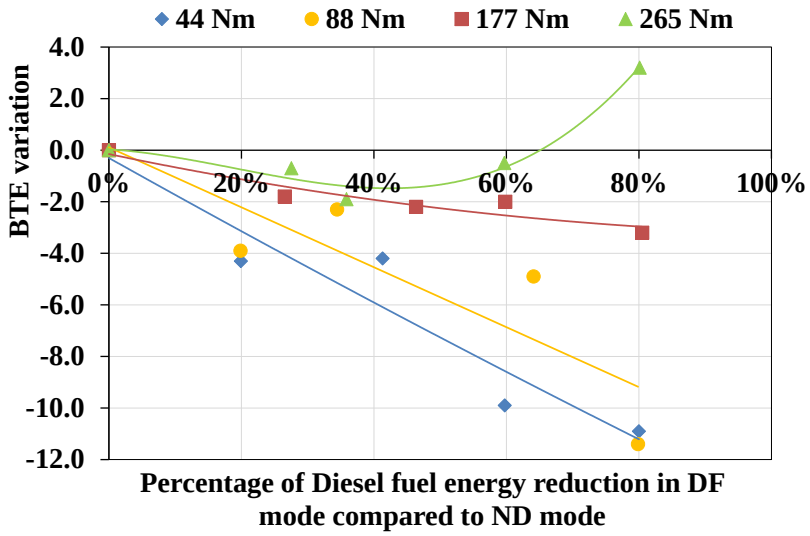

Figure 12. Impact of DF combustion on BTE, before optimization

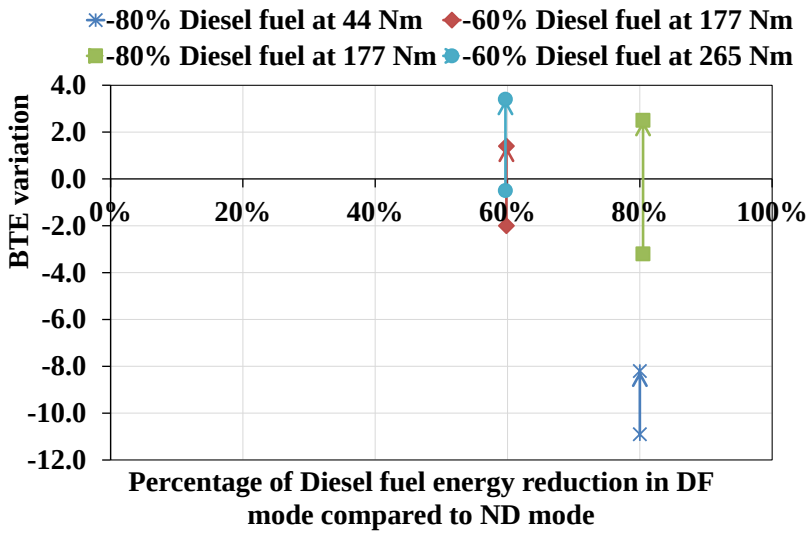

Figure 13. Impact of the optimization process on BTE

3.3.1 Combustion analysis at 3000 rpm – 177 Nm / BMEP = 8 bar

In the present section, the experimental results related to the operating point at 3000 rpm – 177 Nm / BMEP = 8 bar are discussed.

Figure 14 depicts the influence of increasing amounts of NG on in-cylinder pressure and Apparent Heat Release Rate (AHRR). The latter parameter corresponds to the difference between the heat provided by the combustion process and the heat transferred to the combustion chamber walls. It was calculated from the measured in-cylinder pressure, applying the "First Law of Thermodynamics" to a constant mass of ideal gas. The value of the ratio of specific

heats at constant pressure and constant volume was evaluated separately for compression and expansion phases. Moreover, the value of such coefficient changes from case to case.

Looking at Figure 14, three peaks of AHRR can be detected on each curve, except the one with the maximum substitution of diesel with NG ("-80% Diesel fuel +93% NG" DF case). If the ND case is taken into account, the first two peaks correspond to the combustion of the small amounts of diesel due to the pilot and pre injections. As far as the third peak is concerned, it corresponds to the combustion of the fuel that enters the combustion chamber during the main injection. When the diesel is surrounded by a lean NG-air mixture, the first two peaks of AHRR increase, while the third one decreases. This depends on the fact that the integral of the AHRR curve is about constant for a give operating condition. The rising of the first two peaks can be explained considering that the diesel due to the pilot and pre injections ignites also part of the NG-air mixture that surrounds the jets. Moreover, the higher the AFR of the premixed charge, the larger the amount of the NG-air mixture that burns together with the diesel.

Since the maximum peak of AHRR is lower in DF mode with respect to ND operation, also the PPRR is reduced.

Focusing on the in-cylinder pressure traces of Figure 14, it can be noted that all the DF cases show a lower pressure compared to the ND case during the compression stroke, despite the same value of boost pressure. This evidence is due to the higher heat capacity of the NG-air mixtures in comparison to pure air, and the ensuing reduction of the polytropic index. Moreover, NG density is lower than that of air.

However, as shown in Figure 14, CDC is quite similar to the DF combustion, apart from the "-80% Diesel fuel +93% NG" DF case. In the latter DF case, the peak in-cylinder pressure is higher than the other cases. This behaviour can be observed in Figure 15, which reports the Apparent Heat Release (AHR) curves. The CA50 is shifted from 22.6° ATDC (ND case) to 16.4° ATDC ("-80% Diesel fuel +93% NG" DF case).

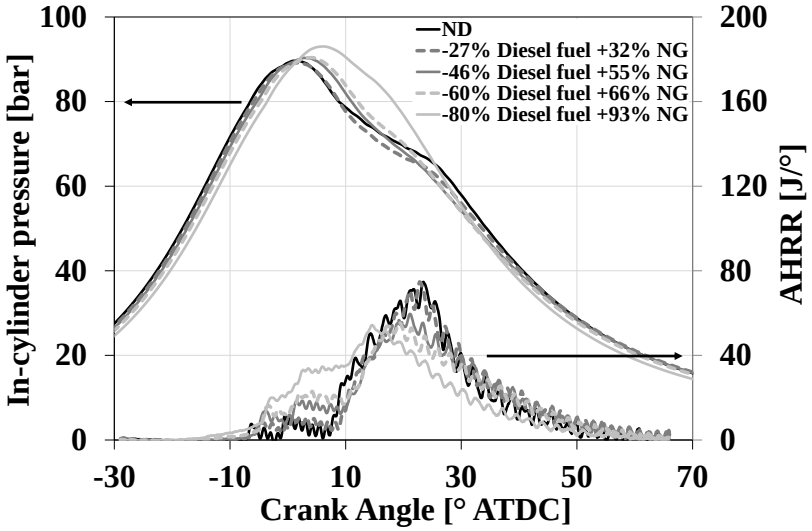

Figure 14. Comparison among ND and DF cases in terms of in-cylinder pressure and AHRR at 3000 rpm – BMEP = 8 bar; DF cases are not optimized

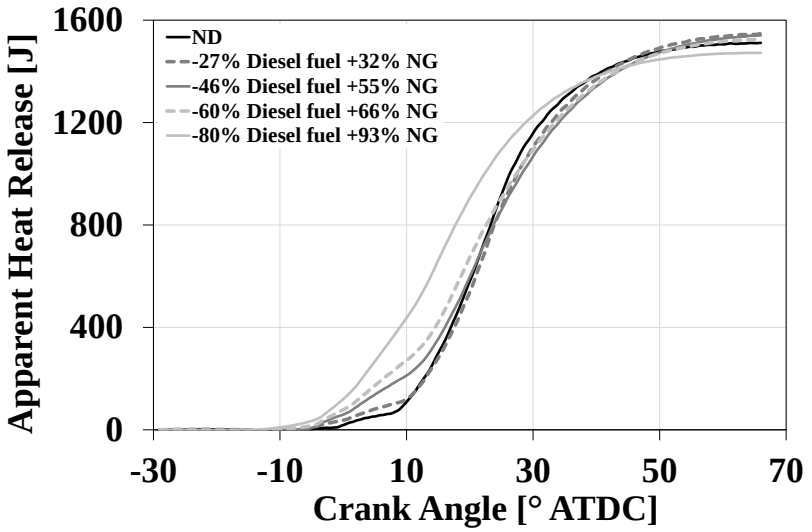

Figure 15. Comparison among ND and DF cases in terms of AHR at 3000 rpm – BMEP = 8 bar; DF cases are not optimized

With the aim to verify the completeness of the combustion process, the combustion efficiency (η_c) is evaluated by means of the following formula:

$$\eta_c = \frac{(P_{in} - \frac{UHC}{10^6}\frac{16}{29}\dot{m}_{air}\,LHV_{NG}\,10^3 - \frac{CO}{10^6}\frac{28}{29}\dot{m}_{air}\,LHV_{CO}\,10^3)}{P_{in}}100 \quad (6)$$

where:

$P_{in} = \dot{m}_{NG}.LHV_{NG} + \dot{m}_{D}.LHV_{D}$ is the power associated to NG and Diesel fuel, in kW; $\dot{m}_{NG}$ is the NG mass flow rate, in g/s; LHV_{NG} is the Lower Heating Value of NG, in MJ/kg; $\dot{m}_{D}$ is the Diesel fuel mass flow rate, in g/s; LHV_{D} is the Lower Heating Value of Diesel fuel, in MJ/kg; UHC is the concentration of CH_4 equivalent Unburnt Hydrocarbons, in ppm; $\frac{16}{29}$ is the ratio between the molar mass of CH_4 and standard air; $\dot{m}_{air}$ is the air mass flow rate delivered to the engine, in kg/s; CO is the concentration of carbon monoxide, in ppm; $\frac{28}{29}$ is the ratio between the molar mass of carbon monoxide and standard air; LHV_{CO} is the Lower Heating Value of CO, in MJ/kg.

It should be noted that Equation (6) does not take into account contribution of H_2, since it could not be measured during the experimental campaign. However, η_c can provide reliable information.

In Figure 16, Figure 17 and Figure 18, ND and DF cases are compared in terms of η_c, BTE and raw emissions. The DF cases that derive from the optimization of "-60% Diesel fuel +66% NG" and "-80% Diesel fuel +93% NG" DF cases are included, i.e., "-60% Diesel fuel +57% NG" and "-80% Diesel fuel +74% NG" DF cases, respectively.

Table 9 reports, for the DF cases at higher percentage of diesel energy reduction ($|X_D[\%] - 100| > 60\%$), the engine control parameters which were optimized and the corresponding values before and after optimization. As it can be noted, both rail pressure and the SOI advance of diesel injection were increased. For the DF case with the maximum substitution of diesel with NG, the optimization involved also the intake air pressure, that was decreased.

Table 9. Summary of optimized engine control parameters at 3000 rpm – 177 Nm / BMEP = 8 bar

DF cases	SOI main [°CA AFTDC]	Rail pressure [bar]	Boost pressure [bar]
-60% Diesel fuel +66% NG	0.0	800	1.8
-60% Diesel fuel +57% NG	- 6.0	850	1.8
-80% Diesel fuel +93% NG	- 1.0	750	1.8
-80% Diesel fuel +74% NG	- 6.0	1050	1.4

Figure 16 clearly shows that the higher the substitution of diesel with NG, the lower the η_c. In particular, passing from the ND case to "-80% Diesel fuel +93% NG" DF case, η_c decreases from 99.8% to 96.8%. This is due to the increasing substitution of diesel with a LRF, that forms with air an ultra-lean mixture (λ_{NG-air} passes from 5.80 for "-27% Diesel fuel +32% NG" DF case to 1.97 for "-80% Diesel fuel +93% NG" DF case). However, the optimization process permits to recover, at least, part of the lost efficiency. As an example, passing from "-80% Diesel fuel +93% NG" DF case to "-80% Diesel fuel +74% NG" DF case, η_c improves by 1.5% (from 96.8% to 98.3%). This result was achieved by increasing the diesel injection pressure (from 750 to 1050 bar) and advancing the diesel SOI (from -1 to -6 °CA AFTDC) in order to promote break-up, evaporation and turbulent mixing of diesel. As a result, the diesel burns faster, involving a larger fraction of the premixed NG-air mixture. Moreover, the resulting higher combustion temperatures speed up the chemical kinetics and hence, the oxidation of the remaining premixed charge.

As shown in Figure 17, also BTE tends to decrease passing from the ND case to the DF cases, if a specific optimization is not applied. However, the optimization of the diesel injection strategy, and, in one case, of the boost pressure, permits to improve the BTE ("-60% Diesel fuel +57% NG" DF case: 36.4%; "-80% Diesel fuel +74% NG" DF case: 37.5%), even in comparison with the ND case (35%), despite the slightly lower η_c. This is due to the enhanced combustion phasing of the DF cycle, which compensate the lower η_c.

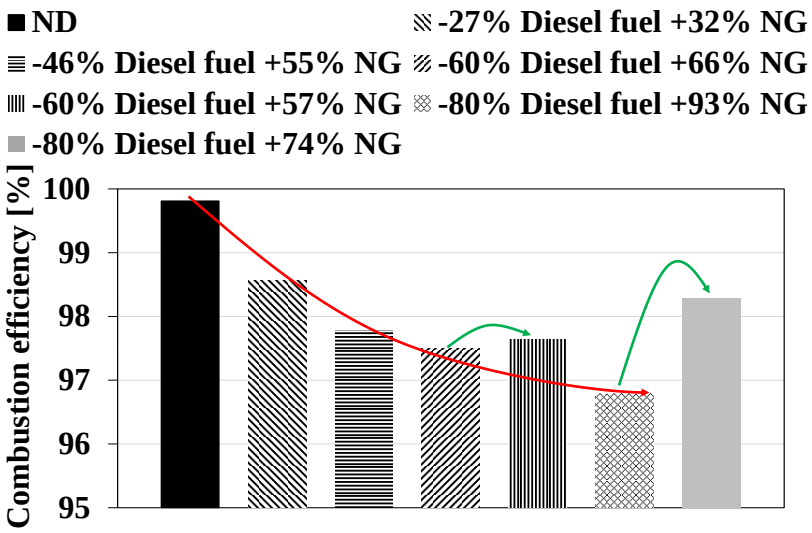

Figure 16. Comparison among ND and DF cases in terms of ηc at 3000 rpm – BMEP = 8 bar

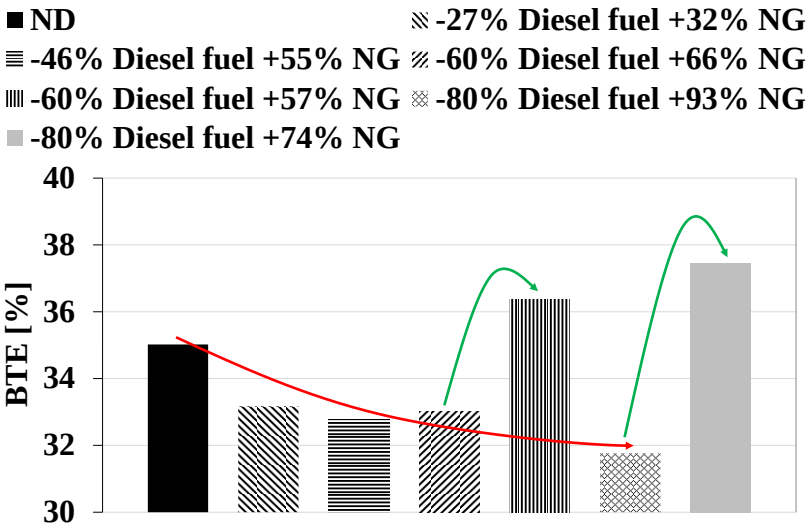

Figure 17. Comparison among ND and DF cases in terms of BTE at 3000 rpm – BMEP = 8 bar

Figure 18a shows a strong increase (at least one order of magnitude) of CO and UHC emissions when passing from ND to DF operation. It clearly appears that the larger the substitution of diesel with NG, the higher the CO and UHC emissions. In fact, as the mass of diesel is lower, it is harder to ignite the lean premixed charge, because of the reduction of the heat released by the oxidation of the diesel. Moreover, the relevant increase of CO and UHC emissions depends on the low reactivity of the homogeneous NG-air mixture, due to its high AFR and the chemical stability of NG, as confirmed by Cameretti et al.[107] However, thanks to the optimization process, CO and UHC emissions can be mitigated. The maximum reduction of CO and UHC emissions was obtained passing from the "-80% Diesel fuel +93% NG" DF case to the "-80% Diesel fuel +74% NG" DF case, and it was greater than 55% for both of them.

Nevertheless, higher CO and UHC raw emissions, in comparison to the CDC, can be accepted, provided that a specific oxidation catalyst is implemented. In fact, the majority of UHC emissions of the DF NG-diesel combustion is CH_4. Due to its higher auto-ignition temperature with respect to other hydrocarbons, as well as to the lower exhaust gas temperature of a DF NG-diesel engine, oxidation of unburned CH_4 in the oxidation catalyst may be complicated. However, Yamamoto et al.[108] proved that a high load of Pt-Pd/alumina is able to improve oxidation of CH_4, even in low temperature conditions. Furthermore, Hutter et al.[109] proved that CO oxidation helps to increase the exhaust gas temperature, promoting the oxidation of the unburned CH_4.

Figure 18a also reports the trend of CO_2 emissions, which follow the opposite trend of CO and UHC emissions. In particular, CO_2 emissions show a maximum reduction of about 26% compared to the ND case. This is due to the high concentrations of CO and UHC emissions, but also thanks to the hydrogen-to-carbon ratio of CH_4, that is the highest among hydrocarbons. Looking at Figure 18b, it can be noticed that the non-optimized DF cases show lower NO_x emissions compared with the ND case, with a maximum reduction of 36.2% ("-80% Diesel fuel +93% NG" DF case). This is due to the reduction of the third peak of AHRR (see Figure 14), that helps to lower the maximum combustion temperatures, and, as a consequence, the genesis of NO_x. Unfortunately, due to the increase of the main injection advance, the optimized DF cases show NO_x emissions similar to those ones of the ND case.

Figure 18b shows a clear trend regarding PM emissions. They decrease as the mass of diesel is decreased. In particular, passing from the ND case to the "-80% Diesel fuel +74% NG" DF case, PM emissions drop from 2.7 g/h to about 1.1 g/h. Since the soot primarily forms within the combusting diesel spray, the decrease of the diesel mass reduces the main source of soot, and hence PM emissions. Furthermore, NG does not contain PAH, and their genesis in the NG flame is primarily due to C_2H_2 and C_2H_5, that are intermediate products of the oxidation of C_2H_6 and C_3H_8, which represent a very small fraction of NG. Finally, due to the competition between diesel and NG for the OH, the diesel ignition delay time increase, improving vaporization and mixing of the HRF.[67]

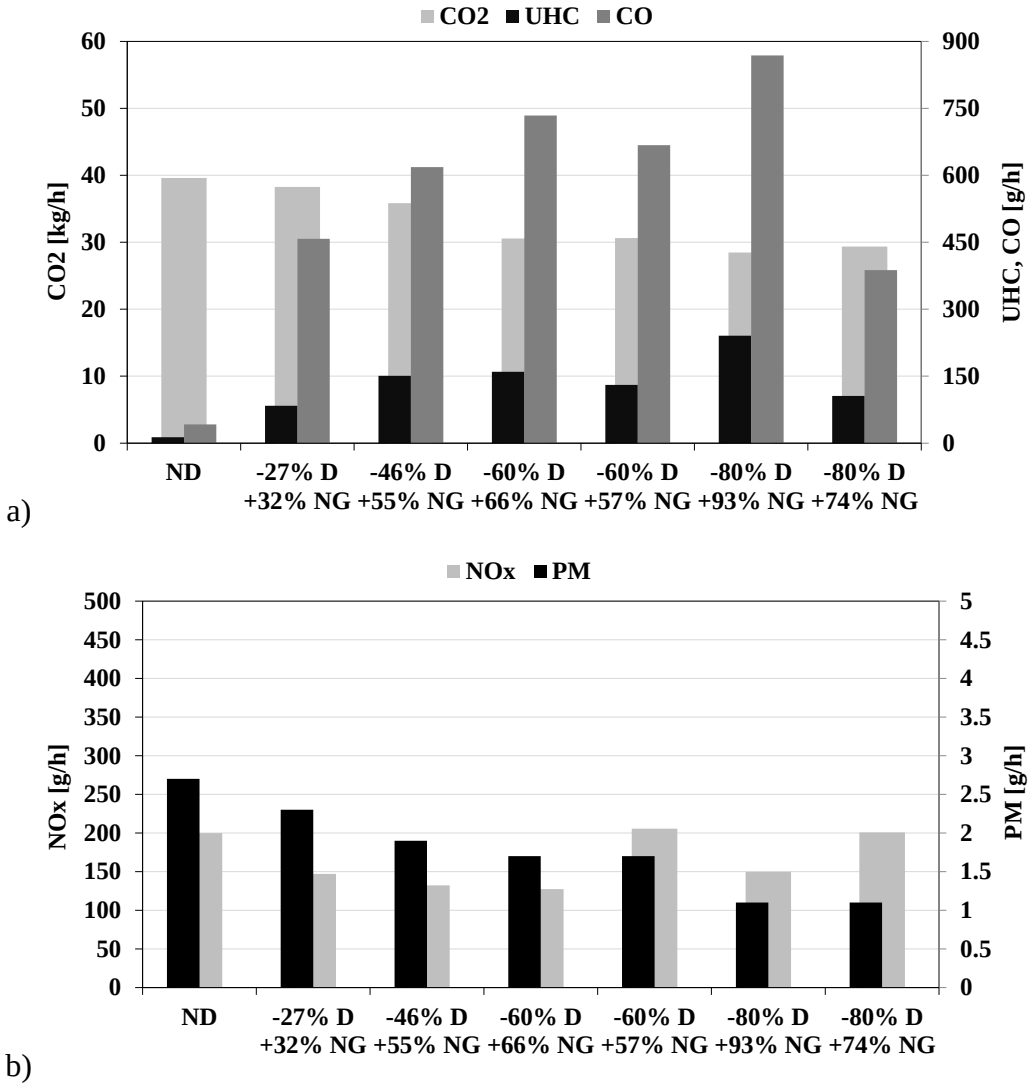

Figure 18. Comparison among ND and DF cases in terms of CO_2, UHC, CO, NO_x and PM emissions at 3000 rpm – BMEP = 8 bar

Figure 19a-b and Figure 20a-b show the influence of the optimization on in-cylinder pressure, AHRR and AHR of the DF cases with a diesel energy reduction higher than 60%. As it can be seen, if the third peak of AHRR is shifted towards TDC, the peak in-cylinder pressure increases, leading to higher maximum temperatures that promote both the oxidation of the hydrocarbons (lower CO and UHC emissions; higher η_c) and the NO_x production. It is also important to notice that, shifting the CA50 towards TDC, the efficiency of the cycle improves thanks to the higher in-cylinder pressure during the expansion stroke.

Finally, Figure 19c and Figure 20c compare the diesel injection strategies before and after the optimization. The diesel injection strategies of the ND cases are also reported.

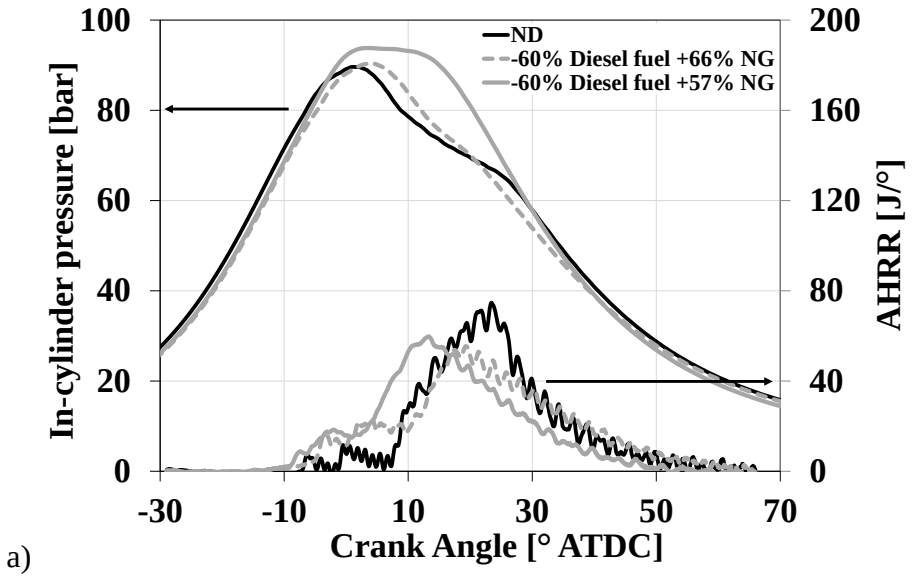

a)

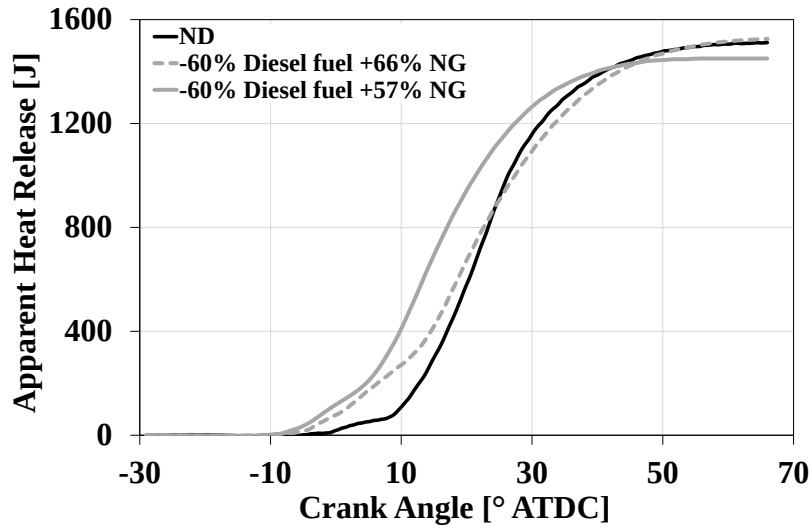

b)

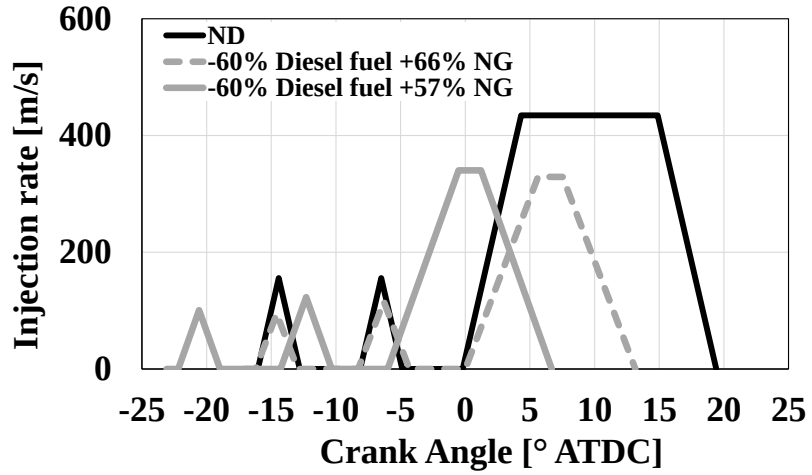

c)

Figure 19. Effects of the Diesel fuel injection optimization on in-cylinder pressure and AHRR (a), and AHR (b) at 3000 rpm – BMEP = 8 bar, "-60% Diesel fuel" DF cases

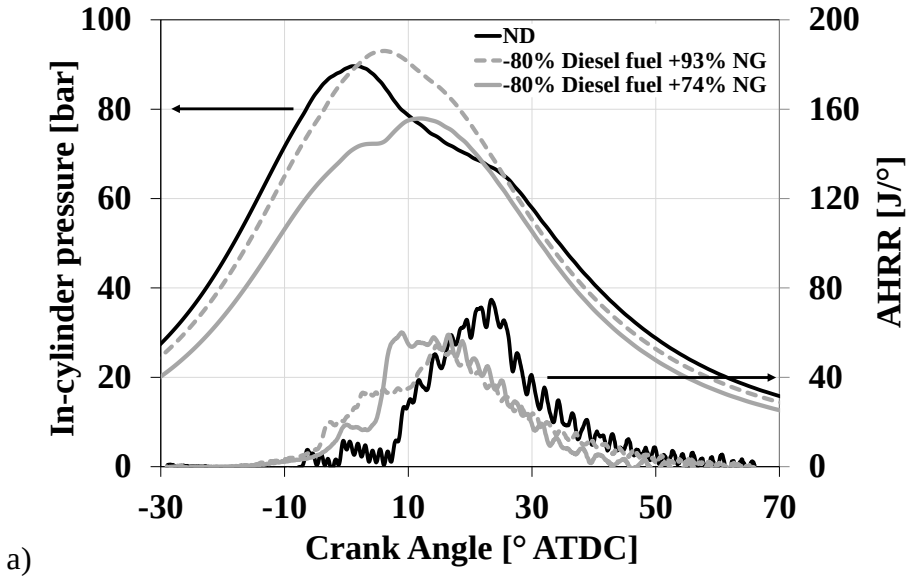

a)

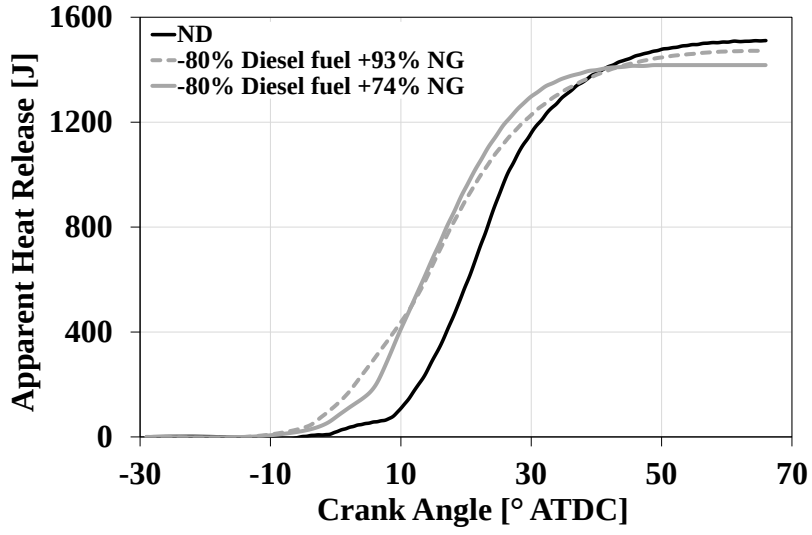

b)

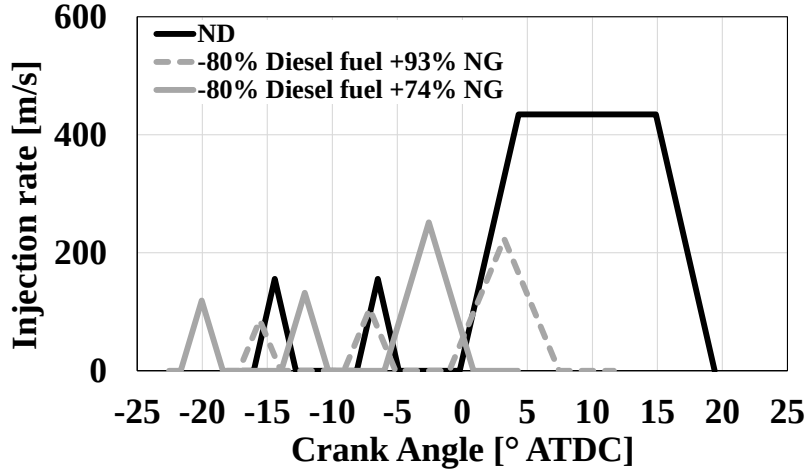

c)

Figure 20. Effects of the Diesel fuel injection optimization on in-cylinder pressure and AHRR (a), and AHR (b) at 3000 rpm – BMEP = 8 bar, "-80% Diesel fuel" DF cases

3.3.2 Combustion analysis at 3000 rpm – 265 Nm / BMEP = 12 bar

In the following section, the operating point corresponding to 3000 rpm – 265 Nm / BMEP = 12 bar is presented.

Figure 21 compares the in-cylinder pressure and AHRR of ND and DF cases. As in the previous operating point, the AHRR shows three peaks of AHRR. However, the lowering of the third peak is obtained only for "-60% Diesel fuel +63% NG" DF case and "-80% Diesel fuel +75% NG" DF case.

Focusing on the in-cylinder pressure traces, it appears that the in-cylinder pressure of the ND case is always higher than that one of the DF cases, except for the "-80% Diesel fuel +75% NG" DF case, which shows a higher peak in-cylinder pressure. This is due to the fact that such DF case is characterized by a faster combustion (at least during its first stages), inducing the CA50 to shift towards TDC by about 5 °CA (see Figure 22).

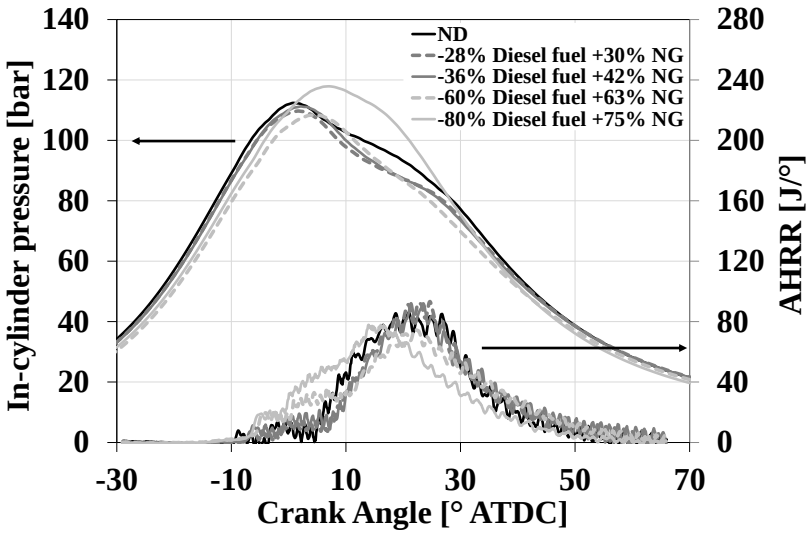

Figure 21. Comparison among ND and DF cases in terms of in-cylinder pressure and AHRR at 3000 rpm – BMEP = 12 bar. DF cases are not optimized

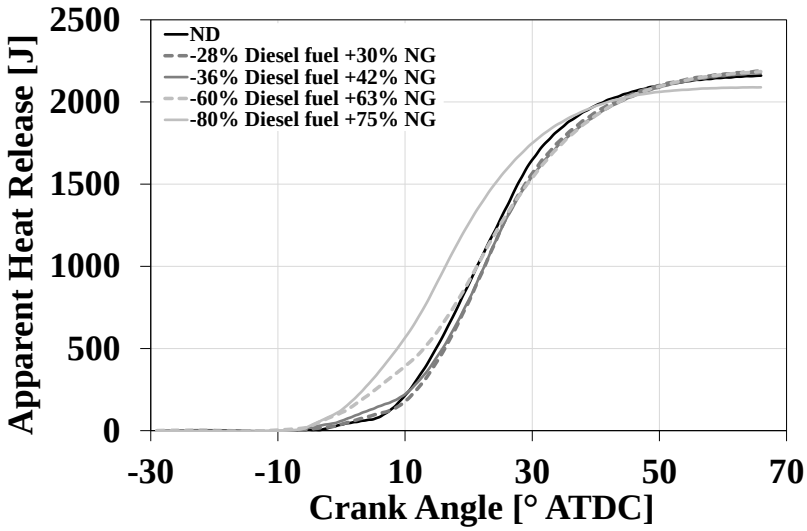

Figure 22. Comparison among ND and DF cases in terms of AHR at 3000 rpm – BMEP = 12 bar. DF cases are not optimized

Figure 23 and Figure 24 compares the ND and DF operations in terms of η_c and BTE, respectively. These figures include two more DF cases ("-36% Diesel fuel +35% NG" DF case and "-60% Diesel fuel +52% NG" DF case), which were obtained by optimizing "-36% Diesel fuel +42% NG" DF case and "-60% Diesel fuel +63% NG" DF case, respectively. In detail, both the diesel injection pressure and the diesel SOI advance were increased (see Table 10).

Table 10. Summary of optimized engine control parameters at 3000 rpm – 265 Nm / BMEP = 12 bar

DF cases	SOI main [°CA AFTDC]	Rail pressure [bar]
-36% Diesel fuel +42% NG	0.0	1250
-36% Diesel fuel +35% NG	- 5.0	1550
-60% Diesel fuel +63% NG	0.0	850
-60% Diesel fuel +52% NG	- 8.0	1100

Figure 23 shows, coherently to the results found at 3000 rpm – 177 Nm / BMEP = 8 bar (see Figure 16), a worsening of η_c as the Diesel fuel is replaced by NG. However, the decrease of η_c is more limited at 3000 rpm – 265 Nm / BMEP = 12 bar, since the corresponding DF cases are characterized by a richer, and hence more reactive, NG-air mixture.

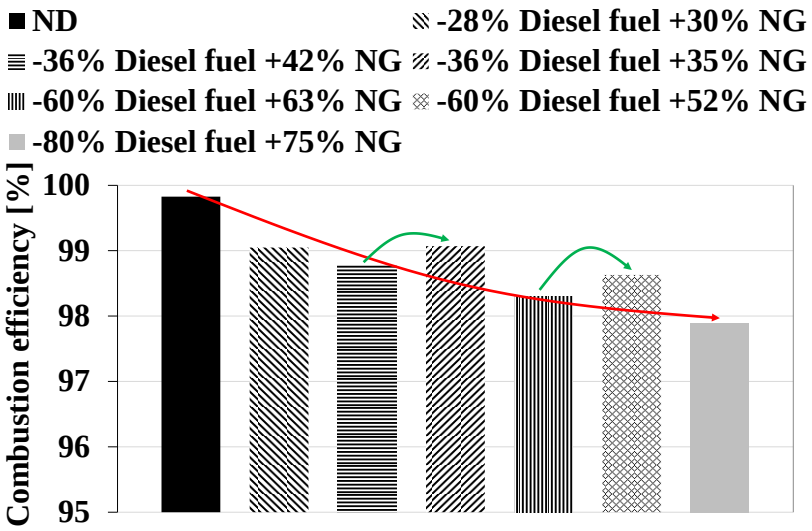

Figure 23. Comparison among ND and DF cases in terms of ηc at 3000 rpm – BMEP = 12 bar

Figure 24 shows that BTE tends to worsen passing from ND to DF operation. However, the optimization of the diesel injection strategy permits to achieve values of BTE equal to or higher than the ND case. In detail, passing from "-36% Diesel fuel +42% NG" DF case to "-36% Diesel fuel +35% NG" DF case, the same BTE of the ND case can be obtained, while passing from "-60% Diesel fuel +63% NG" DF case to "-60% Diesel fuel +52% NG" DF case, the BTE improves by 3.9% (from 35.3% to 39.2%).

Finally, it is important to noted that the "-80% Diesel fuel +75% NG" DF case is characterized by a BTE higher than the ND case (+3.7%) without any optimization of the diesel injection strategy.

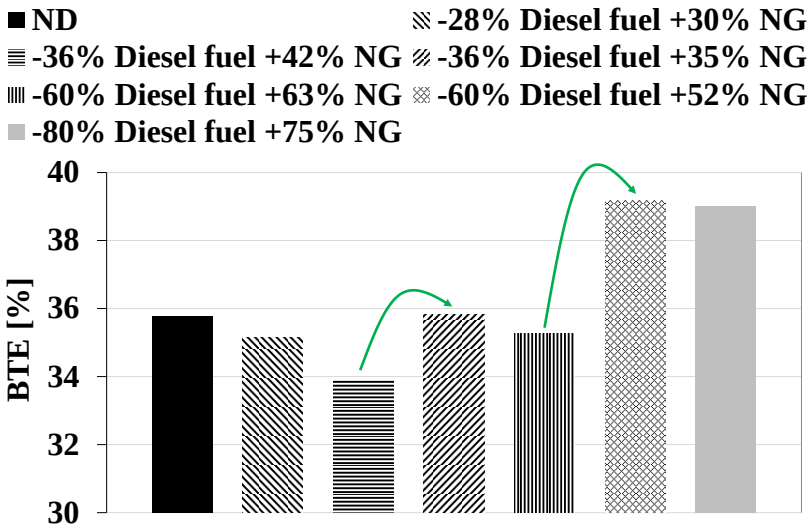

Figure 24. Comparison among ND and DF cases in terms of BTE at 3000 rpm – BMEP = 12 bar

Figure 25 reports the CO_2, CO, UHC, NO_x and PM emissions.

Figure 25a shows that CO_2 emissions decrease (up to -31%), while CO and UHC emissions increase (up to one order of magnitude), as the substitution of the HRF with the low reactivity one increases. Coherently to the results found at 3000 rpm – 177 Nm / BMEP = 8 bar (see Figure 18), the optimization of the diesel injection strategy permits to mitigate CO and UHC emissions (maximum reduction of CO and UHC emissions: 45.6% and 42.9%, respectively).

Focusing on Figure 25b, it can be noticed that NO_x emissions of the DF cases are smaller than in ND operation, with a maximum reduction of NO_x emissions equal to 51%. However, when the diesel injection strategy is optimized, NO_x emissions are slightly higher than in ND mode. This evidence is due to the increase of the SOI main advance (see Figure 26c), which shifts the CA50 towards TDC by about 7 °CA (see Figure 26b). Consequently, as shown in Figure 26a, the peak in-cylinder pressure, and hence the maximum combustion temperatures, increase, leading to higher NO_x emissions. This result highlights a strong correlation among CO/UHC emissions and NO_x emissions: as the formers increase, the latter decrease, and vice versa.

Finally, Figure 25b depicts a reduction of PM emissions as the substitution of diesel with the gaseous fuel increases, consistently with the results at 3000 rpm – 177 Nm / BMEP = 8 bar (see Figure 18). In particular, passing from the ND case to the “-80% Diesel fuel +75% NG” DF case, PM emissions are more than halved (from 3.1 g/h to 1.4 g/h).

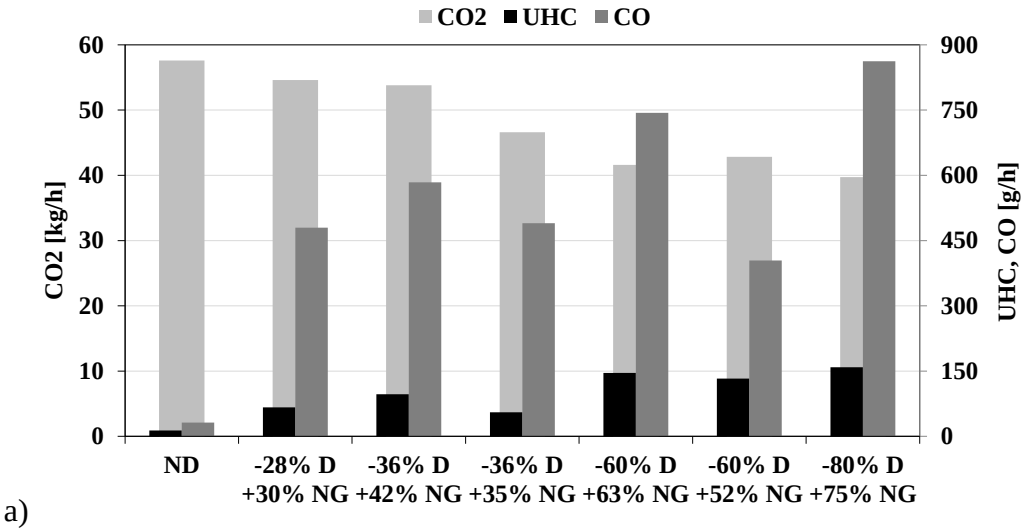

a)

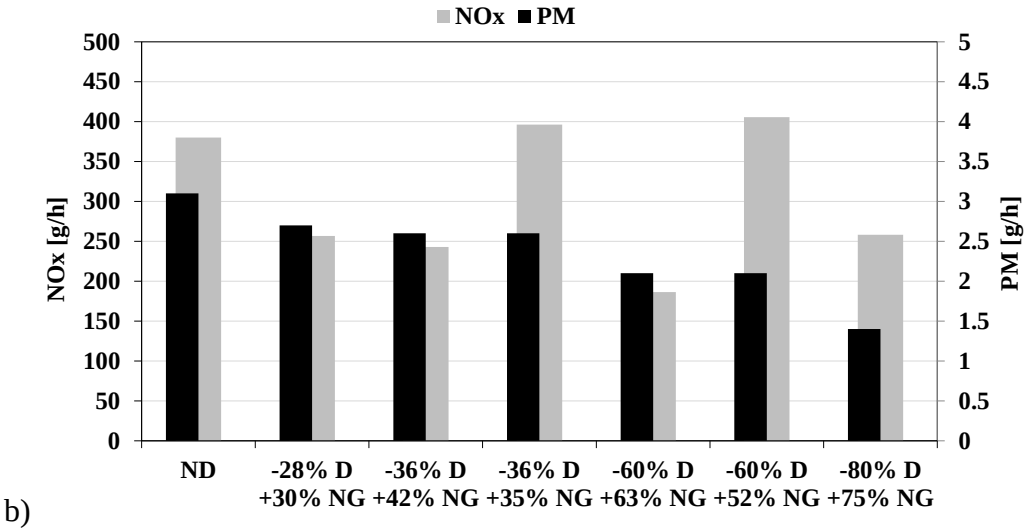

b)

Figure 25. Comparison among ND and DF cases in terms of CO_2, UHC, CO, NO_x and PM emissions at 3000 rpm – BMEP = 12 bar

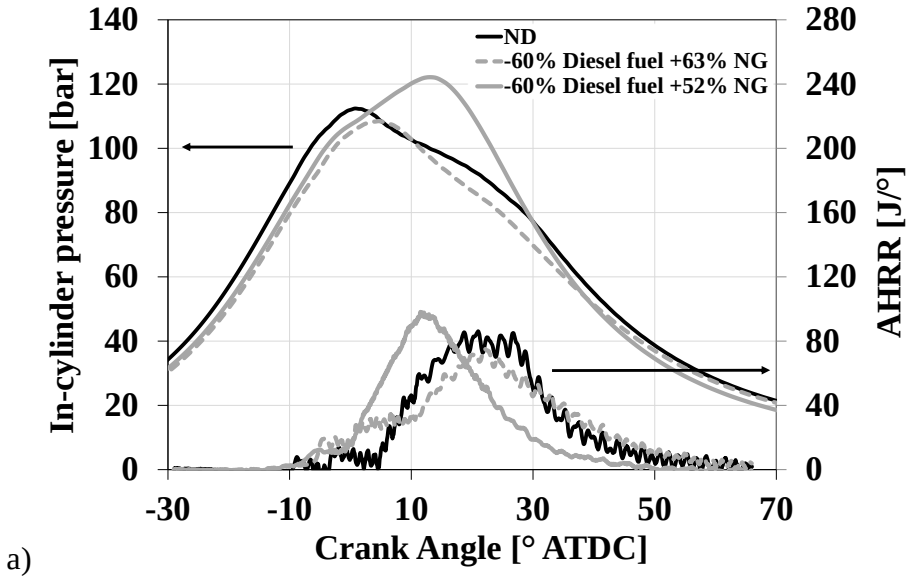

a)

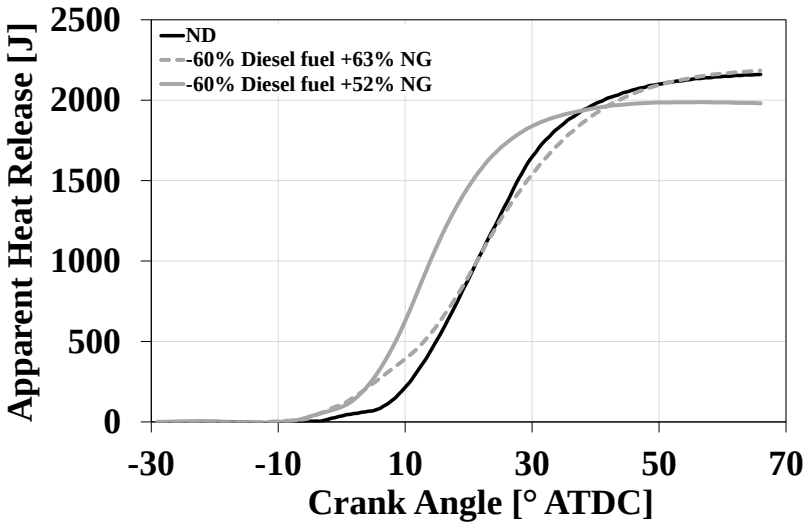

b)

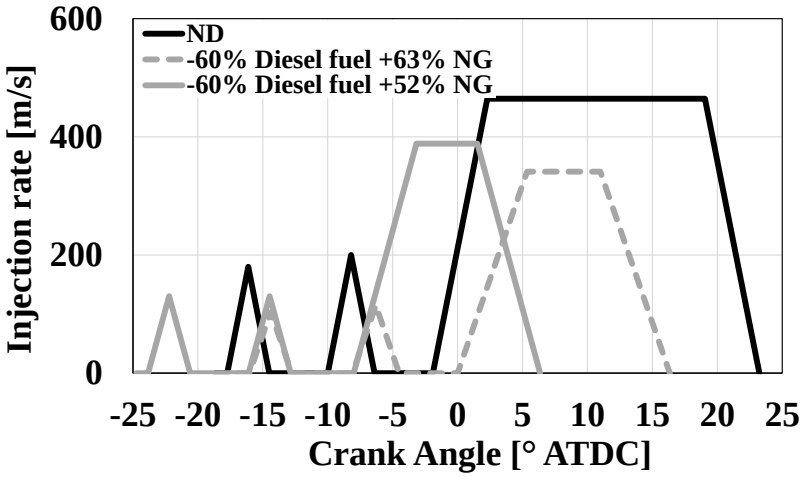

c)

Figure 26. Effects of the Diesel fuel injection optimization on in-cylinder pressure and AHRR (a), and AHR (b) at 3000 rpm – BMEP = 12 bar, "-60% Diesel fuel" DF cases

3.4 Conclusions

Based on the analysis of the experimental results, it can be concluded that the best DF cases are "-80% Diesel fuel +74% NG" DF case at 3000 rpm – 177 Nm / BMEP = 8 bar and "-80% Diesel fuel +75% NG" DF case at 3000 rpm – 265 Nm / BMEP = 12 bar, which correspond to the maximum substitution of diesel with NG.

Table 11 compares the specific emissions of the best DF cases with the corresponding ND cases. Passing from the ND to DF mode, CO_2 emissions are reduced by 38% at 3000 rpm – 177 Nm / BMEP = 8 bar and by 44% at 3000 rpm – 177 Nm / BMEP = 12 bar. The reduction of PM emissions is higher than 200% at both operating points, while the NO_x emissions could be lowered only at the highest investigated load (-46%). On the other hand, both CO and UHC raw emissions increase by one order of magnitude passing from ND to DF operation. However, if a properly designed oxidation catalyst with an average oxidation efficiency of 95% for CO and 90% for UHC is employed, also these emissions can be strongly reduced (see Table 11).

Therefore, the investigated engine, operated in DF NG-diesel mode, could be able to comply with the limits imposed by the European Stage V emission standard[100] without a de-NOx device nor a particulate filter (see Table 12). However, further investigations are required, since also the Particle Number (PN) must be measured.

Table 11. Specific emissions of the investigated engine

	3000 rpm – 177 Nm "-80% Diesel fuel +74% NG" DF case			**3000 rpm – 365 Nm "-80% Diesel fuel +75% NG" DF case**		
	ND	**DF**	**Diff [%]**	**ND**	**DF**	**Diff [%]**
CO_2 [g/kWh]	667	483	-38	719	500	-44
PM [mg/kWh]	45	13.3	-238	37.5	12.5	-200
NO_x [g/kWh]	3.33	3.33	0	4.75	3.25	-46
CO [g/kWh]	0.67	0.25*	-167	0.38	0.38*	0
UHC [g/kWh]	0.22	0.17*	-30	0.16	0.15*	-8
(*) CO and UHC are calculated after the oxidation catalyst						

Table 12. DF engine emissions compared to the Stage V limits

	3000 rpm – 177 Nm "-80% Diesel fuel +74% NG" DF case	**3000 rpm – 365 Nm "-80% Diesel fuel +75% NG" DF case**	**Stage V limits**
NO_x + HC [g/kWh]	3.5	3.4	4.7
PM [mg/kWh]	13.3	12.5	15.0

Furthermore, DF NG-diesel combustion concept guarantees a smoother combustion, and hence lower noise and vibrations, compared to CDC. In detail, the PPRR is reduced from 2.71 bar/°CA (ND case) to 2.14 bar/°CA ("-80% Diesel fuel +74% NG" DF case) at 3000 rpm / BMEP = 8 bar and from 3.62 bar/°CA (ND case) to 3.38 bar/°CA ("-80% Diesel fuel +75% NG" DF case) at 3000 rpm / BMEP = 12 bar. These results confirm that NG permits to obtain a stable and controllable combustion even at medium-high loads and high compression ratios (compression ratio on the investigated engine: 17.5), as opposed to other LRFs, such as gasoline.[10,51]

DF NG-diesel combustion also guarantees a higher BTE compared to CDC. In fact, it increases from 35% to 37.5% at 3000 rpm / BMEP = 8 bar and from 35.8% to 39% at 3000 rpm / BMEP = 12 bar.

Moreover, since NG is primarily made up of CH_4, it can be easily substituted with bio-methane, that is a renewable fuel since it is produced from biomass.

Last but not least, a DF NG-diesel engine can be switched to ND operation, offering a higher fuel flexibility.

Finally, the following conclusions can be drawn:

- Without a specific optimization of the engine control parameters, the higher the substitution of diesel with NG, the lower the η_c and BTE, while CO and UHC emissions increase by one order of magnitude. CO_2, NO_x and PM emissions are always lower;
- The worsening of CO, UHC and BTE is generally mitigated as the load increases, keeping constant the substitution of diesel with NG;
- By means of the optimization of the diesel injection strategy and the boost pressure, BTE can be improved, even compared to the ND operation at medium-high loads;

- The optimization process also guarantees a relevant reduction of CO and UHC emissions. However, NO_x emissions increase, becoming comparable to those ones measured in ND operation;
- At low load, the optimization carried out in the study was not able to completely recover the drop of BTE. Therefore, further investigations are required in order to extend DF NG-diesel operation at low loads.

4 Numerical Modelling

The comprehensive experimental campaign described in Section 3 was fundamental to collect the data required to build and validate some 3D-CFD models of the investigated engine, with the aim to get a deeper insight into the DF combustion concept. In particular, the numerical investigations reported in Section 5 and Section 8 were carried out by means of a customized version of the KIVA-3V code.[110] Therefore, in this section, the main models implemented in such 3D-CFD code are described.

KIVA-3V solves the conservation equations for evaporating fuel sprays coupled with the 3-dimensional turbulent fluid dynamics equations of compressible, multi-component, reactive gases in an engine cylinder with arbitrary shaped piston geometry.

The DF combustion model[111] implemented in the customized version of the code, coupled with chemical kinetics, is based on two sub-models: the generalised Partially Stirred Reactor (PaSR) model[112] and the Fame Propagation model[113].

NG can be modelled as a multi-component mixture of methane (CH_4), ethane (C_2H_6), propane (C_3H_8), butane (C_4H_{10}) and other species such as nitrogen (N_2) and CO_2, while the Diesel Oil Surrogate (DOS) model represents the Diesel fuel.[114] In detail, The DOS model adopts a single component liquid fuel (equivalent chemical formula: $C_{14}H_{28}$) having the same main properties of real diesel and a 70/30 vol% blend of n-heptane (C_7H_{16}) and toluene (C_7H_8) for the fuel vapor.

The mechanism developed to simulate the DF NG-diesel combustion is made up of 81 species and 421 reactions. The validation of the chemical kinetic mechanism was carried out according to measurements of ignition delay times in shock-tube experiments and flame propagation data for constituent components of NG. The SENKIN code[115] was used to calculate ignition delay times under constant volume conditions, while the PREMIX[116] code was used to calculate the laminar flame speeds for NG.

The customized version of the KIVA-3V code also includes the Hybrid Kelvin–Helmholtz/Rayleigh–Taylor (KH-RT) break-up model and a Droplet Collision model, characterised by a mesh independent formulation, for the prediction of the Diesel spray evolution during injection phase.[117]

4.1 Hybrid Kelvin–Helmholtz/Rayleigh–Taylor break-up model

The Hybrid Kelvin–Helmholtz/Rayleigh–Taylor (KH-RT) break-up model proposed by Reitz[118–120] was implemented in the customized version of the KIVA-3V code. It includes two break-up modes. The KH and the RT modes.

Based on the KH break-up mode (see Figure 27), the new child parcels, that are stripped from the parent parcel, are characterised by the following radius:

$$r_c = B_0 \Lambda \tag{7}$$

while the radius of the parent parcel is reduced according to the following equation:

$$\frac{dr}{dt} = -\frac{r - r_c}{\tau_{kh}}, \qquad \tau_{kh} = 3.788 \cdot B_1 \frac{D}{\Lambda \Omega} \tag{8}$$

where:

- B_0 = 0.61;
- B_1 = 40;
- Ω is the growth rate of the fastest growing, and thus most unstable, surface wave:

$$\Omega = \frac{0.34 + 0.38 \cdot We_g{}^{1.5}}{(1+Oh)(1+T^{0.6})} \sqrt{\frac{\sigma}{\rho_d \mathrm{r}^3}} \tag{9}$$

- Λ is the corresponding wavelength:

$$\Lambda = 9.02\mathrm{r} \frac{\left(1+0.45\sqrt{Oh}\right)\left(1+0.4T^{0.7}\right)}{\left(1+0.865We_g^{1.67}\right)^{0.6}} \tag{10}$$

- We_g is the Weber number of the gas:

$$We_g = \frac{\rho_g u_{rel}^2 r}{\sigma} \tag{11}$$

- Oh is the Ohnesorge number:

$$Oh = \frac{\sqrt{We_l}}{Re_l} \tag{12}$$

- We_l is the liquid Weber number, which requires the liquid density instead of that one of the gas;
- Re_l is the liquid Reynolds number:

$$Re_l = \frac{\rho_l |u_{rel}| r}{\mu_l} \tag{13}$$

- T is the Taylor number:

$$T = Oh\sqrt{We_g} \tag{14}$$

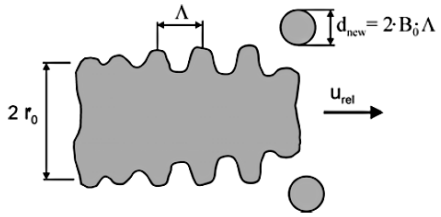

Figure 27. Representation of the KH instability droplet formation process[118]

As far as the RT break-up mode is concerned, the wavelength $\Lambda_t = \frac{\pi}{K}$,
where:

$$K = \sqrt{\frac{|g_t(\rho_l - \rho_g)|}{3\sigma}}, \qquad g_t = \left(\boldsymbol{g} + \frac{d\boldsymbol{u}_d}{dt}\right)\frac{\boldsymbol{u}_d}{|\boldsymbol{u}_d|} \tag{15}$$

is compared to the droplet size. If $\Lambda_t < r$, it is assumed that RT waves have started to grow on the surface droplets. The life time of the growing RT waves is then tracked, and when the life time exceeds the characteristics RT time $\tau_t = 1/\Omega_t$,
where:

$$\Omega_t = \sqrt{\frac{2}{\sqrt{27\sigma}}\frac{|g_t(\rho_l - \rho_g)|^{\frac{3}{2}}}{\rho_l - \rho_g}} \tag{16}$$

Catastrophic break-up occurs, immediately creating much smaller droplets than the KH break-up mode.

The RT break-up splits the parent parcel so that the new statistical number is increased by a factor of r/Λ_t and the new parent droplet size is corrected in order to guarantee the mass conservation.

4.2 Droplet collision model

The Droplet collision model implemented in the customised version of KIVA-3V states that: "*Collision between two parcels occurs if their trajectories intersect and the intersection point is reached at the same time, and within the integration step*".[117]

To reduce the computational cost of such a droplet collision model, two further conditions must be met:

1. The parcels have a chance of colliding if they travel towards each other, i.e.:

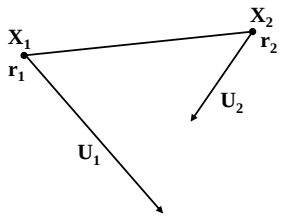

Figure 28. Two parcels traveling towards each other[117]

$$U_{12} = (U_1 - U_2)\frac{x_2 - x_1}{|x_2 - x_1|} > 0 \tag{17}$$

2. The parcels' relative displacement must be larger than the distance between them:

$$U_{12}\Delta t > |x_2 - x_1| - (r_1 + r_2) \tag{18}$$

4.3 Partially stirred reactor model

The generalised PaSR model was implemented in the customised KIVA-3V code to account for the turbulence-chemistry interaction at the micro-scales.

If a shortest chemical characteristic time for a reference reaction is lower than the micro-mixing time, the following equations can be written:

$$\frac{dc^1}{dt} = \frac{c^1 - c^0}{\tau} = -\frac{c}{\tau_c}, \frac{c - c^1}{\tau_{mix}} = -\frac{c}{\tau_c} \tag{19}$$

based on the graph reported in Figure 29, where c^0 is the concentration (mean molar density) in the feed of the reactor (the cell), c^1 is the concentration at the exit of the reactor (i.e. the initial value for the next time step), c is the concentration in the reaction zone, τ is the time integration step, τ_c is the chemical reaction time, τ_{mix} is the micro-mixing time. It represents the chemical reaction time, while II the micro-mixing time.

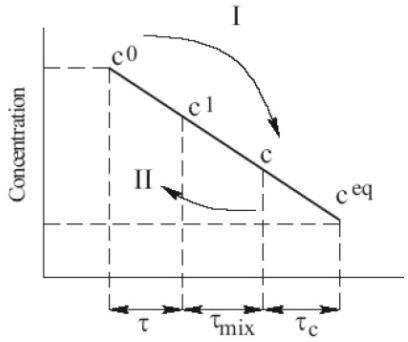

Figure 29. Rate diagram of processes for the PaSR model[114]

After algebraic manipulation, Equation (19) can be rewritten as follows:

$$\frac{c^1-c^0}{\tau} = -\left(\frac{c^1}{\tau_c}\right)\cdot\kappa = -\frac{1}{2}H\left(\frac{c^1}{\tau_c},\frac{c^1}{\tau_{\text{mix}}}\right) \tag{20}$$

where:

$\kappa = \frac{\tau_c}{(\tau_{\text{mix}}+\tau_c)}$ and H is a harmonic mean.

As it can be noticed from Equation (20), the turbulent combustion time is the sum of two terms: mixing time and reaction time.

If the reference s-species is considered, its net rate of production can be expressed as follows:

$$\frac{c_s^1-c_s^0}{\tau} = f_r(c^1)\cdot\kappa = \frac{c_s^0 f_r^0}{c_s^0 + \text{term}\,\bar{r}\,\tau + \text{term}\,\bar{r}\,\tau_{mix}} \tag{21}$$

where:

f_r^0 is the net rate of chemical production, while $\text{term}\,\bar{r}$ is the mass depletion rate, namely:

$$\begin{aligned} f_r(c) = \quad & (v_r'' - v_r')\dot{\omega}_r(c) = \text{term}\,\overset{+}{r} - \text{term}\,\bar{r} = \\ & = \text{term}\,\bar{r} - \frac{c_s}{\tau_c} \end{aligned} \tag{22}$$

where:

v_r'' and v_r' are stoichiometric coefficients of the backward and forward steps, while $\dot{\omega}_r$ represents the rate progression variable of the r-reaction.

It should be noted that the micro-mixing time corresponds to the Kolmogorov's time.[121]

Defining the references species as those ones with a smallest concentration among the species defining the depletion rate in the linear form (8), they are similar to the deficient specie of the Mgnussen-Hjertager model.[122] Introducing such a reference species for each reaction permits to approximate the nonlinear rate expression $\mathrm{term}\,\bar{r}$ to the linear one $\frac{c_s}{\tau_c}$. Then, substituting Equation (22) into Equation (21), the following equation is obtained:

$$\begin{aligned} f_r(c) \quad &= (\,\mathrm{term}\,\bar{r}^{+} - c_s/\tau_c)\frac{\tau_c}{\tau_c+\tau_{mix}} = \\ &= \mathrm{term}_r^{+}\,\frac{\tau_c}{\tau_c+\tau_{mix}} - \frac{c_s}{\tau_c+\tau_{mix}} \end{aligned} \tag{23}$$

Taking not account the chemical equilibrium conditions $f_r(c) = 0$, namely, $\mathrm{term}_r^{+} = c_s{}^{eq}/\tau_c$, the final PaSR formulation in the $\tau_c \to 0$ is:

$$\lim_{\tau_c \to 0} f_r(c) = \frac{c_s^{eq} - c_s}{\tau_{mix}} \tag{24}$$

4.4 Flame Propagation model

As far as the Flame Propagation model is concerned, the Turbulent Flame speed Closure (TFC) model proposed by Lipatnikov and Chomiak[113] was implemented in the customised version of KIVA-3V.

The laminar flame speed required by the TFC model was calculated by the PREMIX code. However, it is convenient to approximate the laminar flame speed as a correlation that couples the latter parameter with initial mixture pressure, temperature and equivalence ratio (ϕ).

The correlation proposed by Metghalchi and Keck[123] (Equation (25)) is applicable for a very narrow range of ϕ values. Therefore, it is not recommended for DF combustion modelling.

$$S_L = S_{L0}\left(\frac{T}{T_0}\right)^{\alpha}\left(\frac{p}{p_0}\right)^{\beta} \tag{25}$$

where:

T and p are the unburned gas temperature and pressure, respectively; T_0 and p_0 represent the standard temperature and pressure, respectively; α and β are approximation coefficients; S_{L0} is the laminar flame speed under standard conditions; S_L is the actual laminar flame speed.

The correlation proposed by Gülder[124] (Equation (26)) is more general than Equation (25). However, as will be demonstrated in Section 4.6.1, it was not sufficiently accurate for DF combustion modelling.

$$S_L = ZW\phi^{\eta}\exp\left[-\xi(\phi-1.075)^2\right]\left(\frac{T}{T_0}\right)^{\alpha}\left(\frac{p}{p_0}\right)^{\beta} \tag{26}$$

where:

Z, W, η, ξ, α and β are tabulated coefficients.

Hence, a new correlation, based on laminar flame speed calculations performed by the PREMIX code, was developed. Such correlation was established to be of the form of Equation (25).

First of all, S_{L0} was evaluated by means of the PREMIX code using the NG combustion mechanism,[121] consisting of 74 species that take part in 366 reactions, for values of ϕ between 0.5 and 1.5. The NG was assumed to be composed by a blend of four species: CH_4 (87.8 vol%), C_2H_6 (5.9 vol%), C_3H_8 (4.6 vol%) and C_4H_{10} (1.7 vol%).

Then, the calculated laminar flame speeds were fitted to a polynomial correlation:

$$\begin{aligned} F = {} & a(\phi-1)^7 + b(\phi-1)^6 + c(\phi-1)^5 + d(\phi-1)^4 \\ & + e(\phi-1)^3 + f(\phi-1)^2 + g(\phi-1) + h \end{aligned} \tag{27}$$

The comparisons among calculated (PREMIX, new correlation (Equation (27)) and Gülder's correlation) and experimental laminar flame speeds are reported in Section 4.6.1.

4.5 Dual fuel combustion model

The DF combustion model[111] is composed by the generalised PaSR model[112] and the Flame Propagation model[113] described in Section 4.3 and Section 4.4, respectively.

First of all, the mass balance equation which follows is considered (Equation (28)). It should be noted that the spray source is neglected.

$$\frac{\partial c_m}{\partial t} + \nabla \cdot (c_m \mathbf{u}) = \nabla \cdot \left[\rho D \nabla \left(\frac{c_m}{\rho}\right)\right] + \dot{\rho}_m^{c1} + \dot{\rho}_m^{c2} \tag{28}$$

where:

$c_m = \frac{\rho_m}{W_m}$, $m = 1,..,s,..,N_m$; c_m is the mole density of species m, while W_m is its molecular mass; $\mathbf{u}$ is the velocity vector; $(\dot{\rho}_m^{c1} + \dot{\rho}_m^{c2})$ takes into account the two combustion modes (PaSR and TFC) chemical sources.

In particular:

$$\begin{aligned} &\dot{\rho}_m^{c1} \approx \frac{c_m}{\tau_{c1}},\ \dot{\rho}_m^{c2} \approx \frac{c_m}{\tau_{c2}} \\ &\dot{\rho}_m^{c1} + \dot{\rho}_m^{c2} = \frac{c_m}{\tau_c} \end{aligned} \tag{29}$$

where:

τ_{c1} and τ_{c2} are the characteristic times of the two combustion modes, while τ_c is the characteristic time of the entire combustion process. The relation among τ_c, τ_{c1} and τ_{c2} is the following:

$$\tau_c = \frac{\tau_{c1}\tau_{c2}}{\tau_{c1}+\tau_{c2}} = \frac{1}{2}H(\tau_{c1}, \tau_{c2}) \tag{30}$$

If $\tau_{c1} \gg \tau_{c2}$, Equation (30) reduces to $\tau_c \cong \tau_{c2}$, which means that the combustion mode 2 is the dominant one.

τ_{c1} can be expressed as follows:[112]

$$\tau_{c1}^{-1} = -\frac{[\dot{\rho}]_{sr}^0}{(c_s^0 + R_D^0 \tau + \tau_{\mathrm{mix}})} \tag{31}$$

where:

$R_D^0 = b_{sr} k_{br}(T) \prod_m^{N_m} c_m^{b'_{mr}} + a_{sr} k_{fr}(T) \prod_m^{N_m} c_m^{a'_{mr}}$ derives from the Arrhenius kinetics, $k_{fr}, k_{br}, a_{sr}, b_{sr}$, are the parameters of the chemical reaction r; s is the index of the reference species selected among the species participating in the reaction r; τ is the time integration step; $\tau_{mix} \sim \frac{k}{\varepsilon}$ is the micro-mixing time, that corresponds to the Kolmogorov's time.[121]

As far as the laminar flame propagation model is concerned, the reaction rate expression derives from the equation of the flame speed obtained by the integration of the mass balance equation in the form of a travelling wave solution, namely:

$$S_{m,l} = \frac{\int_{f_1}^{f_2} \dot{\rho}_m^{c2} dx}{c_{mf_2} - c_{mf_1}} \approx \frac{\dot{\rho}_m^{c2} \int_{f_1}^{f_2} dx}{c_{mf_2} - c_{mf_1}} \approx \dot{\rho}_m^{c2} |\nabla c_m|^{-1} \quad (32)$$

where:

f_1 and f_2 are flame boundaries in physical space; $S_{m,1}$ is the laminar flame speed.

$S_{m,1}$ was calculated under unburned gas conditions using the PREMIX code of the CHEMKIN-II package.[125]

If c_m is assumed to be equivalent to an overall combustion progress variable $\tilde{c} \in [0,1]$, then:

$$\begin{aligned} \dot{\rho}^{c2} &= S_l |\nabla \tilde{c}| = \frac{\tilde{c}}{\tau_{c2}} \\ \tau_{c2}^{-1} &= \frac{|\nabla \tilde{c}|}{\tilde{c}} S_l \end{aligned} \quad (33)$$

The turbulent flame speed (S_t) was assumed dependent on the laminar flame speed and properties of the turbulence, such as $u' \sim k^{\frac{1}{2}}$:

$$S_t \sim u'^{3/4} S_l^{1/4} \left(\frac{l}{\delta_l}\right)^{1/4} \quad (34)$$

The conservation equation that governs the flame propagation process is:

$$\begin{aligned} \frac{\partial}{\partial t}(\bar{\rho}\tilde{c}) + \nabla \cdot (\bar{\rho}\tilde{c}\mathbf{u}) = \quad & \nabla \cdot [\bar{\rho} D \nabla \tilde{c}] + \rho_u S_t |\nabla \tilde{c}| \\ & + \bar{\rho}(1 - \tilde{c})/\tau_f(T) \end{aligned} \quad (35)$$

where:

ρ_u refers to the density of the unburnt mixture calculated by the PREMIX code.

The terms $\bar{\rho}(1 - \tilde{c})/\tau_f(T)$ in Equation (35) represents the flame formation from high temperature regions induced by the combustion of pilot injections.

The final solution algorithm involved the integration of Equations (28), (35) and (30).

4.6 Chemical-kinetic mechanism for NG-diesel mixtures

The development and validation of the chemical kinetic mechanism for NG-diesel mixtures were carried out according to measurements of ignition delay times in shock-tube experiments and flame propagation data for constituent components of NG. The SENKIN code was used to

calculate ignition delay times under constant volume conditions,[111,114] while the PREMIX code was used to calculate the laminar flame speeds for NG.[111]

4.6.1 Natural gas

As already said, NG was considered to be a blend of CH_4 (about 90 vol%) , C_2H_6, C_3H_8 and C_4H_{10}.

As it can be seen from Figure 30, the NG combustion mechanism[121] (74 species that take part in 366 reactions) showed good agreement with experimental auto-ignition data under engine relevant conditions.[126]

It should be noticed that the calculated ignition delay times for NG are shorter then CH_4 at high temperatures. This is due to the fact that NG contains, besides CH_4, more reactive hydrocarbons (C_2H_6, C_3H_8 and C_4H_{10}).

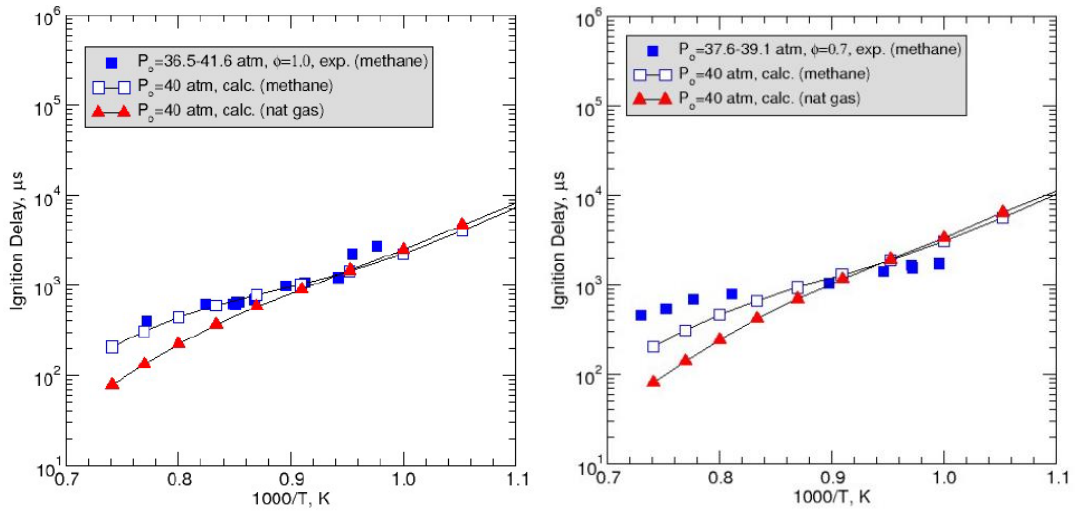

Figure 30. Calculated ignition delay times for stoichiometric and lean NG-air mixtures[111]

As far as the comparison among experimental[127] and calculated (PREMIX and Gülder's correlation) laminar flame speeds for NG at standard conditions is concerned, Figure 31 demonstrates that the predictions provided by the PREMIX code guarantee a better agreement with experimental data than the Gülder's correlation.

Moreover, as it can be seen in Figure 32, the new correlation (Equation (27) in Section 4.4; referred to as "Approximation" in Figure 32) showed a better agreement with the PREMIX calculations than the Gülder's correlation at typical engine conditions.

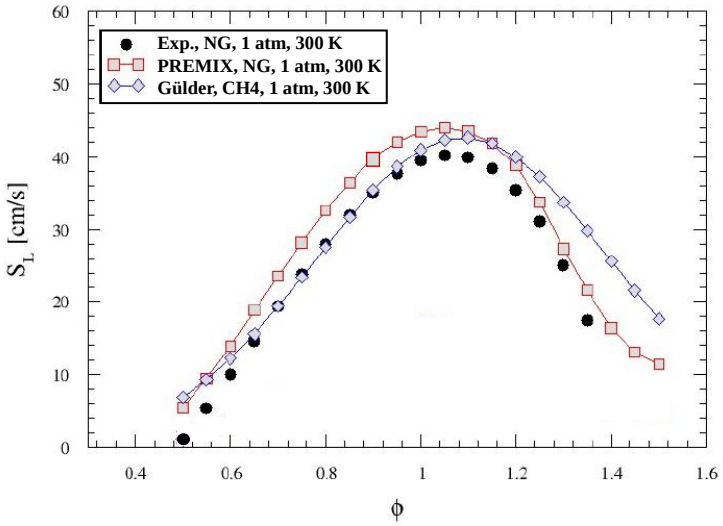

Figure 31. Comparison among experimental and calculated (PREMIX and Gülder's correlation) laminar flame speeds for NG at standard conditions[111]

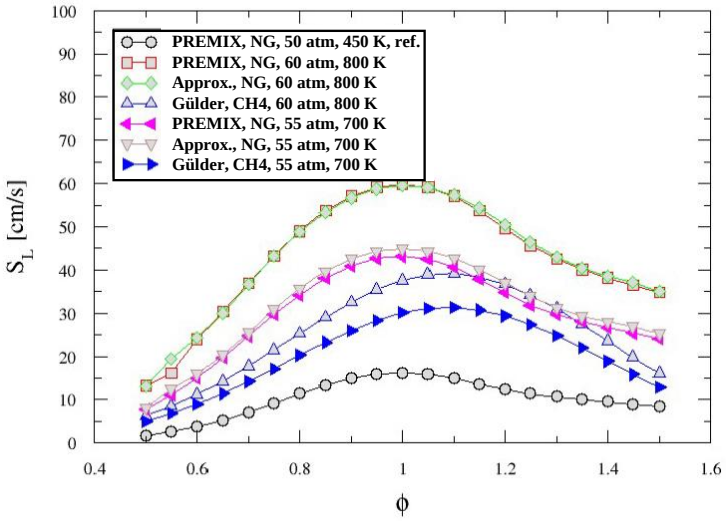

Figure 32. Comparison among calculated (PREMIX, new correlation and Gülder's expression) laminar flame speeds for typical engine conditions[111]

4.6.2 Diesel Oil Surrogate model

With the aim to accurately model real diesel fuel, the DOS model was implemented in the framework of KIVA-3V.

The DOS model consists in representing the liquid diesel fuel through a single-component substance with equivalent chemical formula corresponding to $C_{14}H_{28}$. However, the properties

of the real diesel fuel are used and compiled in the KIVA-3V fuel library. As far as the diesel fuel vapor is concerned, it is modelled by means of a 70/30 vol% blend of n-heptane (C_7H_{16}) and toluene (C_7H_8).

The aliphatic hydrocarbon (n-heptane) represents the main component of the blend since its CN (56) is similar to the one of real diesel fuel. Considering that the CN of toluene is equal to about 9, the calculated CN of the DOS model is about 47.[128]

The single-component liquid fuel model is assumed to decompose into the two-component fuel vapor model through the following pyrolysis reaction:

$$1.5C_{14}H_{28} + 0.5O_2 \Rightarrow 2C_7H_{16} + C_7H_8 + H_2O \tag{36}$$

This approach is due to the fact that the oxidation scheme of real diesel fuel is not known.

The detailed chemical oxidation sub-mechanisms for n-heptane and toluene consists of 70 species taking part in 310 reactions. Based on shock-tube ignition measurements of toluene-air mixtures at Diesel relevant conditions,[129] the toluene kinetic model was improved thanks to the addition of a set of reactions containing the double ketone $C_6H_4O_2$:

$$\begin{aligned} &C_6H_5 + O_2 = C_6H_4O_2 + H \\ &C_6H_4 + O_2 \Rightarrow 2CO + C_2H_2 + CH_2CO_2 \\ &C_6H_5O + O \Rightarrow C_6H_4O_2 + H \\ &C_6H_5O + HO_2 = C_6H_4O_2 + H_2O \end{aligned} \tag{37}$$

The resulting oxidation mechanism of the diesel fuel model is able to adequately predict the ignition delay time of both n-heptane and toluene, as shown in Figure 33, which compares calculated ignition delay times for stoichiometric and lean n-heptane/air and toluene/air mixtures and shock-tube experimental data at high pressure conditions. The kinetic simulations were carried out by means of the SENKIN code for a constant volume, adiabatic case.

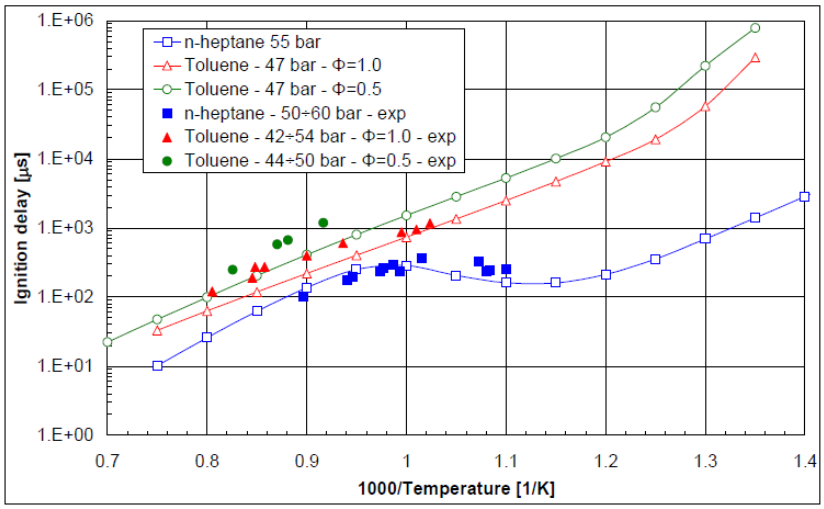

Figure 33. Comparison between calculated ignition delay times for stoichiometric and lean n-heptane/air and toluene/air mixtures and shock-tube experimental data for high pressure conditions[114]

4.7 Soot formation

Acenaphthylene ($C_{12}H_8$), referred to as A2R5, was selected as the soot precursor. Therefore, the chemical mechanism also includes the reaction path of the polycyclic rings formation that leads to A2R5, and then to soot, starting from the phenyl radical (C_6H_5) (see Figure 34).

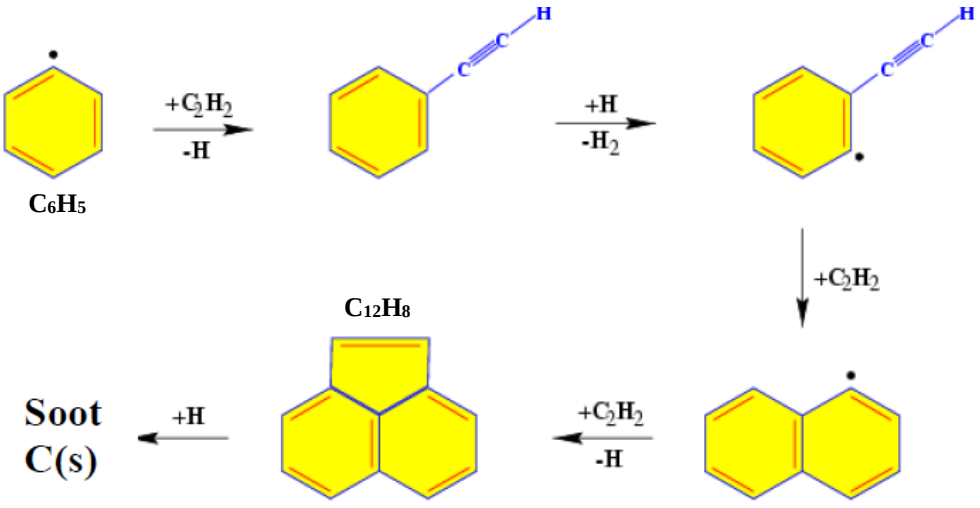

Figure 34. Reaction path from C_6H_5 to soot particles[114]

The genesis of soot particles from A2R5 is assumed to be the following "graphitization" reaction:

$$A2R5 \Rightarrow 12C(S) + 4H_2 \tag{38}$$

The thermal properties of soot (referred to as C(S)) are those ones of graphite.

4.8 NO interaction with combustion chemistry

In order to take into account the interaction between NO and combustion chemistry, which takes place when internal or external EGR is used, the following reactions were added to the chemical mechanism:

$$\begin{aligned} &NO + HO_2 = NO_2 + OH \\ &NO_2 + H = NO + OH \\ &NO_2 + O = NO + O_2 \end{aligned} \tag{39}$$

In (4), NO and NO_2 react with the radical HO_2 forming the highly reactive hydroxyl radical (OH), which is able to speed up the combustion process. However, if a large amount of NO is present in the premixed charge, the subtraction of H and O radicals (last two reactions in (4)) becomes dominant, slowing down the combustion process.

As far as the NO_x formation is concerned, the Zeldovich thermal mechanism and a low-temperature nitrogen (N_2) oxidation branch via N_2O were implemented in the chemical mechanism.

5 Numerical optimization of the diesel injection strategy on a light-duty Diesel engine operated in dual fuel natural gas-diesel combustion mode at 3000 rpm – 265 Nm / BMEP = 12 bar

5.1 Introduction and aim

In this section, a first numerical study performed with a customized version of the KIVA-3V code, is presented. In particular, the investigation was aimed at exploring the influence of the number of diesel injections per cycle and of the diesel SOI on DF combustion characteristics and emissions. The study was focused on the operating point at 3000 rpm – 265 Nm / BMEP = 12 bar and the DF case corresponding to "-60% Diesel fuel +52% NG".

The description of the activity has been reported in a paper entitled "Numerical Optimization of the Injection Strategy on a Light Duty Diesel Engine Operating in Dual Fuel (CNG-Diesel) Mode" and published in the International Journal of Heat and Technology (IIETA, International Information and Engineering Technology Association).[130]

Further numerical investigations were carried out by means of KIVA-3V and the commercial code ANSYS Forte in order to explore the effects on performance and emissions of different LRFs. Besides NG, various H_2-NG blends and biogas were considered. Such investigations are presented and discussed in Sections 6, 7 and 8.

5.2 Description of the 3D-CFD engine model

In the present activity, a customized version of the KIVA-3V code,[110] fully described in Section 4, was employed.

Table 13 summarizes the main sub-models included in the customized version of KIVA-3V.

Table 13. Main models included in the customized version of the KIVA-3V code

Turbulence model	RNG k-ε model
Break-up model	Hybrid KH-RT model
Droplet collision model	Droplet trajectories
Combustion model	PaSR coupled with chemical kinetics
Flame Propagation model	TFC / PREMIX code for aspirated fuel
Fuel Composition	Natural Gas / Diesel Oil Surrogate

The computational grid, that was built using the K3prep pre-processor included in the KIVA-3V package,[131] consists in a 60° sector mesh, thanks to the axial-symmetry of the combustion chamber and the homogeneous spatial distribution of the 6 holes of the diesel injector.

Figure 35 depicts the sector mesh, used for the present computational analysis, at TDC. As a standard practice, the cylinder head is modelled as a flat surface. Such a simplification is acceptable since the influence of the neglected geometric details is comparable to the uncertainties on boundary and initial conditions. In order to match the compression ratio of the investigated engine, the squish height was properly adjusted. A minimum of 5 cells layers was imposed in the squish region at TDC. Outside the squish region, the typical cell size is about 0.5-1.0 mm. The mesh consists of about 110.000 cells at BDC and of about 25.000 at TDC.

As demonstrated by a previous analysis,[132] the above-mentioned meshing criteria guarantee a good compromise between accuracy and computational cost.

Initial and boundary conditions come from the experimental campaign presented in Section 3. As far as the initial flow field is concerned, it was calculated in a previous numerical investigation on the same baseline engine.[133]

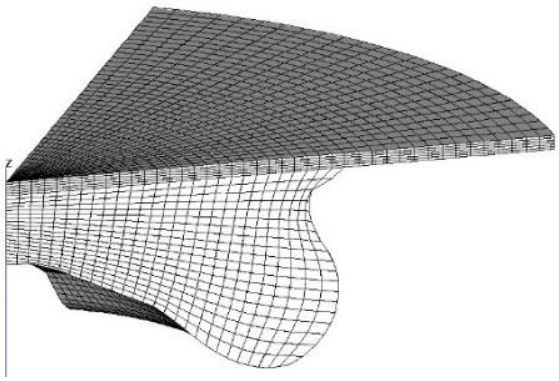

Figure 35. Sector mesh at TDC

The composition of NG is described in Table 14.

Table 14. NG composition

Chemical species	Volumetric fraction [vol%]
CH_4	96.0
C_2H_6	2.5
C_3H_8	0.5
N_2	1.0

5.3 Validation of the KIVA-3V engine model

As already said in Section 5.1, the numerical analysis was focused on the engine operating point corresponding to the highest load investigated, namely, 3000 rpm – 265 Nm / BMEP = 12 bar. Therefore, the validation of the 3D-CFD model was based on selected cases at the above-mentioned engine operating condition. In particular, the following cases were chosen:

- ND case;
- "-36% Diesel fuel +35% NG" DF case;
- "-60% Diesel fuel +52% NG" DF case;
- "-80% Diesel fuel +75% NG" DF case.

The DF cases are characterized by a BTE equal to or higher than that one in ND operation (see Figure 24). For the sake of simplicity, the selected cases are referred as follow:

- ND case → NG0
- "-36% Diesel fuel +35% NG" DF case → NG35
- "-60% Diesel fuel +52% NG" DF case → NG52
- "-80% Diesel fuel +75% NG" DF case → NG75

The objective of the validation process is to define a unique setting of calibration parameters able to accurately capture the experimental in-cylinder pressure, RoHR and raw emissions of the validation cases. It should be noticed that soot emissions were not used during the validation process, since the experimental accuracy was not satisfactory due to the low concentrations of such pollutant (the measures were close to the lower threshold of the instrument) for diesel energy reduction higher than 60%.

The main calibration parameters used to validate the model are related to the heat transfer, to the diesel injection strategy (SOI of pilot, pre and main injections; injection duration; diesel mass distribution among the injections) and to the diesel break-up (fuel temperature; KH and RT break-up models time constants).

Figure 36 compares experimental and numerical in-cylinder pressure traces and RoHR. As it can be seen, measured and predicted results are in very good agreement.

Figure 36 also reports the diesel injection strategies of the validation cases.

Figure 37 shows the comparisons between predicted and measured gaseous emissions. In detail, a satisfying accordance can be observed regarding CO_2 emissions. As far as CO and UHC emissions are concerned, the 3D-CFD model is able to capture their dependence on the NG substitution rate. However, the absolute values predicted by the model are affected by an error.

Considering NO_x emissions, the KIVA-3V model tends to slightly underestimate them in comparison to the experimental ND case. Conversely, NO_x emissions are slightly overpredicted at high substitution rates of NG. However, also in this case, the dependence of NO_x emissions on NG substitution rate is correctly captured.

Despite the model was not calibrated against soot emissions, the prediction of the latter pollutant is reported in Figure 38. As is can be noticed, the strong reduction of soot emissions, observed during the experimental campaign, is correctly captured by the 3D-CFD model.

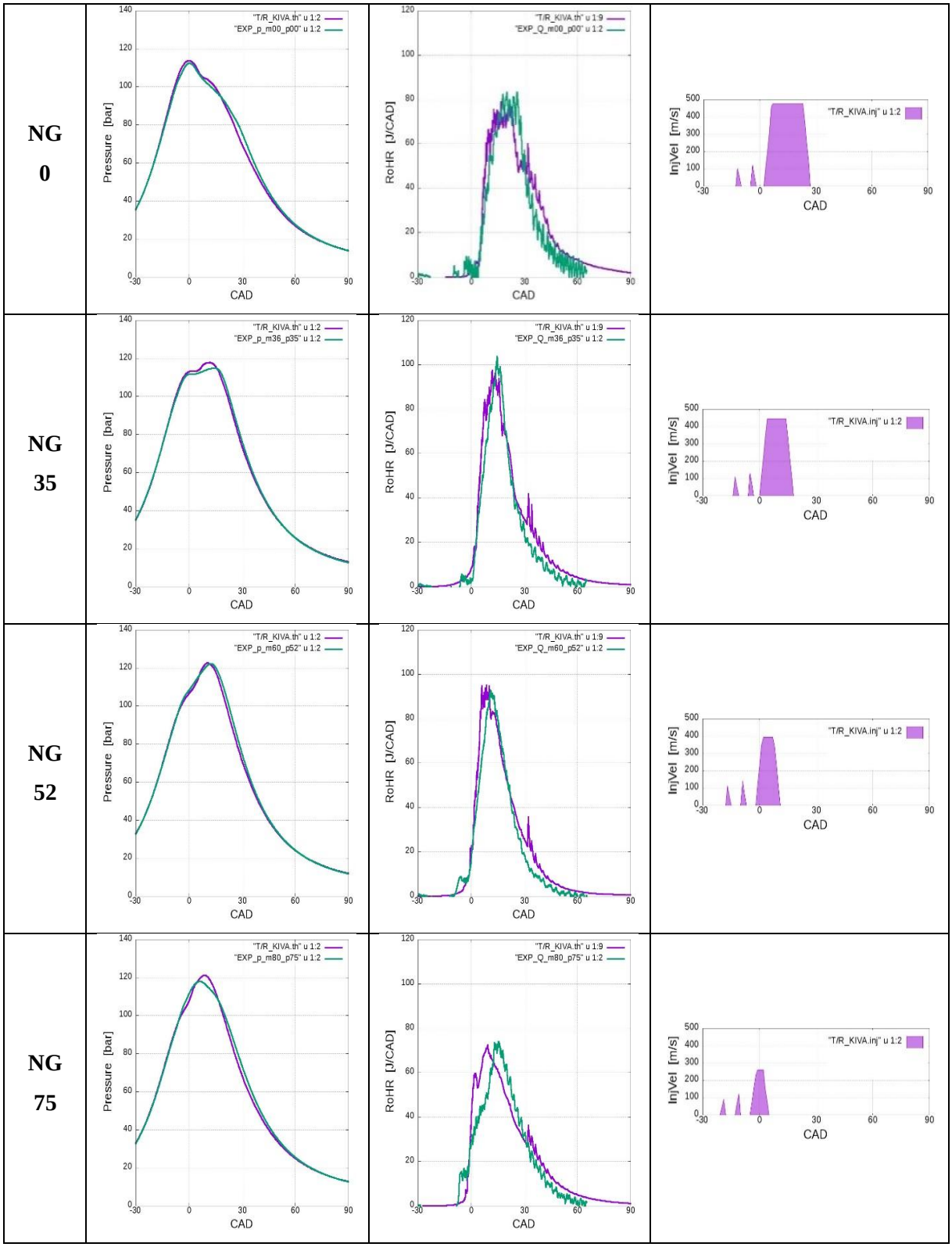

Figure 36. Comparison between experimental and numerical results in terms of in-cylinder pressure and RoHR. The third row shows the diesel injection velocity

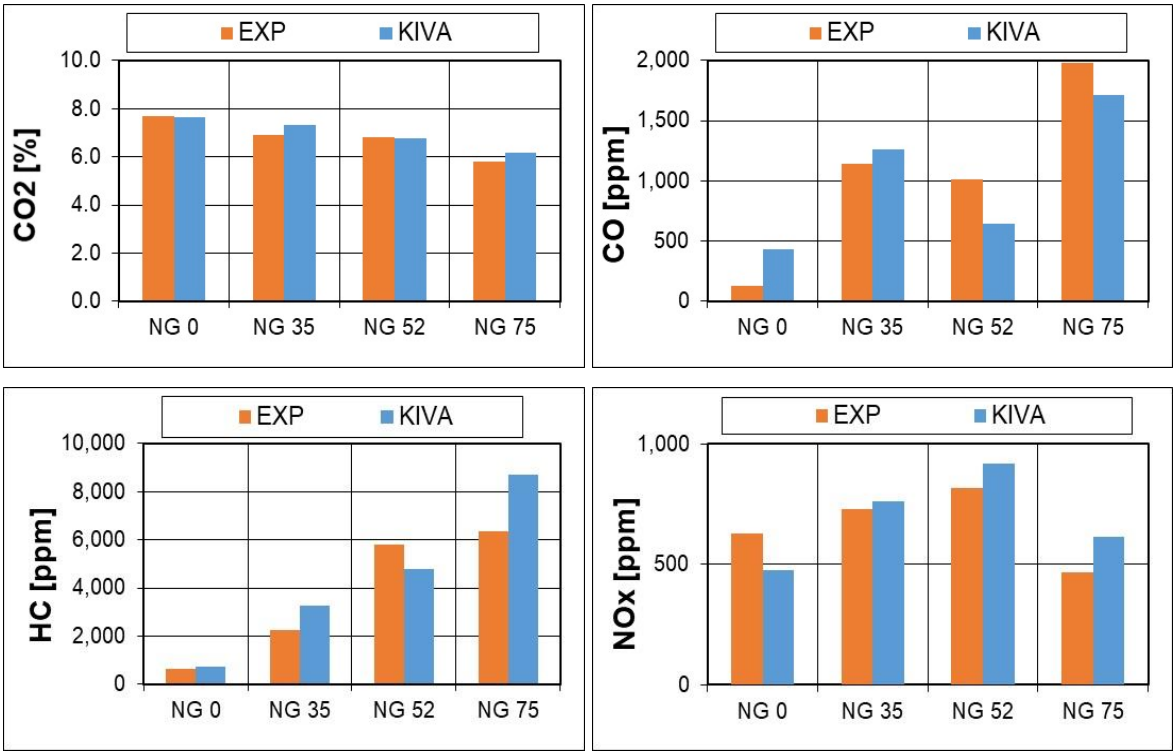

Figure 37. Comparison between experimental and numerical results in terms of CO_2, CO, UHC and NO_x emissions

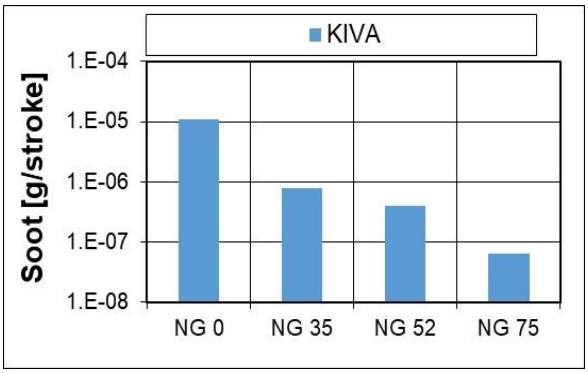

Figure 38. Soot concentrations calculated by the numerical model

5.4 Influence of the diesel injection strategy on DF NG-diesel combustion at medium-high load and high substitution rate of NG

By means of the validated model, a sensitivity analysis of the DF NG-diesel combustion at 3000 rpm – 265 Nm / BMEP = 12 was performed, focusing the investigation on the DF case corresponding to "-60% Diesel fuel +52% NG", referred to as NG52.

First of all, the influence of the number of injections was analysed, in order to define the best split injection strategy. In particular, the following combinations were compared:

- 3 injections (referred to as “inj 111”): pilot, pre and main injections;
- 2 injections (referred to as “inj 011”): pre and main injections;
- 2 injections (referred to as “inj 101”): pilot and main injections;
- 1 injection (referred to as “inj 001”): only main injection.

As the pilot and/or the pre injections were suppressed, the duration of the main injection was correspondingly increased to maintain constant the diesel fuel mass injected per cycle. The second sensitivity analysis was about the phasing of the injection law, which was shifted by steps of 2 °CA in both directions.

Figure 39, Figure 40, Figure 41 and Figure 42 report the numerical results for the two sensitivity analyses in terms of in-cylinder pressure and temperature, RoHR, gross Indicated Mean Effective Pressure (IMEP*), gaseous and soot emissions.

Looking at Figure 39 and Figure 40, it can be concluded that the number of injections does not significantly influence in-cylinder pressure, temperature, RoHR, IMEP* and CO_2 emissions. However, as the pilot and/or the pre injections are skipped, an increase of the ignition delay can be observed, that causes a higher peak of RoHR. Therefore, also NO_x emissions slightly increase. As far as CO and soot emissions are concerned, they show an evident worsening passing from 3 to 2 or 1 injections (CO emissions: +92%; soot emissions: one order of magnitude higher). This is due to the fact that, as the pilot and/or pre injections are eliminated, the mass of diesel injected during the main injection is greater. As a consequence, a locally richer mixture is generated.

Figure 41 and Figure 42 clearly show that the combustion process starts in advance and shortens if the diesel injection law is advanced. In fact, the RoHR curve is shifted towards the TDC and shows a slimer profile with a higher peak value. As a results, also the peaks of in-cylinder pressure (+10 bar) and temperature become higher and shifted towards the TDC. Obviously, NO_x emissions increase (+11%). Advancing the diesel injection law has a positive effect on IMEP* (+2%), while does not significantly change CO, CO_2 and soot. If the diesel injection low is delayed, the opposite trends can be observed.

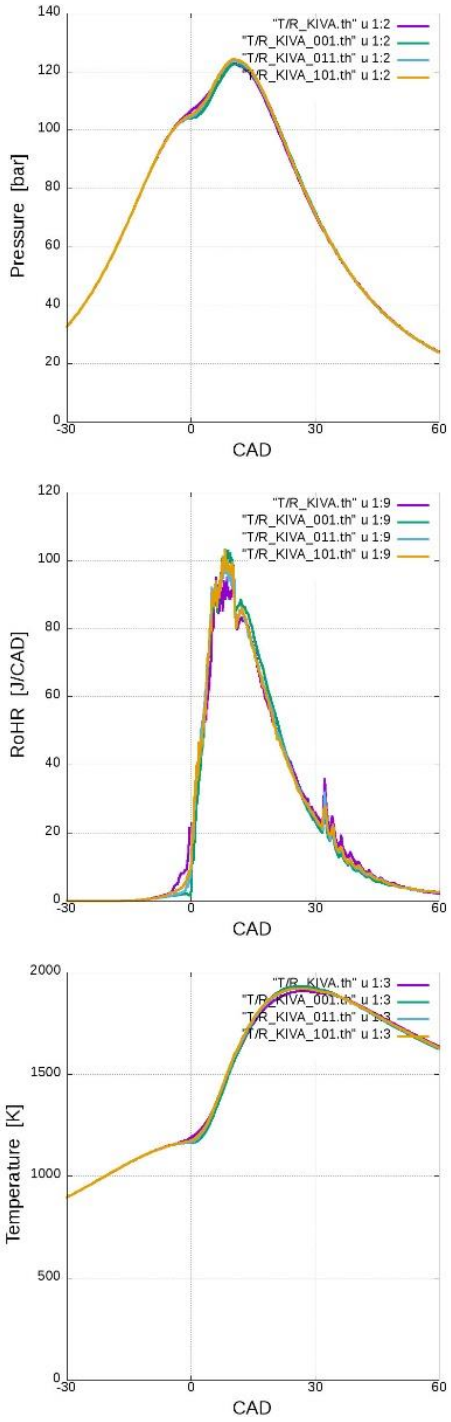

Inj 111 (red lines): pre, pilot and main injections

Inj 001 (green lines): only main injection

Inj 011 (blue lines): pre and main injections

Inj 101 (yellow lines): pilot and main injections

Figure 39. Effects of different diesel split injection strategies on in-cylinder pressure, RoHR and in-cylinder temperature; selected DF case: NG52

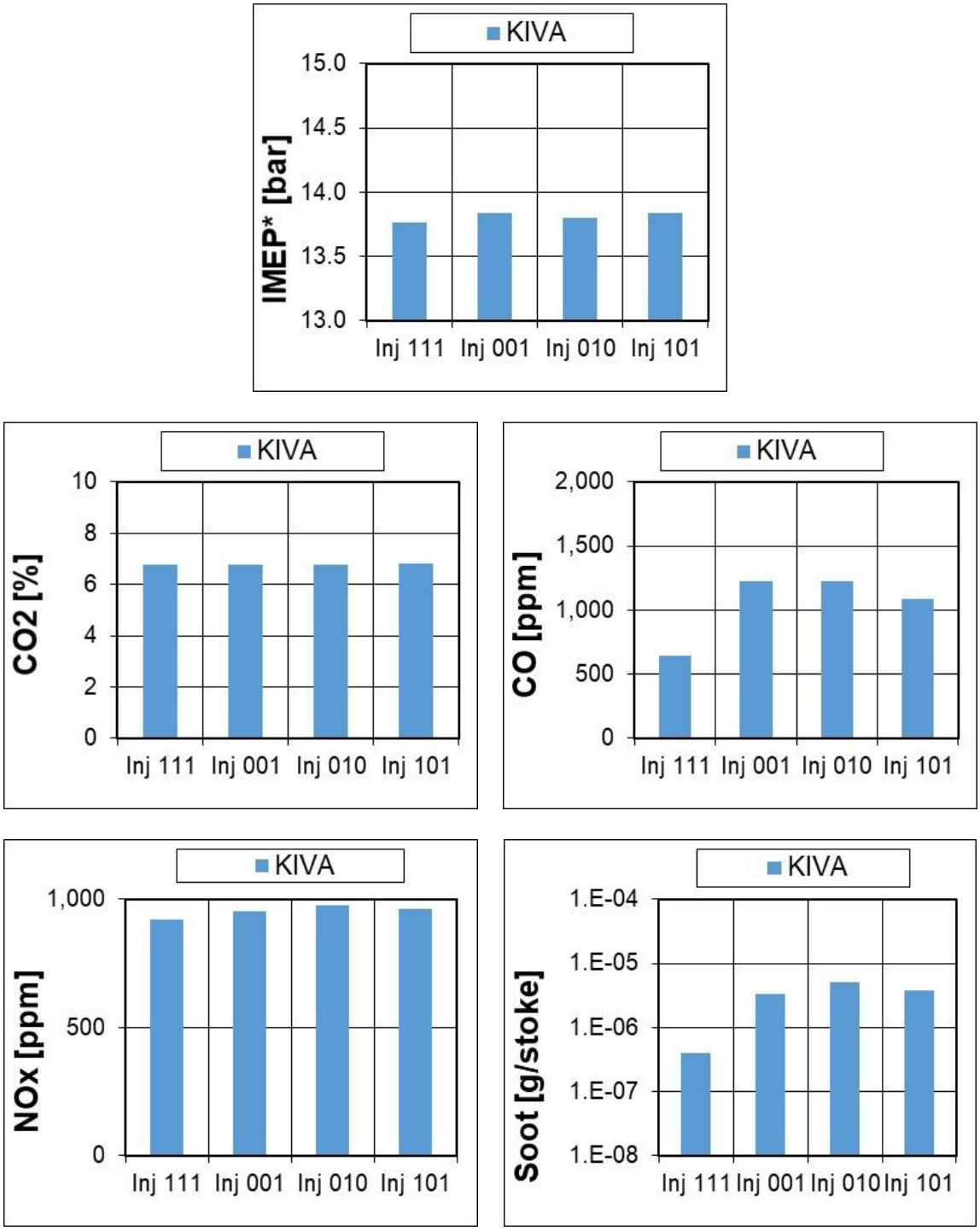

Inj 111 (red lines): pre, pilot and main injections

Inj 001 (green lines): only main injection

Inj 011 (blue lines): pre and main injections

Inj 101 (yellow lines): pilot and main injections

Figure 40. Effects of different diesel split injection strategies on CO_2 and pollutant emissions; selected DF case: NG52

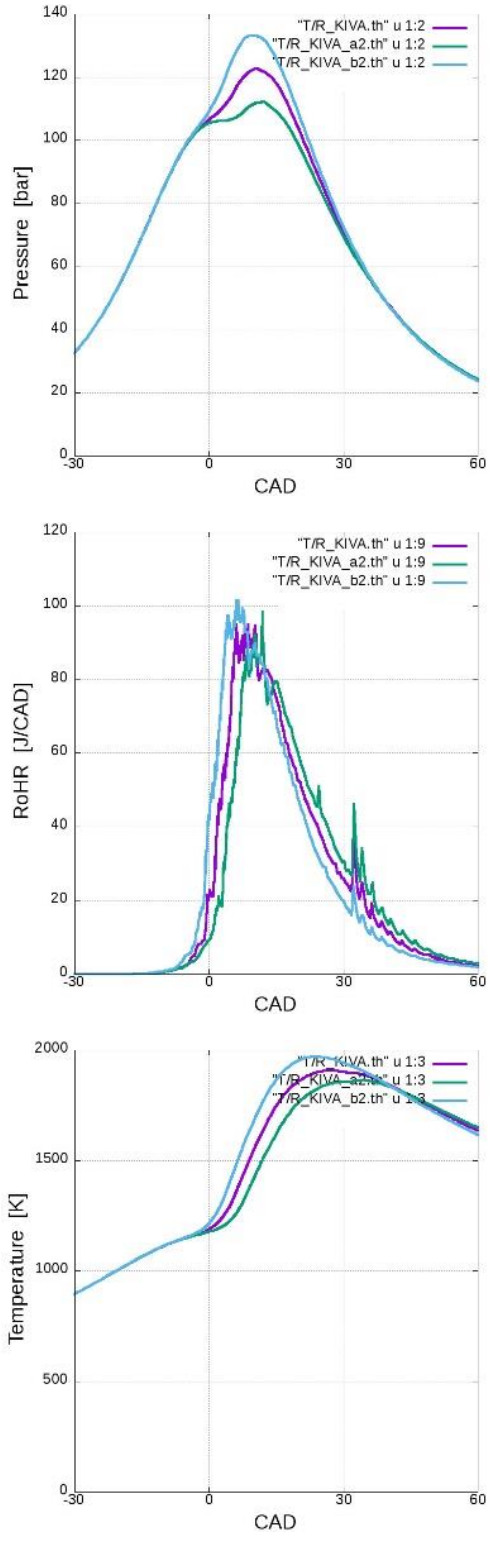

Figure 41. Effects of the diesel injection timing on in-cylinder pressure, RoHR and in-cylinder temperature; selected DF case: NG52

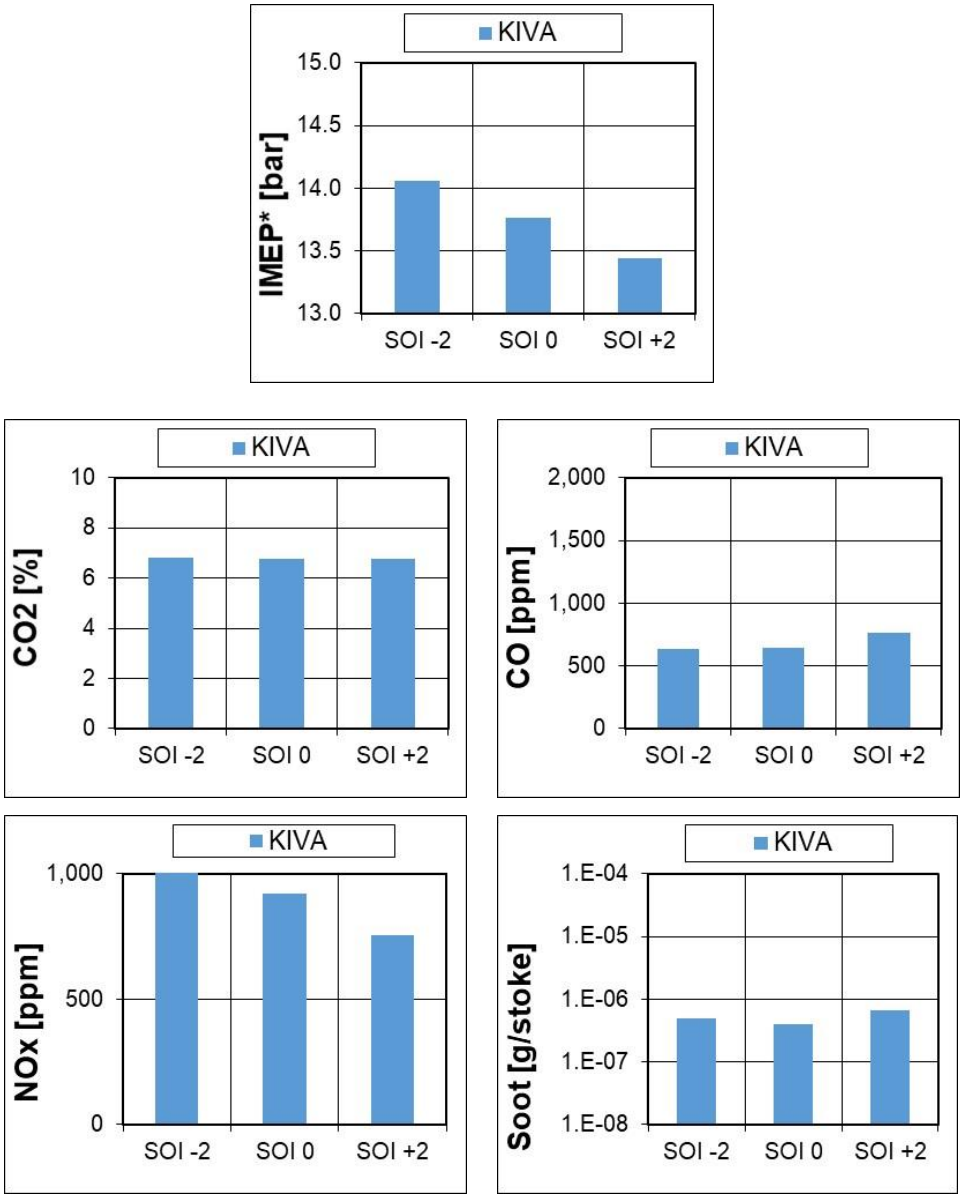

Figure 42. Effects of the diesel injection timing on CO2 and pollutant emissions; selected DF case: NG52

5.5 Conclusions

The validated KIVA-3V model has the capability to accurately predict the experimental in-cylinder pressure, RoHR and CO2 emissions. As far as CO, UHC and NOx emissions are concerned, the model is able to capture their dependence on the NG substitution rate, but not the absolute values.

The sensitivity analysis on the number of injections revealed that the best split injection strategy at medium-high load (3000 rpm – 265 Nm / BMEP = 12 bar) and high substitution rate of diesel

with NG ("-60% Diesel fuel +52% NG" DF case) is composed by three injections: pilot, pre and main injections. It should be noted that the latter split injection strategy corresponds to the one adopted during the experimental investigation.

If triple injection law is advanced, a performance improvement can be obtained (IMEP* enhancement: +2%), at the expense of higher NO_x emissions (+11%).

6 Investigation on the effects of using hydrogen enriched natural gas on combustion and emissions of a light-duty Diesel engine operated in dual fuel natural gas-diesel combustion mode at low load

6.1 Introduction and aim

As discussed in Section 3.3, passing from CDC to DF NG-diesel operation, almost all the tested DF cases showed lower BTE compared to the corresponding ND case, except for the DF case at the highest investigated load (265 Nm / BMEP = 12 bar) and with the highest substitution rate of diesel with NG ("-80% Diesel fuel +75% NG" DF case). On selected DF cases, an optimization process was applied in order to recover the lost efficiency. Only for the DF case corresponding to the lowest investigated load (44 Nm / BMEP = 2 bar) it was not possible to match the value of BTE that characterises the corresponding ND case. In fact, at the latter condition, the DF NG-diesel combustion is critical because of the excessively lean NG-air mixture (AFR = 39), which is hard to ignite and burn, and the small amount of energy released by the diesel combustion due to the high substitution rate with NG (80%). As a result, DF operation at low load is not convenient, requiring switching to CDC.

Therefore, it was decided to numerically investigate the capability of H_2 enriched NG to extend the operating range of the DF NG-diesel combustion at low loads.

Different H_2/NG mixtures, with the H_2 mole fraction ranging from 0% to 30%, were considered, and the effects on combustion and CO_2 and pollutant emissions were analysed by means of the commercial code ANSYS Forte on the "-80% Diesel fuel +175%NG" DF case at 3000 rpm – 44 Nm/BMEP = 2 bar.

The results of the present numerical investigation have been reported in a paper entitled "Influence of H2 enrichment for improving low load combustion stability of a Dual Fuel light duty Diesel engine" and published in the International Journal of Engine Research (SAGE Journals) for the Special Issue entitled "Current and future use of H2 and H2-based e-fuels in combustion engines and fuel cells".[134]

6.2 3D-CFD model description and validation

As mentioned above, the numerical investigation presented in the following section was performed by means of the commercial code ANSYS Forte.[135]

The main models available in ANSYS Forte are summarized in Table 15.

Table 15. Main models available in ANSYS Forte

Turbulence model	RANS RNG k-ε
Wall Slip model	Law of the Wall
Droplet collision model	Adaptive Collision Mesh model
Breakup model	Kelvin-Helmholtz/Rayleigh-Taylor coupled with Unsteady Gas-Jet model
Fuel vaporization model	Discrete Multi-Component model
Wall Film model	Particle Numerical model
Combustion model	G-Equation
Laminar Flame Speeds	Table Library model

Simulations were carried out from Intake Valve Closing (IVC) and Exhaust Valve opening (EVO), assuming that the premixed charge is a homogeneous mixture of air, residuals (10 weight%, based on the results of a validated GT-Power model of the investigated engine) and H_2-NG blend, with the mole fraction of H_2 that ranges from 0% to 30%. This assumption is based on the fact that the NG injectors are located 500 mm before the intake manifold. Therefore, NG and air have enough time to mix, forming a homogeneous charge.

Chemical and physical properties of NG and H_2-NG blends are presented in Table 16.

As it can be noticed from Table 16, as the amount of H_2 in the H_2-NG blend increases, the mass of the port injected fuel progressively decreases in order to keep the energy associated to the premixed charge constant. This is due to the lower LHV of NG compared to the one of H_2 (49 MJ/kg and 120 MJ/kg, respectively).

Table 16. Chemical and physical properties of NG and H_2/NG blends

			NG	NG +5% H_2	NG +10% H_2	NG +15% H_2	NG +20% H_2	NG +25% H_2	NG +30% H_2
Composition	[vol %]	CH_4	96.00%	91.20%	86.400%	81.600%	76.800%	72.000%	67.200%
		C_2H_6	2.500%	2.375%	2.250%	2.125%	2.000%	1.875%	1.750%
		C_3H_8	0.500%	0.475%	0.450%	0.425%	0.400%	0.375%	0.350%
		N_2	1.000%	0.950%	0.900%	0.850%	0.800%	0.750%	0.700%
		H_2	0.000%	5.000%	10.000%	15.000%	20.000%	25.000%	30.000%
Density [kg/m^3]			0.69	0.66	0.63	0.60	0.57	0.54	0.51
LHV [MJ/kg]			49.00	49.45	49.94	50.48	51.08	51.75	52.50
LHV [MJ/Nm^3]			33.93	32.73	31.54	30.34	29.15	27.96	26.76
αs [-]			16.84	16.95	17.07	17.20	17.34	17.51	17.69
RLHV [MJ/kg]			2.91	2.92	2.93	2.94	2.95	2.96	2.97
lower Wobbe index (Wl)[136] [MJ/Nm^3]			44.74	44.15	43.55	42.95	42.35	41.74	41.14
Mass [mg/cycle/cyl]			21.11	20.92	20.71	20.49	20.25	19.99	19.70

Diesel fuel was modelled as a 67/33 w% blend of n-decane ($C_{10}H_{22}$) and 1-methyl naphthalene ($C_{11}H_{10}$), characterized by a CN of 55 and a LHV equal to 42.84 MJ/kg, which is close to that one of the real diesel used during the experimental campaign (43.5 MJ/kg).

The laminar flame speeds of diesel fuel, NG and H_2 are computed by the Table Library model, which is based on CHEMKIN calculations and able to capture the influence of fuel composition, pressure, temperature, equivalence ratio and residuals on the fly.

Soot is modelled as a gaseous species, considering the following processes:

- nucleation pathways through benzene and phenyl;

- growth dominated by HACA mechanism;
- oxidation through O_2 and OH.

As in the numerical analysis performed by means of KIVA-3V (see Section 5), a sector mesh was used. Also in this case, the cylinder head was modelled as a flat surface (see Figure 43). Moreover, the crevice above the top piston ring was designed slightly thicker and deeper than the real one in order to match the compression ratio, keeping the exact squish height.

The average cell size was set at 1.3 mm. A minimum of 4 cells layers was imposed in the squish region at TDC, while 3 cells layers were enforced between piston and liner. As a results, the mesh consists of 21,760 cells at TDC and 105,728 cells at BDC.

The Gasjet model proposed by Abani et al.[137] was used in order to reduce the grid size dependency of the Lagrangian-Droplet Eulerian-Fluid approach, permitting to accurately capture the diesel spray evaporation also on relatively coarse grids. Another possibility would be the adoption of an adaptive mesh refinement in the spray zone with a grid size of 0.25 mm, as proposed by Senecal et al.[138] However, such meshing approach is not available in ANSYS Forte.

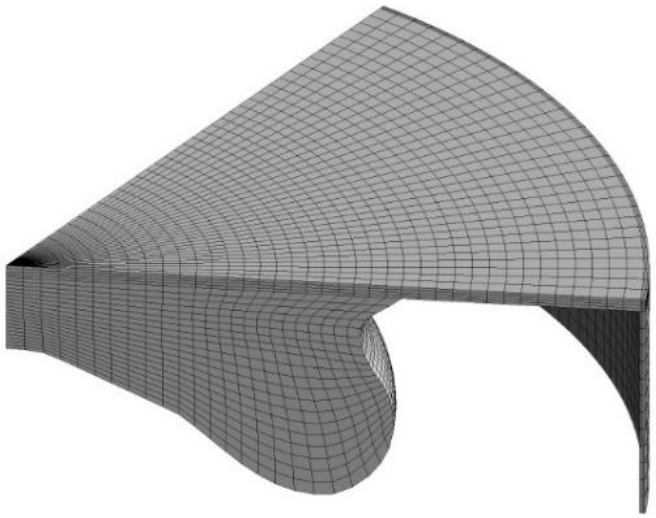

Figure 43. Sector mesh at TDC

Table 17 compares the engine control parameters of the experimental DF case, i.e., "-80% Diesel fuel +175%NG" DF case at 3000 rpm – 44 Nm / BMEP = 2 bar), with those ones set in the corresponding numerical model and resulting from the validation process.

Table 18 lists additional parameters of the numerical set-up.

Table 17. Main engine control parameters of the validation case (3000 rpm – 44 Nm / BMEP = 2 bar, "-80% Diesel fuel +175%NG" DF case)

Engine parameter	**Exp.**	**Num.**
trapped mass [mg/cycle/cyl]	899.07	909.52
air mass [mg/cycle/cyl]	788.06	797.19
NG mass [mg/cycle/cyl]	21.11	21.37
diesel mass [mg/cycle/cyl]	2.42	2.42
diesel injection pressure [bar]	670	670
diesel SOI [°CA AFTDC]	-18.56	-18.56
diesel in pilot injection [mass%]	25.6	25.6
diesel in pre injection [mass%]	25.6	25.6
diesel in main injection [mass%]	48.8	48.8
residuals [mass%] *	n.a.	10
EGR [%]	0	0
SR	1.8	1.8
* based on the results of a validated GT-Power model of the full engine		

Table 18. Additional parameters of the numerical set-up

Parameter	Value
KH break-up model time constant	20
RT break-up model time constant	1
Spray included angle [°]	150
Spray cone angle [°]	15
Fuel temperature [K]	340
Piston temperature [K]	550
Cylinder head temperature [K]	500
Cylinder liner temperature [K]	450

Figure 44 depicts the experimental diesel injection profile. As it can be seen, a split injection strategy with three shots was used during the tests for the selected DF case.

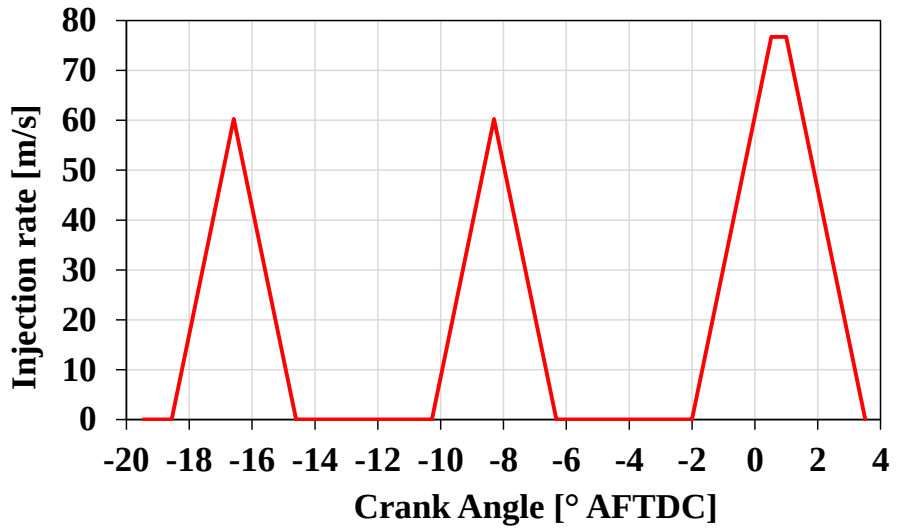

Figure 44. Diesel fuel injection profile at 3000 rpm – 44 Nm / BMEP = 2 bar, "-80% Diesel fuel +175%NG" DF case

Figure 45 compares experimental and numerical in-cylinder pressure and AHRR, revealing a satisfying agreement between experiments and predictions. This result is confirmed in Table 19 by the comparison in terms of IMEP* and peak in-cylinder pressure.

IMEP* corresponds to the gross Indicated Mean Effective Pressure evaluated between IVC and EVO:

$$\mathrm{IMEP}^{*} = \frac{1}{V_d}\int_{\mathrm{IVC}}^{\mathrm{EVO}} \mathrm{pdV} \tag{40}$$

where V_d is the unit displacement.

Focusing on the first part of combustion (see AHRR curves in Figure 45), a small discrepancy between experimental and predicted results can be observed. This is probably due to lower CN of the diesel fuel surrogate compared to the one of the real diesel.

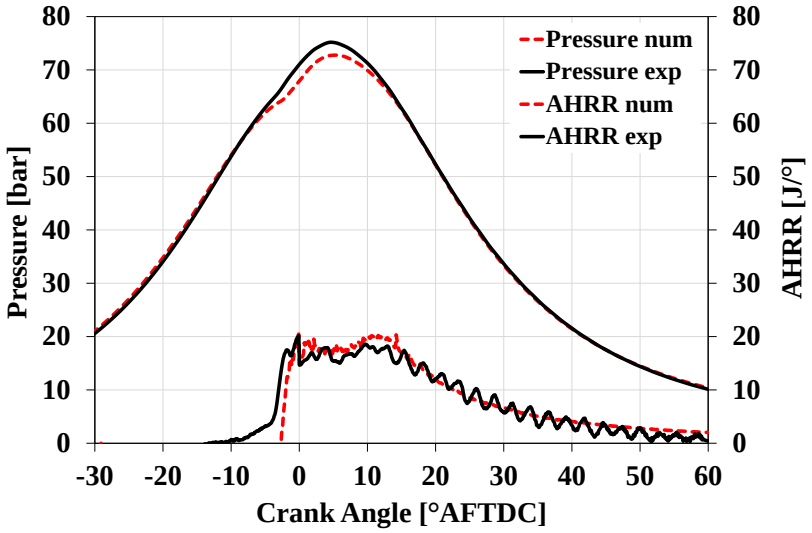

Figure 45. Comparison between measured and predicted in-cylinder pressure and AHRR of DF NG-diesel operation at 3000 rpm – 44 Nm / BMEP = 2 bar, "-80% Diesel fuel +175%NG" DF case

Table 19. Comparison between measured and predicted IMEP*, peak in-cylinder pressure and emissions at 3000 rpm – 44 Nm / BMEP = 2 bar, "-80% Diesel fuel +175%NG" DF case

	IMEP* [bar]	**Peak in-cylinder pressure [bar]**
Exp.	3.84	75.19
Num.	3.89	72.77
Error [%]	1.36	3.21

Figure 46 compares experimental and predicted combustion phasing parameters, namely, CA5, CA10, CA50, CA90 and combustion duration (CA10-90). Except the error in the very first part of combustion, the agreement is good, especially in terms of CA10, CA50 and combustion duration.

Finally, Figure 47 compares experimental and numerical CO, UHC and NO_x specific emissions. Except for UHC, the uncertainties of the experimental emissions measurements apparatus is also reported (green lines). The model is able to accurately predict NO_x emissions, while the difference between experimental and numerical CO specific emissions is acceptable for the purpose of the study. As far as UHC emissions are concerned, the measured emissions were well above the full scale of the instrument for the selected DF case. Therefore, experimental UHC emissions are not reliable and they were not considered for the validation of the 3D-CFD model.

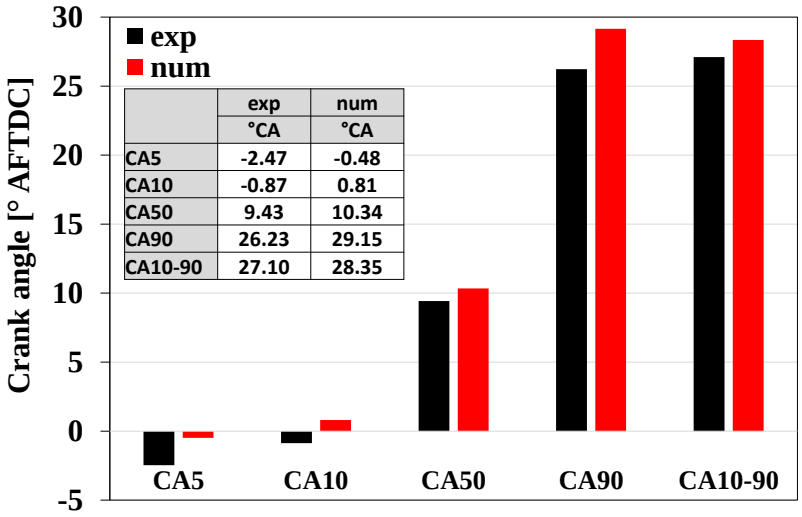

	exp °CA	num °CA
CA5	-2.47	-0.48
CA10	-0.87	0.81
CA50	9.43	10.34
CA90	26.23	29.15
CA10-90	27.10	28.35

Figure 46. Comparison between measured and predicted combustion phasing parameters of DF NG-diesel operation at 3000 rpm – 44 Nm / BMEP = 2 bar, "-80% Diesel fuel +175%NG" DF case

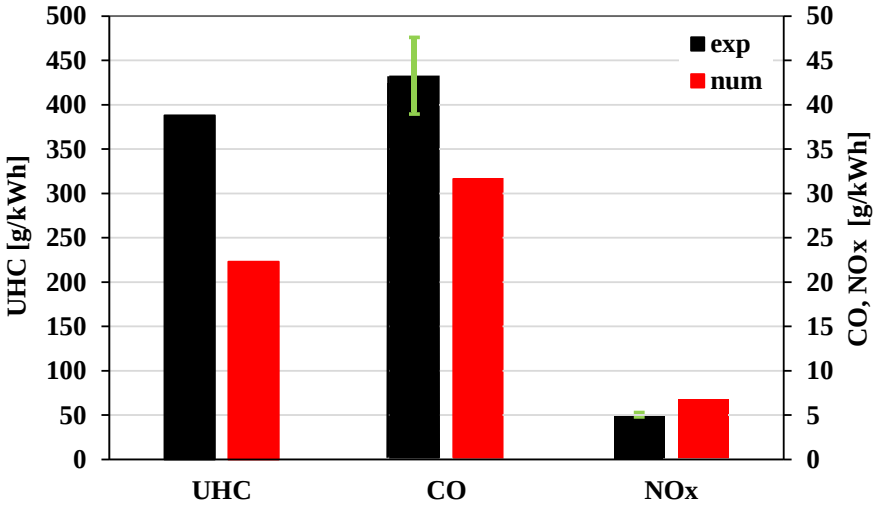

Figure 47. Comparison between experimental and numerical emissions of DF NG-diesel operation at 3000 rpm – 44 Nm / BMEP = 2 bar, "-80% Diesel fuel +175%NG" DF case

6.3 Results and discussion

In the following section, the results of the present activity are discussed.

Figure 48 depicts predicted in-cylinder pressure and AHRR for different H_2-NG blends, with the H_2 mole fraction that ranges between 0% and 30%, by steps of 5%. For the sake of completeness, the CDC is also reported. Focusing on the DF cases, as the H_2 mole fraction increases, the peak in-cylinder pressure increases too, with a maximum variation of about 11% (from 72.8 bar to 80.7 bar). This evidence is due to the higher peak of AHRR related to the increasing content of H_2 in the H_2-NG blend.

Moreover, if CDC and DF operations are compared, strong differences can be noticed. The AHRR curve in ND operation is characterized by three peaks, corresponding to the burning of pilot, pre and main injections, respectively. Such distinction among the three injections in the AHRR profile cannot be done in DF operations, since the combustion process is dominated by the propagation of flame fronts within the premixed charge, ignited by the hot spots distributed in the periphery of the diesel spray plumes. Furthermore, combustion is shifted towards TDC in DF operations, and, as a consequence, the peak in-cylinder pressure increases and shifts toward TDC. In particular, switching from CDC to the DF NG-diesel case (DF_0 vol%H2), the peak in-cylinder pressure increases by 8.5%

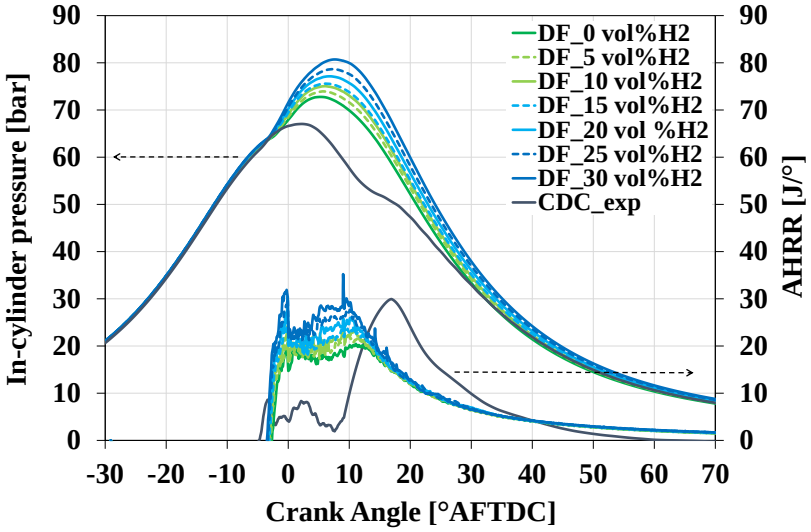

Figure 48. Influence of H_2 content in the H_2/NG mixture on in-cylinder pressure and AHRR

Figure 49 shows that CA50 is reduced from 10.4 °CA up to 8.7 °CA. This evidence depends on:

- the reduction of the ignition delay (defined as the difference between CA5 and pilot SOI), which passes from 18.1 up to 17.2 °CA (see Figure 50);
- the reduction of CA10-90 (defined as the difference between CA90 and CA10), that reduces from 28.35 °CA up to 26.10 °CA (see Figure 51).

The reduction of CA10-90 is also responsible for a slight increase of PPRR, that reaches a maximum value of 2.6 bar/° for DF_30 vol%H_2 case. It should be noted that such a maximum value is below the acceptable level for passenger car engines, i.e., 5 bar/°.

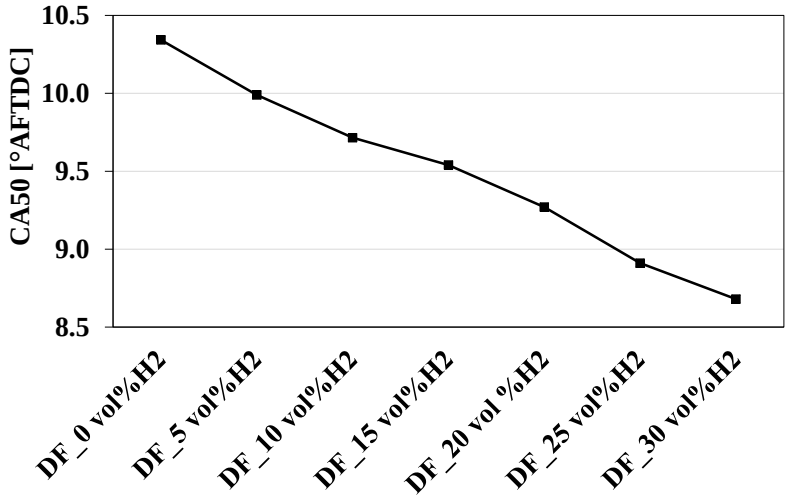

Figure 49. Influence of H_2 content in the H_2/NG mixture on CA50

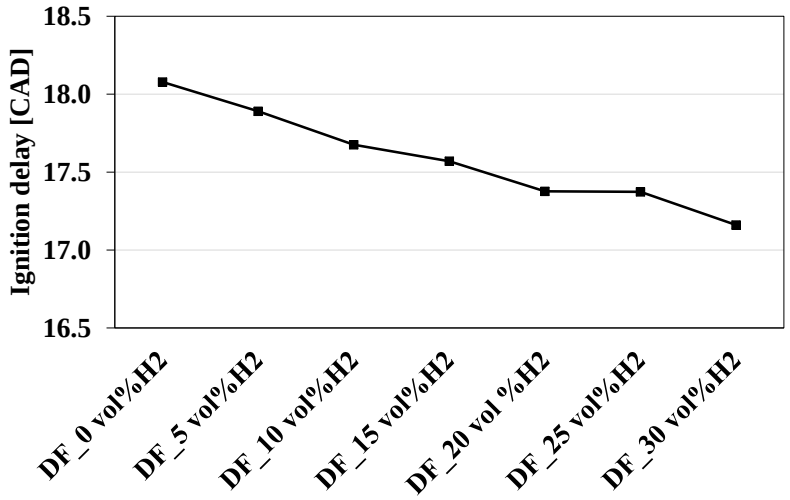

Figure 50. Influence of H_2 content in the H_2/NG mixture on ignition delay

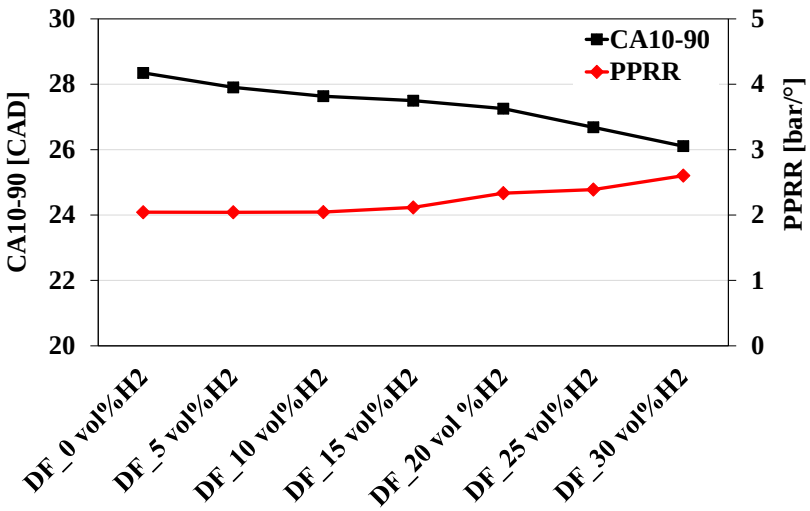

Figure 51. Influence of H_2 content in the H_2/NG mixture on CA10-90 and PPRR

The use of H_2-NG blends also favours the completion of combustion, as demonstrated by Figure 52, which reports the combustion efficiency (η_c) calculated from the numerical results as follow:

$$\eta_c = \frac{(E_{in} - m_{UHC\_EVO}LHV_{UHC} - m_{H_2\_EVO}LHV_{H_2} - m_{CO\_EVO}\,LHV_{CO})}{E_{in}}100 \quad (41)$$

where:

$E_{in} = m_D LHV_D + m_{(H_2+NG)}LHV_{(H_2+NG)}$ is the energy provided by the Diesel fuel and the H_2-NG mixture; $m_{(H_2+NG)}$ is the mass per cycle of the H_2-NG mixture; $LHV_{(H_2+NG)}$ is the Lower Heating Value of the H_2-NG mixture; m_D is the mass per cycle of Diesel fuel; LHV_D is the Lower Heating Value of Diesel fuel; m_{UHC_EVO} is the mass per cycle of Unburnt Hydrocarbons at Exhaust Valve Opening; LHV_{UHC} is the Lower Heating Value of Unburnt Hydrocarbons; $m_{H_2\_EVO}$ is the mass per cycle of hydrogen at Exhaust Valve Opening; LHV_{H_2} is the Lower Heating Value of hydrogen; m_{CO_EVO} is the mass per cycle of carbon monoxide at Exhaust Valve Opening; LHV_{CO} is the Lower Heating Value of carbon monoxide.

Figure 52 shows that η_c drops passing from CDC to DF operation. However, as the H_2 content in the premixed charge increases, the penalization of η_c is progressively reduced. In detail, the worsening of η_c is reduced from 40%, comparing CDC with DF NG-diesel case (DF_0 vol%H2), to 21.6%, considering DF_30 vol%H2. That is, η_c improves by 31% when passing from DF_0 vol% H_2 to DF_30 vol% H_2.

A similar trend is shown by the Gross Indicated Thermal Efficiency (GITE*):

$$GITE^* = \frac{1}{m_D LHV_D + m_{(H_2+NG)}LHV_{(H_2+NG)}} \int_{IVC}^{EVO} pdV \quad (42)$$

Passing DF_0 vol% H_2 to DF_30 vol% H_2, GITE* enhances by 37.8%. This is due to the improvement of η_c and a faster combustion, which correspond to a more efficient cycle. However, the gap in terms of efficiency between CDC and DF operations could not be fully cancelled.

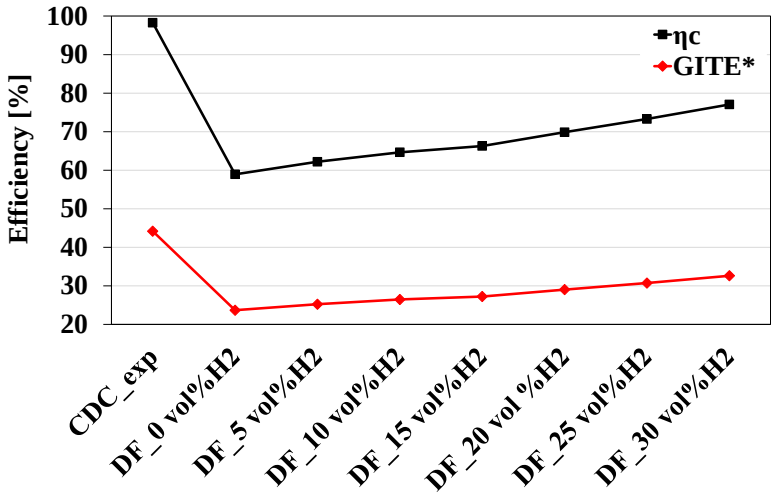

Figure 52. Influence of H_2 content in the H_2/NG mixture on η_c and GITE*

As far as CO_2 specific emissions are concerned, they can be strongly mitigated thanks to the addition of H_2 in the NG-air mixture, as shown by Figure 53. In numbers, CO_2 specific emissions are reduced by 36.4% passing from CDC to DF_30 vol%H_2. This outcome depends on the substitution of diesel (80% in terms of energy compared to the ND operation) with NG, whose main component is CH_4 (96 vol%; characterized by the highest hydrogen-to-carbon ratio among hydrocarbons), and, above all, with H_2, that cannot produce CO_2. In fact, CO_2 specific emissions decrease by up to 30.7% when the H_2 mole fraction in the premixed charge is increased from 0 vol% to 30 vol%. Unfortunately, it is necessary to take into account the fact that this advantage is reduced due to the adoption of an oxidation catalyst, due to the conversion of UHC and CO to CO_2.

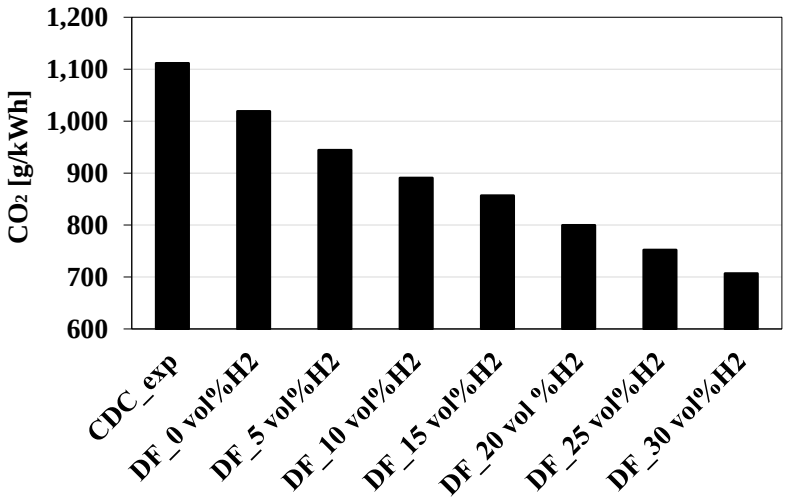

Figure 53. Influence of H_2 content in the H_2/NG mixture on CO_2 emissions

However, the higher η_c and the lower carbon content of the premix charge, connected to the H_2 addition, guarantee a strong mitigation of both CO and UHC specific emission (by up to 54.1% and 70.4%, respectively) when comparing the DF_0 vol% H_2 case to the DF_30 vol% H_2 case, as shown by Figure 54. In particular, the decrease of CO and UHC specific emission is due, besides the lower carbon content of the premix charge, to the increase of the OH radical pool related to the oxidation of H_2. Figure 55 clearly shows the connection between the unburned CH_4, which represents the main constituent of UHC emissions in DF operation, and the concentration of OH. However, even with the higher rate of H_2, CO and UHC specific emissions in ND operation are lower.

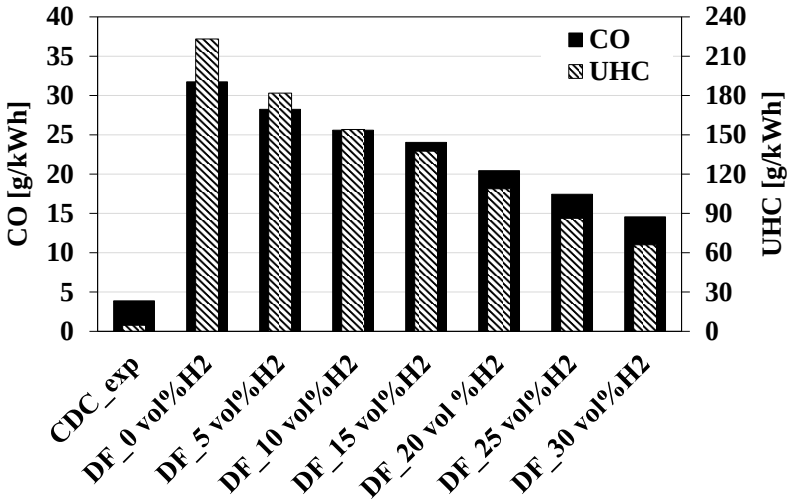

Figure 54. Influence of H_2 content in the H_2/NG mixture on CO and UHC emissions

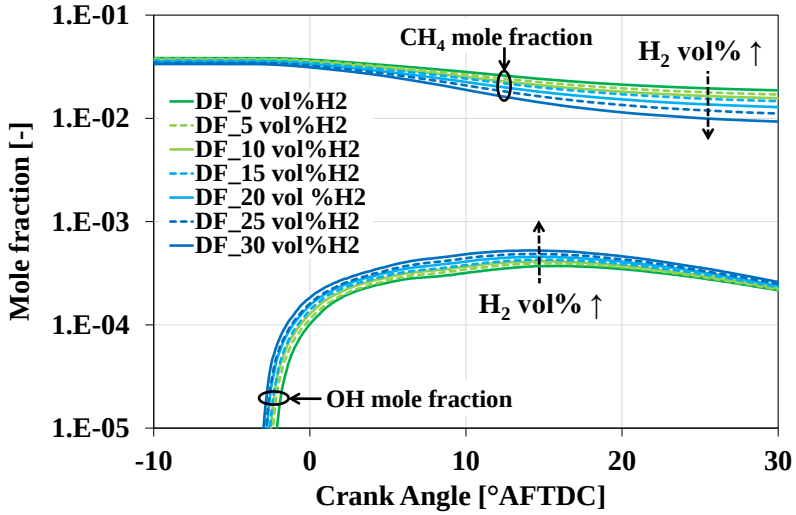

Figure 55. Influence of H_2 content in the H_2/NG mixture OH concentration and CH_4 oxidation

As shown by Figure 56, in DF NG-diesel operation, most of the UHC is located in periphery of the combustion chamber due to the quenching of the flame front that propagates in the premixed charge. However, as clearly show by Figure 57, the use of a H_2-NG blend (30vol%H_2-NG blend is represented in Figure 57) improves CH_4 oxidation in the end gas region thanks to the higher concentration of OH. Figure 56 and Figure 57 depict, besides the contours of CH_4 and OH mole fractions, also the distribution of Temperature and n-$C_{10}H_{22}$ mole fraction on two cut planes coincident with the diesel spray axis, at different crank angles, during the combustion process. n-$C_{10}H_{22}$ is chosen to represent diesel since it is the main constitute of the selected diesel surrogate.

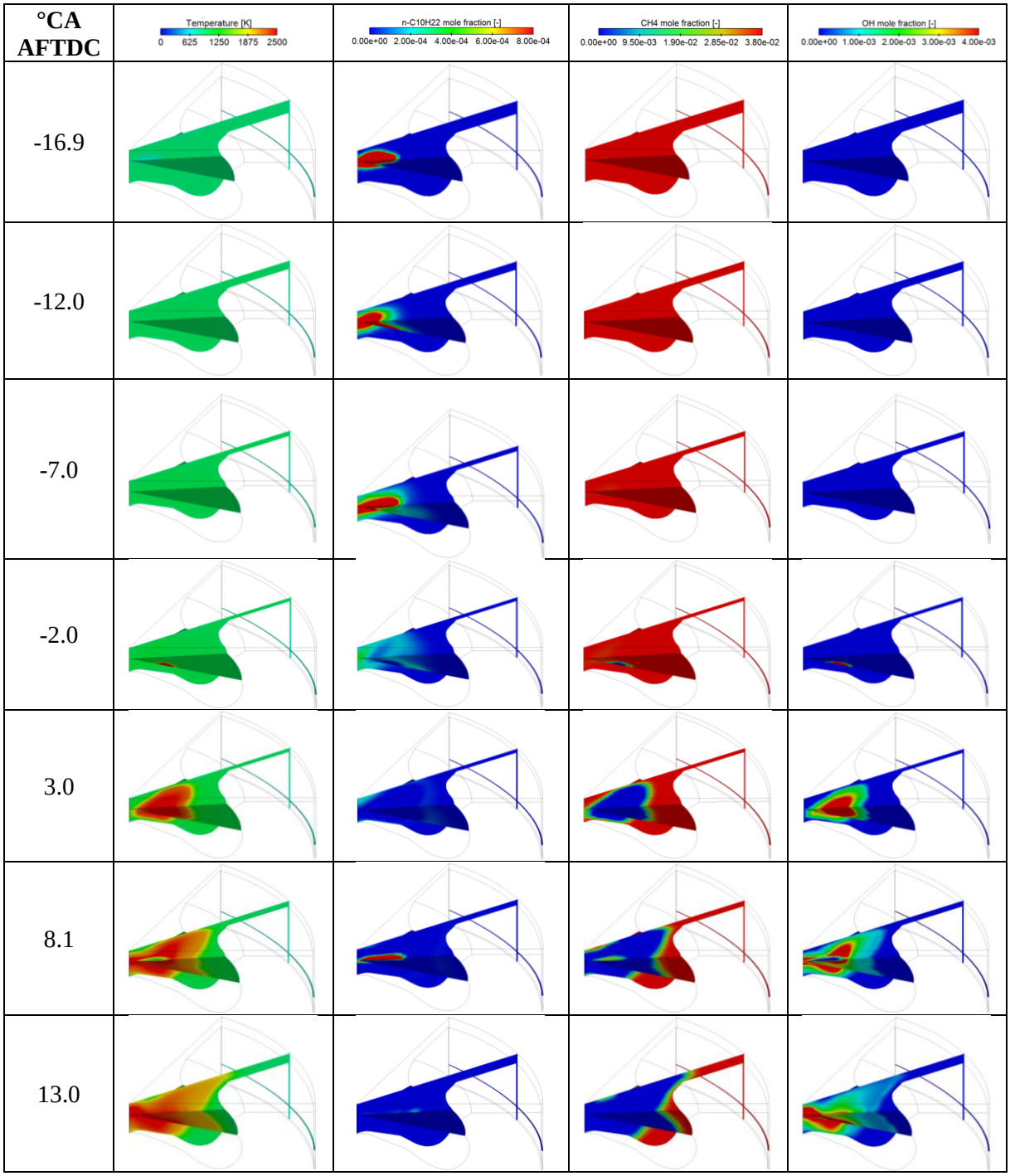

Figure 56. Contours of temperature, $C_{10}H_{22}$, CH_4 and OH concentrations (mole fractions) plotted on two orthogonal cut planes including the diesel spray axis at different °CA (DF NG-diesel combustion, H_2 content: 0 vol%)

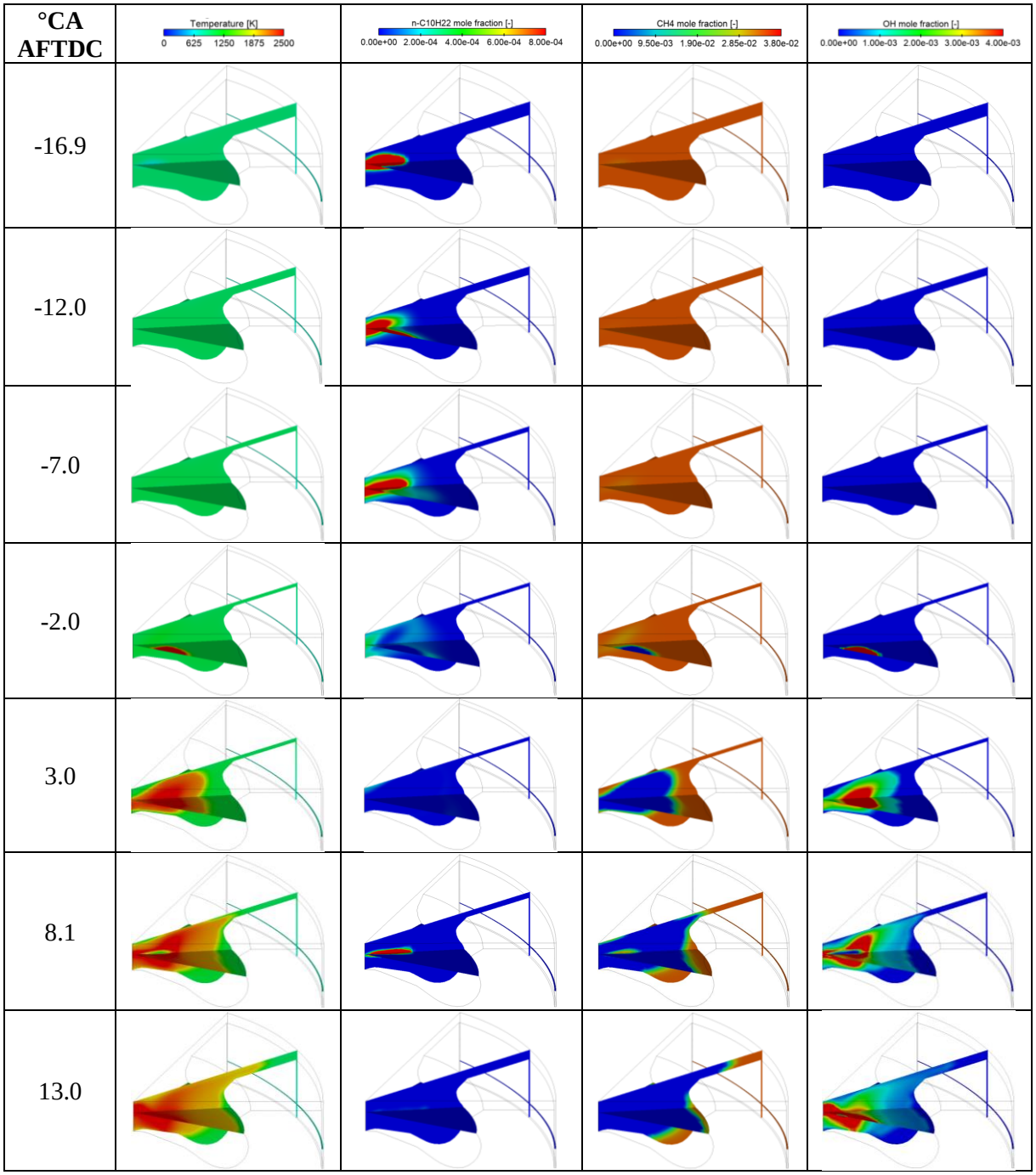

Figure 57. Contours of temperature, $C_{10}H_{22}$, CH_4 and OH concentrations (mole fractions) plotted on two orthogonal cut planes including the diesel spray axis at different °CA (DF NG-diesel combustion, H_2 content: 30 vol%)

Despite the peak in-cylinder pressure increases in DF operation as the H_2 mole fraction in the premixed charge grows up, NO_x specific emissions show the opposite trend, as shown by Figure 58. In fact, as the H_2 content in the H_2-NG blend increases from 0 vol% to 30 vol%, NO_x specific emissions are reduced by 15.9%, leading to a value of NO_x specific emissions in DF mode lower than that one in ND operation (5.72 g/kWh and 5.85 g/kWh, respectively).

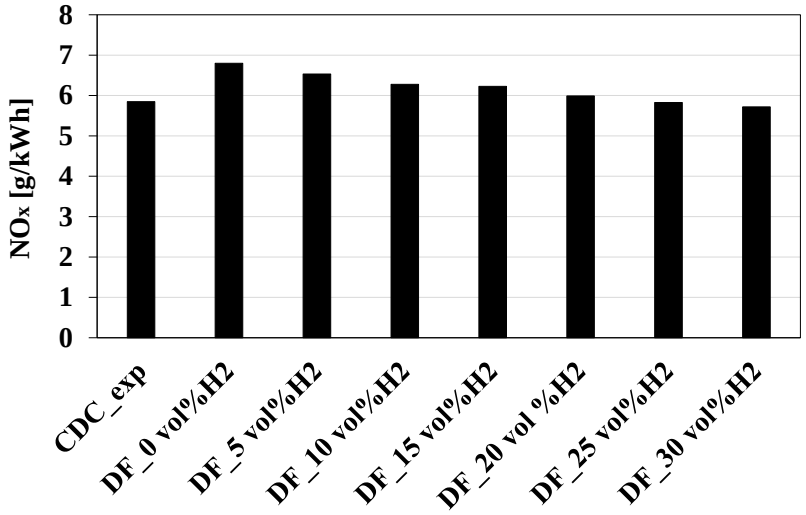

Figure 58. Influence of H_2 content in the H_2/NG mixture on NO_x

The strong reduction of diesel achieved switching from ND to DF operation (-80% in terms of energy) also permits to almost cancel soot specific emissions, which drop below 0.001 g/kWh.

6.4 Conclusions

In order to extend the DF NG-diesel operation to low loads, the effects of H_2 enriched NG on combustion characteristics and CO_2 and pollutant emissions were investigated. Various H_2-NG blends, with the H_2 mole fraction ranging from 0% to 30%, by steps of 5%, were considered.
In summary, as the H_2 content in the H_2-NG mixture increases from 0 vol% to 30 vol%, the following conclusions can be draw:

- peak in-cylinder pressure increases by 11% (from 72.8 bar to 80.7 bar) and CA50 is shifted from 10.3° to 8.7 °CA AFTDC, due to the reduction of ignition delay (5%) and combustion duration (7.9%);
- PPRR increases by 27.4%, but its maximum value (2.6 bar/°) is lower than the maximum acceptable value passenger cars engine, i.e., 5 bar/°;

- CO_2 specific emissions decrease by 30.7%, due to the lower carbon content of the premixed charge and for the increase of GITE* (37.8%);
- CO and UHC specific emissions drop by 54.1% and 70.4%, respectively, thanks to the increase of the OH radical pool;
- the increase of the OH concentration during the combustion process improves the propagation of the flame front, reducing the early flame quenching;
- the strong decrease of CO and UHC emissions reflects on combustion efficiency, which grows up by 31%;
- NO_x emissions decrease by 15.9%;
- soot emissions, in DF combustion, are always lower than 0.001 g/kWh.

In conclusions, the use of H_2 enriched NG permitted to enhance DF NG-diesel combustion at low loads, strongly reducing CO and UHC emissions, and, consequently, improving both combustion and thermal efficiency. However, even with the H_2-NG blend characterized by the highest H_2 content, it was not possible to achieve the values of CO and UHC specific emissions, combustion efficiency and GITE* of the CDC. Conversely, CO_2 specific emissions strongly decreased and NO_x emissions slightly improved compared to ND operation, with acceptable values of peak in-cylinder pressure and PPRR.

7 Optimization of the diesel injection strategy and sensitivity analysis to the swirl ratio of a light-duty Diesel engine operated in dual fuel hydrogen enriched natural gas-diesel combustion at low load

7.1 Introduction and aim

As demonstrated by the numerical activity reported in the previous section (Section 6), the use of H_2 as a combustion enhancer for the lean premixed NG-air charge permits to strongly mitigate the disadvantages that affect DF NG-diesel combustion at low load compared with CDC. However, CO and UHC specific emissions of the former combustion technique remain higher than in ND operation.

Therefore, a further numerical study was carried out with the aim to further improve DF NG-diesel combustion at low load, enabling to extend such combustion strategy to the entire engine operating range.

In particular, starting from the so called "DF_30 vol% H2" case (see Section 6.3), an optimization of the diesel injection strategy and a sensitivity analysis of DF combustion to the SR were performed.

At the moment of writing, the results presented in this section are being reported in a dedicated paper.

7.2 Methodology

The ANSYS Forte model described in Section 6.2 was employed also for the present study, since the starting condition was the DF H_2/NG-diesel case with 30 vol% of H_2 in the H_2-NG blend (defined as "DF_30 vol% H2" in Section 6.3), at 3000 rpm 44 Nm / BMEP = 2 bar.

As mentioned above, an optimization of the diesel injection strategy was performed, based on the results of the previous numerical investigation (see Section 6), in terms of:

- number of injections per engine cycle;
- SOI of each injection;
- diesel mass distribution among the injections.

Moreover, a sensitivity analysis to the SR was carried out.

In particular, a split diesel injection strategy composed by 2 injections per engine cycle was taken into account. Hence, the influence on performance of the SOI of the first injection

(defined as “SOI1”) and of the SOI of the second injection (defined as “SOI2”) was analysed. The SOI1 was varied from -80 to -30 °CA AFTDC, by increments of 5 °CA, while the SOI2 was swept from -30 to -10 °CA AFTDC, by increments of 5 °CA. Then, a sensitivity analysis to the diesel mass distribution between the two injection was conducted, varying the diesel mass fraction of the first injection between 0.4 and 0.8, by steps of 0.05.

Finally, a sensitivity analysis to the SR was performed, varying it between 0.8 and 1.8 (baseline value), by increments of 0.2.

7.3 Results and discussion

In this section, the results of the numerical analysis are discussed.

Figure 59 depicts the distributions of n-$C_{10}H_{22}$ and CH_4 mole fractions on two cut planes at 8.1 °CA AFTDC, namely, during the third diesel injection. As it can be noticed, the last diesel injection occurs when the premixed charge located in the central part of the combustion chamber has already burnt, since it is ignited by the diesel pilot and pre injections. Therefore, the third diesel injection modestly contribute to the oxidation of the premixed charge. Moreover, the associated diesel mass is mainly characterized by a diffusive combustion, favouring the formation of soot.

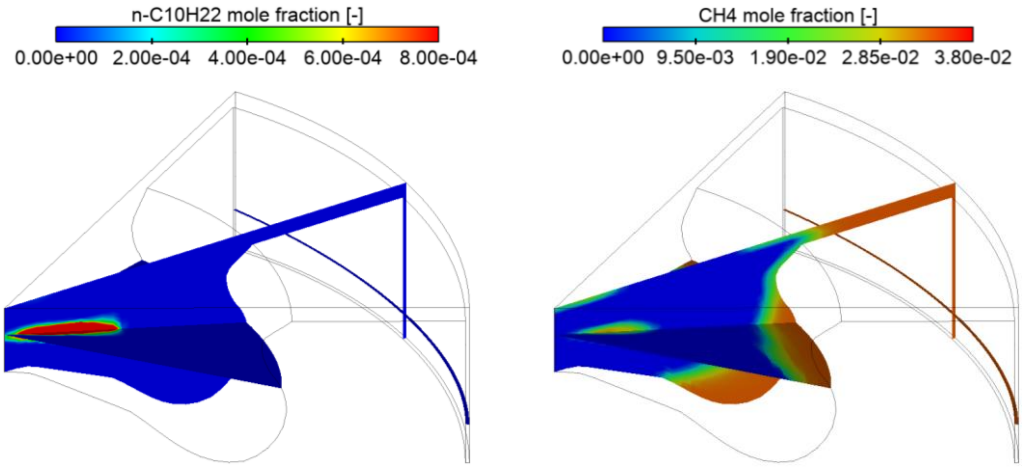

Figure 59. Contours of n-$C_{10}H_{22}$ and CH_4 mole fractions plotted on two orthogonal cut planes including the diesel spray axis at 8.1 °CA AFTDC (DF H_2/NG-diesel combustion, H_2 content: 30 vol%)

In the light of the above-mentioned considerations, it was decided to eliminate the third injection, moving to a split diesel injection strategy with two injections.

With the aim to optimise the modified diesel injection strategy, a sensitivity analysis of the DF 30vol%H_2/NG-diesel combustion to the SOI1 and SOI2 was performed. As previously specified, the SOI1 sweep ranges from -80 to -30 °CA AFTDC, by increments of 5 °CA, while the SOI2 sweep ranges from -30 to -10 °CA AFTDC, by increments of 5 °CA. As fare as the diesel mass fraction of injection 1 is concerned, it is imposed equal to 0.6.

Figure 60 reports the contours of IMEP*, η_c, GITE* and PPRR as a function of SOI1 and SOI2. It should be noted that the bottom right corner of the contour maps (delimited by a red dashed line) was not investigated since corresponds to SOI1/SOI2 combinations that cannot be realised. In fact, such SOI1/SOI2 combinations would imply that the two injections overlap each other. As it can be seen, IMEP*, η_c and GITE* tend to increase as SOI1 and SOI2 are retarded (i.e., the two injections are shifted towards TDC). However, such combustion parameters are mainly dependent on SOI2.

As far as PPRR is concerned, it is weakly influenced by SOI1 and SOI2 when SOI1 is lower than -45 °CA AFTDC. Conversely, if SOI1 is higher than -45 °CA AFTDC and SOI2 is higher than -25 °CA AFTDC, PPRR shows a stronger dependence on the injections phasing.

It is interesting to noticed that in the region defined above, all the considered combustion parameters reach their highest values. Therefore, the best SOI1/SOI2 combination falls in this portion of the contour maps. In particular, such combination is the one providing the best trade-off between IMEP* (and hence η_c and GITE*) and PPRR.

The highest values of IMEP* (6.24 bar) and GITE* (38.02%) correspond to SOI1 = -35 °CA AFTDC and SOI2 = -20 °CA AFTDC. At the selected SOI1/SOI2 combination, PPRR is lower than 5 bar/° (4.89 bar/°), while η_c is equal to 86.65%. However, the maximum value of η_c (86.71%) is reached when SOI1 = -30 °CA AFTDC and SOI2 = -20 °CA AFTDC, where IMEP* and GITE* show values lower than their maximum (6.23 bar and 37.94%, respectively), and PPRR is higher than 5 bar/° (5.21 bar/°). Therefore, the best SOI1/SOI2 combination, represented by a black full dot on the maps, correspond to:

- SOI1= -35 °CA AFTDC
- SOI2 = -20 °CA AFTDC

Passing from the diesel injection strategy depicted in Figure 44 to that one described above, IMEP* increases by 16.4% (from 5.36 bar to 6.24 bar), η_c improves by 12.4% (from 77.06% to 86.65%) and GITE* enhances by 16.6% (from 32.62% to 38.02%), at the expense of a higher PPRR (from 2.60 bar/° to 4.89 bar/°), but still lower than the limit value of 5 bar/°.

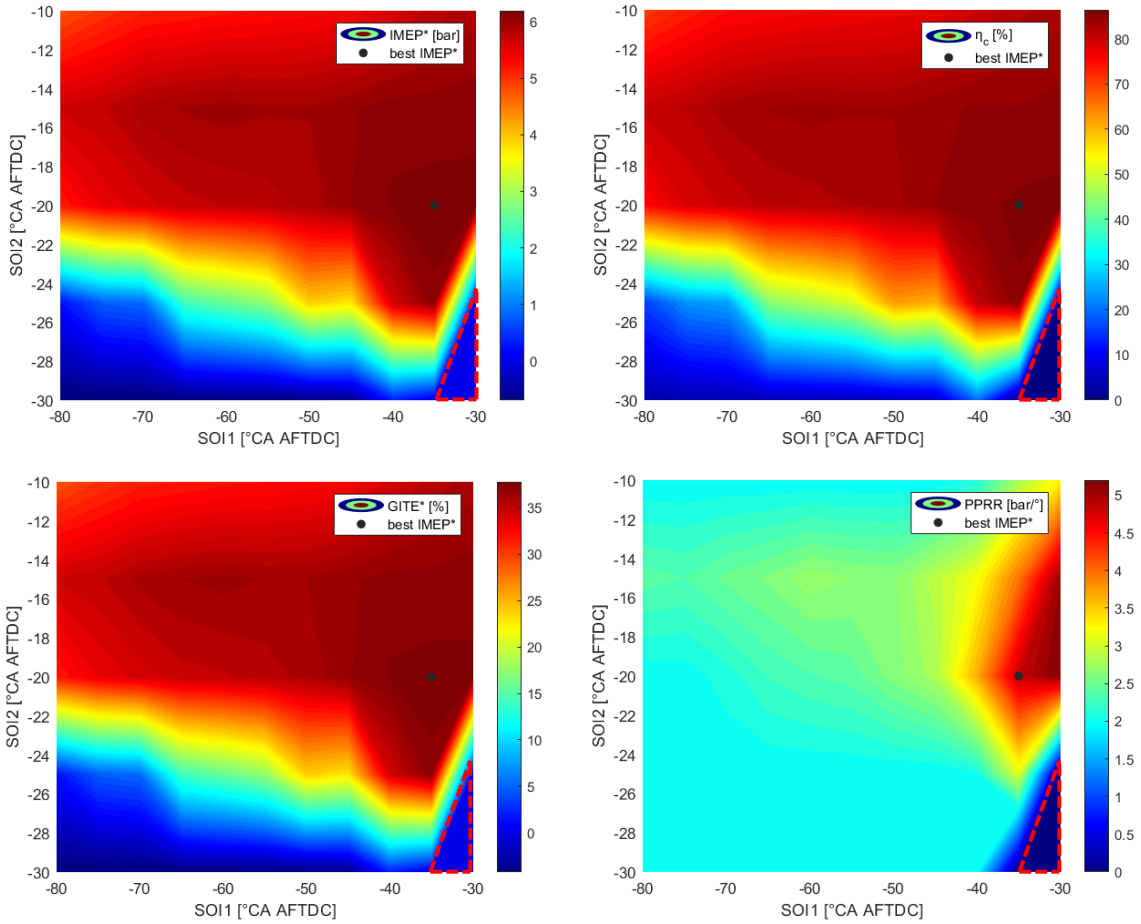

Figure 60. IMEP*, η_c, GITE* and PPRR contours as a function of SOI1 and SOI2

Once the best SOI1/SOI2 combination was defined, a sensitivity analysis to the diesel mass distribution between the two injections was performed. It is worth remembering that the initial injection 1 mass fraction is 0.6.

Figure 61 shows the trend of IMPE* as the diesel mass fraction of injection 1 is increased from 0.4 to 0.8. As it can be seen, IMEP* is almost constant (and equal to 6.24 bar) up to 0.65. Beyond this value, IMPE* drops up to 3.41 bar when the injection 1 mass fraction equals 0.8. This evidence is due to the fact that, as the injection 1 mass fraction increases from 0.4 to 0.65, CA50 is moved from 0.71 °CA to 4.56 °CA (+3.85 °CA), respectively (see Figure 62). Therefore, up to injection 1 mass fraction equal to 0.65, CA50 exhibits values representative of an efficient combustion. Then, the increase of injection 1 mass fraction from 0.65 to 0.8 shifts CA50 from 4.56 °CA to 16.32 °CA (+11.76 °CA), causing the combustion process to deteriorate.

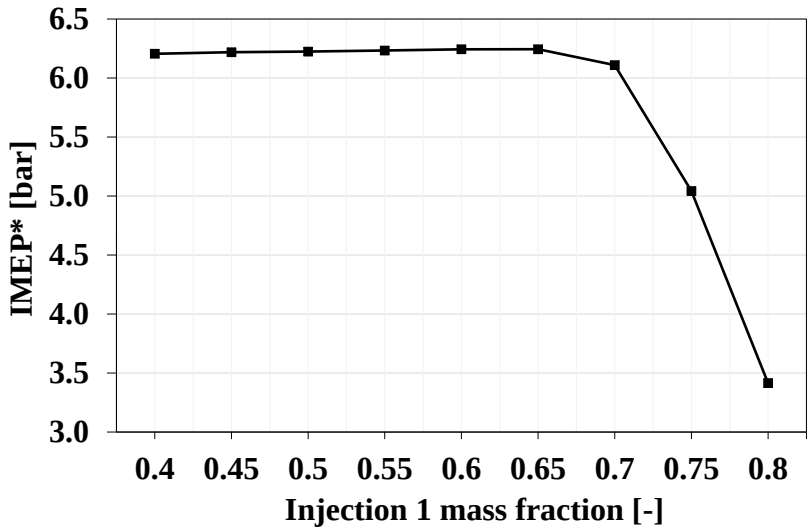

Figure 61. Influence of injection 1 mass fraction on IMEP*

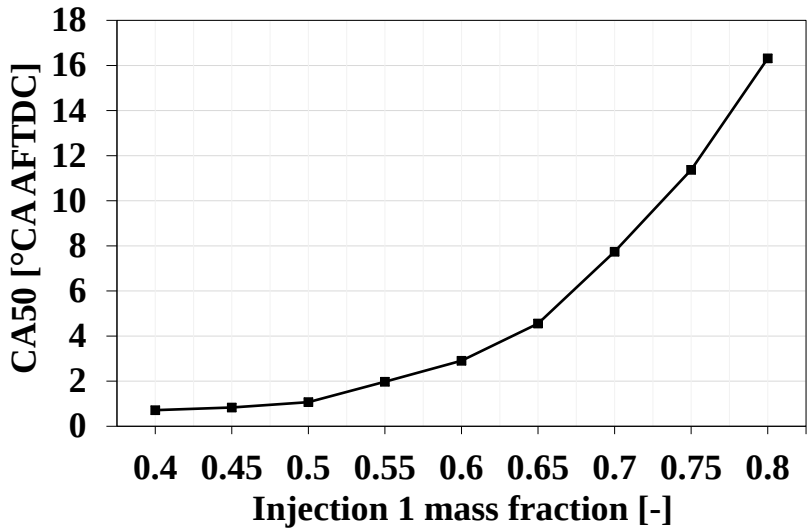

Figure 62. Influence of injection 1 mass fraction on CA50

Looking at Figure 63 and Figure 64, the behaviour of CA50 can be understood. Figure 63 reports the ignition delay, while Figure 64 shows the combustion duration (CA10-90) and the PPRR.

When the injection 1 mass fraction passes from 0.4 to 0.65, the ignition delay increases from 13.71 °CA to 17.01 °CA (+3.3 °CA), while CA10-90 reduces from 24.43 °CA to 21.25 °CA (-3.18 °CA). The opposite trends of the ignition delay and CA10-90 almost compensate each other, limiting the shifting of CA50 away from the TDC. However, as the injection 1 mass fraction passes from 0.65 to 0.8, both the ignition delay and CA10-90 increase. In detail, the

ignition delay passes from 17.01 °CA to 25.42 °CA (+8.41 °CA), while CA10-90 increases from 21.25 °CA to 28.43 °CA (+7.18 °CA). As a result, CA50 moves far away from the TDC. As far as the PPRR is concerned, it decreases from 6.18 bar/° to 2.02 bar/° as the CA50 shifts away from the TDC.

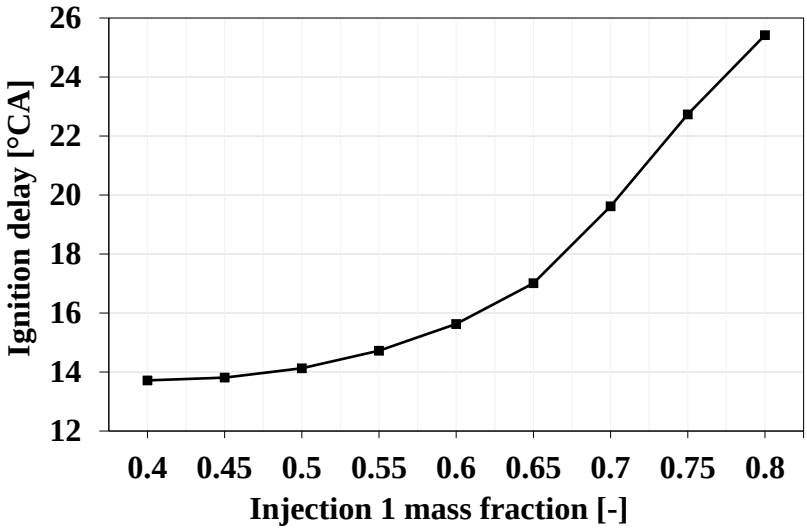

Figure 63. Influence of injection 1 mass fraction on ignition delay

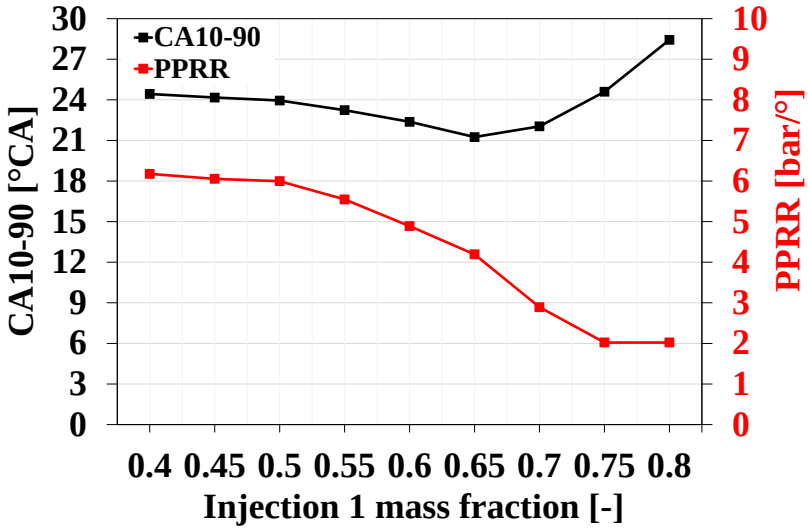

Figure 64. Influence of injection 1 mass fraction on CA10-90 and PPRR

Figure 65 confirms that the combustion efficiency, and hence the GITE*, are almost constant up to injection 1 mass fraction equal to 0.65. Beyond this value, η_c and GITE* drop from 86.5% to 56.9%, and from 38.0% to 20.8%, respectively.

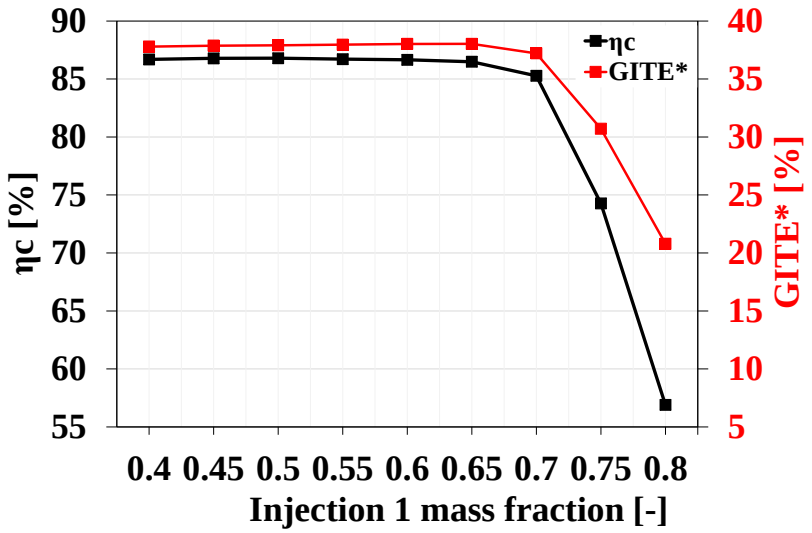

Figure 65. Influence of injection 1 mass fraction on combustion efficiency and GITE*

As a consequence, as the injection 1 mass fraction passes from 0.4 to 0.65, CO_2 specific emissions slightly decrease (-2.2%; see Figure 66), while CO and UHC specific emissions remain constant (see Figure 67). Beyond injection 1 mass fraction equal to 0.65, CO and UHC specific emissions strongly increase (by up to one order of magnitude), while CO_2 specific emissions further reduce for injection 1 mass fraction equal to 0.7, then increase by up to 69% with respect to the minimum value.

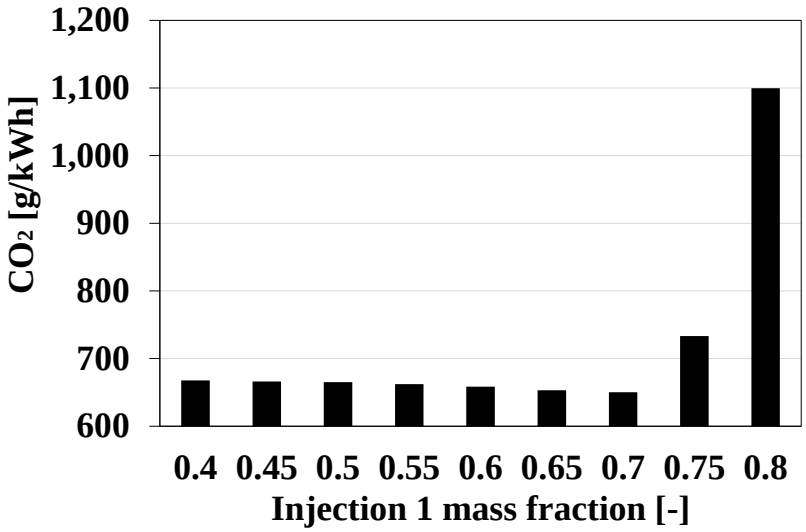

Figure 66. Influence of injection 1 mass fraction on CO_2 emissions

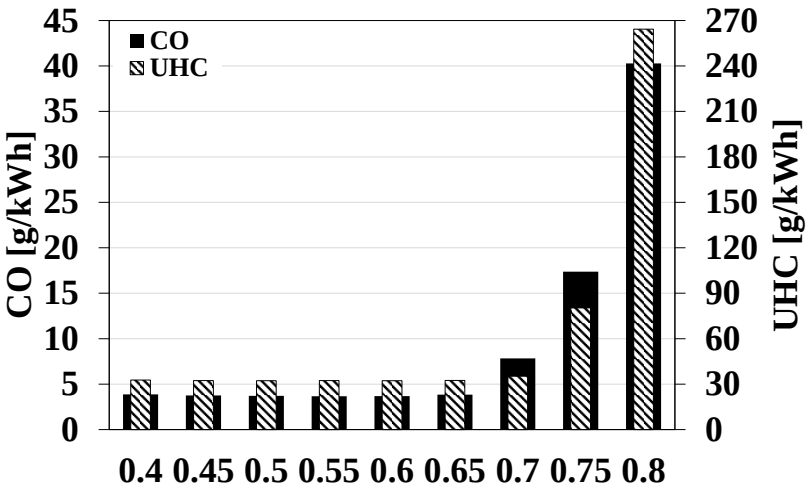

Figure 67. Influence of injection 1 mass fraction on CO and UHC emissions

Due to the shifting of CA50 away from the TDC, as the injection 1 mass fraction increases from 0.4 to 0.8, peak in-cylinder pressure decreases from 113.43 bar to 65.56 bar (see Figure 68). As a result, NO_x specific emissions drop by about 97% (see Figure 69).

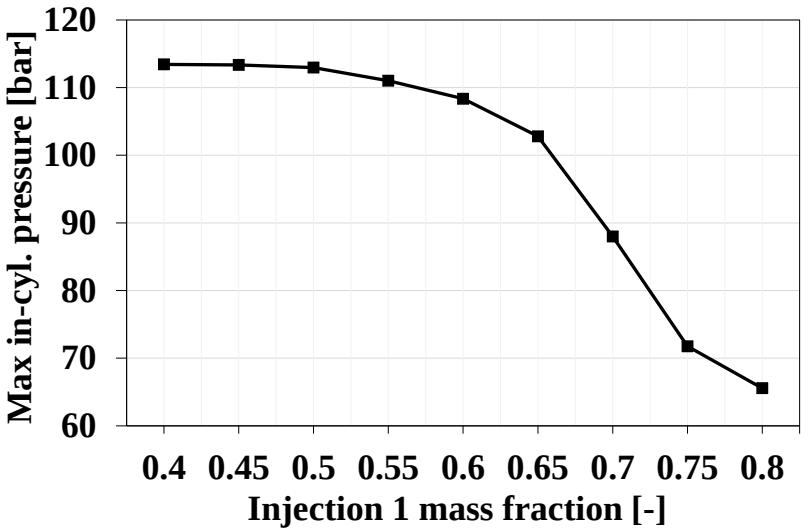

Figure 68. Influence of injection 1 mass fraction on maximum in-cylinder pressure

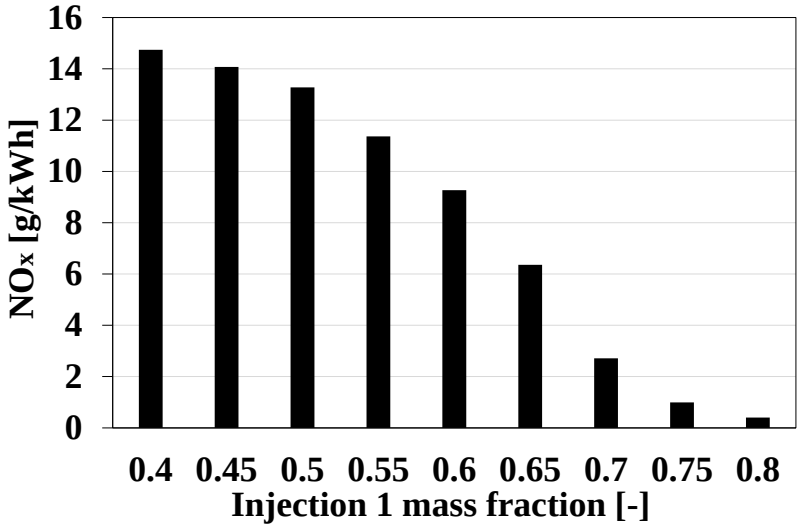

Figure 69. Influence of injection 1 mass fraction on NO_x emissions

Based on the previous analysis, the injection 1 mass fraction that represents the best compromise between performance and emissions corresponds to 0.7. In fact, at the expense of a slight worsening of IMEP* (-2.15%; η_c and GITE* worsen by 1.59% and 2.15%, respectively), it is possible to obtain a strong reduction of NO_x specific emissions (-70.73%).

The following step was to determine the best SR in the range between 0.8 and 1.8 (baseline value), by steps of 0.2. In fact, the actual SR is optimal for Diesel combustion, which requires a high level of turbulence in order to promote the mixing between diesel and air during the diffusive combustion. However, passing from CDC to DF combustion, a lower mass of diesel is injected (in this case, -80% of diesel in terms of energy, compared to ND operation). Moreover, in DF operation, the diesel is injected with a higher advance with respect to ND case. Hence, a lower level of turbulence is required in DF mode.

Figure 70 reports the trend of IMEP* as a function of SR. As it can be seen, IMEP* increases from 6.11 bar to 6.29 bar (+2.8%) as SR is decreased from 1.8 to 0.8. At the same time, CA50 lowers from 7.74 °CA AFTDC to 3.12 °CA AFTDC (see Figure 71). A similar trend can be observed for the ignition delay, which decreases from 19.62 °CA AFTDC to 16.22 °CA AFTDC, as shown in Figure 72. As far as CA10-90 is concerned, it decreases from 22.04 °CA to 20.24 °CA as SR passes from 1.8 to 1.4, while for values of SR lower than 1.4, CA10-90 increases up to 22.43 °CA (see Figure 73). Therefore, as SR is reduced from 1.8 to 1.4, both the ignition delay and the combustion duration decrease, shifting the centre of mass of the

combustion process (CA50) towards the TDC. Conversely, when SR is reduced below 1.4, the ignition delay and CA10-90 show opposite trends. However, CA50 moves closer to the TDC. As expected, PPRR increases as the CA50 shifts towards the TDC.

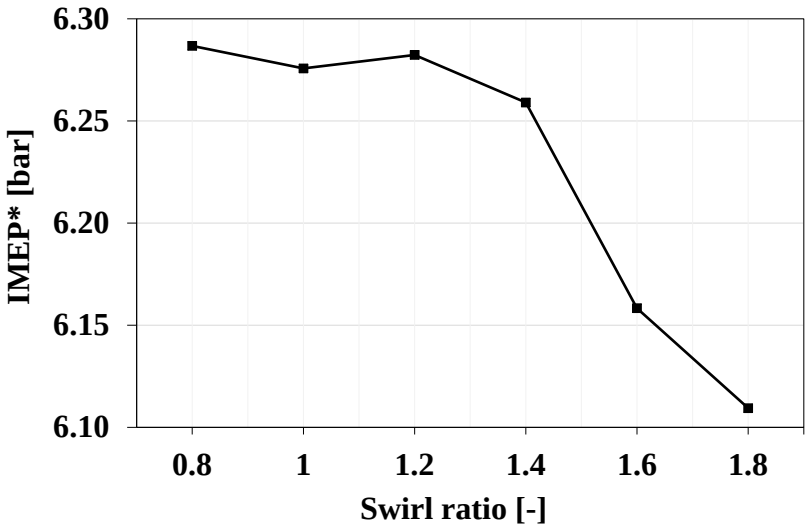

Figure 70. Influence of swirl ratio on IMEP*

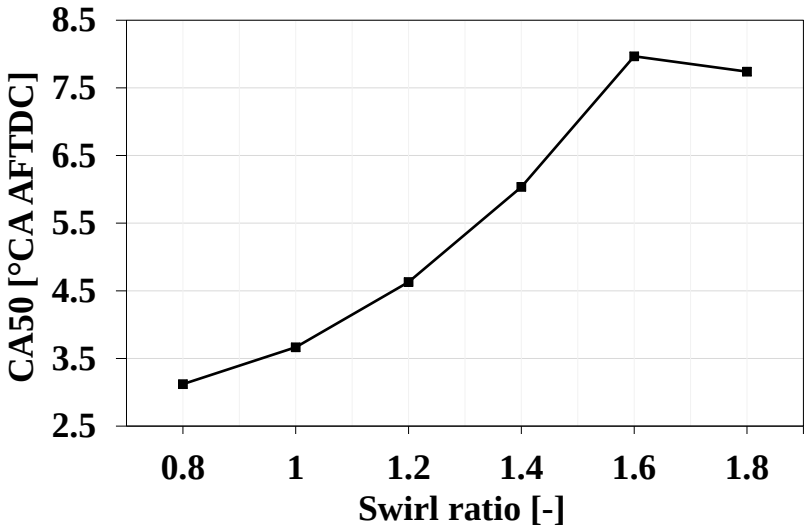

Figure 71. Influence of swirl ratio on CA50

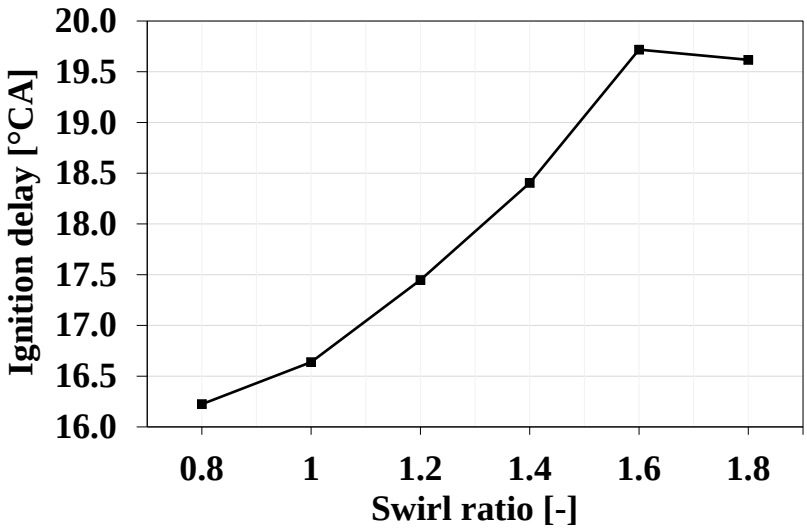

Figure 72. Influence of swirl ratio on ignition delay

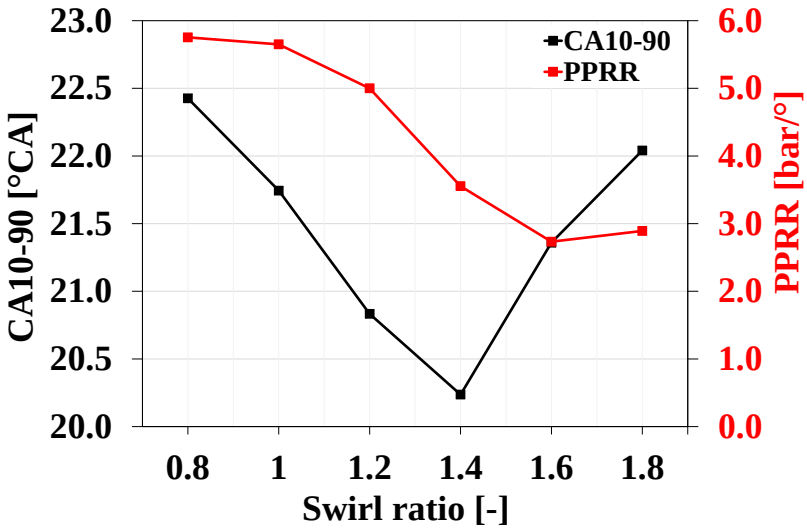

Figure 73. Influence of swirl ratio on CA10-90 and PPRR

As it can be noticed from Figure 74, η_c increases from 85.27% to 85.86% as SR passes from 1.8 to 1.4. Conversely, when SR is reduced below 1.4, η_c decreases up to 84.91%.

It clearly appears that there is a close correspondence between the trends of the combustion efficiency and CA10-90. Namely, a faster combustion is also a more complete (and hence efficient) process, and vice versa.

As far as GITE* is concerned, it follows the same trend of IMPE*, i.e., it increases (from 37.21% to 38.29%) as SR is reduced.

It is interesting to noticed that GITE* slightly increases even though η_c decreases when SR il lower than 1.4. This is due to the fact that the lower is SR, the lower is the wall heat transfer, which compensates the worsening of the combustion efficiency.

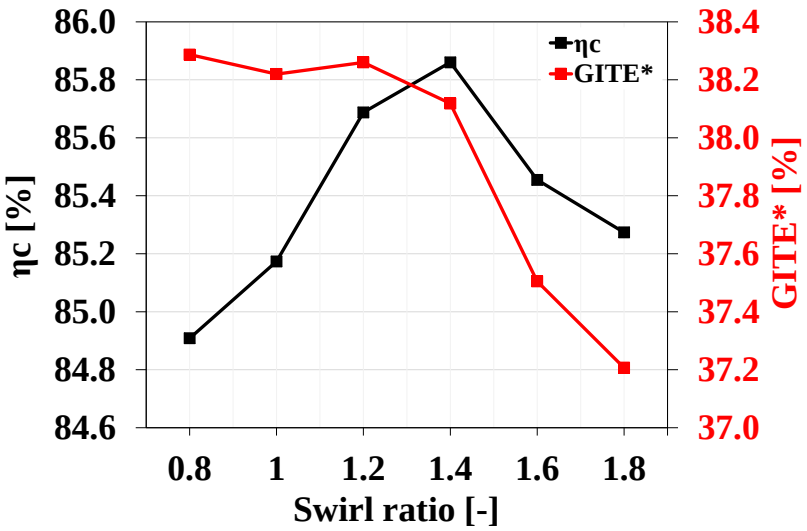

Figure 74. Influence of swirl ratio on combustion efficiency and GITE*

The enhancement of GITE* reflects on CO_2 specific emissions, which decrease by up to 1.86% as SR passes from 1.8 to 0.8 (see Figure 75).

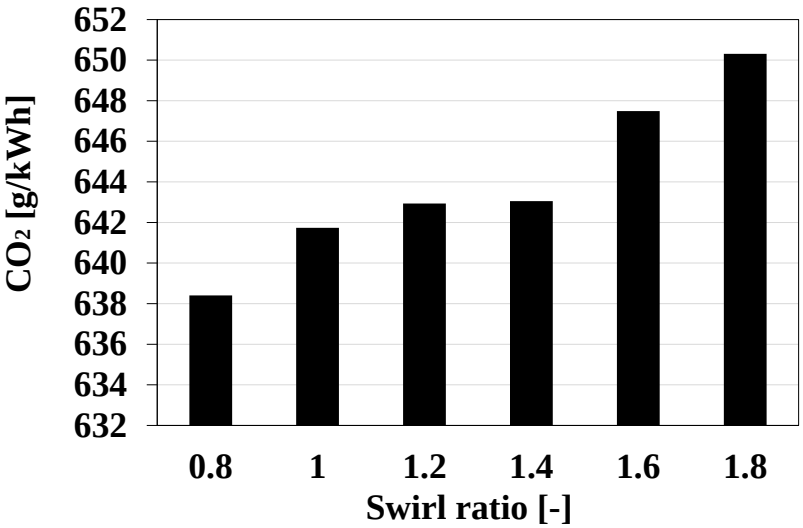

Figure 75. Influence of swirl ratio on CO_2 emissions

Conversely, the trend of η_c reflects on CO and UHC specific emissions. In particular, as SR is reduced from 1.8 to 1.4, CO and UHC specific emissions decrease by about 40.1% and 4.7%, respectively. When SR is further reduced below 1.4, CO and UHC specific emissions increase by about 1% and 7.5%, respectively.

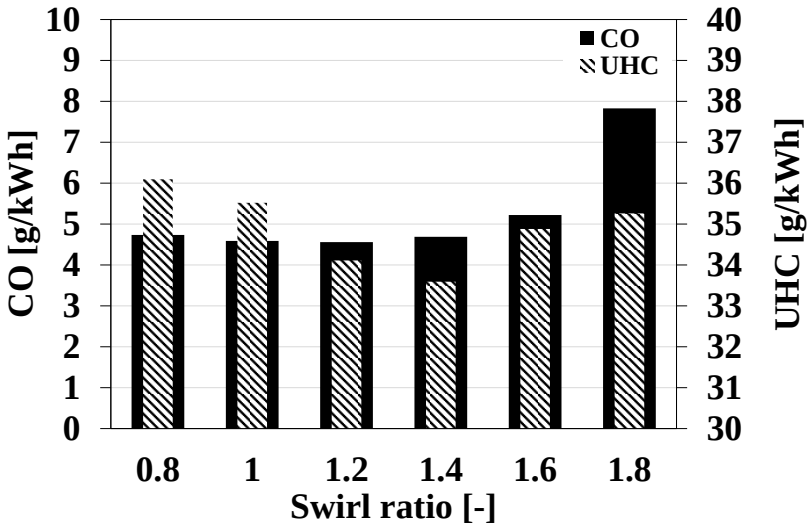

Figure 76. Influence of swirl ratio on CO and UHC emissions

As far as the peak in-cylinder pressure is concerned (see Figure 77), it increases as IMEP* increases. As a consequence, also NO_x specific emissions increase (from 2.71 g/kWh to 7.15 g/kWh as SR is reduced from 1.8 to 0.8; see Figure 78)

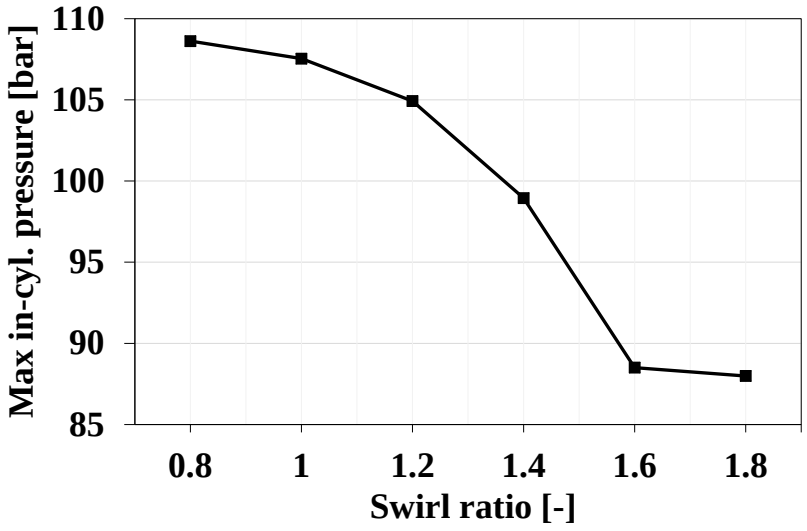

Figure 77. Influence of swirl ratio on maximum in-cylinder pressure

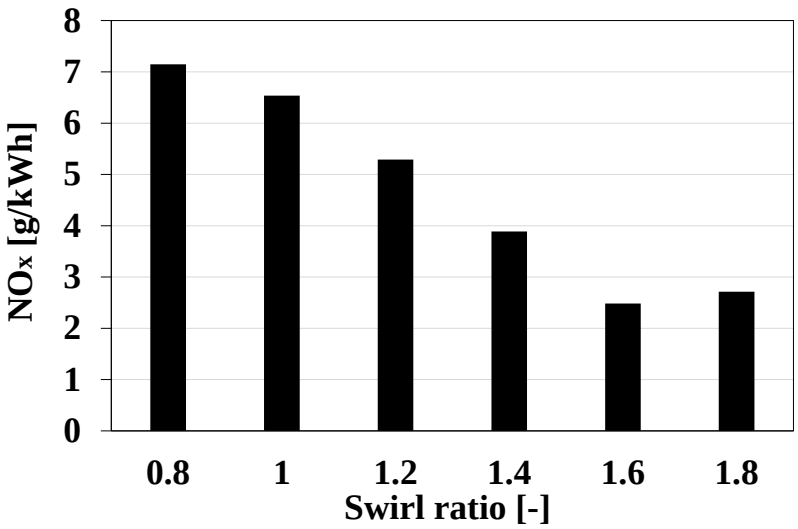

Figure 78. Influence of swirl ratio on NO_x emissions

Based on the sensitivity analysis on SR of the DF 30vol%H_2/NG-diesel combustion, it can be concluded that SR has a lower influence on combustion characteristics and CO_2 and pollutant emissions compared to the diesel injection strategy. Anyway, the SR = 1.4 was selected as the best compromise between performance and emissions. In fact, it guarantees the highest value of η_c and, correspondingly, the lowest values of CO and UHC emissions. Moreover, peak in-cylinder pressure is lower than 100 bar and both GITE* and IMEP* are close to highest values achievable acting on SR.

In conclusion, a comparison among CDC, DF NG-diesel, DF 30vol%H_2/NG-diesel, before and after the optimization process described above, is reported below.

Figure 79 compares the above-mentioned combustion techniques in terms of IMEP*. The transition between CDC and DF NG-diesel was experimentally realised keeping IMEP* constant. Then the substitution of NG with a 30vol%H_2-NG mixture and an optimization of the diesel injection strategy and SR permitted to improve IMEP* by about 61%.

At the same time, the peak in-cylinder pressure increased from 67.04 bar to 98.95 bar, as shown in Figure 80.

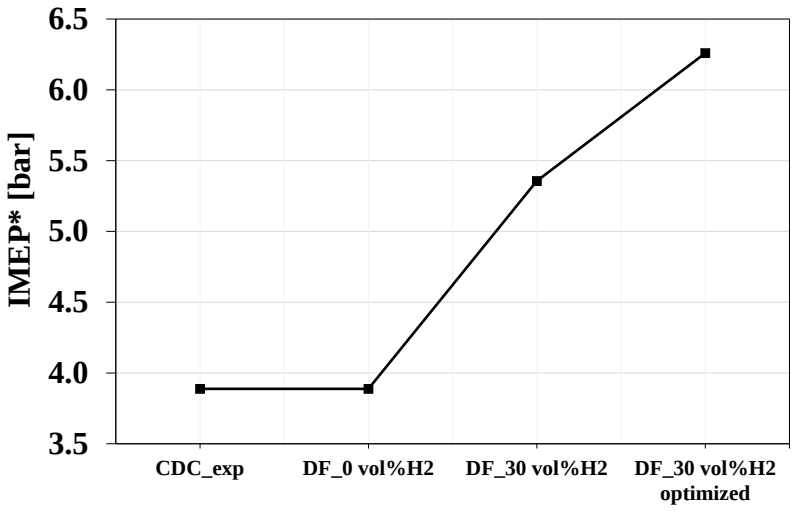

Figure 79. Comparison among CDC, DF NG-diesel and DF 30vol%H2/NG-diesel combustion before and after optimization of SR and diesel injection strategy in terms of IMEP*

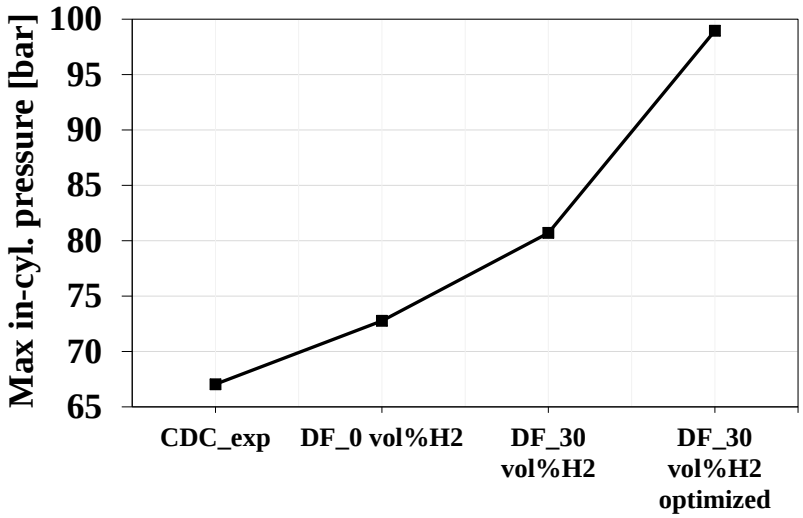

Figure 80. Comparison among CDC, DF NG-diesel and DF 30vol%H2/NG-diesel combustion before and after optimization of SR and diesel injection strategy in terms of maximum in-cylinder pressure

Passing from CDC to the optimized DF 30vol%H_2/NG-diesel, CA50 is shifted close to the TDC (from 16.2 °CA AFTDC to 6.0 °CA AFTDC; see Figure 81) since the combustion duration is reduced from 27.9 °CA to 20.2 °CA (see Figure 82). As a result, PPRR increases (from 2 bar/° to 3.55 bar/°). However, PPRR remains below the threshold of 5 bar/° (limit value for passenger car engines).

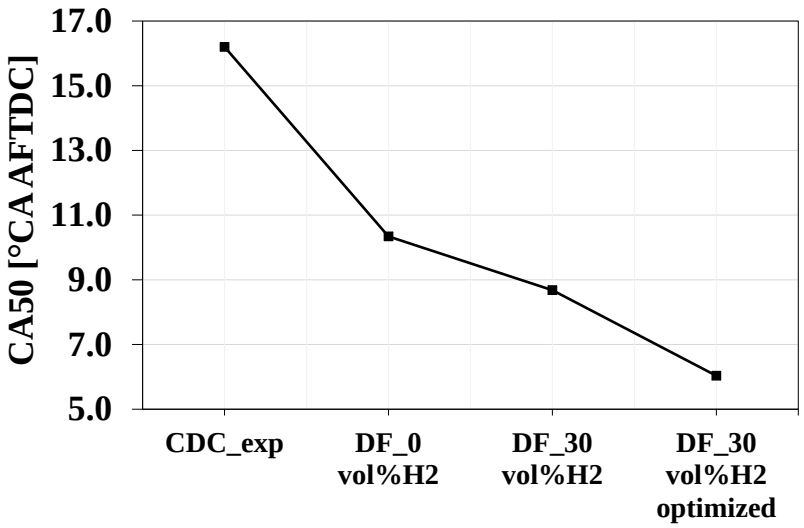

Figure 81. Comparison among CDC, DF NG-diesel and DF 30vol%H2/NG-diesel combustion before and after optimization of SR and diesel injection strategy in terms of CA50

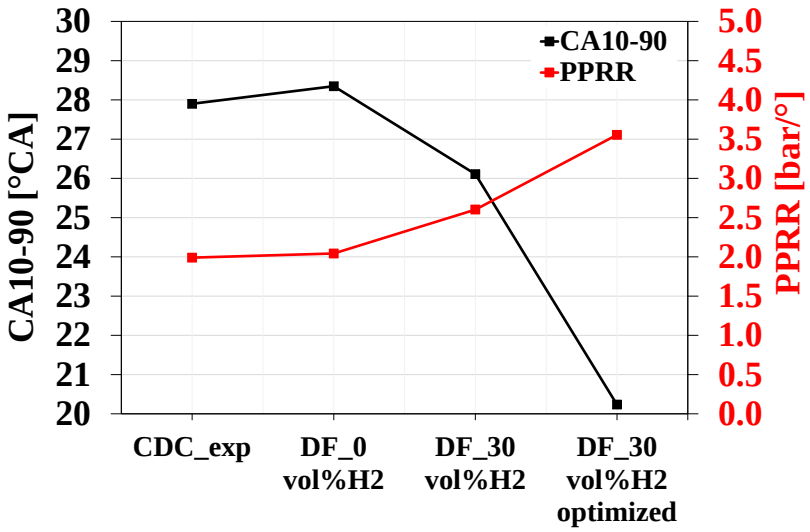

Figure 82. Comparison among CDC, DF NG-diesel and DF 30vol%H2/NG-diesel combustion before and after optimization of SR and diesel injection strategy in terms of CA10-90 and PPRR

Looking at Figure 83 and Figure 84, passing from ND operation to DF NG-diesel combustion, both η_c and GITE* worsen due to the high CO and UHC emissions (one order of magnitude higher than in CDC) that characterize the latter combustion concept. However, thanks to the addition of H_2 to the NG-air mixture (H_2 extends the LFL of the NG-air mixture), and the optimization of the diesel injection strategy and of SR, η_c and GITE* can be strongly enhanced (by up to 45.7% and 61.0%, respectively). As far as CO and UHC specific emissions are concerned, they can be reduced by up to 85%.

Despite the strong improvement of η_c and GITE* mentioned above, it was not possible to match the values that characterise ND operation. As a consequence, CO and UHC specific emissions of the optimized DF 30vol%H_2/NG-diesel case are higher than those ones of CDC. However, it should be noticed that CO specific emissions of DF 30vol%H_2/NG-diesel case are very close to those ones in ND operation.

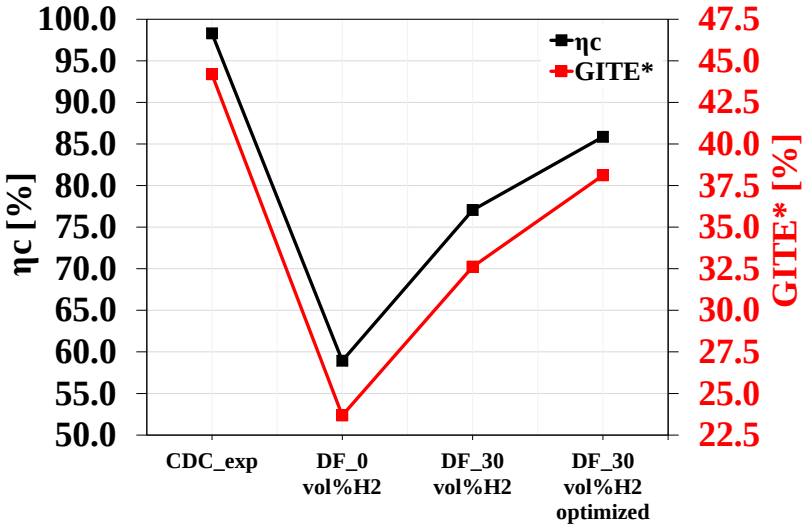

Figure 83. Comparison among CDC, DF NG-diesel and DF 30vol%H2/NG-diesel combustion before and after optimization of SR and diesel injection strategy in terms of η_c and GITE*

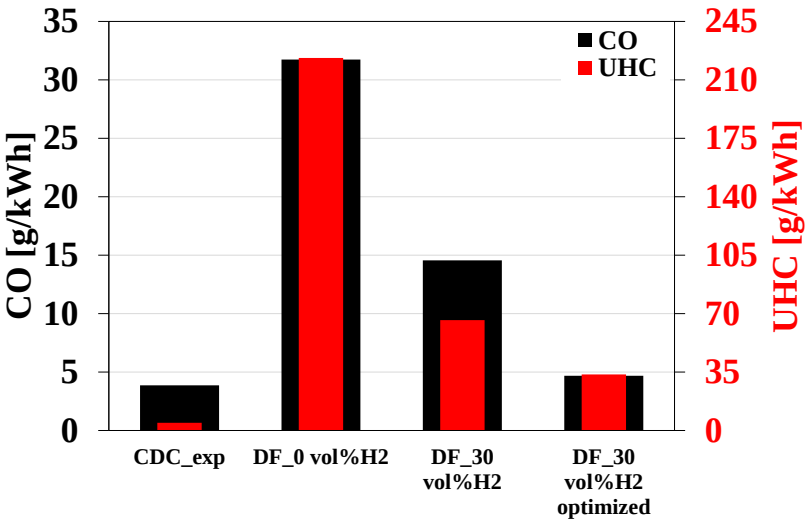

Figure 84. Comparison among CDC, DF NG-diesel and DF 30vol%H2/NG-diesel combustion before and after optimization of SR and diesel injection strategy in terms of CO and UHC emissions

Despite DF operations are characterised by lower GITE* with respect to ND operation, CO_2 specific emissions are always lower for the former combustion concept, starting from the DF NG-diesel mode. This is due to the relevant substitution of diesel (80% in terms of energy compared to CDC) with NG, which is primarily composed by CH_4, i.e., the hydrocarbon with the highest hydrogen-to-carbon ratio. Moreover, the use of a H_2/NG mixture with 30 vol% of H_2 further reduce CO_2 specific emissions (see Figure 85).

Finally, as it can be noticed from Figure 86, the DF 30vol%H_2/NG-diesel case shows lower NO_x specific emissions that in ND mode, despite the higher maximum in-cylinder pressure.

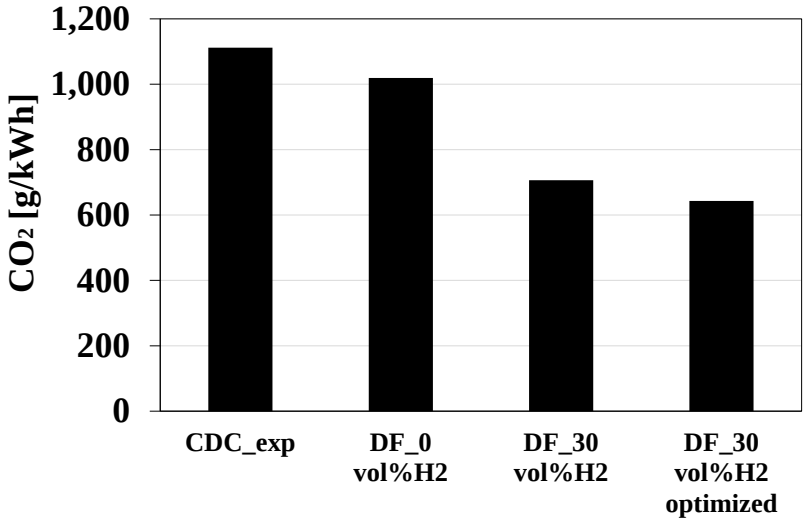

Figure 85. Comparison among CDC, DF NG-diesel and DF 30vol%H2/NG-diesel combustion before and after optimization of SR and diesel injection strategy in terms of CO_2 emissions

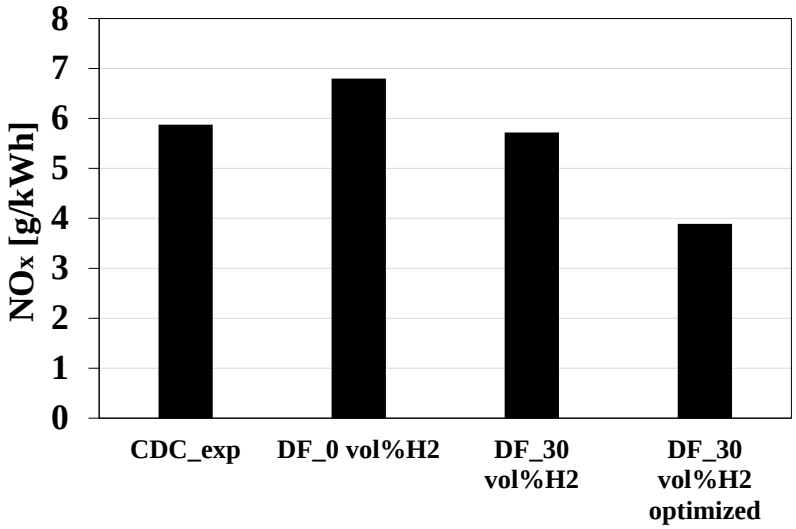

Figure 86. Comparison among CDC, DF NG-diesel and DF 30vol%H2/NG-diesel combustion before and after optimization of SR and diesel injection strategy in terms of NOx emissions

7.4 Conclusions

With the aim to extend the DF NG-diesel operating range to low loads, the use of H_2/NG mixtures was numerically investigated. The best results were obtained with a H_2/NG mixture containing 30 vol% of H_2. However, the improvements in terms of combustion efficiency, GITE*, CO and UHC specific emissions were not enough to match the values of CDC. Therefore, further analyses were carried out. In particular, the objective of the new study was to numerically optimize the diesel injection strategy and the SR for the DF 30vol%/NG-diesel case.

First of all, based on the results of the previous activity (see Section 6), the diesel injection strategy was modified passing from three to two injections per engine cycle. Then, the following sensitivity analyses of the DF combustion were performed:

- sensitivity analysis to the SOI of the first and second injection;
- sensitivity analysis to the diesel mass distribution between the two injections;
- sensitivity analysis to the SR.

Such analyses revealed that the best SOI1/SOI2 combination is SOI1 = -35 °CA AFTDC and SOI2 = -20 °CA AFTDC, with the diesel mass fraction of injection 1 equal to 0.7. As far as the SR is concerned, the best compromise between performance and emissions was achieved for SR = 1.4.

As a result:

- IMEP* improves by about 61% passing from CDC to the optimised DF 30vol%/NG-diesel case;
- PPRR increases due to the faster combustion that characterises the optimised DF 30vol%/NG-diesel case. However, it remains lower than 5 bar/°;
- combustion efficiency and GITE* can be enhanced by about 45.7% and 61.0% passing from the reference DF NG-diesel case to the optimised DF 30vol%/NG-diesel case;
- CO and UHC specific emissions are reduced by about 85% comparing the reference DF NG-diesel case to the optimised DF 30vol%/NG-diesel case;
- CO_2 specific emissions are decreased by about 42% passing from CDC to the optimised DF 30vol%/NG-diesel case;
- NO_x specific emissions can be reduced by about 33.8% if CDC and the optimised DF 30vol%/NG-diesel case are compared.

It should be noted that combustion efficiency and GITE* of the optimised DF 30vol%/NG-diesel case are still lower than in CDC, despite the strong improvement cited above. Therefore, further investigations are required in order to eliminate the remaining gap.

8 Interchangeability between natural gas and biogas in dual fuel operation using diesel as the high reactivity fuel

8.1 Introduction and aim

In order to reduce the carbon footprint of the transport and energy production sectors, renewable fuels, such as bio-methane and biogas, can play a prominent role.

As far as biogas is concerned, its composition, and hence its chemical and physical properties, are strongly dependent on the biomass used in the production process, as demonstrated by Table 20, that reports the main components and properties of biogas.

Table 20. Chemical and physical characteristics of biogas[139]

Constituents	**Range**
CH_4 [vol. fraction - %]	30÷73
CO_2 [vol. fraction - %]	20÷40
N_2 [vol. fraction - %]	5÷40
O_2 [vol. fraction - %]	0÷5
H_2 [vol. fraction - %]	1÷3
H_2S [vol. fraction - %]	0÷0.01
Properties	**Values**
Density [kg/m^3]	0.65-0.91
ON [-]	130
Auto-ignition temperature [°C]	632-813
Lower Heating Value [MJ/Nm^3]	10÷25

Therefore, the interchangeability between NG and biogas in DF operation was theoretically investigated. In particular, DF biogas-diesel operation, considering various biogas blends, was compared with DF NG-diesel mode at 3000 rpm – 177 Nm / 8 bar BMEP, taking the "-80% Diesel fuel +74% NG" DF case as a reference.

The 3D-CFD analysis was performed by means of the KIVA-3V model properly adapted in order to represent the different operating point.

Finally, with the aim to assess the advantages in terms of BTE, the DF biogas-diesel operation is compared to a SI generator set engine fuelled with biogas.

The work described in this section has been reported in a paper entitled "Application to micro-cogeneration of an innovative dual fuel compression ignition engine running on biogas" and published in the International Journal of Thermofluids (Elsevier).[140]

8.2 3D-CFD model description and validation

As mentioned above, the KIVA-3V model presented in Section 5 was used also in the present investigation. Boundary and initial conditions of the model were modified in accordance with the operating condition taken into account, namely, "-80% Diesel fuel +74% NG" DF case at 3000 rpm – 177 Nm / 8 bar BMEP (see Section 3.3.1). Then, the accuracy of the model was validated against experimental in-cylinder pressure and RoHR.

Since the NG used during the experimental campaign was composed mainly of CH_4 (96 vol%; see Table 14), the validation of the model was carried out modeling the premixed charge in two ways:

- a homogeneous mixture of NG and air;
- a homogeneous mixture of CH_4 and air.

Figure 87 and Figure 88 compare measured and predicted in-cylinder pressure and RoHR for NG-air and CH_4-air cases, respectively. As it can be noted, the numerical results are in very good agreement with the experimental in-cylinder pressure and RoHR. Moreover, there are no appreciable differences between the use of CH_4 as a NG surrogate and the exact modelling of the latter fuel.

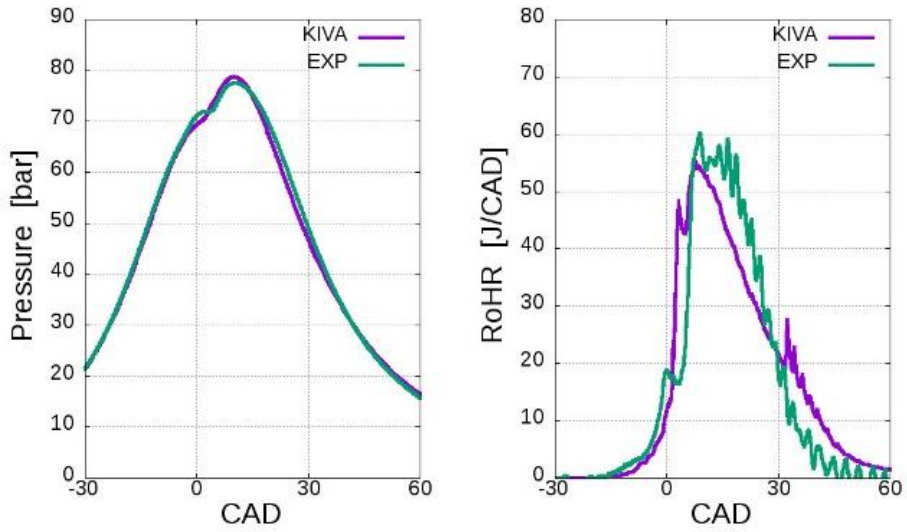

Figure 87. Comparison between experimental and numerical results in terms of in-cylinder pressure and RoHR; premixed charge: NG-air mixture

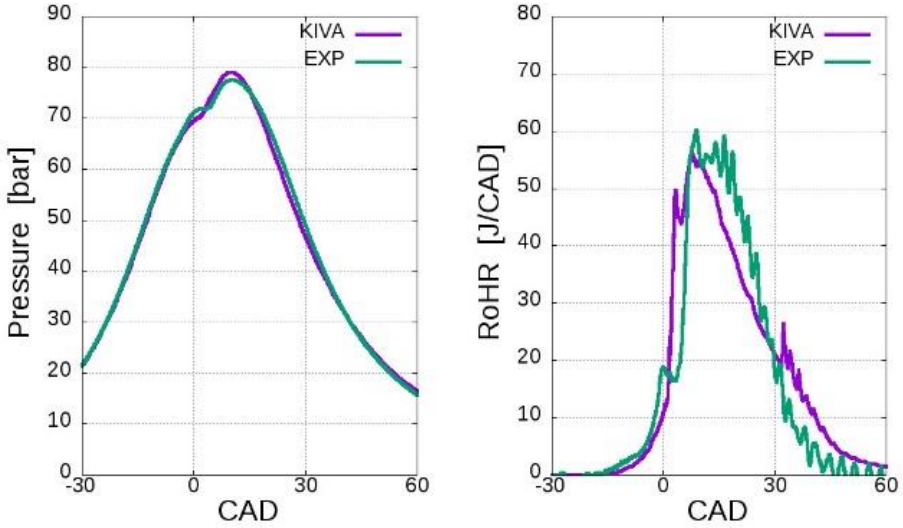

Figure 88. Comparison between experimental and numerical results in terms of in-cylinder pressure and RoHR; premixed charge: CH_4-air mixture

As far as biogas is concerned, it was modelled as a mixture of CH_4 and CO_2.

In order to assess the interchangeability between NG and biogas in DF mode, taking into account the variability of the composition of the biofuel, 3 mixtures of CH_4 and CO_2 were considered:

- 75 vol% CH_4 / 25 vol% CO_2 → referred to as BG75;
- 65 vol% CH_4 / 35 vol% CO_2 → referred to as BG65;
- 50 vol% CH_4 / 50 vol% CO_2 → referred to as BG50.

Table 21 lists the main properties of BG75, BG65, BG50, NG and CH_4, besides the corresponding compositions. As it can be seen, the LHV and the lower Wobbe-index (Wl) of the 3 biogas surrogates are quite different from those ones of NG and CH_4, which represents a measure of the interchangeability of gaseous fuels for engines. That is, if two gases have different compositions but the same Wl, they have similar volumetric energy contents, explosion limits and knock resistance.[141] While the lower LHV of the biogases can be easily managed by increasing the amount of fuel in the premixed charge, the lower Wl requires a readjustment of some engine control parameters.

Table 21. Composition and main properties of the fuels considered

		NG	CH_4	BG50	BG65	BG75
Composition [vol %]	N2	1.0%	0.0%	0.0%	0.0%	0.0%
	CH4	96.0%	100.0%	50.0%	65.0%	75.0%
	C2H6	2.5%	0.0%	0.0%	0.0%	0.0%
	C3H8	0.5%	0.0%	0.0%	0.0%	0.0%
	CO2	0.0%	0.0%	50.0%	35.0%	25.0%
Density	kg/m3	0.694	0.668	1.255	1.079	0.962
LHV	MJ/kg	49.00	50.00	13.31	20.12	26.05
LHV	MJ/Nm3	34.00	33.40	16.70	21.71	25.05
WI[136]	MJ/Nm3	44.71	44.76	16.33	22.89	27.98

The DF biogas-diesel combustion simulations were performed starting from the same in-cylinder pressure, temperature, turbulent kinetic energy, turbulence length scale and SR used in the validation cases. This permitted to isolate the effects on performance due to the presence of CO_2 in the premixed charge. Furthermore, with the aim to guarantee the same amount of energy to the premixed charge, the DF biogas-diesel combustion simulations shared the same mass of CH_4 of the DF CH_4-diesel combustion simulation, which was taken as a reference. As a result, as the mass of CO_2 in the premixed charge was increased, the mass of air was reduced, with a consequent reduction of AFR.

8.3 Results and discussions

In the following section the results of the numerical investigation are presented and discussed. Figure 89 compares BG50 (50% CH_4), BG65 (65% CH_4), BG75 (75% CH_4) and the reference case (100% CH_4) in terms of in-cylinder pressure and RoHR. As the fraction of CO_2 in the premixed charge increases, the RoHR slightly decreases in the first part of combustion while the peak of RoHR strongly decreases. As a results, the peak in-cylinder pressure is reduced (by up to 7 bar) and the combustion duration is extended, determining a worsening of the combustion efficiency (about -4% for BG50, about -2% for BG65 and about -1% for BG75) and of IMEP* (about -7% for BG50, about -4% for BG65 and about -2% for BG75). This evidence is due to the fact that the CO_2 present in the biogas acts as an inert gas.

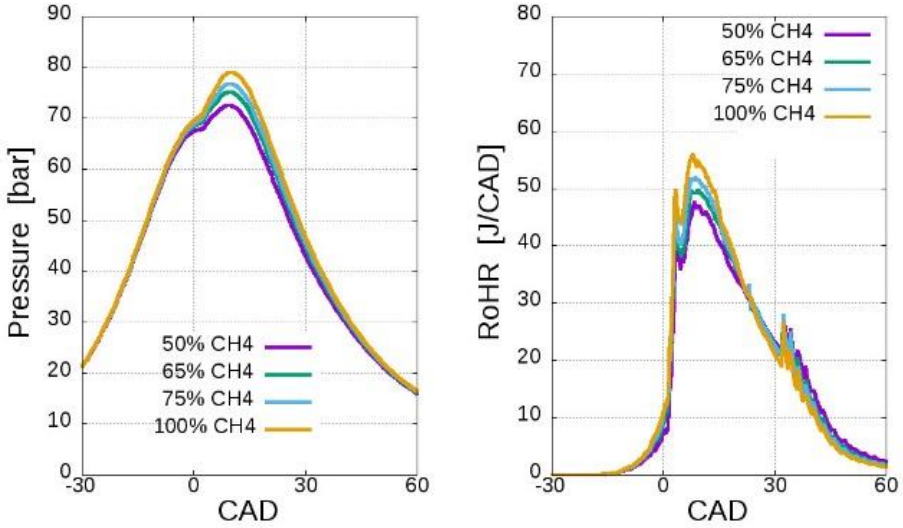

Figure 89. Comparison between BG50 (50% CH4), BG65 (65% CH4), BG75 (75% CH4) and 100% CH4 in terms of in-cylinder pressure and RoHR

In order to recover the lost efficiency, due to the presence of CO_2 in the biogas, a further set of simulations was carried out advancing the diesel injection law by steps of 1 °CA up to 4 °CA with respect to the reference case ("-80% Diesel fuel +74% NG" DF case at 3000 rpm – 177 Nm / 8 bar BMEP).

Figure 90, Figure 91 and Figure 92 report the effects on in-cylinder pressure and RoHR of the SOI sweep for BG50, BG65 and BG75, respectively. As expected, as the diesel injection law is advanced with respect to the reference case (purple lines), the RoHR is shifted towards the TDC. Moreover, the combustion process becomes faster and more impulsive, inducing a higher peak in-cylinder pressure.

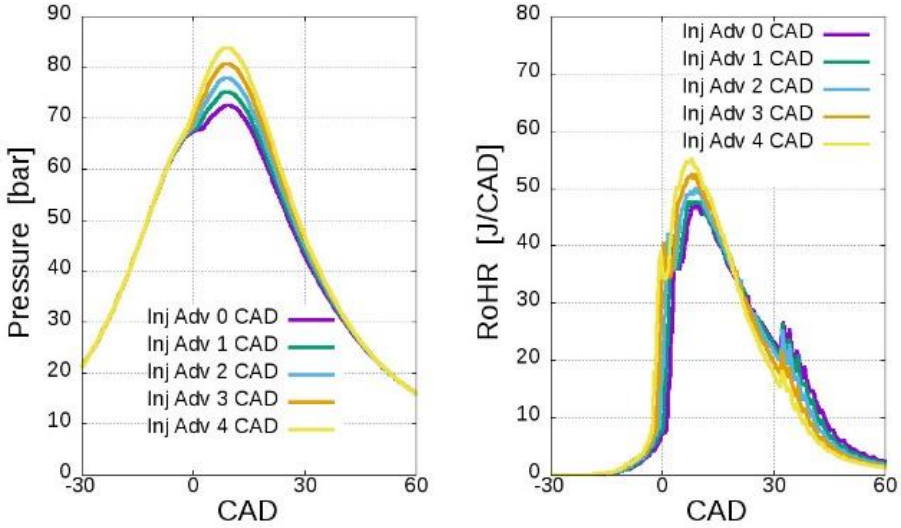

Figure 90. Influence of diesel SOI on in-cylinder pressure and RoHR for the BG50 case

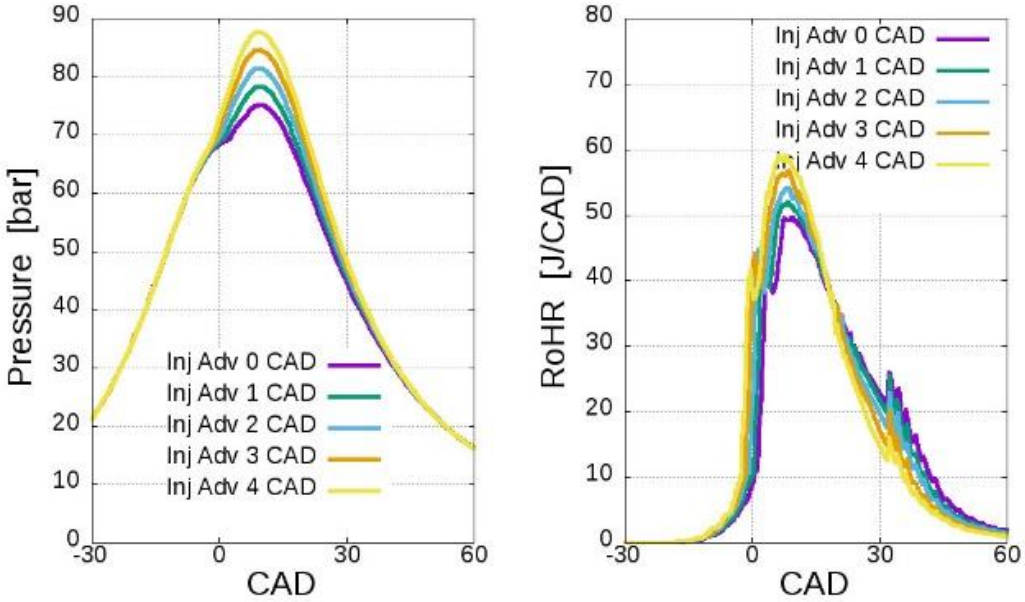

Figure 91. Influence of SOI on in-cylinder pressure and RoHR for the BG65 case

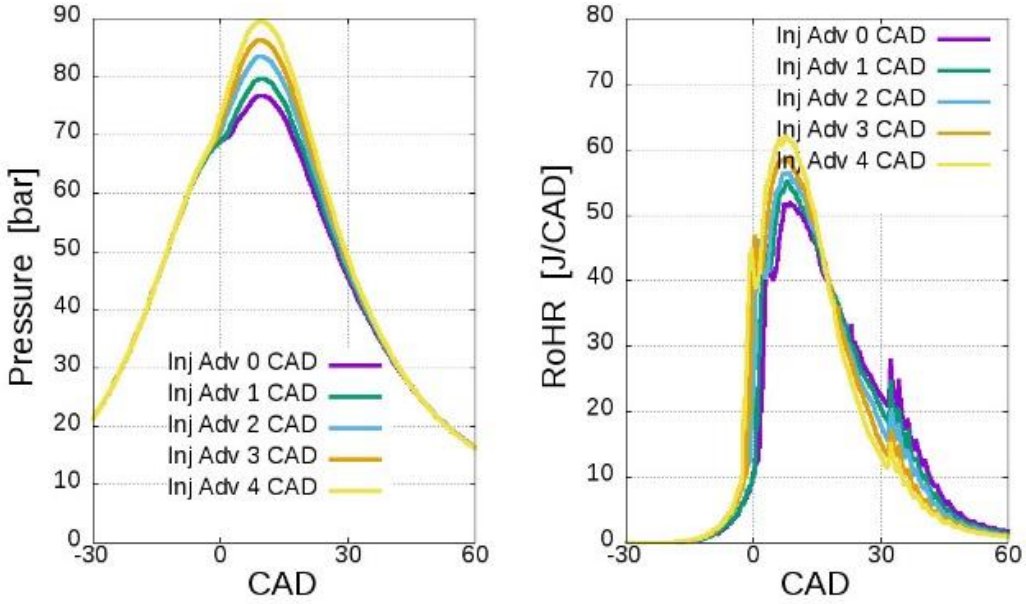

Figure 92. Influence of SOI on in-cylinder pressure and RoHR for the BG75 case

Finally, Figure 93, Figure 94 and Figure 95 show the influence on combustion efficiency, peak in-cylinder pressure, IMEP* and variation of IMEP* of the SOI advance sweep for BG75, BG65 and BG50.

It should be noted that, in this case, IMEP* was evaluated between -40 and +60 °CA AFTDC, instead of between IVC and EVO as in Sections 5 and 6.

As already said, passing from the reference case (grey bars) to the biogas blends with increasing CO_2 content, both combustion efficiency and IMEP* worsen (up to about 4% and 7%, respectively), while the peak in-cylinder pressure drops from 79 bar up to 72.5 bar. However, by simply advancing the diesel injection strategy, the same performance of the reference case can be reached. In particular, for the BG75 case, an advance of 1 °CA was enough to achieve the same combustion efficiency and IMEP* of the reference case, while for the BG65 and BG50 cases an advance of 2 and 4 °CA, respectively, was necessary. This is due to the fact that the combustion process is speeded up by advancing the diesel injection law, as demonstrated by, Figure 90, Figure 91 and Figure 92favouring the completion of combustion and increasing the work output.

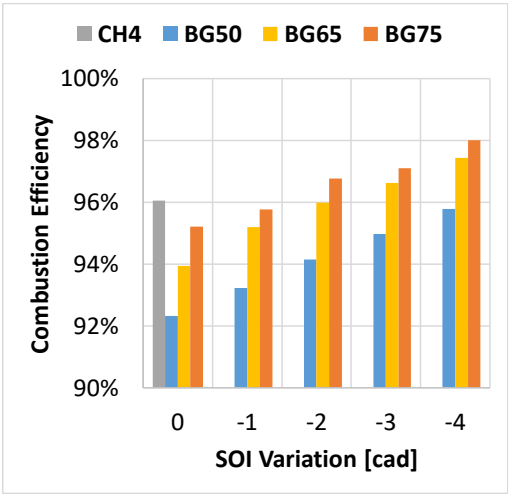

Figure 93. Influence of SOI advance on combustion efficiency peak in-cylinder pressure

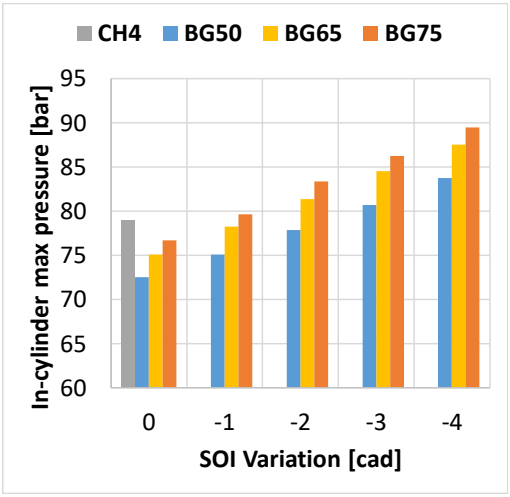

Figure 94. Influence of SOI advance on peak in-cylinder pressure

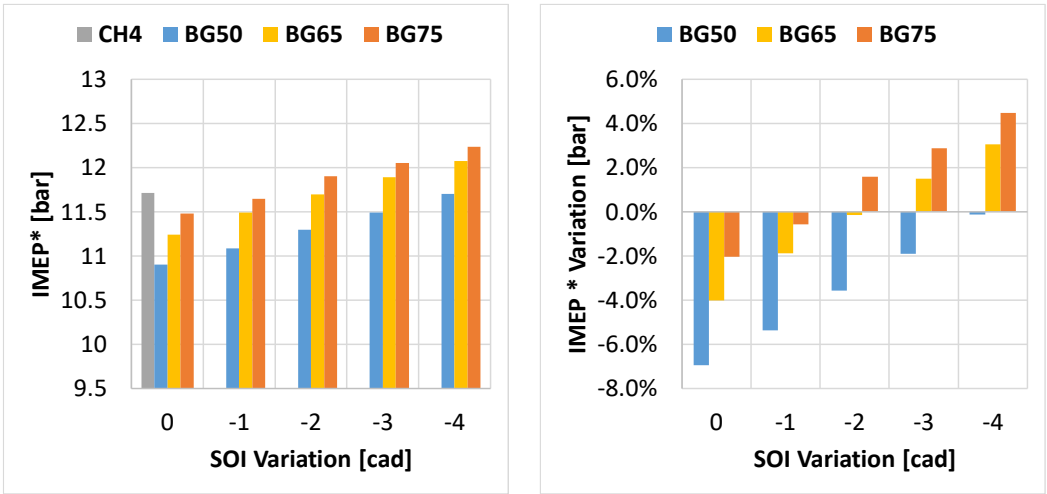

Figure 95. Influence of SOI on IMEP* and IMEP* variation with reference to the CH4 case

8.4 Comparison with a SI generator set engine running on biogas

In this section, the theoretical DF biogas-diesel engine is compared with a commercial SI generator set, fuelled with biogas, able to deliver a maximum power comparable to that one corresponding with the highest load investigated during the experimental activity reported in Section 3 (i.e. 83 kW). The main features of the SI generator set are listed in **Table 22**.[142]

Table 22. Main features of the SI generator ser running on biogas

Manufacturer	HIMOINSA
Combustion Type	SI
Cylinders Lay-out	In-line
Number of cylinders	6
Air metering	Naturally aspirated
Bore x Stroke [mm]	130x150
Displacement [L]	11.946
Compression Ratio	12:1
Injection system	PFI
Rated rpm@50 Hz	1500
Max. Power at rated rpm [kW]	82.5
Max. BMEP at rated rpm [bar]	5.5
Fuel consumption at Max. Power, rated rpm [Nm^3/h]	36.8
BSFC at Max. Power, rated rpm [g/kWh]	513.8
Max. Specific Power, rated rpm [kW/L]	6.9

The performance reported in Table 22 refers to a biogas composed by a 65/35 vol% blend of CH_4 and CO_2. Therefore, the BG65 case with optimized SOI is taken into account for the comparison.

The datasheet of the SI generation set[142] engine reports the fuel consumption for four loads:

- load 100% (corresponding to the maximum power at the rated speed = 82.5 kW): fuel consumption = 36.8 Nm^3/h;
- load 75% (61.9 kW): fuel consumption = 29.9 Nm^3/h;
- load 50% (41.3 kW): fuel consumption = 23 Nm^3/h;
- load 25% (20.6 kW): fuel consumption = 15.9 Nm^3/h.

Since a single operating condition corresponding to 3000 rpm – 177 Nm / 55.5 kW was investigated on DF biogas-diesel engine, some hypotheses were made with the aim to obtain the performances at the other loads:

- engine speed is the same for all the loads and equal to 3000 rpm;
- by means of the optimization of the engine control parameters, the same combustion pattern, with same efficiency, of the investigated case can be obtained also in the other operating points;
- Friction Mean Effective Pressure (FMEP) is supposed to be constant since the engine revolution speed is the same and the combustion pattern is maintained.

Figure 96 shows the comparison between the DF biogas-diesel engine and the SI power generation set fuelled with biogas in terms of BTE, as a function of the power delivered. The trend of BTE for the baseline Diesel engine is also reported.

As expected, the DF engine is characterized by the highest BTE over the entire operating range. Moreover, both the DF and the baseline Diesel engines show a higher overall efficiency with respect to the SI engine, thanks to the higher thermodynamic and pumping efficiencies. In detail, the maximum difference between the DF and the SI engine in terms of BTE is at low load and equal to 34%. This depends on the high throttling losses of the latter engine. At 3000 rpm – 177 Nm / 55.5 kW, the fuel saving guaranteed by the DF engine is about 21%.

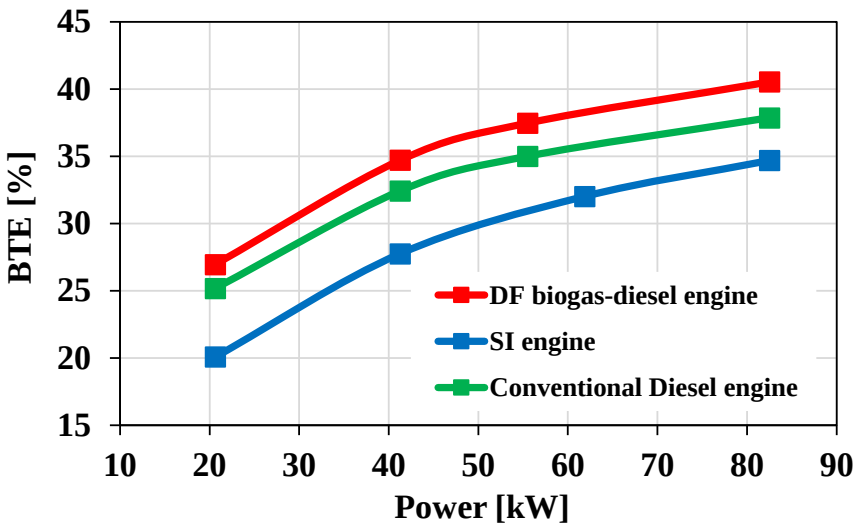

Figure 96. Comparison among the DF biogas-diesel engine, the SI generator set engine and the conventional Diesel engine

8.5 Conclusions

As demonstrated by the numerical investigation discussed above, DF combustion is weakly affected by the CO2 content in the premixed charge, and simply optimizing the diesel SOI, the drop of the combustion efficiency can be easily recovered. Moreover, as the CO2 content in the biogas increases, a higher fuel mass flow rate is required so as to assure that the fuel energy entering the cylinders remains constant. Obviously, this implies that the composition of the biogas is monitored, for example as proposed by Rahmouni et al.[143]

9 Numerical investigation on port gasoline injection in a modern 2-Stroke Diesel engine for dual fuel operation

9.1 Introduction and aim

From the review of the literature presented in Section 2, it clearly appears that DF pilot-ignited/RCCI combustions have been widely investigated on 4S Diesel engines, while the application of such combustion strategies to 2S engines is limited to DF NG-diesel 2S large-bore stationary/marine engines.

However, 2S HSDI Diesel engines may be particularly suitable to operate in DF pilot-ignited/RCCI combustions thanks to the double number of power strokes per unit time relative to 4S engines, solving one of the main problems that affects LTC engines, namely, the low power density.[12]

The main issue connected to the implementation of DF pilot-ignited/RCCI combustion to 2S HSDI Diesel engines could be the preparation of the premixed charge, due to the slip of the port injected LRF in the exhaust system during the scavenging process.

Based on the previous considerations, the goal of the numerical study described in this section is to determine the most effective solution to inject gasoline in a modern 2S HSDI Diesel engine, in order to implement the DF combustion concept.

It should be noted that gasoline represents a test fuel. In fact, such analysis is intended as a preliminary study aimed at providing a guidance for future numerical and experimental investigations using low carbon-content, renewable fuels, such as ethanol.

9.2 The investigated engine

The investigated engine is a modern 2S loop scavenged, 3-cylinder, HSDI Diesel engine, which derives from a modular 2S engine able to adopt two types of combustion systems: Gasoline Direct Injection (GDI) and Direct Injection Common Rail Diesel. The design of such modular 2S engine is described in dedicated papers.[144–146]

The peculiarities of the investigated engine are:

- external scavenge pump;
- oil sump as on 4S engines;
- domed piston;
- combustion chamber in the head.

Further details of the investigated engine are listed in Table 23, while Figure 97 shows the CAD model of one cylinder of the selected engine.

Table 23. Main features of the investigated engine

N° of cylinders	3
Cylinders arrangement	In-line
Bore x Stroke [mm]	83.0 x 109.5
Compression ratio [-]	19.8
Total displacement [L]	1777.5
N° of intake ports	5
Height of each intake port [mm]	12.45
Intake Port Opening (IPO) [°CA ATDC]	135
Intake Port Closing (IPC) [°CA ATDC]	225
N° of exhaust ports	2
Height of each exhaust port [mm]	40.31
Exhaust Port Opening (EPO) [°CA ATDC]	98
Exhaust Port Closing (EPC) [°CA ATDC]	262

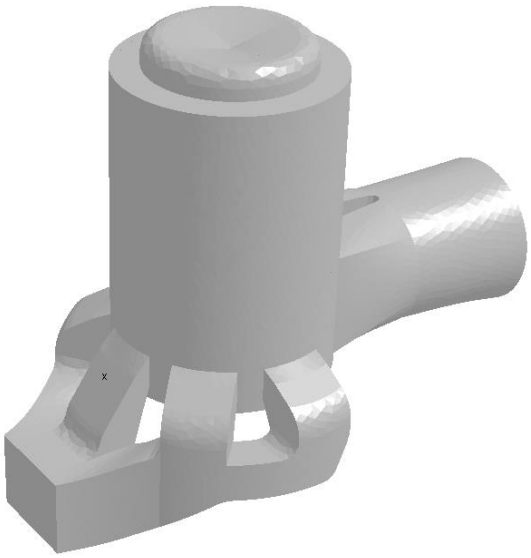

Figure 97. CAD model of one cylinder of the investigated engine

9.3 3D-CFD model description and methodology

The present numerical study was carried out by means of the commercial 3D-CFD code ANSYS Forte.[135]

The operating point of interest is 4000 rpm - full load, corresponding to the maximum power condition.

The first step was to analyse the gas exchange process in order to detect the best crank angle interval to inject gasoline. Then, four different gasoline injection alternatives were investigated and compared, with the aim to define the best one, namely, the one that minimises the slip of gasoline in the exhaust system and the impingement on the intake ducts walls.

As far as the numerical set-up is concerned, both boundary and initial conditions for the 3D-CFD simulations were provided by a 1D-CFD model of investigated engine.

Figure 98 shows the intake, in-cylinder and exhaust pressure profiles predicted by the 1D-CFD model.

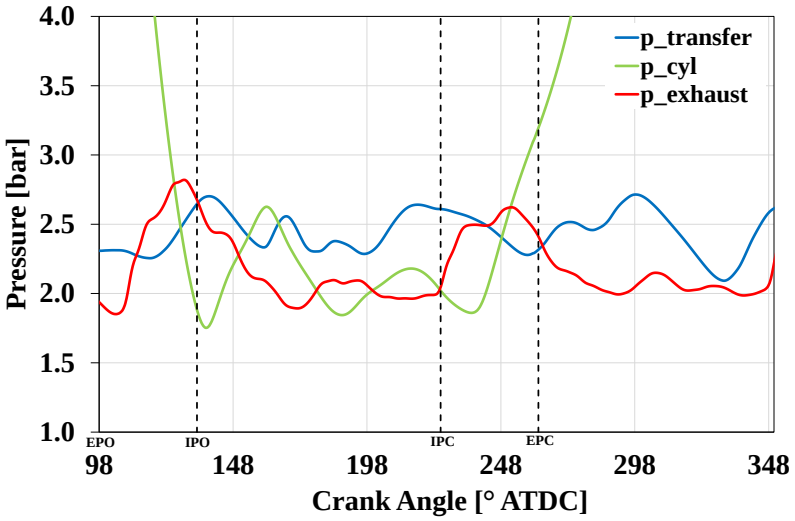

Figure 98. Intake, in-cylinder and exhaust pressure profiles predicted by the 1D-CFD model

The analysis of the gas exchange process was carried out running simulations between 98 °CA ATDC (EPO) and 262 °CA ATDC (EPC), while to evaluate the various gasoline injection alternatives and the mixture formation, simulations were extended to 350 °CA ATDC.

In both types of simulations, the charge in the intake ducts was initialised as O_2, while N_2 was used to model the combustion products that fill the cylinder and the exhaust ducts.

Based on a sensitivity analysis to the computational grid, the selected global mesh size is 2 mm, since it represents the best compromise between accuracy and computational cost.
Local refinements were also applied, both fixed and solution dependent (see Table 24). It should be noted that the solution dependent refinement based on the fuel vapor mass fraction was activated only during the gasoline injection simulations.

Table 24. Fixed and solution dependent local refinements applied to the mesh

	Cell size	Refinement method
All walls	1 mm	1 layer
Open boundaries	1 mm	2 layers
Port walls	1	2 layers
Intake ducts-cylinder interface	1 mm	14 mm radius sphere
Exhaust ducts-cylinder interface	1 mm	25 mm radius sphere
Velocity magnitude	1 mm	Gradient of velocity magnitude
Fuel vapor mass fraction	0.5 mm	Gradient of fuel vapor mass fraction

Figure 99 shows the average trend of the number of fluid cells for the gasoline injection simulations.

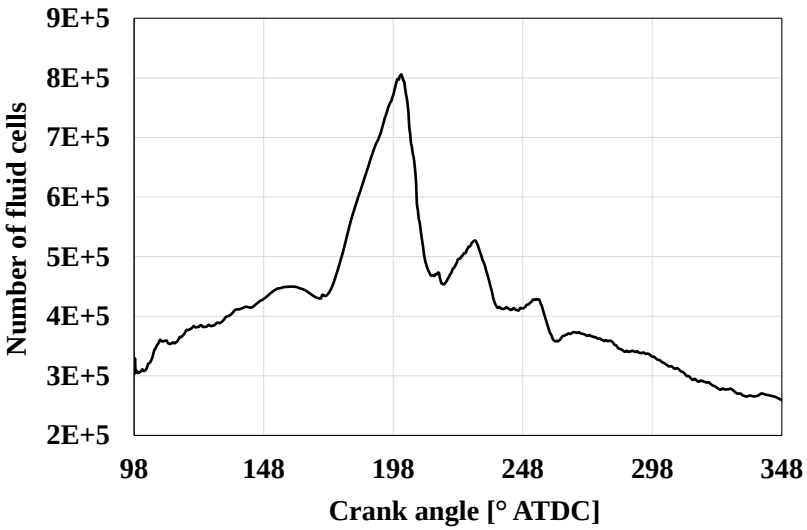

Figure 99. Average trend of the number of fluid cells for the gasoline injection simulations

The main numerical models employed during the simulations are reported in Table 25. As before, the droplet collision model and the spray brake-up model were activated only during the gasoline injection simulations.

Table 25. Main numerical models employed[135]

Equation of state	Ideal gas
Turbulence model	RANS RNG k-epsilon
Wall heat transfer	Enabled
Wall treatment	Law of the wall
Droplet collision model	Adaptive collision mesh model
Droplet size distribution	Rosin-Rammler
Spray brake-up model	KH-RT + unsteady gas jet model

9.4 Gas exchange process analysis

In the following, the results of the numerical analysis of the gas exchange process are reported. Figure 100 depicts the net mass fluxes through the intake and exhaust ports. A positive net mass flow rate through the intake ports means that there is a net flow that goes from the intake ports to the cylinder, while a negative net mass flow rate through the exhaust ports means that the net flux goes from the cylinder to the exhaust ports. Therefore, as it can be noticed, no backflows exist from the cylinder to the intake ports. Conversely, a backflow from the exhaust ports to the cylinder occurs between 232 °CA ATDC and 253 °CA ATDC.

As it can be seen from Figure 101, the in-cylinder mass trapped at EPC (262 °CA ATDC) is equal to 794.36 mg, which is in good agreement with the prediction of the 1D-CFD model, i.e., 789.72 mg (error: 0.59%).

Figure 102 shows that the fresh charge represents the 66% of the in-cylinder mass trapped.

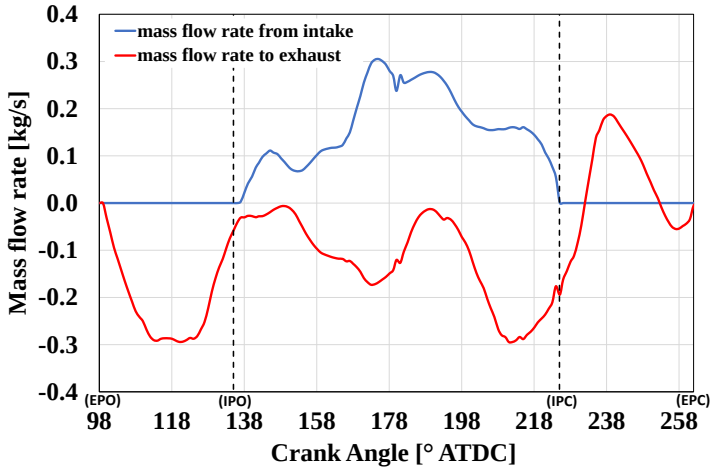

Figure 100. Net mass fluxes through intake and exhaust ports

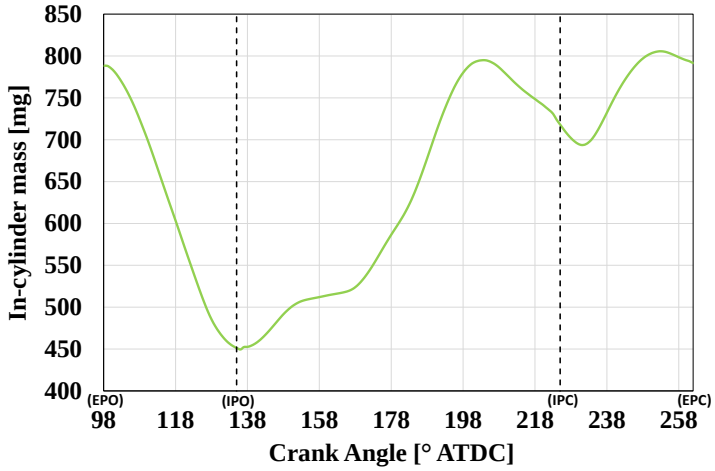

Figure 101. In-cylinder mass

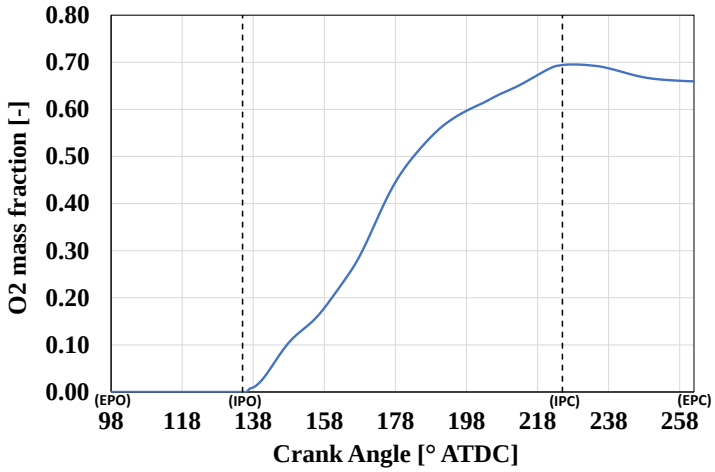

Figure 102. In-cylinder O_2 mass fraction

Figure 103 depicts the characterization of the scavenging process of the investigated engine in terms of the charging efficiency, scavenging efficiency, retaining efficiency and the scavenging model. As it can be noticed, the scavenging process is mainly a perfect displacement scavenging.

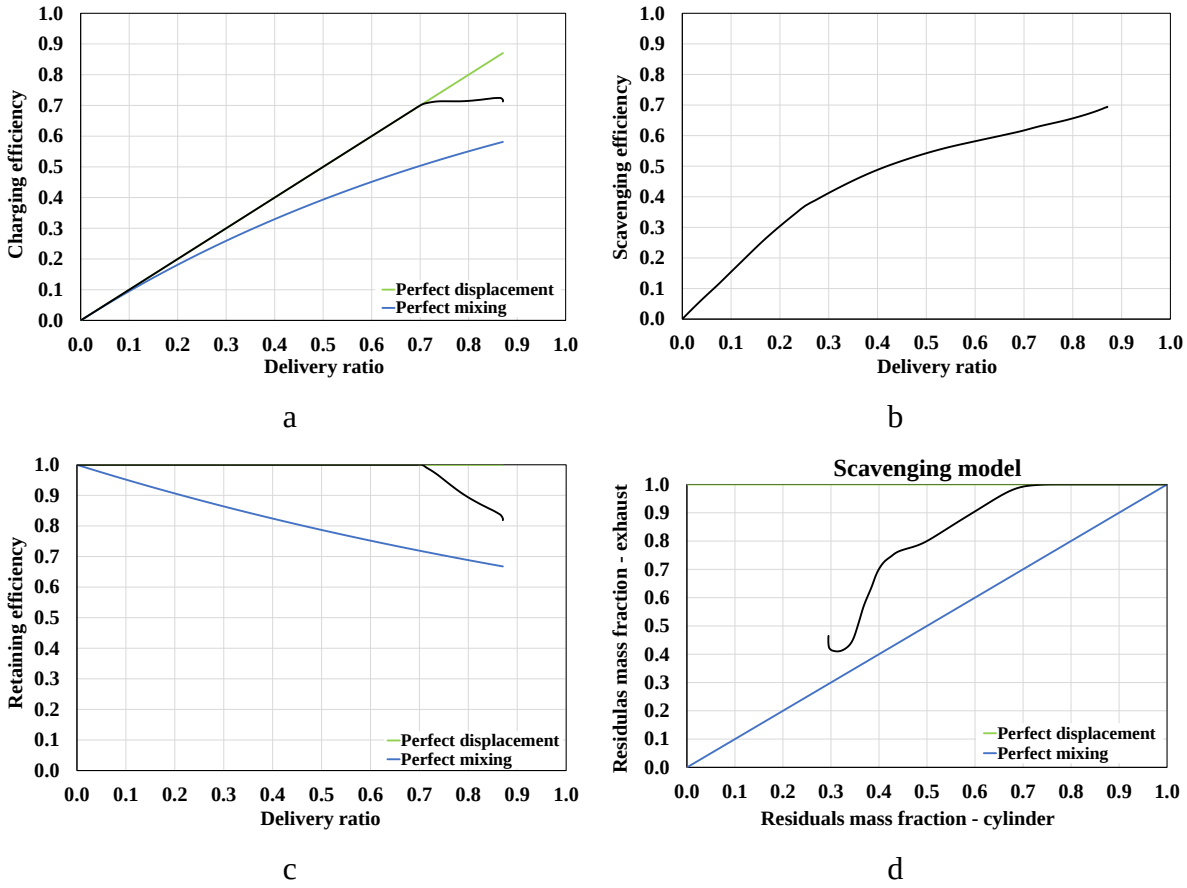

Figure 103. Charging efficiency (a), scavenging efficiency (b), retaining efficiency (c) and scavenging model (d)

A visualization of the scavenging process is reported on the symmetry plane and on the plane normal to the symmetry plane and containing the cylinder axis (see Figure 104 and Figure 105, respectively).

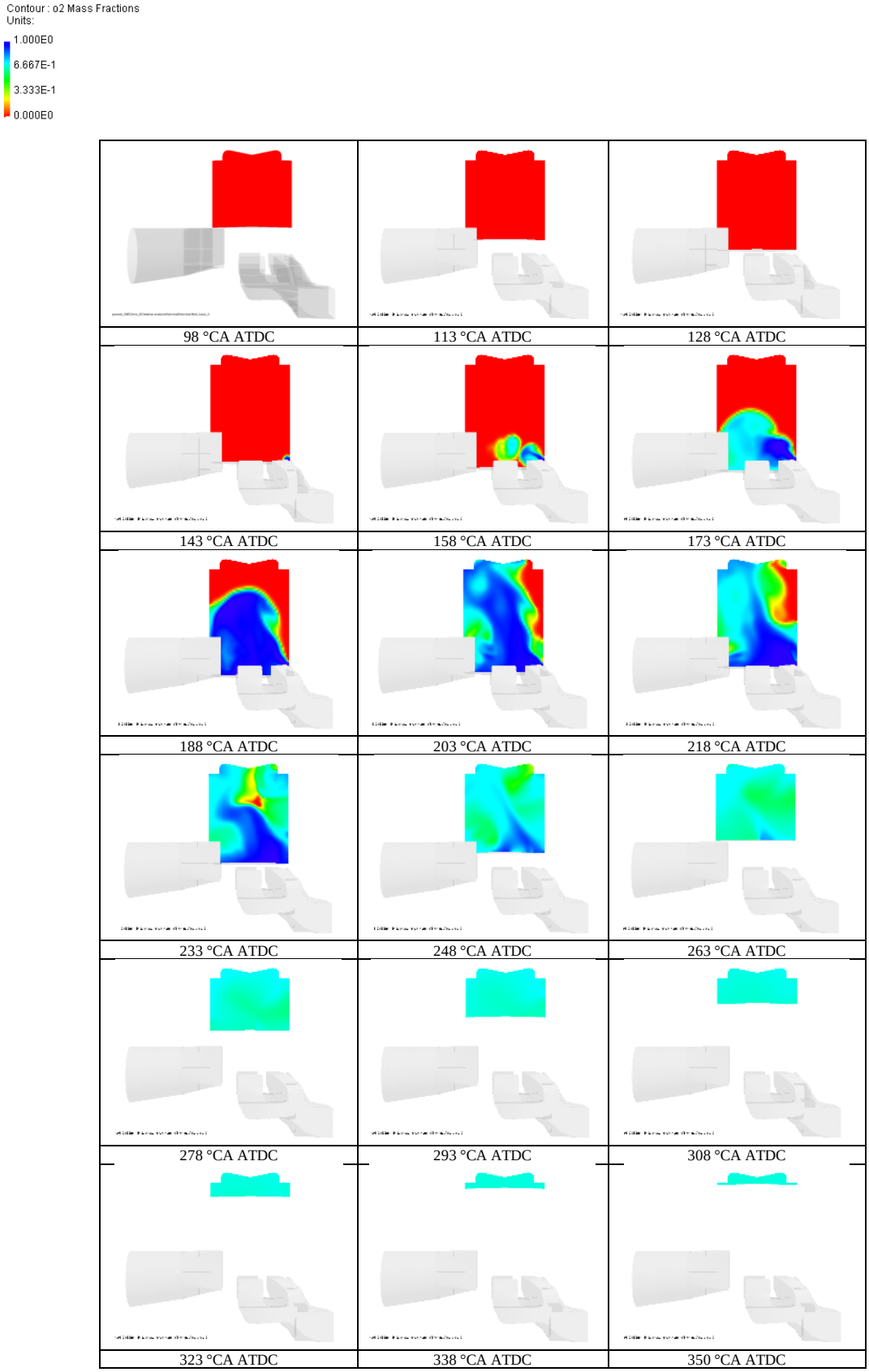

Figure 104. Contours of O_2 mass fraction on the symmetry plane at different °CA

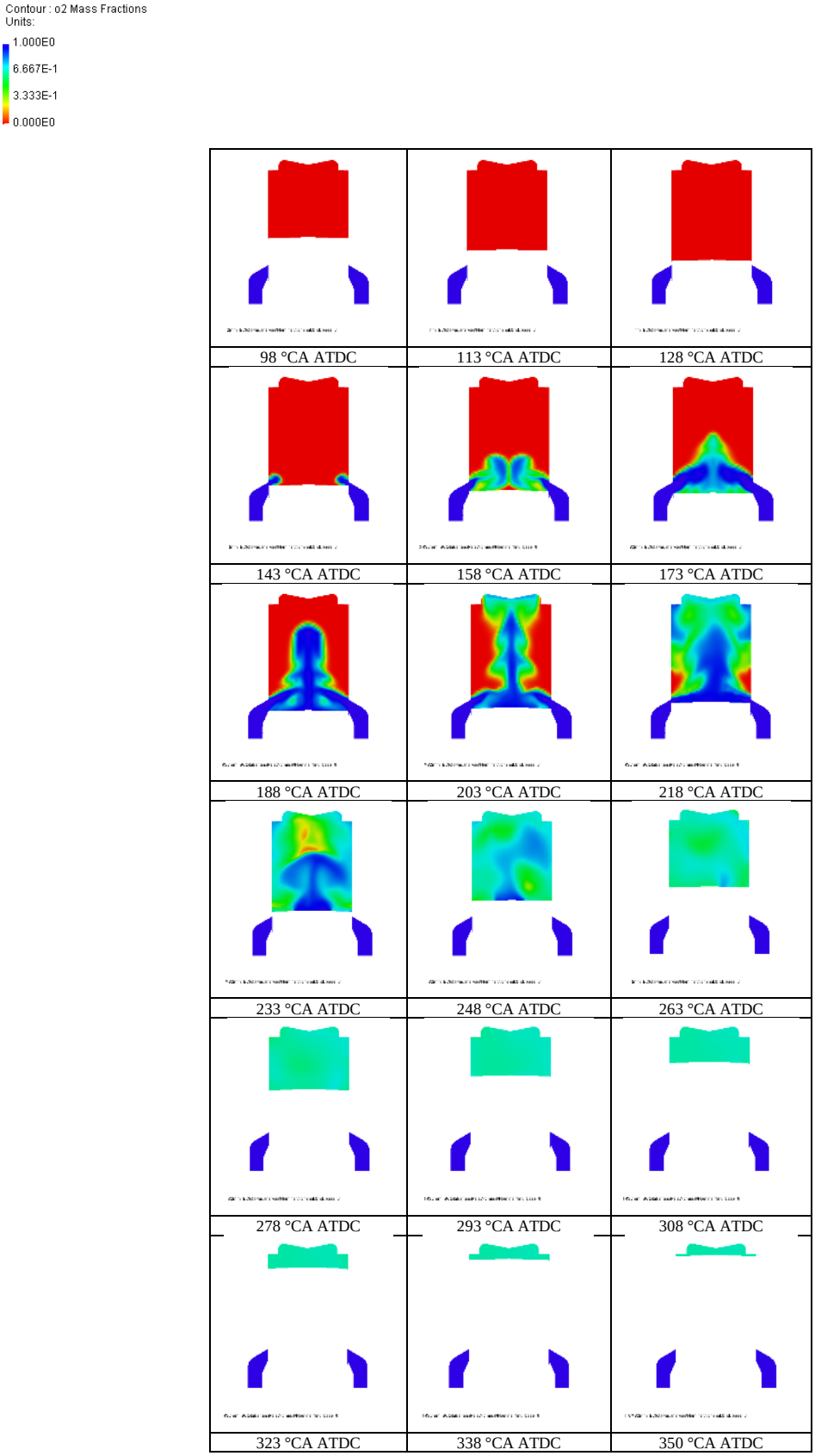

Figure 105. Contours of O_2 mass fraction on a plane normal to the symmetry plane and containing the cylinder axis at different °CA

9.5 Gasoline injection and mixture formation analysis

As previously mentioned, four different gasoline injection alternatives were explored.

In detail, each alternative adopts two standard PFI gasoline injectors. However, location and/or orientation of the injectors differ from one alternative to another, as described in the following:

A. Port fuel injection in the opposite direction of the airflow;

B. Port fuel injection in the same direction of the airflow;

C. Low Pressure Direct Injection (LPDI) - downwards: the injectors are positioned in the cylinder wall on the opposite side to the exhaust ports, downwards towards the cylinder axis;

D. Low Pressure Direct Injection (LPDI) - upwards: the injectors are positioned in the cylinder wall on the opposite side to the exhaust ports, upwards towards the cylinder axis.

As far as LPDI is concerned, it was chosen to investigate also this injection strategy in view of the outstanding results in terms of UHC emissions reduction obtained by various researchers.[147–153]

Figure 106 shows the schematic representations of the four gasoline injection alternatives described above, highlighting location and orientation of the PFI injectors by means of blue arrows, while Table 26 reports the main injection parameters.

The injection timings shown in Table 26 were defined based on the scavenging analysis reported in the previous section, and on the predictions of the 1D-CFD model of the investigated engine (see Figure 98).

In particular, considering the PFI in the opposite direction of the airflow, it was decided to start injecting gasoline immediately after 164 °CA ATDC, namely, when the in-cylinder pressure becomes lower than that one in the intake system.

If the PFI in the same direction of the airflow is considered, the injection timing was delayed compared to the previous alternative and fixed at 170 °CA ATDC, so as to exploit the lower path that the fuel follows to enter the cylinder, reducing, at the same time, the risk of fuel short-circuiting.

Finally, as far as the LPDI alternatives are considered, the injection timing was further delayed (SOI = 180 °CA ATDC), since the fuel is injected directly into the cylinder. Therefore, it is not mandatory to inject the fuel before IPC. However, in order to promote the droplets break-up and to minimise the fuel short-circuiting (especially for the LPDI - downwards), it is convenient to inject the fuel when a strong flow of fresh charge still enters the cylinder.

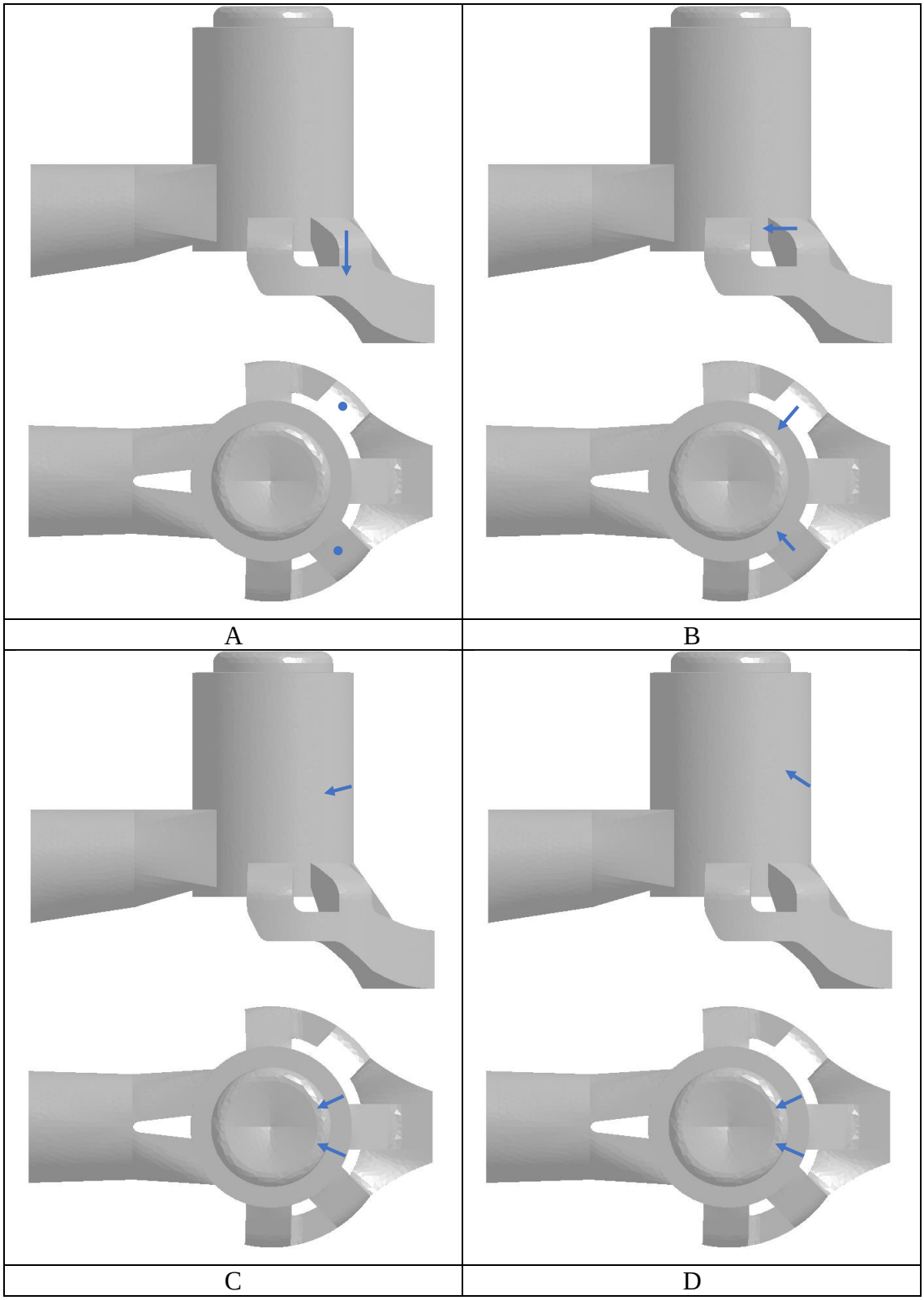

Figure 106. Schematic representations of the four investigated gasoline injection alternatives

Table 26. Main injection parameters

	A	B	C	D
N° of injectors	2			
Type of injectors	PFI			
N° of holes	12			
Holes diameter [mm]	0.18			
Fuel mass [mg]	30			
SOI [°CA]	164	170	180	180
Duration of injection [°CA]	34			
Mass flow rate [g/s]	10.59			
Rail pressure [bar]	8			

Table 27 and Figure 107 report the results of the gasoline injection simulations.

It appears that the main issues affecting PFI in the opposite direction of the airflow is that a relevant fraction (15%) of the injected gasoline adheres to the walls of the intake ducts, while 6.7% short-circuits.

PFI in the same direction of the airflow, jointly with the possibility to approach the intake port-cylinder interface, permits to avoid wall wetting on the intake ducts walls. However, the fraction of gasoline that short-circuits increases from 6.7% to 7.6% compared to the previous alternative.

LPDI, besides avoiding wall wetting on the intake ducts walls, guarantees a wider angular interval suitable for the injection compared to the PFI alternatives. Therefore, it is possible to delay SOI and, consequently, reduce the fraction of gasoline that flows directly to the exhaust during the scavenging process. Moreover, short-circuiting can be further mitigated if injectors are oriented upwards. Therefore, the most promising alternative is LPDI with upward orientation of the injectors.

Table 27. Results of gasoline injection simulations

	A	B	C	D
Film mass (mass fraction) of fuel on intake walls @ IPO	4.47 mg (15%)	0 mg (0%)	0 mg (0%)	0 mg (0%)
In-cylinder trapped fuel vapor mass (mass fraction) @ IPO	23.48 mg (78.3%)	27.71 mg (92.4%)	29.38 mg (97.9%)	29.77 mg (99.2%)
Fuel short-circuit	6.7%	7.6%	2.1%	0.8%

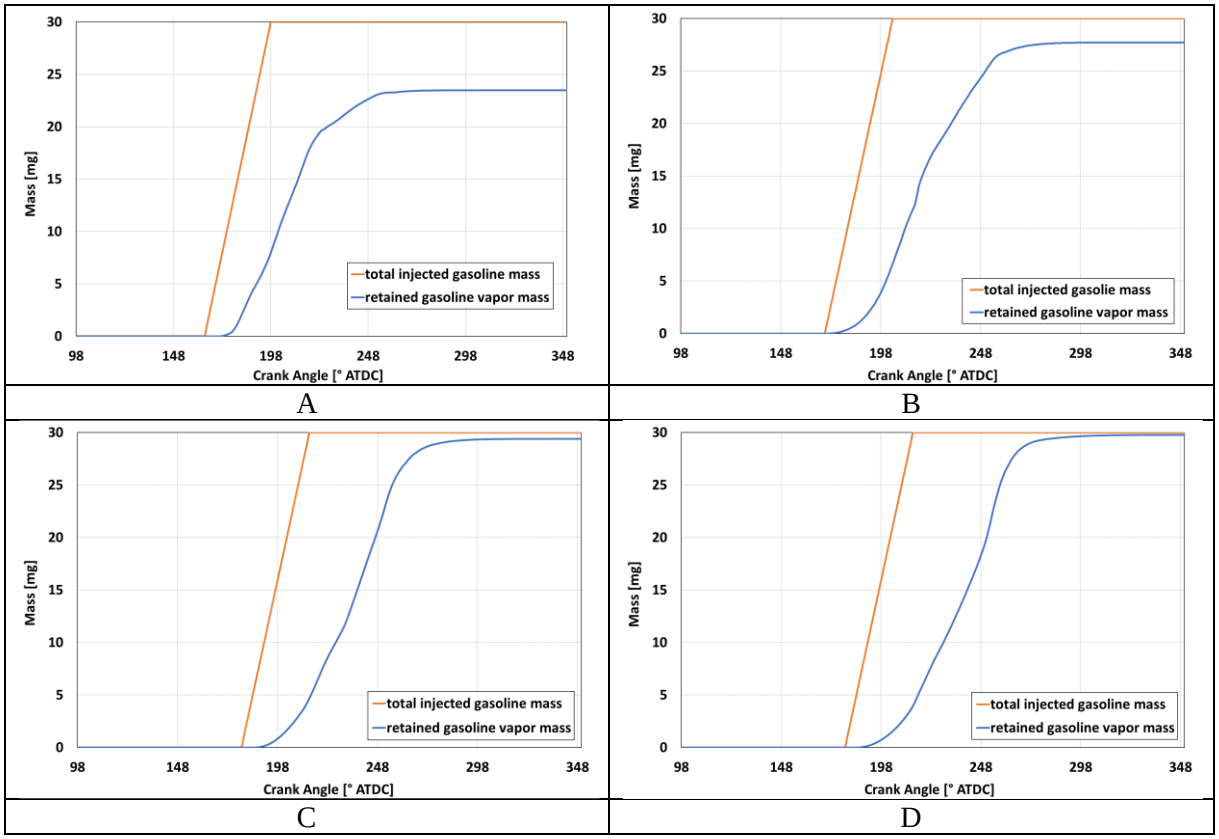

Figure 107. Comparison between total injected and retained fuel mass for the four gasoline injection solutions

Figure 108 depicts the fuel injection phasing of the LPDI upwards alternative, while Figure 109 and Figure 110 report the visualization of the gasoline-air mixture formation on the symmetry plane and on the plane normal to the symmetry plane and containing the cylinder axis.

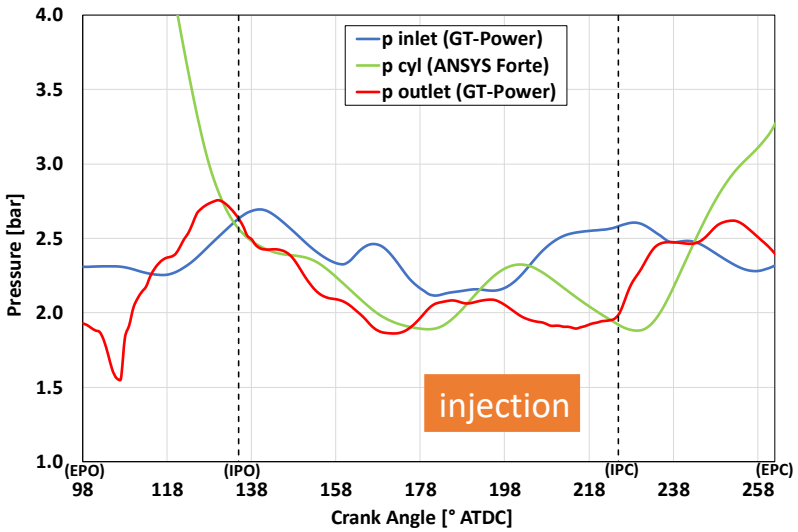

Figure 108. Gasoline injection phasing of the LPDI upwards alternative

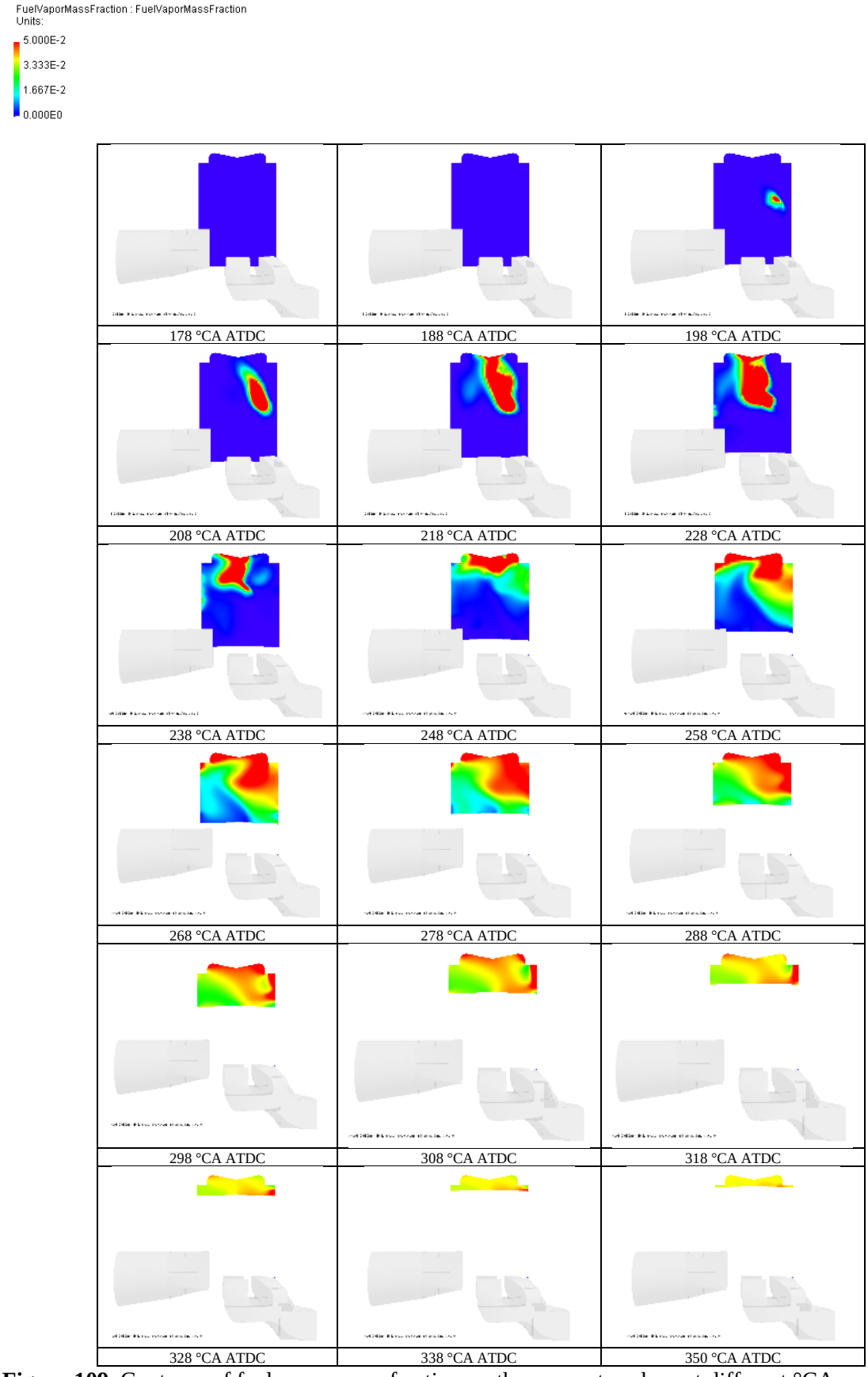

Figure 109. Contours of fuel vapor mass fraction on the symmetry plane at different °CA

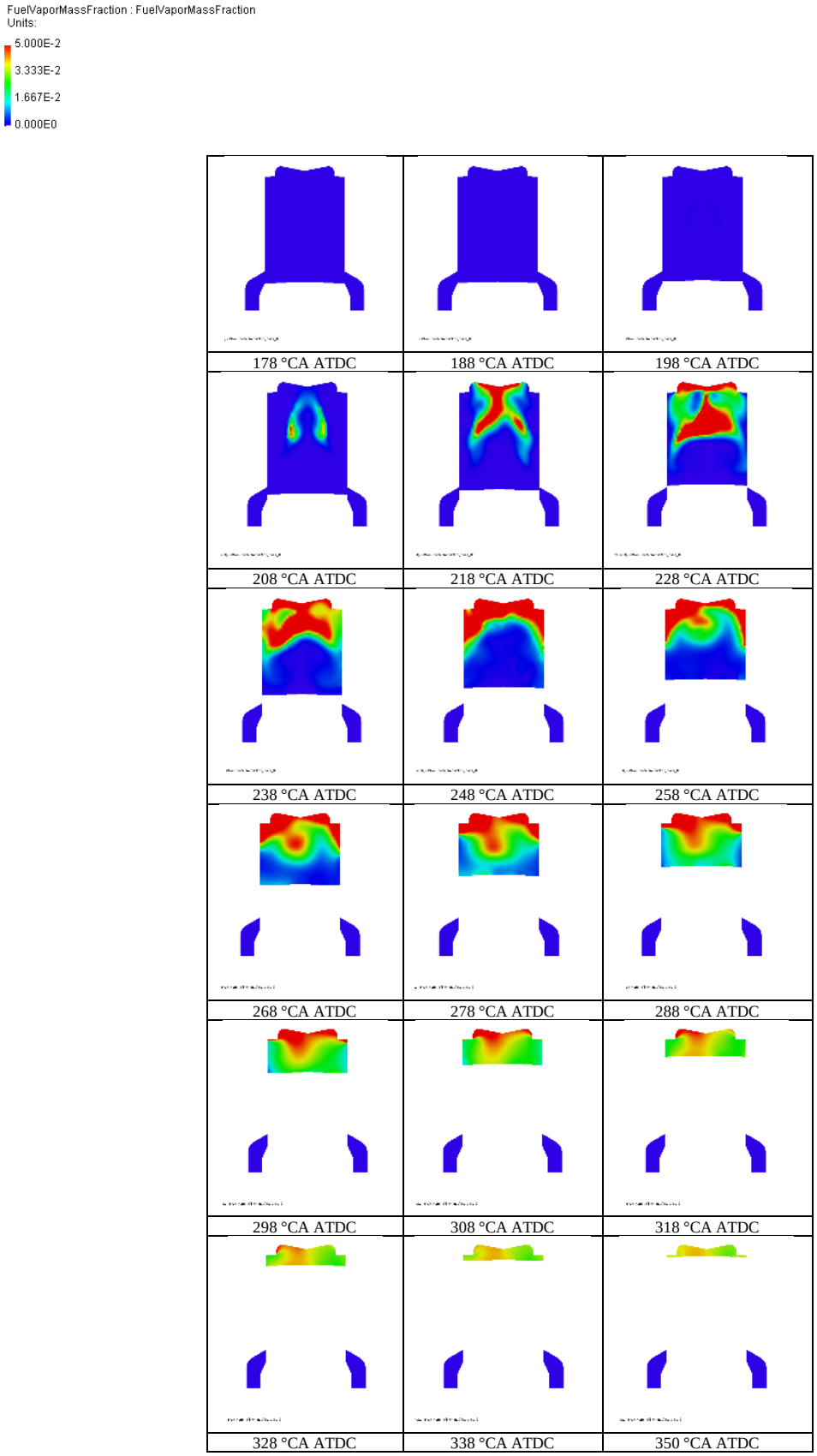

Figure 110. Contours of fuel vapor mass fraction on a plane normal to the symmetry plane and containing the cylinder axis at different °CA

9.6 Conclusions

The present numerical study was aimed at investigating the injection of a LRF (in this case gasoline) in a modern 2S HSDI Diesel engine in order to operate it in DF mode.

The first step was the characterise of the scavenging process of the selected engine in order to detect the best injection timing for each alternative. Then, four different alternatives were simulated and compared:

- Port fuel injection in the opposite direction of the airflow;
- Port fuel injection in the same direction of the airflow;
- Low Pressure Direct Injection (LPDI) - downwards: the injectors are positioned in the cylinder wall on the opposite side to the exhaust ports, downwards towards the cylinder axis;
- Low Pressure Direct Injection (LPDI) - upwards: the injectors are positioned in the cylinder wall on the opposite side to the exhaust ports, upwards towards the cylinder axis.

The best alternative was found to be LPDI – upwards, since it is able to avoid the fuel impingement on the intake ducts walls and minimise the short-circuiting to the exhaust system of gasoline (0.8% of the total amount of injected gasoline).

10 Development of a hybrid power-unit for Formula SAE race car: vehicle lap simulation

10.1 Introduction and aim

As discussed in the introduction of this thesis (see Section 1), among the various strategies able to reduce the environmental impact of the transport sector, hybridization is one of the most valuable.

In the activity reported in this section, hybridization is applied to a Formula SAE race car, in order to improve its performance and the powertrain efficiency, so as to reduce fuel consumption and CO_2 emissions.

In particular, the work described in the following consisted in the development of a 0D (lumped) model for lap simulation, with the aim to compare a real conventional (combustion) Formula SAE race car with a virtual hybrid electric Formula SAE vehicle in terms performance (lap time, fuel consumption, ecc.) and CO_2 emissions. The tool used to build the 0D model is MATLAB-Simulink.

The present study has been reported in a paper entitled "Development of a Hybrid Power Unit for Formula SAE Application - ICE CFD-1D Optimization and Vehicle Lap Simulation" and presented at the ICE2019 – 14th International Conference on Engines & Vehicles (SAE Naples).[154]

10.2 Description of the investigated powertrain

The Conventional (combustion) Vehicle (CV) is equipped with a 4-cylinder in-line, 600 cm^3, motorcycle engine, manufactured by Suzuki (GSX-R 600) and properly modified as required by the SAE rules.[155] The main modification is the installation of a 20 mm restrictor, downstream of a single throttle body.

The Hybrid Electric Vehicle (HEV) features the Ducati 959 Panigale engine (2-cylinder, V90, 955 cc, peak power 150 HP at 10500 rpm, peak torque 102 Nm at 9000 rpm), which was modified in order to house a Promo EM in place of the head of the vertical cylinder. The EM is connected to the crankshaft of the ICE by means of the chain of the valvetrain, so that to create a parallel hybrid powertrain, P1 type.

Figure 111 shows both the baseline Ducati 959 Panigale engine and the modified (hybrid) version.

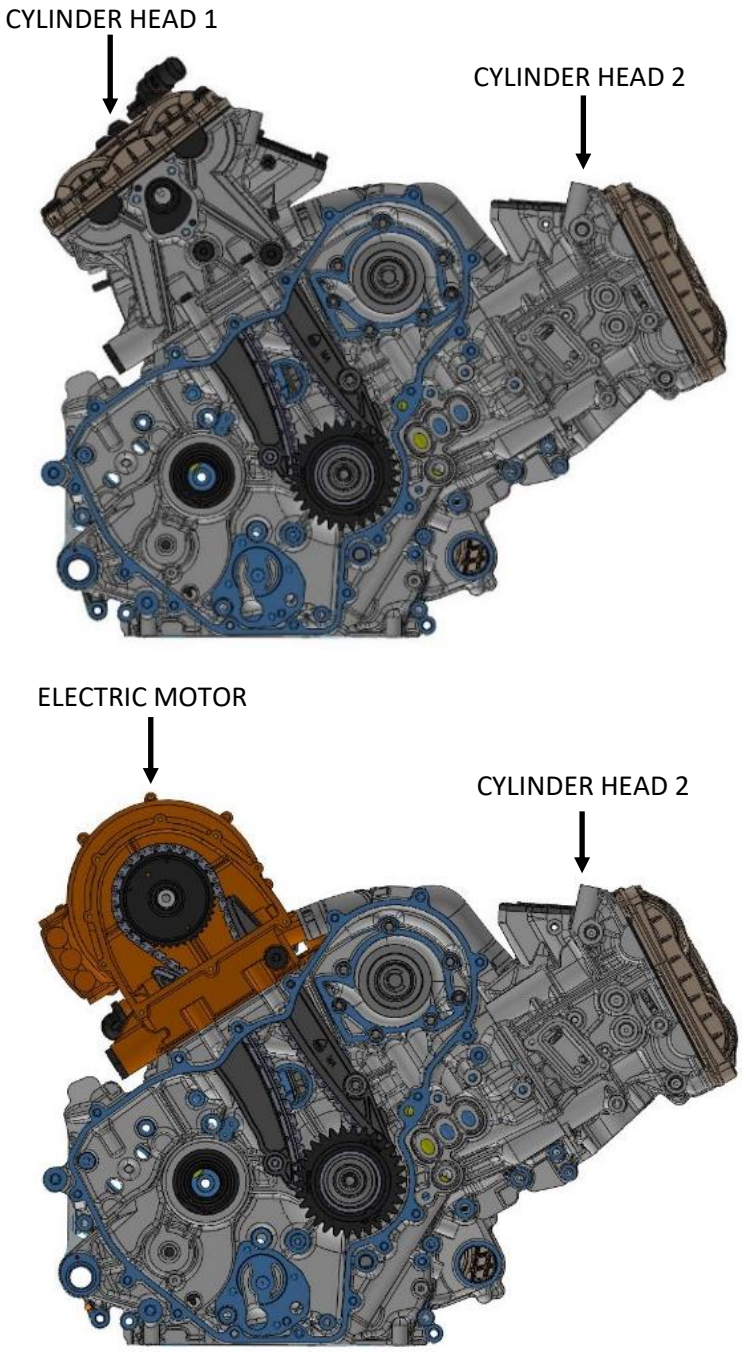

Figure 111. Comparison between the baseline Ducati 959 Panigale engine and the modified (hybrid) version

Besides the above-mentioned modification, brand new intake and exhaust systems are required, with the former that must include a 20 mm restrictor, installed downstream of the throttle body, while the latter must be designed in order to comply with the noise limits imposed by the SAE rules.[155]

Therefore, an optimization of the modified engine was carried out by means of a 1D-CFD (GT-Power) model validated against the experimental measurements taken on the baseline engine. Figure 112 shows the CAD model of the optimised hybrid power-unit, while Wide Open Throttle (WOT) torque and power of as a function of engine revolution speed and the contour map of BSFC of the optimised engine predicted by the experimentally validated GT-Power model are reported in Figure 113 and Figure 114, respectively.

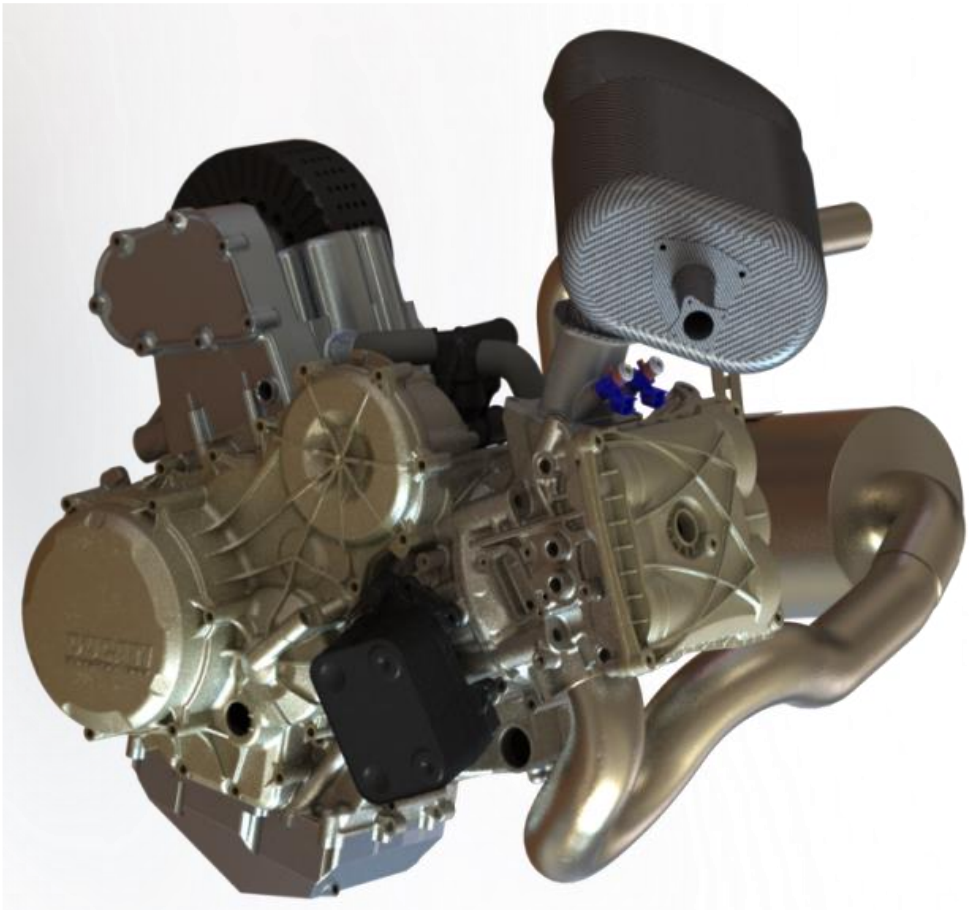

Figure 112. CAD model of the optimised hybrid power-unit

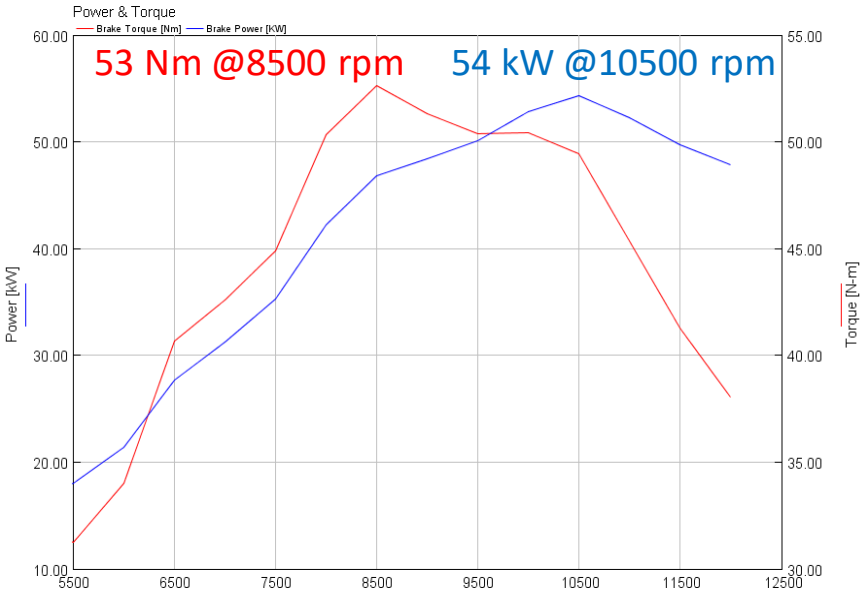

Figure 113. WOT torque and power as a function of engine revolution speed of the optimized ICE predicted by the validated 1D-CFD model

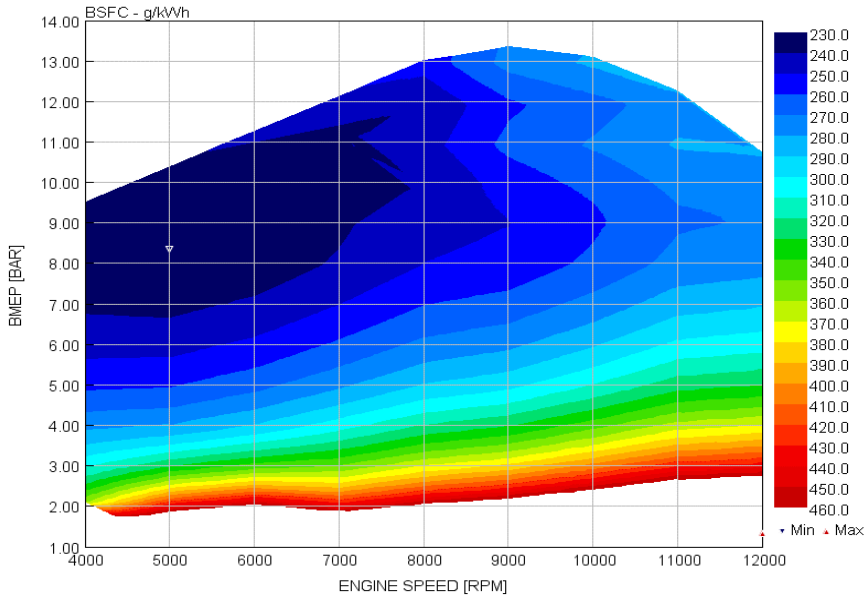

Figure 114. Contours of BSFC of the optimized ICE predicted by the validated 1D-CFD model

Figure 115 depicts the continuous and peak power and torque curves of the selected Promo EM, while Table 28 lists its main features.

Figure 116 compares full load brake torque and power available at the engine crankshaft for the CV and HEV.

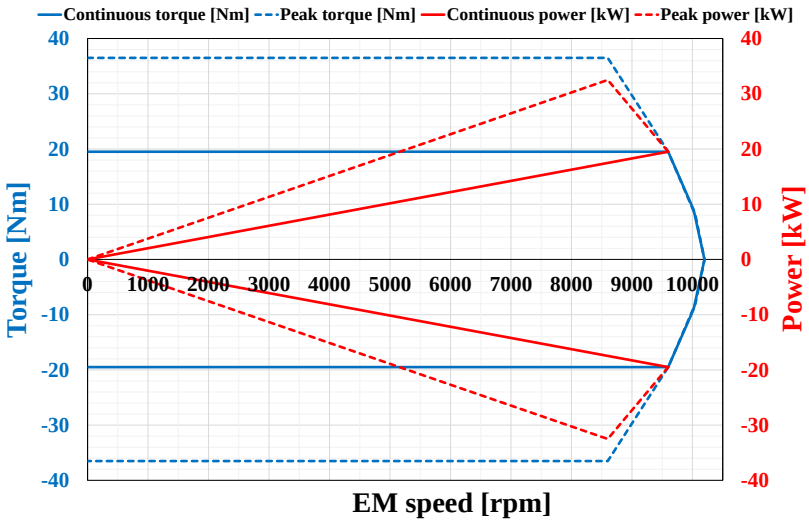

Figure 115. Continuous and peak power and torque curves of the Promo EM

Table 28. Main features of the selected Promo EM

Supply Voltage	96	VAC
Continuous torque	19.5	Nm
Speed @ continuous	0-9600	rpm
Continuous power	19.5	kW
Speed @ continuous	9600	rpm
Peak torque	36.5	Nm
Speed @ peak torque	0-8600	rpm
Peak power	32.5	kW
Speed @ peak power	8600	rpm

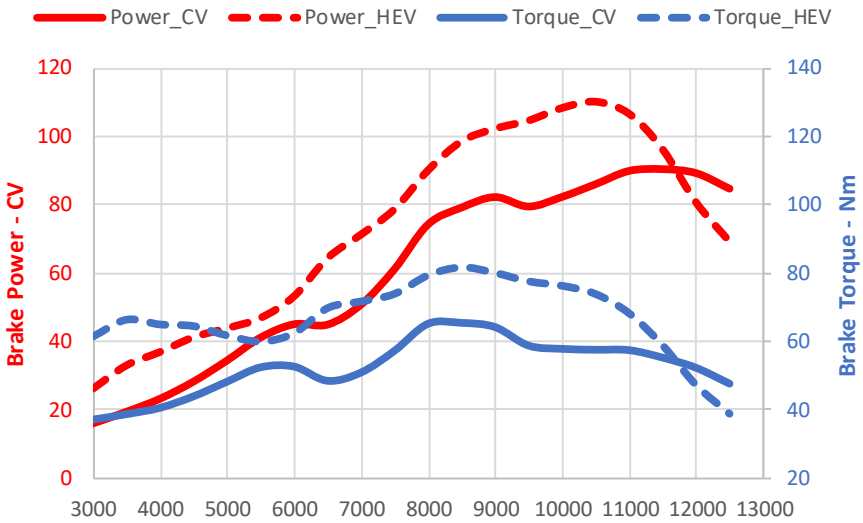

Figure 116. Brake torque and power as a function of engine speed available at the engine crankshaft for the CV and HEV

The total weight of EM and inverter is lower than 12 kg, that is close to the weight of the head of the vertical cylinder, its intake and exhaust pipes, and the alternator, which are removed. Hence, the only additional weight of the hybrid power-unit is due to the battery pack, whose weight depends on the required capacity, which is the minimum one that guarantees the completion of the Endurance event (22 km), while exchanging the maximum electric power allowed by the SAE rules (30 kW),[155] and its energy density. A lithium-ion battery with an energy density of about 750 kJ/kg was chosen.

10.3 Lap time simulation: methodology and 0D model description

The lap time simulation of the HEV Formula SAE race car is based on telemetry data of the CV during the Endurance event of the Formula Student UK. Therefore, it is possible to reproduce the race under the same initial and boundary conditions of the CV, highlighting the differences among the two powertrains in terms of lap time, fuel consumption and CO_2 emissions. Moreover, based on the net electric energy consumption, it is possible to determine the capacity, and hence the exact weight, of the battery pack of the HEV.

In detail, from the telemetry data of CV, the velocity profile of only one lap is taken as a reference, supposing that it is repeated 22 times during the race.

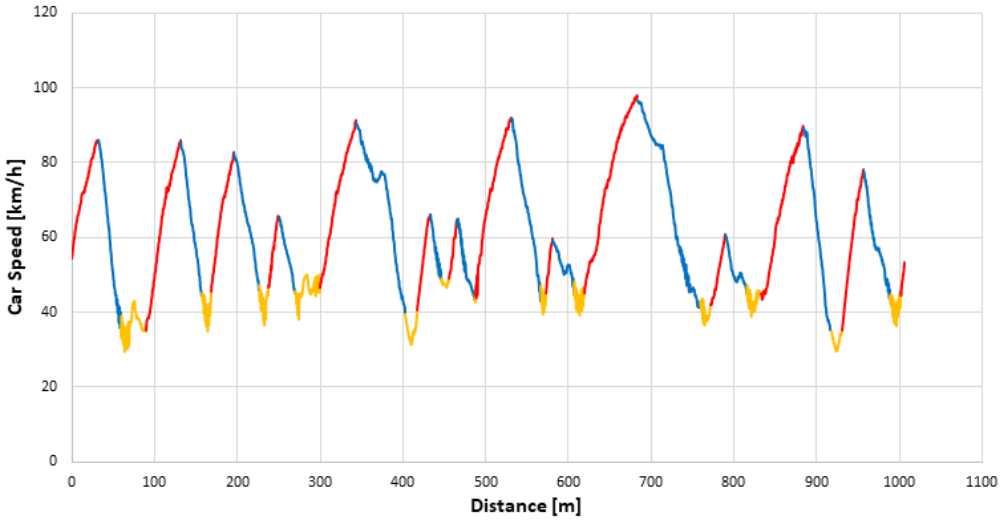

Figure 117. Combustion vehicle speed during one lap of an Endurance event

As it can be noticed from Figure 117, the reference lap can be split into:

- acceleration tracts (highlighted in red);

- braking tracts (highlighted in blue);
- low speed tracts (highlighted in yellow).

Starting from the reference velocity profile of the CV, the target velocity profile as a function of distance, provided to the 0D model as an input, is obtained. In particular, in the acceleration sectors, the target velocity was set very high, so as to force the ICE and the EM to operate at maximum load, minimizing the lap time. During deceleration and low-speed sectors, it is supposed that the vehicle speed does not depend on the power-unit and is imposed equal to the one of the CV (see Figure 118).

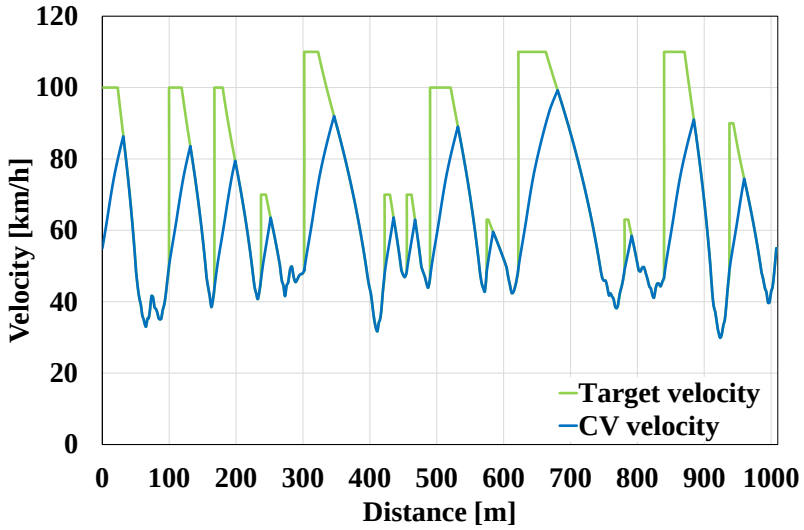

Figure 118. Comparison between target and CV speed

As mentioned in the introduction of this section activity (Section 10.1), the lap simulation of HEV and EV was carried out by means of two MATLAB-Simulink models.

The HEV model is characterised by the schematic structure shown in Figure 119. As it can be seen, the target velocity profile as a function of distance is provided to the model as an input. The cruise control, that simulates the driver, is composed by two PID controllers, the former for the accelerator pedal and the later for the brake pedal. It compares the target vehicle velocity with the effective one, and generates a correction based on their difference. Such correction, corresponding to an action on the accelerator or brake pedal, enters the powertrain block.

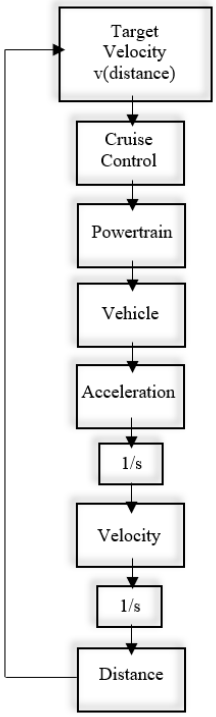

Figure 119. Schematic representation of the MATLAB-Simulink models used for the lap simulation of the HEV and EV Formula SAE race cars

The powertrain block is composed by five sub-models:

- Gearbox: based on the effective vehicle speed and the shifting strategy, it evaluates the right gear and, as a consequence, the engine rotational speed;
- ICE: based on the engine rotational speed and the accelerator pedal, it defines the torque provided by the engine and its instantaneous fuel consumption. Figure 120 reports the engine operating points on the efficiency contour map. As it can be seen, the engine revolution speed never falls below 4000 rpm. Such threshold was imposed in order to get a fast transient response. Moreover, the ICE block is able to estimate the negative torque, due to engine friction and pumping losses, applied to the transmissions in motoring conditions. These losses are evaluated by means of a correlation calculated by a specific GT-Power simulation.
- Electric Motor-Generator: based on the EM rotational speed and the accelerator pedal, it defines the torque delivered by the EM. The regenerative braking torque provided by the EM is evaluated based on the standard vehicle dynamics analysis, with two main hypotheses:
  - the braking torque is equally split between the front and the rear wheels;

- the rear brakes provide a torque only if the electric generator has already reached its upper limit (36.5 Nm or 30 kW).

This leads to the following equation:

$$T_{EM} + T_{rb} + T_{fpl} = \frac{R_w}{2}\left[\left(m + \frac{4J}{{R_w}^2}\right)a - F_{ad} - F_{rr}\right] \quad (43)$$

where:

T_{EM} is the regenerative braking torque applied by the EM to the rear wheels; T_{rb} is the torque provided by the rear brakes to the rear wheels; T_{fpl} is the torque corresponding to the friction and pumping losses of the ICE and applied to the rear wheels; R_w is the wheel radius; m is the vehicle mass; J is the transmission inertia calculated at the wheels; a is the vehicle acceleration; F_{ad} is the aerodynamic resistance; and F_{rr} is the rolling resistance.

Figure 121 reports the operating points of the EM on the efficiency contour map. Due to the direct coupling between ICE and EM, the lower threshold of the EM rotational speed corresponds to 3000 rpm.

- Battery Pack + Inverter: the inverter is modelled by means of its efficiency, while the electric power dissipated into the battery pack is estimated according to the following equations:

$$P_{loss} = {R_{int}}^2 i \quad (44)$$

$$i = \frac{V_{oc} - \sqrt{{V_{oc}}^2 - 4R_{int}P_e}}{2R_{int}} \quad (45)$$

where:

P_{loss} is the electric power dissipated due to the battery internal resistance, R_{int}; i is the battery current; V_{oc} is the open circuit voltage of the battery; P_e is the electric power exchanged by the battery.

Furthermore, the battery pack + inverter sub-model permits to calculate the energy consumption and energy recovery, as well as the State of Charge (SoC) of the battery itself. Figure 122 shows the SoC trend during the lap simulation.

- Brakes: this block determines the braking torque based on the brake pedal position defined by the corresponding PID controller.

The Powertrain block provides the (traction or braking) torque, required by the vehicle to follow the target velocity, to the Vehicle block. Then, by means of the vehicle dynamics analysis, the acceleration of the vehicle can be calculated, and hence the effective velocity and the actual distance.

In the Appendix, the structure of the MATLAB-Simulink model of the HEV is reported.

As far as the power split strategy between ICE and EM is concerned, it is defined as follow. During acceleration, both the ICE and the EM work in full load conditions. During braking, the EM works as a generator, applying a braking torque. It is worth remembering that the SAE rules permit the battery pack to exchange with the EM a maximum power equal to 30 kW.

In the low-speed tracts, four strategies are possible:

1. ICE operates at a higher load than that required, with the excess of energy which is stored in the battery;
2. ICE provides exactly the power required by the driver;
3. ICE provides a fraction of the required power, with the EM that provides the remaining;
4. All the required power is provided by the EM.

The first strategy could be applied when the battery SoC is lower than a certain limit and in order to reduce the size of the battery pack necessary to complete the race. However, burning gasoline to recharge the battery does not permit to minimize overall CO_2 emissions, which are calculated according to the SAE rules:

$$CO_2\ [kg] = 2.31V_f + 0.65E \tag{46}$$

where:

V_f is the volume of consumed fuel, in liters; E is the net electric energy consumed by the battery, in kWh.

The second strategy permits to reduce the size of the battery since no electric energy is used in the low-speed tracts. On the other hand, only gasoline in used to produce energy, which induces a strong penalization in terms of CO_2 emissions.

The third strategy permits to limit fuel consumption, and hence CO_2 emissions, at the cost of a bigger battery pack.

Finally, the fourth strategy does not appear as a practical solution, since the engine cannot be decoupled from the EM, implying a relevant electrical energy consumption, and, as a consequence, a cumbersome battery pack.

Based on the considerations discussed above, the third strategy was chosen.

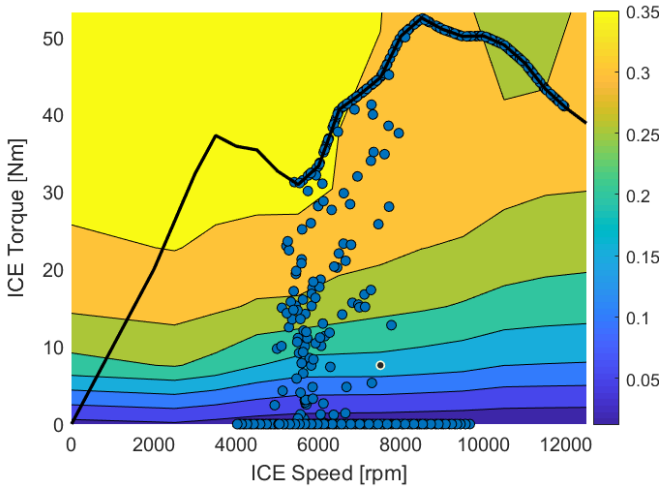

Figure 120. ICE operating conditions in terms of ICE speed, torque and BTE

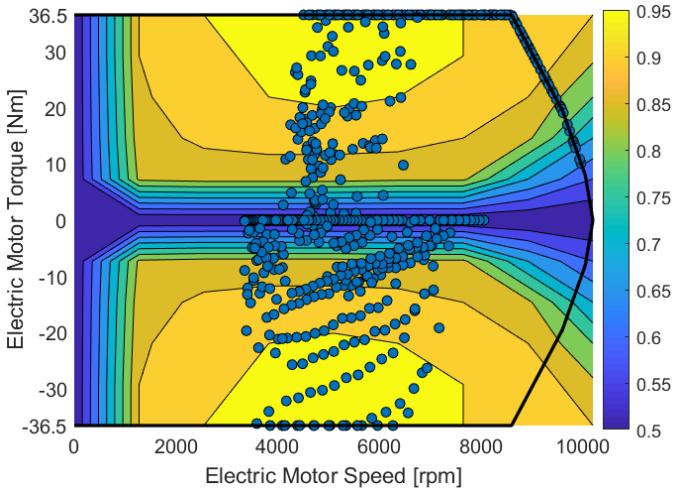

Figure 121. EM operating conditions in terms of EM speed, torque and efficiency

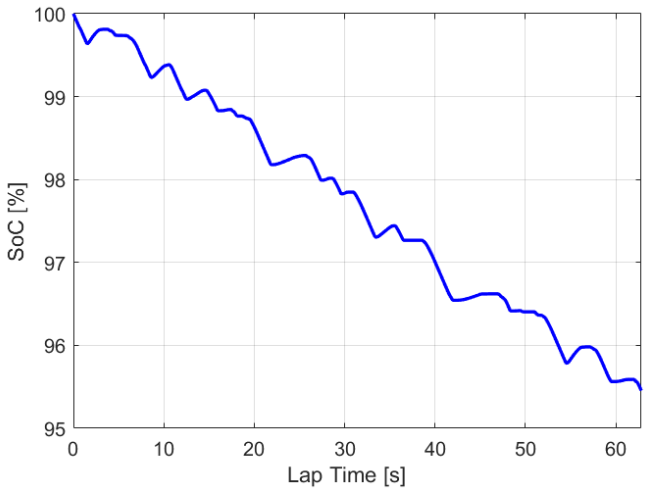

Figure 122. SoC trend during the lap simulation

10.4 Results and discussions

Table 29 summarises the main results of the lap simulation of the HEV, and compares them with the telemetry data of the CV.

Thanks to the higher power-to-mass ratio (+15.3 %) of the HEV with respect to CV, the former vehicle is able to get a lower lap time (-1.48 s).

Moreover, the HEV is characterised by slightly lower CO_2 emissions (-0.082 kg) compared to the CV. However, if the specific CO_2 emissions (mass of CO_2 emissions divided by the useful energy provided to the vehicle) are considered, the advantage of the HEV increases (specific CO_2 emissions reduced by 30 %). This is due to the fact that the useful energy provided by the hybrid powertrain to the vehicle is higher than the one provided by the conventional powertrain.

Furthermore, if the CV useful energy is corrected, so as to consider the lower weight (300 versus 317 kg), the final result is that specific CO_2 emissions are reduced by 26.2% with HEV.

Finally, thanks to the lap simulation it was possible to calculate the minimum battery pack capacity of the HEV that guarantees the completion of the Endurance event, i.e., 3.57 kWh.

Table 29. Summary of the lap simulation results for HEV

	CV	HEV
Reference car + driver mass [kg]	300	300
Additional car mass [kg]	0	17
Maximum installed power [kW]	66.5	81
Maximum power / total mass [kW/kg]	0.222	0.256
Power / mass increase from CV [%]	-	15.3
Lap time [s]	64.52	63.04
Lap time gap from CV [s]	-	-1.48
Electric energy consumption, 22 laps [kWh]	0	3.57
Fuel consumption, 22 lap [l]	3.329	2.289
CO_2 emissions, 22 laps [kg]	7.690	7.608
Useful energy provided to the car, 22 laps [kWh]	5.805	8.201
Specific CO_2 emissions [kg/kWh]	1.325	0.928
Mass corrected specific CO_2 emissions [kg/kWh]	1.258	0.928
Specific CO_2 emissions reduction from CV [%]	-	26.3

10.5 Conclusions

In order to compare a conventional (combustion) Formula SAE race car with a virtual hybrid electric Formula SAE race car, a MATLAB-Simulink model of the latter vehicle was built. Such model was used to simulate a lap, evaluating fuel consumption, electrical energy consumption, electrical energy recovered and CO_2 emissions.

The hybrid power-unit, including the electric motor and the inverter, has about the same weight and size of the internal combustion engine of the combustion vehicle. The only additional mass is due to the battery pack, whose size depends on the required capacity to complete the Endurance event, besides its energy density.

The hybrid power-unit is characterised by a higher power/mass ratio with respect to the combustion vehicle (from 0.22 to 0.26 kW/kg). This enhancement permits to reduce the lap time by 1.48 s compared to the conventional vehicle.

As far as specific CO_2 emissions are reduced, the HEV guarantees a reduction by 26.2 %.

Finally, the minimum battery capacity required by the HEV to complete the race is 3.57 kWh.

Conclusions

In this thesis, an experimental and numerical investigation on Dual Fuel (DF) combustion concept, using different low reactivity fuels (natural gas (NG), biogas, hydrogen enriched natural gas), is presented. The goal of this work was to characterise DF combustion, highlighting pros and cons and then proposing practical solutions to mitigate its main drawbacks.

The first step was the experimental analysis of DF NG-diesel combustion, applied to a light-duty Diesel engine. Four operating points were selected in order to cover the range between low and medium-high loads (BMEP = 2, 4, 8 and 12 bar, corresponding to 44, 88, 177 and 265 Nm), at 3000 rpm. The results show that the higher is the substitution rate of diesel with NG, the lower is combustion efficiency and Brake Thermal Efficiency (BTE), while CO and UHC emissions increase by one order of magnitude. Conversely, CO_2, NO_x and PM emissions are always lower than in ND operation. However, the worsening of CO, UHC and BTE is generally mitigated as the load increases. Moreover, thanks to the optimization of the diesel injection strategy and the boost pressure, CO and UHC emissions can be strongly reduced (but still higher than in ND operation) at the expense of higher NO_x emissions (comparable to those ones measured in ND operation), while BTE can be improved, even compared to ND operation at medium-high loads (i.e., 3000 rpm – 177 Nm and 265 Nm). Conversely, at low loads, the optimization is not able to fully recover the drop of BTE due to the overly lean NG-air premixed charge. As a result, at low loads, it is convenient to switch back to Conventional Diesel Combustion (CDC).

Based on the experimental data, a first 3D-CFD model of the investigated engine was built by means of a customized version of the KIVA-3V code. The goal of this activity was to optimise the diesel injection strategy of the DF case with a substitution rate of diesel with NG equal to 60% (in terms of energy with respect to the ND operation) at 3000 rpm – 265 Nm. It was found that the number of diesel injections per cycle has negligible effects on gross Indicated Mean Effective Pressure (IMEP*), CO_2 and NO_x emissions, while CO and soot emissions show minimum values when a triple diesel injection strategy is adopted (the one used during the experimental activity). As far as the Start Of Injection (SOI) is concerned, a performance improvement can be obtained, at the expense of higher NO_x emissions, if the diesel SOI is advanced.

In order to extend the operating range of DF NG-diesel combustion to low loads, a numerical study was performed using the commercial code ANSYS Forte. In particular, the addition of hydrogen (H_2) to the NG-air premixed charge was investigated considering the DF case with the highest substitution rate of diesel with NG (80%) at 3000 rpm – 44 Nm, where the highest drop of BTE was experimentally observed. Various H_2-NG blends were taken into account, with the H_2 mole fraction ranging from 0% to 30%, by steps of 5%. As the H_2 content in the H_2-NG mixture increases from 0 vol% to 30 vol%, CO and UHC specific emissions drop by 54.1% and 70.4%, respectively, thanks to the increase of the OH radical pool and the lower carbon content of the premixed charge. CO_2 specific emissions decrease by 30.7% and the Gross Indicated Thermal Efficiency (GITE*) increases up to 37.8%. Finally, despite the peak in-cylinder pressure passes from 72.8 bar to 80.7 bar and Peak Pressure Rise Rate (PPRR) increases up to 2.6 bar/°, NO_x specific emissions decrease by 15.9%.

However, even with the H_2-NG blend characterized by the highest H_2 content (30 vol%), it was not possible to achieve the values of CO and UHC specific emissions, combustion efficiency and GITE* of the CDC. Therefore, the optimisation of the diesel injection strategy in terms of number of injections per cycle, SOI of each injection and diesel mass distribution among the injections, besides a sensitivity analysis to the swirl ratio, were performed. The best compromise between performance and emissions improvements could be obtained with a double diesel injection strategy characterised by SOI1 = -35 °CA AFTDC, SOI2 = -20 °CA AFTDC and a diesel mass fraction of injection 1 equal to 0.7. As far as the swirl ratio (SR) is concerned, SR = 1.4 was selected. In detail, CO and UHC specific emissions were reduced by about 85%, while combustion efficiency and GITE* could be enhanced by about 45.7% and 61.0%, respectively, with respect to the reference DF NG-diesel case. At the same time, CO_2 specific emissions were decreased by about 42% and NO_x specific emissions decreased by about 33.8% compared to CDC. It should be noted that combustion efficiency and GITE* of the optimised DF 30vol%/NG-diesel case are still slightly lower than in CDC, despite the strong improvement mentioned above.

The attention was then focused on a different low reactivity fuel, namely, biogas. Hence, the interchangeability between NG and biogas was analysed, since the two gases have a different Wobbe index and the biogas composition is strongly dependent on the biomass used for its production. A new KIVA-3V model was built in order to investigate DF biogas-diesel combustion, considering various biogases, at 3000 rpm – 177 Nm, taking the DF case with the

highest substitution rate of diesel with NG (80%) as a reference. The results showed that DF combustion is weakly affected by the substitution of NG with biogas, and by the CO_2 content in the biogas. Moreover, a slight modification of the diesel SOI is sufficient to restore the performance of the reference DF NG-diesel case. In particular, the maximum reduction of IMEP* (-7%) was observed passing from NG to the biogas with 50 vol% CO_2. However, by simply advancing the diesel SOI by 4 °CA, the performance of the reference DF NG-diesel case could be restored.

After having extensively investigated DF combustion on a 4-Stroke Diesel engine, the application of such combustion concept to a modern 2-Stroke high-speed direct-injection Diesel engine was taken into account. In particular, a preliminary study was carried out, by means of ANSYS Forte, with the aim to identify the solution able to inject the low reactivity fuel (gasoline was chosen as a test fuel) minimising the fuel wall film on the intake ducts walls and the fuel short-circuiting during the scavenging process. It was found that the best solution is the Low Pressure Direct Injection (LPDI) with the injectors oriented towards the TDC.

Finally, the last section of this thesis (Section 10) is dedicated to the development of a 0D MATLAB-Simulink model able to simulate a lap of a virtual hybrid electric Formula SAE race car. The results of the simulation were compared with the telemetry data of a real combustion Formula SAE vehicle referred to the same Endurance event (Formula Student UK). The comparison showed that the hybrid vehicle guarantees a lower lap time (-1.48 s), besides lower CO_2 emissions (-26.2 %). Furthermore, the simulation results permitted to estimate the net electric energy consumption of the hybrid vehicle, and hence the minimum battery capacity required by it to complete the race: 3.57 kWh.

In conclusion, DF NG-diesel combustion is a very effective strategy to reduce CO_2, NO_x and soot emissions, besides improving BTE, at medium and high loads compared to CDC. Moreover, DF operation appears to be a flexible combustion concept, since it is weakly affected by the substitution of NG with a low reactivity gaseous fuel with a different Wobbe index, such as biogas. Therefore, DF combustion offers a superior fuel flexibility that other combustion concepts.

In order to manage the higher CO and UHC emissions that characterises DF NG-diesel combustion with respect to ND operation, a specific oxidation catalyst is required, since the majority of the UHC emissions are composed by unburnt methane. However, a possible strategy

able to reduce such pollutants could be the addition of H_2 to the premixed charge. Such strategy needs to be investigated in order to assess the trade-off between CO and UHC emissions improvement and the increase of peak in-cylinder pressure, PPRR and NO_x emissions. However, it is worth remembering that the use of H_2-NG blends was successfully applied at low load. In fact, it permitted to obtain lower CO_2, NO_x and soot emissions and comparable CO emissions with respect to ND operation, with a PPRR lower than 5 bar/°CA, confirming the fact that H_2 is a very effective solution to achieve the carbon neutrality of the internal combustion engine.

A further future development is certainly represented by the application of DF combustion to the 2-Stroke cycle engine. The main advantage offered by the latter is the double number of power strokes per unit time compared to 4-Stroke engines, permitting to solve one of the main issues that affect DF pilot-ignited/RCCI engines, namely, the low power density. In this thesis, a preliminary study on a 2-Stroke loop scavenged engine, aimed at defining the best injection strategy for the low reactivity fuel, was carried out. However, a very promising alternative could be the 2-Stroke opposed piston engine, thanks to the efficient scavenging process that characterises the latter. Therefore, further investigations, both numerical and experimental, are required in order to successfully apply the DF combustion concept to 2-Stroke engines.

References

1. What is a COP? *UN Climate Change Conference (COP26) at the SEC – Glasgow 2021*, https://ukcop26.org/uk-presidency/what-is-a-cop/ (accessed 3 January 2022).

2. Masson-Delmotte V, Zhai P, Pirani A, et al. (eds). *Climate Change 2021: The Physical Science Basis. Contribution of Working Group I to the Sixth Assessment Report of the Intergovernmental Panel on Climate Change*. Cambridge University Press, 2021.

3. COP26 Goals. *UN Climate Change Conference (COP26) at the SEC – Glasgow 2021*, https://ukcop26.org/cop26-goals/ (accessed 2 December 2021).

4. The European Green Deal, https://eur-lex.europa.eu/resource.html?uri=cellar:b828d165-1c22-11ea-8c1f-01aa75ed71a1.0002.02/DOC_1&format=PDF (accessed 18 January 2022).

5. NextGenerationEU, https://europa.eu/next-generation-eu/index_en (accessed 30 September 2021).

6. Møller KT, Jensen TR, Akiba E, et al. Hydrogen - A sustainable energy carrier. *Prog Nat Sci Mater Int* 2017; 27: 34–40.

7. IEA – International Energy Agency. *IEA*, https://www.iea.org (accessed 18 January 2022).

8. Ritchie H, Roser M. Energy. *Our World Data*, https://ourworldindata.org/renewable-energy (2020, accessed 18 January 2022).

9. Hydrogen, https://www.snam.it/en/energy_transition/hydrogen/hydrogen/index.html (accessed 25 April 2021).

10. Reitz RD, Duraisamy G. Review of high efficiency and clean reactivity controlled compression ignition (RCCI) combustion in internal combustion engines. *Prog Energy Combust Sci* 2015; 46: 12–71.

11. Wei L, Geng P. A review on natural gas/diesel dual fuel combustion, emissions and performance. *Fuel Process Technol* 2016; 142: 264–278.

12. Agarwal AK, Singh AP, Maurya RK. Evolution, challenges and path forward for low temperature combustion engines. *Prog Energy Combust Sci* 2017; 61: 1–56.

13. Toulson E, Schock HJ, Attard WP. A Review of Pre-Chamber Initiated Jet Ignition Combustion Systems. pp. 2010-01–2263.

14. Zhao J. Research and application of over-expansion cycle (Atkinson and Miller) engines – A review. *Appl Energy* 2017; 185: 300–319.

15. Roberts M. Benefits and Challenges of Variable Compression Ratio (VCR). pp. 2003-01–0398.

16. Zhou F, Dede E, Joshi S. Application of Rankine Cycle to Passenger Vehicle Waste Heat Recovery - A Review. *SAE Int J Mater Manuf* 2016; 9: 224–235.

17. Aghaali H, Ångström H-E. A review of turbocompounding as a waste heat recovery system for internal combustion engines. *Renew Sustain Energy Rev* 2015; 49: 813–824.

18. Mustafi NN, Raine RR. A Study of the Emissions of a Dual Fuel Engine Operating with Alternative Gaseous Fuels. 12.

19. Pedrozo VB, May I, Guan W, et al. High efficiency ethanol-diesel dual-fuel combustion: A comparison against conventional diesel combustion from low to full engine load. *Fuel* 2018; 230: 440–451.

20. Saccullo M, Benham T, Denbratt I. Dual Fuel Methanol and Diesel Direct Injection HD Single Cylinder Engine Tests. pp. 2018-01–0259.

21. Zheng Z, Xia M, Liu H, et al. Experimental study on combustion and emissions of dual fuel RCCI mode fueled with biodiesel/n-butanol, biodiesel/2,5-dimethylfuran and biodiesel/ethanol. *Energy* 2018; 148: 824–838.

22. Chen Z, Yao M, Zheng Z, et al. Experimental and Numerical Study of Methanol/Dimethyl Ether Dual-Fuel Compound Combustion. *Energy Fuels* 2009; 23: 2719–2730.

23. Abnett K, Jessop S. EU drafts plan to label gas and nuclear investments as green. *Reuters*, 1 January 2022, https://www.reuters.com/markets/commodities/eu-drafts-plan-label-gas-nuclear-investments-green-2022-01-01/ (1 January 2022, accessed 3 January 2022).

24. Rankin J. EU in row over inclusion of gas and nuclear in sustainability guidance. *The Guardian*, 21 December 2021, https://www.theguardian.com/world/2021/dec/21/eu-in-row-over-inclusion-of-gas-and-nuclear-in-sustainability-guidance (21 December 2021, accessed 3 January 2022).

25. Alderman L, Pronczuk M. Europe Plans to Say Nuclear Power and Natural Gas Are Green Investments. *The New York Times*, 2 January 2022, https://www.nytimes.com/2022/01/02/business/europe-green-investments-nuclear-natural-gas.html (2 January 2022, accessed 3 January 2022).

26. A hydrogen strategy for a climate-neutral Europe, https://ec.europa.eu/energy/sites/ener/files/hydrogen_strategy.pdf (accessed 18 January 2022).

27. Dimitriou P, Tsujimura T. A review of hydrogen as a compression ignition engine fuel. *Int J Hydrog Energy* 2017; 42: 24470–24486.

28. Bowman CT. Kinetics of pollutant formation and destruction in combustion. *Prog Energy Combust Sci* 1975; 1: 33–45.

29. LAVOIE GA, HEYWOOD JB, KECK JC. Experimental and Theoretical Study of Nitric Oxide Formation in Internal Combustion Engines. *Combust Sci Technol*. Epub ahead of print 10 May 2007. DOI: 10.1080/00102206908952211.

30. Heywood JB. *Internal combustion engine fundamentals*. McGraw-Hill Education, 2018.

31. Yamaoka S, Kakuya H, Nakagawa S, et al. *HCCI Operation Control in a Multi-Cylinder Gasoline Engine*. SAE Technical Paper 2005-01–0120, Warrendale, PA: SAE International. Epub ahead of print 11 April 2005. DOI: 10.4271/2005-01-0120.

32. Haraldsson G, Tunestål P, Johansson B, et al. HCCI Closed-Loop Combustion Control Using Fast Thermal Management. pp. 2004-01–0943.

33. Agrell F, Ångström H-E, Eriksson B, et al. Integrated Simulation and Engine Test of Closed Loop HCCI Control by Aid of Variable Valve Timings. pp. 2003-01–0748.

34. Haraldsson G, Tunestål P, Johansson B, et al. HCCI Combustion Phasing with Closed-Loop Combustion Control Using Variable Compression Ratio in a Multi Cylinder Engine. *SAE Trans* 2003; 112: 1233–1245.

35. Saxena S, Bedoya ID. Fundamental phenomena affecting low temperature combustion and HCCI engines, high load limits and strategies for extending these limits. *Prog Energy Combust Sci* 2013; 39: 457–488.

36. Christensen M. *HCCI Combustion - Engine Operation and Emission Characteristics*. Thesis/Doccomp, Lund University, http://lup.lub.lu.se/record/465252 (2002, accessed 28 January 2022).

37. Dec JE, Yang Y. Boosted HCCI for High Power without Engine Knock and with Ultra-Low NOx Emissions - using Conventional Gasoline. *SAE Int J Engines* 2010; 3: 750–767.

38. Manente V, Johansson B, Tunestal P, et al. Influence of Inlet Pressure, EGR, Combustion Phasing, Speed and Pilot Ratio on High Load Gasoline Partially Premixed Combustion. pp. 2010-01–1471.

39. Liu H, Yao M, Zhang B, et al. Effects of Inlet Pressure and Octane Numbers on Combustion and Emissions of a Homogeneous Charge Compression Ignition (HCCI) Engine. *Energy Fuels* 2008; 22: 2207–2215.

40. Opat R, Ra Y, Gonzalez D. MA, et al. Investigation of Mixing and Temperature Effects on HC/CO Emissions for Highly Dilute Low Temperature Combustion in a Light Duty Diesel Engine. pp. 2007-01–0193.

41. Inagaki K, Fuyuto T, Nishikawa K, et al. Dual-Fuel PCI Combustion Controlled by In-Cylinder Stratification of Ignitability. pp. 2006-01–0028.

42. Bessonette PW, Schleyer CH, Duffy KP, et al. Effects of Fuel Property Changes on Heavy-Duty HCCI Combustion. pp. 2007-01–0191.

43. Furutani M, Isogai T, Ohta Y. Ignition Characteristics of Gaseous Fuels and Their Difference Elimination for SI and HCCI Gas Engines. pp. 2003-01–1857.

44. Shudo T, Takahashi T. Influence of Reformed Gas Composition on HCCI Combustion of Onboard Methanol-Reformed Gases. pp. 2004-01–1908.

45. Zheng Z, Yao M, Chen Z, et al. Experimental Study on HCCI Combustion of Dimethyl Ether(DME)/Methanol Dual Fuel. pp. 2004-01–2993.

46. Tomita E, Kawahara N, Piao Z, et al. Effects of EGR and Early Injection of Diesel Fuel on Combustion Characteristics and Exhaust Emissions in a Methane Dual Fuel Engine. pp. 2002-01–2723.

47. Ogawa H, Miyamoto N, Li C, et al. Low Emission and Knock-Free Combustion with Rich and Lean Biform Mixture in a Dual-Fuel CI Engine with Induced LPG as the Main Fuel. pp. 2001-01–3502.

48. Shim E, Park H, Bae C. Comparisons of advanced combustion technologies (HCCI, PCCI, and dual-fuel PCCI) on engine performance and emission characteristics in a heavy-duty diesel engine. *Fuel* 2020; 262: 116436.

49. Neely GD, Sasaki S, Huang Y, et al. New Diesel Emission Control Strategy to Meet US Tier 2 Emissions Regulations. *SAE Trans* 2005; 114: 512–524.

50. Ma S, Zheng Z, Liu H, et al. Experimental investigation of the effects of diesel injection strategy on gasoline/diesel dual-fuel combustion. *Appl Energy* 2013; 109: 202–212.

51. Benajes J, García A, Monsalve-Serrano J, et al. Achieving clean and efficient engine operation up to full load by combining optimized RCCI and dual-fuel diesel-gasoline combustion strategies. *Energy Convers Manag* 2017; 136: 142–151.

52. Xu Y, Kang H, Gong J, et al. A study on the combustion strategy of gasoline/diesel dual-fuel engine. *Fuel* 2018; 225: 426–435.

53. Benajes J, Molina S, García A, et al. An investigation on RCCI combustion in a heavy duty diesel engine using in-cylinder blending of diesel and gasoline fuels. *Appl Therm Eng* 2014; 63: 66–76.

54. Splitter D, Kokjohn S, Rein K, et al. An Optical Investigation of Ignition Processes in Fuel Reactivity Controlled PCCI Combustion. *SAE Int J Engines* 2010; 3: 142–162.

55. Hanson RM, Kokjohn SL, Splitter DA, et al. An Experimental Investigation of Fuel Reactivity Controlled PCCI Combustion in a Heavy-Duty Engine. *SAE Int J Engines* 2010; 3: 700–716.

56. Kavuri C, Kokjohn SL. Computational optimization of a reactivity controlled compression ignition (RCCI) combustion system considering performance at multiple modes simultaneously. *Fuel* 2017; 207: 702–718.

57. Kokjohn S, Hanson R, Splitter D, et al. Fuel Reactivity Controlled Compression Ignition (RCCI) Combustion in Light- and Heavy-Duty Engines. *SAE Int J Engines* 2011; 4: 360–374.

58. Kokjohn S, Reitz R, Splitter D, et al. Investigation of Fuel Reactivity Stratification for Controlling PCI Heat-Release Rates Using High-Speed Chemiluminescence Imaging and Fuel Tracer Fluorescence. *SAE Int J Engines* 2012; 5: 248–269.

59. Klos D, Janecek D, Kokjohn S. Investigation of the Combustion Instability-NOx Tradeoff in a Dual Fuel Reactivity Controlled Compression Ignition (RCCI) Engine. *SAE Int J Engines* 2015; 8: 821–830.

60. Tang Q, Liu H, Li M, et al. Multiple optical diagnostics on effect of fuel stratification degree on reactivity controlled compression ignition. *Fuel* 2017; 202: 688–698.

61. Guan W, Wang X, Zhao H, et al. Exploring the high load potential of diesel–methanol dual-fuel operation with Miller cycle, exhaust gas recirculation, and intake air cooling on a heavy-duty diesel engine. *Int J Engine Res* 2020; 1468087420926775.

62. Ning L, Duan Q, Chen Z, et al. A comparative study on the combustion and emissions of a non-road common rail diesel engine fueled with primary alcohol fuels (methanol, ethanol, and n-butanol)/diesel dual fuel. *Fuel* 2020; 266: 117034.

63. Papagiannakis RG, Rakopoulos CD, Hountalas DT, et al. Emission characteristics of high speed, dual fuel, compression ignition engine operating in a wide range of natural gas/diesel fuel proportions. 2010; 10.

64. Nieman DE, Dempsey AB, Reitz RD. Heavy-Duty RCCI Operation Using Natural Gas and Diesel. *SAE Int J Engines* 2012; 5: 270–285.

65. Lounici MS, Loubar K, Tarabet L, et al. Towards improvement of natural gas-diesel dual fuel mode: An experimental investigation on performance and exhaust emissions. *Energy* 2014; 64: 200–211.

66. Kim W, Park C, Bae C. Characterization of combustion process and emissions in a natural gas/diesel dual-fuel compression-ignition engine. *Fuel* 2021; 291: 120043.

67. Niki Y, Rajasegar R, Li Z, et al. Verification of diesel spray ignition phenomenon in dual-fuel diesel-piloted premixed natural gas engine. *Int J Engine Res* 2020; 1468087420983060.

68. Rochussen J, Kirchen P. Characterization of reaction zone growth in an optically accessible heavy-duty diesel/methane dual-fuel engine. *Int J Engine Res* 2019; 20: 483–500.

69. Wu Z, Rutland CJ, Han Z. Numerical evaluation of the effect of methane number on natural gas and diesel dual-fuel combustion. *Int J Engine Res* 2019; 20: 405–423.

70. Pedrozo VB, Wang X, Guan W, et al. The effects of natural gas composition on conventional dual-fuel and reactivity-controlled compression ignition combustion in a heavy-duty diesel engine. *Int J Engine Res* 2021; 146808742098404.

71. Dev S, Guo H, Lafrance S, et al. An Experimental Study on the Effect of Exhaust Gas Recirculation on a Natural Gas-Diesel Dual-Fuel Engine. pp. 2020-01–0310.

72. Wu Z, Rutland CJ, Han Z. Numerical optimization of natural gas and diesel dual-fuel combustion for a heavy-duty engine operated at a medium load. *Int J Engine Res* 2018; 19: 682–696.

73. Yousefi A. Effect of diesel injection timing on the combustion of natural gas/diesel dual-fuel engine at low-high load and low-high speed conditions. 2019; 9.

74. Korkmaz M, Ritter D, Jochim B, et al. Effects of injection strategy on performance and emissions metrics in a diesel/methane dual-fuel single-cylinder compression ignition engine. *Int J Engine Res* 2019; 20: 1059–1072.

75. Yousefi A, Guo H, Birouk M, et al. Effect of post-injection strategy on greenhouse gas emissions of natural gas/diesel dual-fuel engine at high load conditions. *Fuel* 2021; 290: 120071.

76. Dai X (Hunter), Singh S, Krishnan SR, et al. Numerical study of combustion characteristics and emissions of a diesel–methane dual-fuel engine for a wide range of injection timings. *Int J Engine Res* 2020; 21: 781–793.

77. Lee S, Kim C, Lee S, et al. Diesel injector nozzle optimization for high CNG substitution in a dual-fuel heavy-duty diesel engine. *Fuel* 2020; 262: 116607.

78. Yousefi A, Guo H, Birouk M. Effect of swirl ratio on NG/diesel dual-fuel combustion at low to high engine load conditions. *Appl Energy* 2018; 229: 375–388.

79. Liu J, Wang J, Zhao H. Optimization of the injection parameters and combustion chamber geometries of a diesel/natural gas RCCI engine. *Energy* 2018; 164: 837–852.

80. Hutter R, Ritzmann J, Elbert P, et al. Low-Load Limit in a Diesel-Ignited Gas Engine. *Energies* 2017; 10: 1450.

81. Kozarac D, Sremec M, Bozic M, et al. The Performance and Emissions of a Conventional Natural Gas/Diesel Dual Fuel Engine at Various Operating Conditions. pp. 2019-01–1158.

82. Li Y, Li H, Guo H, et al. A numerical investigation on methane combustion and emissions from a natural gas-diesel dual fuel engine using CFD model. *Appl Energy* 2017; 10.

83. Glassman I, Yetter RA, Glumac NG. Chapter 3 - Explosive and general oxidative characteristics of fuels. In: Glassman I, Yetter RA, Glumac NG (eds) *Combustion (Fifth Edition)*. Boston: Academic Press, pp. 71–146.

84. Pachauri RK, Allen MR, Barros VR, et al. *Climate Change 2014: Synthesis Report. Contribution of Working Groups I, II and III to the Fifth Assessment Report of the Intergovernmental Panel on Climate Change*. Geneva, Switzerland: IPCC.

85. The European Green Deal, https://eur-lex.europa.eu/legal-content/EN/TXT/HTML/?uri=CELEX:52019DC0640&from=EN (accessed 11 April 2021).

86. Yousefi A, Birouk M, Guo H. An experimental and numerical study of the effect of diesel injection timing on natural gas/diesel dual-fuel combustion at low load. *Fuel* 2017; 203: 642–657.

87. Yousefi A, Guo H, Birouk M, et al. On greenhouse gas emissions and thermal efficiency of natural gas/diesel dual-fuel engine at low load conditions: Coupled effect of injector rail pressure and split injection. *Appl Energy* 2019; 242: 216–231.

88. Park H, Shim E, Bae C. Improvement of combustion and emissions with exhaust gas recirculation in a natural gas-diesel dual-fuel premixed charge compression ignition engine at low load operations. *Fuel* 2019; 235: 763–774.

89. Shen Z, Wang X, Zhao H, et al. Numerical investigation of natural gas-diesel dual-fuel engine with different piston geometries and radial clearances. *Energy* 2021; 220: 119706.

90. Miao H, Lu L, Huang Z. Flammability limits of hydrogen-enriched natural gas. *Int J Hydrog Energy* 2011; 36: 6937–6947.

91. Schefer RW. Hydrogen enrichment for improved lean flame stability. *Int J Hydrog Energy* 2003; 11.

92. Rahnama P, Paykani A, Reitz RD. A numerical study of the effects of using hydrogen, reformer gas and nitrogen on combustion, emissions and load limits of a heavy duty natural gas/diesel RCCI engine. *Appl Energy* 2017; 193: 182–198.

93. Ouchikh S, Lounici MS, Tarabet L, et al. Effect of natural gas enrichment with hydrogen on combustion characteristics of a dual fuel diesel engine. *Int J Hydrog Energy* 2019; 44: 13974–13987.

94. Talibi M, Balachandran R, Ladommatos N. Influence of combusting methane-hydrogen mixtures on compression–ignition engine exhaust emissions and in-cylinder gas composition. *Int J Hydrog Energy* 2017; 42: 2381–2396.

95. De Simio L, Iannaccone S. Gaseous and particle emissions in low-temperature combustion diesel–HCNG dual-fuel operation with double pilot injection. *Appl Energy* 2019; 253: 113602.

96. Zhou JH, Cheung CS, Leung CW. Combustion, performance and emissions of a diesel engine with H2, CH4 and H2–CH4 addition. *Int J Hydrog Energy* 2014; 39: 4611–4621.

97. Park S-H, Lee K-M, Hwang C-H. Effects of hydrogen addition on soot formation and oxidation in laminar premixed C 2 H 2 /air flames. *Int J Hydrog Energy* 2011; 36: 9304–9311.

98. Wang J, Huang Z, Tang C, et al. Numerical study of the effect of hydrogen addition on methane–air mixtures combustion. *Int J Hydrog Energy* 2009; 34: 1084–1096.

99. Liu F, Kang Y, Wu H, et al. Effect of Hydrogen Volume Ratio on the Combustion Characteristics of CNG-Diesel Dual-Fuel Engine. pp. 2017-01–2270.

100. Shao Z, Dallmann T, Bandivadekar A. European Stage V non-road emission standards. 9.

101. BFL_914_Genset_EN.pdf, https://www.deutz.com/fileadmin/contents/com/engines/stationaere_anlagen/en/BFL_914_Genset_EN.pdf (accessed 4 January 2022).

102. D5 - EU Stage IIIA/Epa Tier 3 | Power Generation Engine Range | Volvo Penta, https://www.volvopenta.com/industrial/power-generation/power-generation-engine-range/d5-eu-stage-iiia-epa-tier-3/ (accessed 4 January 2022).

103. QSB5G4_0.pdf, https://www.cummins.com/sites/default/files/2019-06/QSB5G4_0.pdf (accessed 4 January 2022).

104. 100 kVA Generator set Diésel HFW-100 T5 Open Skid, https://www.himoinsa.com/eng/electric-generators/3992/generator-set--100kva--open-skid.html (accessed 4 January 2022).

105. 4M11G90-5_DataSheet_Gb.pdf, https://www.baudouin.nl/wp-content/themes/baudouin/files/powerkit-engines/Datasheets/4M11G90-5_DataSheet_Gb.pdf (accessed 4 January 2022).

106. Mattarelli E, Rinaldini CA, Savioli T, et al. Optimization of a High-Speed Dual-Fuel (Natural Gas-Diesel) Compression Ignition Engine for Gen-sets. *SAE Int J Engines* 2021; 14: 03-14-03–0022.

107. Cameretti MC, De Robbio R, Tuccillo R. Performance Improvement and Emission Control of a Dual Fuel Operated Diesel Engine. pp. 2017-24–0066.

108. Yamamoto H, Uchida H. Oxidation of methane over Pt and Pd supported on alumina in lean-burn natural-gas engine exhaust. *Catal Today* 1998; 45: 147–151.

109. Hutter R, De Libero L, Elbert P, et al. Catalytic methane oxidation in the exhaust gas aftertreatment of a lean-burn natural gas engine. *Chem Eng J* 2018; 349: 156–167.

110. Amsden AA. *KIVA-3: A KIVA program with block-structured mesh for complex geometries*. LA-12503-MS, Los Alamos National Lab., NM (United States), https://www.osti.gov/biblio/6605386-kiva-kiva-program-block-structured-mesh-complex-geometries (1 March 1993, accessed 21 January 2022).

111. Golovitchev VI, Imren A. Development of dual fuel combustion models for direct injected heavy duty diesel engines. *Diesel Fuels Charact Perform Environ Impacts Nova Pusblisher*.

112. Golovitchev VI, Nordin N, Jarnicki R, et al. 3-D Diesel Spray Simulations Using a New Detailed Chemistry Turbulent Combustion Model. *SAE Trans* 2000; 109: 1391–1405.

113. Lipatnikov AN, Chomiak J. Turbulent fame speed and thickness: phenomenology, evaluation, and application in multi-dimensional simulations. *Prog Energy Combust Sci* 2002; 74.

114. Golovitchev VI, Montorsi L, Rinaldini CA, et al. CFD Combustion and Emission Formation Modeling for a HSDI Diesel Engine Using Detailed Chemistry. American Society of Mechanical Engineers Digital Collection, pp. 349–358.

115. Lutz AE, Kee RJ, Miller JA. *SENKIN: A Fortran program for predicting homogeneous gas phase chemical kinetics with sensitivity analysis*. SAND-87-8248, Sandia National Labs., Livermore, CA (USA), https://www.osti.gov/biblio/5371815-senkin-fortran-program-predicting-homogeneous-gas-phase-chemical-kinetics-sensitivity-analysis (1 February 1988, accessed 9 January 2022).

116. Kee R, Grcar J, Smooke M, et al. PREMIX: a fortran program for modeling steady laminar one-dimensional premixed flames. *Sandia Rep*; 143.

117. Nordin PN. *Complex chemistry modeling of diesel spray combustion*. Chalmers University of Technology Sweden, 2001.

118. Reitz RD. Modeling atomization processes in high-pressure vaporizing sprays. *At Spray Technol* 1987; 3: 309–337.

119. Su TF, Patterson MA, Reitz RD, et al. Experimental and Numerical Studies of High Pressure Multiple Injection Sprays. *SAE Trans* 1996; 105: 1281–1292.

120. Ricart LM, Xin J, Bower GR, et al. In-Cylinder Measurement and Modeling of Liquid Fuel Spray Penetration in a Heavy-Duty Diesel Engine. *SAE Trans* 1997; 106: 1622–1640.

121. Golovitchev VI, Atarashiya K, Tanaka K, et al. TOWARDS UNIVERSAL EDC-BASED COMBUSTION MODEL FOR COMPRESSION IGNITED ENGINE SIMULATIONS. pp. 2003-01–1849.

122. Magnussen BF, Hjertager BH. On mathematical modeling of turbulent combustion with special emphasis on soot formation and combustion. *Symp Int Combust* 1977; 16: 719–729.

123. Metghalchi M, Keck JC. Burning velocities of mixtures of air with methanol, isooctane, and indolene at high pressure and temperature. *Combust Flame* 1982; 48: 191–210.

124. Gülder ÖL. Turbulent premixed flame propagation models for different combustion regimes. *Symp Int Combust* 1991; 23: 743–750.

125. Kee R, Rupley F, Miller J. *Chemkin-II: A Fortran chemical kinetics package for the analysis of gas-phase chemical kinetics*. SAND-89-8009, 5681118, ON: DE90000917.

126. Huang J, Hill PG, Bushe WK, et al. Shock-tube study of methane ignition under engine-relevant conditions: experiments and modeling. *Combust Flame* 2004; 136: 25–42.

127. Liao SY, Jiang DM, Cheng Q. Determination of laminar burning velocities for natural gas. *Fuel* 2004; 83: 1247–1250.

128. Bogin GE, DeFilippo A, Chen JY, et al. Numerical and Experimental Investigation of *n* -Heptane Autoignition in the Ignition Quality Tester (IQT). *Energy Fuels* 2011; 25: 5562–5572.

129. Davidson DF, Gauthier BM, Hanson RK. Shock tube ignition measurements of iso-octane/air and toluene/air at high pressures. *Proc Combust Inst* 2005; 30: 1175–1182.

130. Cantore G, Mattarelli E, Rinaldini CA, et al. Numerical Optimization of the Injection Strategy on a Light Duty Diesel Engine Operating in Dual Fuel (CNG/Diesel) Mode. *Int J Heat Technol* 2019; 37: 682–688.

131. Amsden AA. *KIVA-3V: A block-structured KIVA program for engines with vertical or canted valves*. LA--13313-MS, 505339.

132. Mattarelli E, Rinaldini CA, Savioli T. Dual Fuel (Natural Gas Diesel) for Light-Duty Industrial Engines: A Numerical and Experimental Investigation. In: Srinivasan KK, Agarwal AK, Krishnan SR, et al. (eds) *Natural Gas Engines : For Transportation and Power Generation*. Singapore: Springer, pp. 297–328.

133. CFD-3D Analysis of a Light Duty Dual Fuel (Diesel/Natural Gas) Combustion Engine | Elsevier Enhanced Reader, https://reader.elsevier.com/reader/sd/pii/S187661021400099X?token=514C68D08370497AD6FB98BFD2593FC3DE2A595ADE4CA8E5D49ED66E3CB94CCCE1D3019FC6CE71D23C732807118551E6&originRegion=eu-west-1&originCreation=20220108161756 (accessed 8 January 2022).

134. Mattarelli E, Alberto Rinaldini C, Caprioli S, et al. Influence of H_2 enrichment for improving low load combustion stability of a Dual Fuel lightduty Diesel engine. *Int J Engine Res* 2021; 146808742110516.

135. ANSYS Forte Theory Manual, https://ansyshelp.ansys.com/Views/Secured/corp/v211/en/forte_th/forte_th.html (accessed 25 April 2021).

136. Regulation No 49 of the Economic Commission for Europe of the United Nations (UN/ECE)), https://eur-lex.europa.eu/legal-content/EN/TXT/HTML/?uri=CELEX:42013X0624(01)&from=EN (accessed 11 April 2021).

137. Abani N, Kokjohn S, Park SW, et al. An Improved Spray Model for Reducing Numerical Parameter Dependencies in Diesel Engine CFD Simulations. pp. 2008-01–0970.

138. Senecal PK, Pomraning E, Richards KJ, et al. Grid-Convergent Spray Models for Internal Combustion Engine CFD Simulations. American Society of Mechanical Engineers Digital Collection, pp. 697–710.

139. Yoon SH, Lee CS. Experimental investigation on the combustion and exhaust emission characteristics of biogas–biodiesel dual-fuel combustion in a CI engine. *Fuel Process Technol* 2011; 92: 992–1000.

140. Legrottaglie F, Mattarelli E, Rinaldini CA, et al. Application to micro-cogeneration of an innovative dual fuel compression ignition engine running on biogas. *Int J Thermofluids* 2021; 10: 100093.

141. Klimstra J. Interchangeability of Gaseous Fuels — The Importance of the Wobbe-Index. p. 861578.

142. Datasheet HIMOINSA HGE-95 T5 BIO.pdf.

143. Rahmouni C, Tazerout M, Le Corre O. A Method to Determine Biogas Composition for Combustion Control. pp. 2002-01–1708.

144. Mattarelli E, Rinaldini CA, Cantore G, et al. *2-Stroke Externally Scavenged Engines for Range Extender Applications*. SAE Technical Paper 2012-01–1022, Warrendale, PA: SAE International. Epub ahead of print 16 April 2012. DOI: 10.4271/2012-01-1022.

145. Cantore G, Mattarelli E, Rinaldini CA. A New Design Concept for 2-Stroke Aircraft Diesel Engines. *Energy Procedia* 2014; 45: 739–748.

146. Mattarelli E, Rinaldini CA, Savioli T. Port Design Criteria for 2-Stroke Loop Scavenged Engines. pp. 2016-01–0610.

147. Winkler F, Kirchberger R, Schoegl O, et al. *Strategies to Reduce Scavenge Losses of Small Capacity 2-Stroke Engines, Pressurized by the Common Market Costs*. 0 ed. 2005-32–0098, Warrendale, PA: SAE International.

148. Winkler F, Oswald R, Schögl O, et al. Application of Low Pressure Direct Injection and Semi-Direct Injection to a Small Capacity Two-Stroke Engine. pp. 2008-32–0059.

149. Oswald R, Ebner A, Kirchberger R. High Efficient 125- 250 cm ^{3} LPDI Two-Stroke Engines, a Cheap and Robust Alternative to Four-Stroke Solutions? pp. 2010-32–0019.

150. Krimplstätter S, Winkler F, Oswald R, et al. Air Cooled 50cm ^{3} Scooter Euro 4 Application of the Two-Stroke LPDI Technology. pp. 2014-32–0008.

151. Winkler F, Oswald R, Schögl O, et al. Layout and Development of a 300 cm^3 High Performance 2S-LPDI Engine. 12.

152. Balduzzi F, Vichi G, Romani L, et al. CFD Analysis of the Effect of the Injection Pressure on a Small 2S LPDI Engine. 10.

153. Romani L, Vichi G, Balduzzi F, et al. Fine-tuning of a two stoke engine in full power configuration provided with a Low Pressure Direct Injection system. *Energy Procedia* 2017; 126: 987–994.

154. Mattarelli E, Rinaldini CA, Scrignoli F, et al. Development of a Hybrid Power Unit for Formula SAE Application: ICE CFD-1D Optimization and Vehicle Lap Simulation. pp. 2019-24–0200.

155. Rules, https://www.imeche.org/events/formula-student/team-information/rules (accessed 16 January 2022).

Appendix

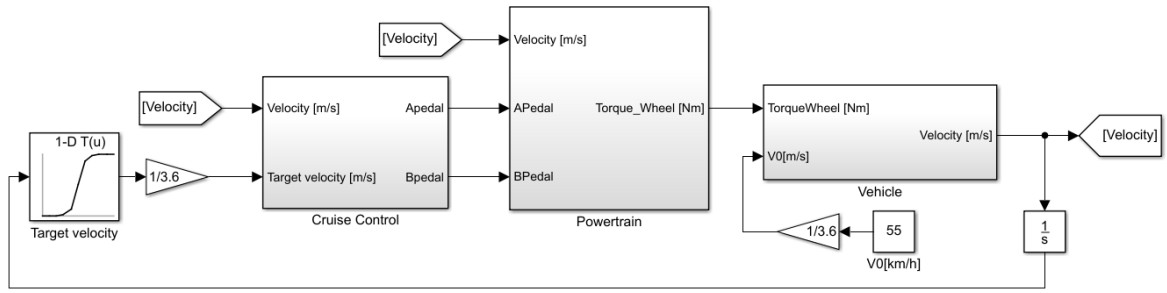

MATLAB-Simulink model of the HEV

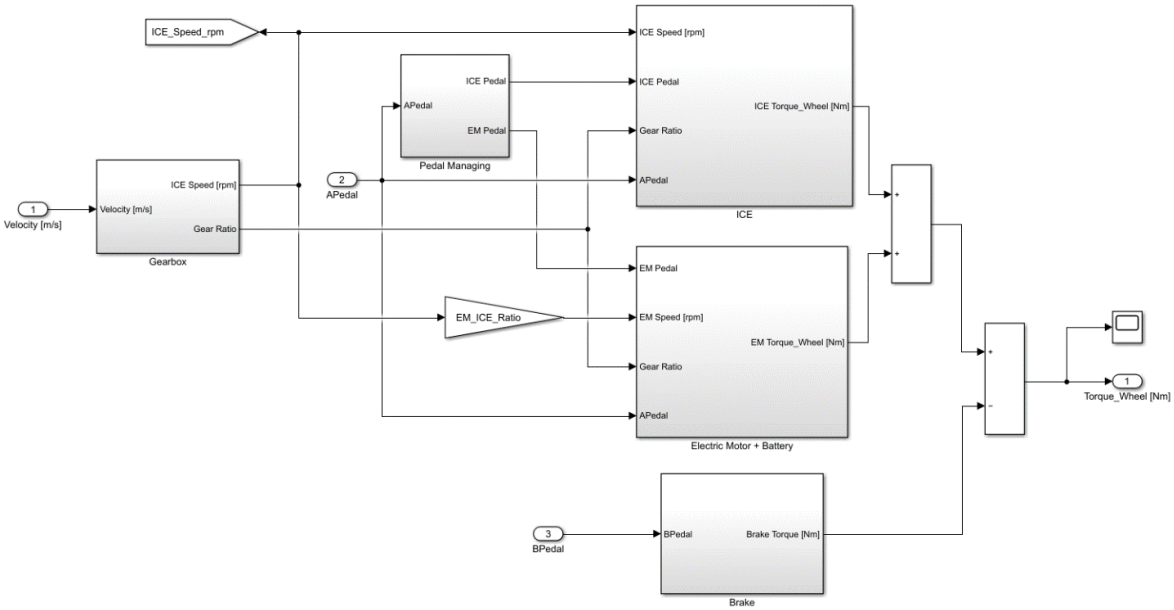

Powertrain sub-model of the MATLAB-Simulink model of the HEV

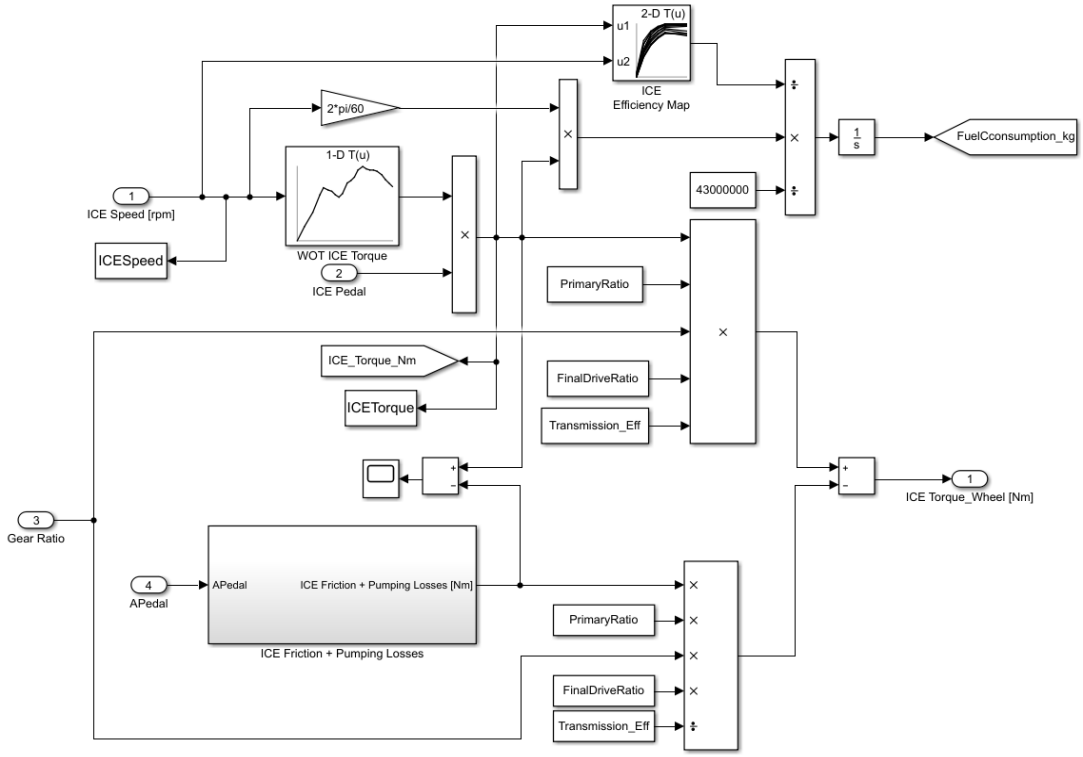

ICE sub-model of the MATLAB-Simulink model of the HEV

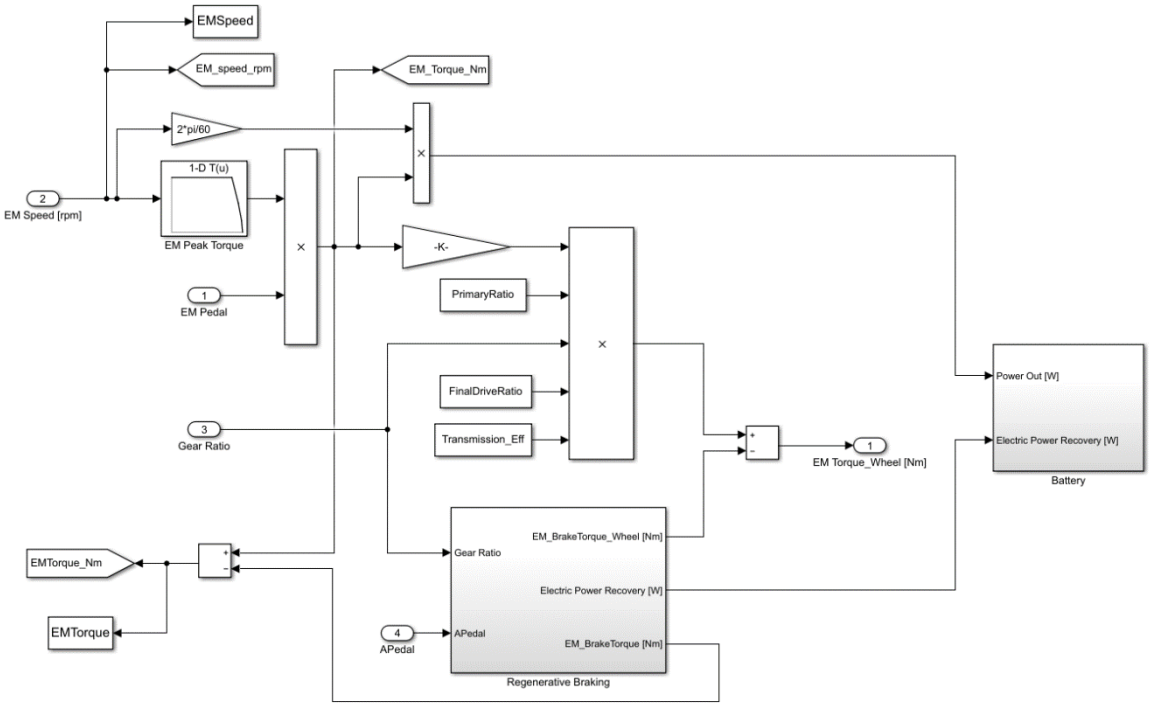

EM sub-model of the MATLAB-Simulink model of the HEV

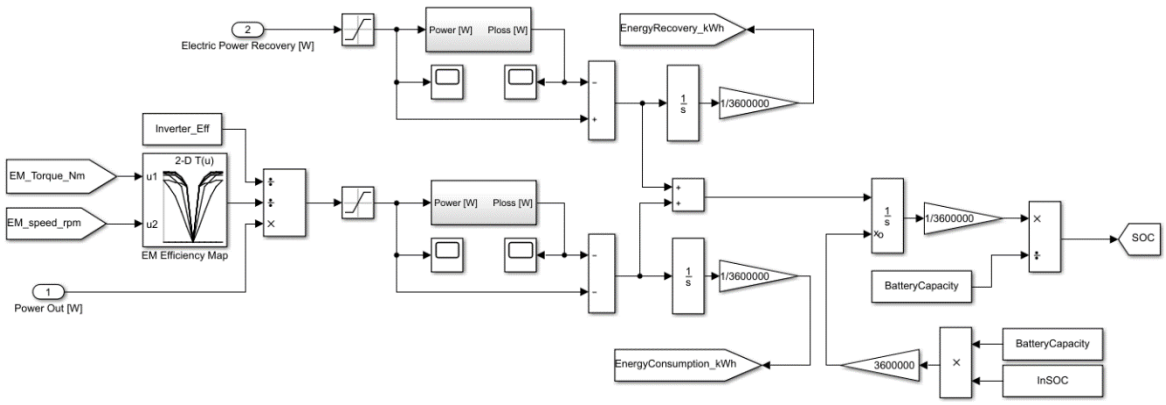

Battery sub-model of the MATLAB-Simulink model of the HEV

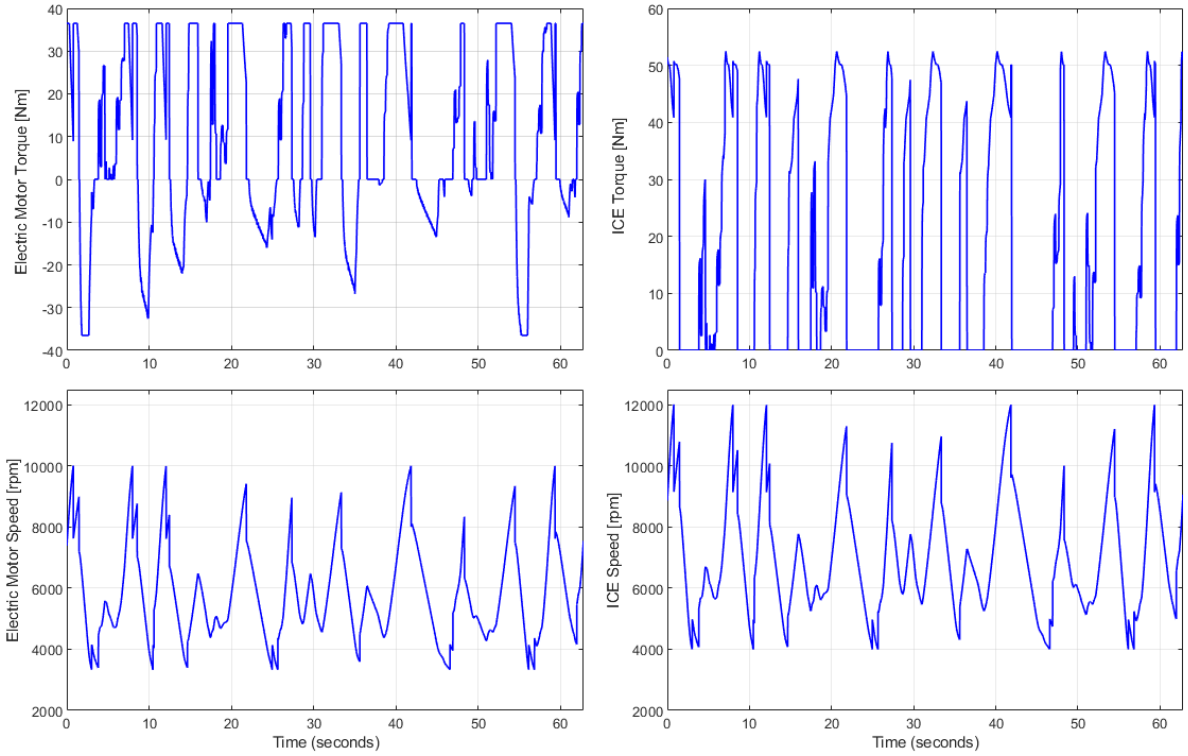

EM (left) and ICE (right) torque and rotational speed predicted by the MATLAB-Simulink